Downloaded from orbit.dtu.dk on: Dec 20, 2017

Technical University of Denmark

High Temperature and Pressure Alkaline Electrolysis

Allebrod, Frank; Mogensen, Mogens Bjerg; Hjelm, Johan; Ebbesen, Sune Dalgaard

Publication date:
2013

Document Version
Publisher's PDF, also known as Version of record

Link back to DTU Orbit

Citation (APA):
Allebrod, F., Mogensen, M. B., Hjelm, J., & Ebbesen, S. D. (2013). High Temperature and Pressure Alkaline Electrolysis. Department of Energy Conversion and Storage, Technical University of Denmark.

DTU Library
Technical Information Center of Denmark

General rights
Copyright and moral rights for the publications made accessible in the public portal are retained by the authors and/or other copyright owners and it is a condition of accessing publications that users recognise and abide by the legal requirements associated with these rights.

- Users may download and print one copy of any publication from the public portal for the purpose of private study or research.
- You may not further distribute the material or use it for any profit-making activity or commercial gain
- You may freely distribute the URL identifying the publication in the public portal

If you believe that this document breaches copyright please contact us providing details, and we will remove access to the work immediately and investigate your claim.

HIGH TEMPERATURE AND PRESSURE ALKALINE ELECTROLYSIS

FRANK ALLEBROD

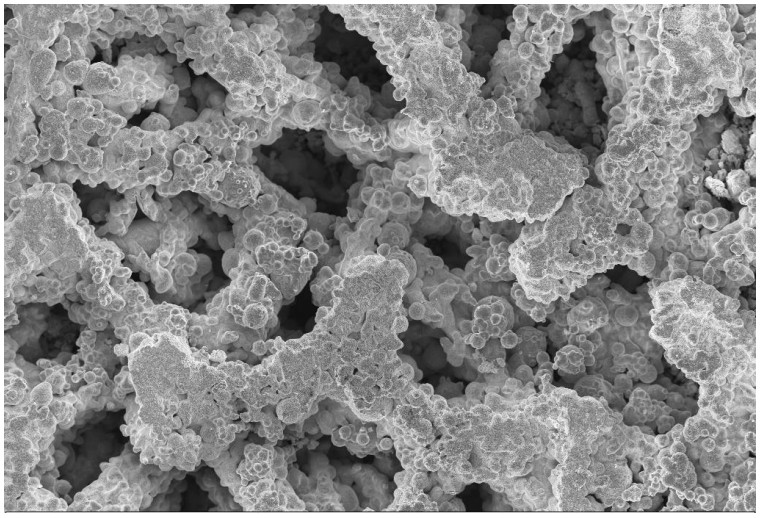

PhD Thesis

1st revised edition

March 2013

DTU Energy Conversion
Department of Energy Conversion and Storage

Frank Allebrod: *High Temperature and Pressure Alkaline Electrolysis*, PhD Thesis, DTU Technical University of Denmark, Department for Energy Conversion and Storage, 1st revised edition, © March 2013

Doctoral thesis defended publicly on 28th January 2013 at Niels Bohr Auditorium, Technical University of Denmark, Risø Campus[1]

Frontpage: Scanning electron microscopy image of an Inconel foam. The Inconel foam was used as a cathode in some of the electrolysis cells in the here presented research.

---

1 **Faculty Opponents:**
1. Prof. Svein Sunde - Norwegian University of Science and Technology
2. Prof. Eivind M. Skou - University of Southern Denmark
3. Dr. Peter Holtappels - Technical University of Denmark

Supervisor
Prof. Mogens Mogensen - Technical University of Denmark

Co- Supervisors
Senior Scientist Johan Hjelm - Technical University of Denmark
Senior Scientist Sune Ebbesen - Technical University of Denmark

To those who stayed

my beloved parents

my beloved girlfriend

my beloved friends

ABSTRACT

The production of energy from renewable sources has the possibility to fulfill the worldwide energy demand. Electricity generation from wind energy converters and photovoltaic systems will be implemented within the European Union to a large extent. The fluctuation of the wind speed and solar radiation raises the necessity to store the produced energy. Hydrogen production by water electrolysis is one of the most promising ways to do so. Alkaline electrolyzers have proven to operate reliable for decades on a large scale (up to 160 MW), but in order to become commercially attractive and compete against conventional technologies for hydrogen production, such as natural gas reforming, the production and investment costs have to be reduced. A reduction of the investment costs may be achieved by increasing the operational pressure and temperature of the electrolyzer, as this will result in: 1) production of pressurized hydrogen and oxygen, 2) improved electrical efficiencies and 3) increased current density, i.e. increased hydrogen production rate for a given electrolyser cell area.

This thesis describes an exploratory technical study mainly in order to examine the possibility to produce hydrogen and oxygen with a new type of alkaline electrolysis cell at high temperatures and pressures. To perform measurements under high pressure and at elevated temperatures it was necessary to build a measurement system around an autoclave which could stand high temperatures up to 250 °C and pressures up to 200 bar as well as extremely caustic environments. Based on a literature study to identify resistant materials for these conditions, Inconel 600 was selected among the metals which are available for autoclave construction. An initial single atmosphere high temperature and pressure measurement setup was build comprising this autoclave. A second high temperature and pressure measurement setup was build based on experiences from the first setup in order to perform automatized measurements. The conductivity of aqueous KOH at elevated temperatures and high concentrations was investigated using the van der Pauw method in combination with electrochemical impedance spectroscopy (EIS). Conductivity values as high as 2.7 S cm^{-1} for 35 wt%, 2.9 S cm^{-1} for 45 wt%, and 2.8 S cm^{-1} for 55 wt% concentrated aqueous solutions were measured at 200 °C. The conductivity of immobilized KOH was determined by the same method in the same temperature and concentration range. Conductivity values as high as 0.67 S cm^{-1} for 35 wt%, 0.84 S cm^{-1} for 45 wt%, and 0.73 S cm^{-1} for 55 wt% concentrated immobilized aqueous solutions were determined at 200 °C.

A new type of an alkaline electrolysis cell was developed in order to operate at high temperatures and pressures. Aqueous potassium hydroxide immobilized electrolyte in porous $SrTiO_3$ was used in those cells. Electrolysis cells with metal foam based gas diffusion electrodes and the immobilized electrolyte we-

re successfully demonstrated at temperatures up to 250 °C and 40 bar. Different electro-catalysts were tested in order to reduce the oxygen and hydrogen overpotentials. Current densities of 1.1 A cm^{-2} and 2.3 A cm^{-2} have been measured at a cell voltage of 1.5 V and 1.75 V, respectively, without using expensive noble metal catalysts. Electrical efficiencies of almost 99 % at 1.1 A cm^{-2} and 85 % at 2.3 A cm^{-2} combined with relatively small production costs may lead to both reduced investment and operating costs for hydrogen and oxygen production. One of the produced electrolysis cells was operated for 350 h. Based on the successful results a patent application covering this novel cell was filed. Based on the successful results a patent application covering this novel cell was filed. Assuming that the developed cells will be scaled up and successfully tested for some thousand hours, they may offer an important role in future energy storage scenarios.

ABSTRAKT

Produktion af energi fra vedvarende energikilder kan potentielt dække verdens energibehov. Elektricitet genereret fra vind- og solenergi vil høst sandsynlig blive udbredt væsentligt i fremtiden i den europæiske union. På grund af fluktuationer i vindhastighed og indstråling fra solen skaber dette et behov for at kunne lagre den producerede energi. Hydrogen produktion vha. elektrolyse er en af de mest lovende måder at gøre dette på. Alkaliske elektrolysatorer har gennem de sidste årtier vist sig pålidelige i storskala (op til 160 MW), men for at blive kommercielt interessante, og for samtidig at kunne konkurrere mod alternative metoder til hydrogenproduktion som naturgas-reformering, må produktions- og investeringsudgifterne reduceres. En reduktion af investeringsudgifterne kan opnås ved at hæve processtemperatur og -tryk, da dette vil resultere i: 1) produktion af tryksat hydrogen og oxygen, 2) forøget elektrisk effektivitet og 3) forøget strømtæthed, dvs. forøget produktionshastighed af hydrogen for et givent elektrolysecelleareal.

Denne afhandling beskriver en række orienterende teknisk forsøg primært med henblik på at undersøge muligheden for at producere brint og ilt med en ny type alkalisk elektrolysecelle ved høje temperaturer og tryk. For at kunne udføre målinger under højt tryk og ved forhøjede temperaturer var det nødvendigt at opbygge et målesystem omkring en autoklave, der kunne tåle høje temperaturer op til 250 °C og tryk op til 95 bar samt yderst basiske betingelser. Baseret på et litteraturstudium med henblik på at identificere resistente materialer til disse betingelser blev Inconel 600 udvalgt blandt de metaller, som er tilgængelige for autoklavebyggeri. En forsøgsopstilling med høj temperatur og tryk blev bygget omkring en sådan autoklave, der ved forsøgsstart blot havde en atmosfære med én gassammensætning. En anden opstilling til automatiserede målinger ved høj temperatur og tryk blev bygget baseret på erfaringer fra den første opstilling. Ledningsevnen af vandig KOH ved forhøjede temperaturer og høje koncentrationer blev undersøgt ved hjælp af van der Pauw

metoden i kombination med elektrokemisk impedansspektroskopi (EIS). Ledningsevneværdier så høje som $2,7\ S\ cm^{-1}$ med 35 vægt% KOH, $2,9\ S\ cm^{-1}$ med 45 vægt%, og $2,8\ S\ cm^{-1}$ med 55 vægt% koncentreret vandige opløsninger blev målt ved 200 °C. Ledningsevnen af immobiliseret KOH blev bestemt ved den samme fremgangsmåde i samme temperatur og koncentrationsområde. Ledningsevneværdier af immobiliserede vandige opløsninger så høje som $0,67\ S\ cm^{-1}$ med 35 vægt%, $0,84\ S\ cm^{-1}$ med 45 vægt%, og $0,73\ S\ cm^{-1}$ med 55 vægt% blev målt ved 200 °C.

En ny type af alkaliske elektrolysecelle, der kan drives ved høj temperatur og tryk, er blevet udviklet. En elektrolyt bestående af vandigt kalium hydroxid immobiliseret i en porøs $SrTiO_3$ struktur blev anvendt i disse celler. Elektrolyseceller med gasdiffusionselektroder baseret på metalskum og den immobiliserede elektrolyt blev demonstreret ved temperaturer op til 250 °C og 40 bar. Strømtætheder på $1,1\ A\ cm^{-2}$ og $2,3\ A\ cm^{-2}$ blev målt med en cellespænding på hhv. 1,5 V og 1,75 V uden brug af dyre ædelmetal-katalysatorer. En elektrisk effektivitet på næsten 99 % ved $1,1\ A\ cm^{-2}$ og 85 % ved $2,3\ A\ cm^{-2}$, kombineret med relativ lave produktionsomkostninger, kan sandsynligvis føre til både reduceret investerings- og driftsomkostninger ved produktion af hydrogen og oxygen. En af de fremstillede celler blev indledningsvis "langtidstests" i 350 timer. Under antagelse af at de udviklede celler vil blive opskaleret og succesfyldt testet i tusinder af timer, kan disse celler muligvis komme til at spille en vigtig rolle i fremtidens scenarier for energilagring.

ACKNOWLEDGMENTS

Many people have contributed either directly or indirectly to this study. First of all I would like to thank my supervisor, Mogens Mogensen, for his ideas, his enthusiasm and patience in teaching, and his enormous efforts to bring this study to the stage it reached. It was a pleasure to be his student and I am looking forward to continue working in his group.

I am especially thankful to Christodoulos Chatzichristodoulou for his work on the automatized high pressure and temperature measurement setup, for his teaching, for worthy discussions along the way and his detailed comments on an earlier draft on this thesis. I am looking forward to continue my research together with him.

In particular I would like to thank Jonathan Hallinder for all his help along the way. It was a great pleasure to share knowledge and other things. I am thankful to him not only for beeing a good collegue, but also a good friend.

Furthermore, I want to thank Ane Sælland Christiansen for her help and contributions to perform measurements using the van der Pauw technique and for translating the abstract of this thesis into danish. Her efforts to integrate me into the danish society are greatly acknowledged.

I would also like to thank my co-supervisors Johan Hjelm and Sune Ebbesen for their worthy help whenever I needed and asked for it. Furthermore, I want to thank my program leader Anke Hagen her great support.

Special thanks goes also to my office mates Jimmy Nielsen, Federica Vico and Ragnar Kiebach for some very good times. I would also like to thank Alberto Lapino and Xiufu Sun for being excellent colleagues and friends. Within this group, Pia Lolk Mollerup is furthermore acknowledged for introducing me into the art of ceramic processing.

Heidi Adler Pedersen and Jens Borchsenius should be named and granted in representation of all the technicians, laboratorians and secretaries, without their help this work would not have been possible.

The financial support from the 2nd generation alkaline electrolysis project, EUDP 63011-0200, is gratefully acknowledged. I am also thankful for additional financial support from the “Catalysis for Sustainable Energy initiative”, funded by the Danish Ministry of Science, Technology and Innovation.

CONTENTS

LIST OF FIGURES

LIST OF TABLES

Part I

INTRODUCTION

1

ENERGY SUPPLY SYSTEM AND HYDROGEN PRODUCTION TECHNOLOGIES

1.1 THE ENERGY SUPPLY SYSTEM IN EUROPE AND DENMARK

Fossil fuels have been used extensively in the past century. The world wide energy demand has been increasing ever since and caused both environmental and human catastrophes like oil pollution and climate change. Reservoirs for fossil fuels are limited and become harder to discover since they are almost consumed in easy accessible areas.

Renewable energies have the potential to reduce the environmental impact. The amount of potentially available energy exceeds the demand by some orders of magnitude. The global influx from the sun to the earth is about $3 - 4\,10^{24}$ J while the demand is about $5\,10^{20}$ J [1]. Furthermore, non solar sources like tidal or geothermal energy enforces the fact that enough renewable energy sources are available to establish a CO_2 neutral energy supply.

The contribution of renewable energy to the gross energy consumption in the European Union (EU) increased continuously within the last decades and reached 10.0 % in 2008. The contributions from coal, mineral oil, gas and nuclear energy are 12 %, 42 %, 29 % and 7 %, respectively [2]. It was decided that the contribution from the renewable energies in the EU should increase to 20 % by 2020 (EU Directive 2009/28/EC). It is furthermore planned that the contribution from particular renewable energy sources should change. According to the targets of each member country, the "mixture" will change from the biomass and hydro-power dominated structure, as shown in the left diagram of figure 1.1, to a more evenly distributed system in 2020, as shown in the right diagram of figure 1.1.

The development of the renewable energy production over the time for Denmark is shown in figure 1.2 [3]; Denmark has very ambitious goals to reach 30% renewable energy by 2020. Denmark was a pioneer in providing wind energy technologies. Wind energy will become even more important in the future for renewable electricity generation.

On- and offshore wind energy will raise strongly until 2020 in the EU as well as in Denmark. The development of electricity generation from wind energy in the EU from 1990 until 2010 is shown in figure 1.3; more than ten times more wind energy was produced in 2010 than in 1998. The fluctuation of the wind speed brings some problems along which remains to be solved. It already happened, and will happen even more in the future, that more electrical energy was generated from wind turbines than demanded. So either some wind energy converters must be switched off, the electrical energy needs to be sold at very low, or for even negative prices, or the energy needs to be dumped. On

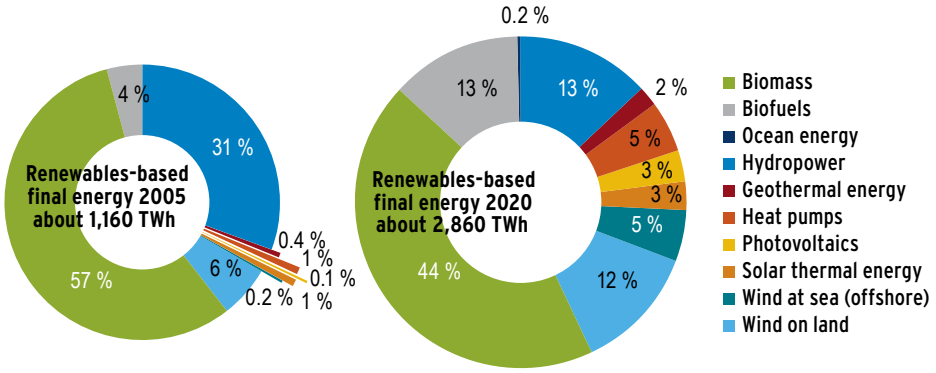

Figure 1.1: Structure of total renewable energy supplies in the EU in 2005 and 2020 on the basis of the national action plans of the EU Member States [2, page 61].

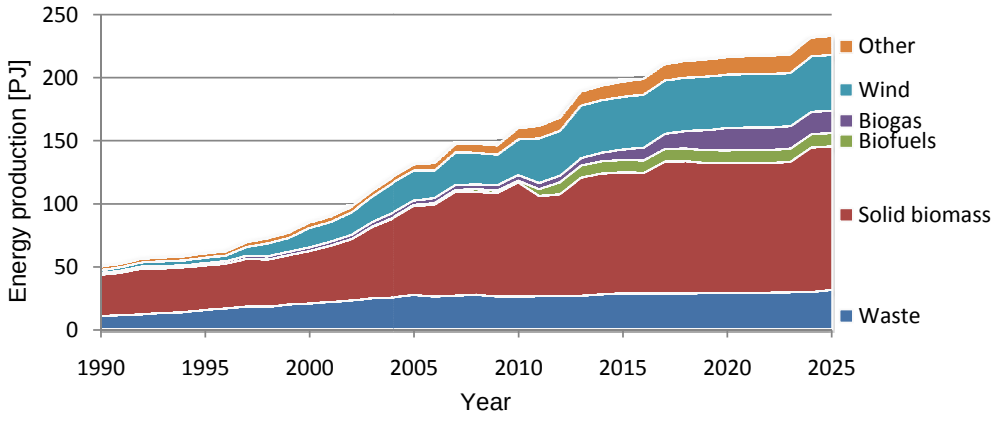

Figure 1.2: Renewable energy production in gross energy consumption [PJ] for Denmark between 1990 and 2025 (predicted values after 2010) [3, page 6]. The gross energy consumption for 1990, 2010 and 2025 was or is predicted to 819, 809 and 834 PJ, respectively.

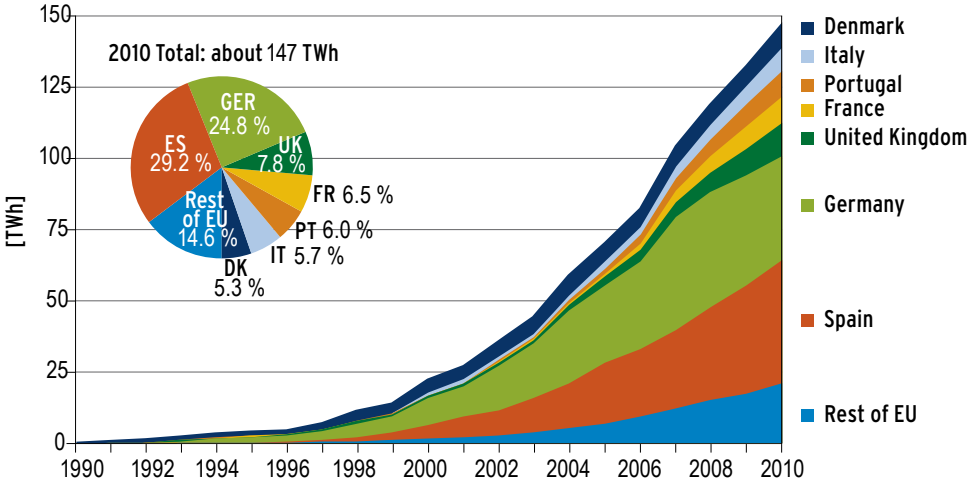

Figure 1.3: Development of electricity generation from wind energy in the EU from 1990 until 2010 [2, page 73].

the other hand, it is necessary to substitute the wind energy part from the energy supply system in times of high electrical load and low wind speeds, when not enough energy can be generated. In order to prevent that this is done by fossil sources, it is necessary to store the surplus of energy at high wind speeds. Promising ways are the production of hydrogen by water electrolysis [4] or the production of sustainable hydrocarbon fuels by recycling CO_2 and H_2O with renewable energy [5].

1.2 HYDROGEN DEMAND AND PRODUCTION TECHNOLOGIES

The worldwide hydrogen demand as of 2012 is ca. $600\,10^9\,\mathrm{Nm^3\,a^{-1}}$ [6]. The major part is produced by reforming of fossil fuels and natural gas, since the production cost for hydrogen by conventional electrolysis is too high and only beneficial if cheap electricity is available. An analysis of the current cost structure for hydrogen production by steam reforming of natural gas calculates the price for hydrogen to be $3.29\,€\,\mathrm{kg^{-1}}$ ($8.36\,€-\mathrm{ct\,kWh^{-1}}$ or $29.25\,€-\mathrm{ct\,Nm^{-3}}$ calculated with the higher heating value (HHV)) while the price for electrolysis varies between $5.09\,€\,\mathrm{kg^{-1}}$ and $20.02\,€\,\mathrm{kg^{-1}}$, depending on the capacity [7]. Due to the rapid penetration of renewable and thus fluctuating energy sources to the energy supply system, periods of energy excess are expected to yield cheap or even negative electricity prices, thereby opening the path for hydrogen production by electrolysis. The decreasing deposits and increasing price of conventional hydrocarbons will further benefit hydrogen production by water electrolysis or other technologies based on renewable energies in the long run. The most relevant technologies for hydrogen production by water electrolysis are polymer electrolyte membrane (PEM) electrolyzers, solid oxide electrolysis cells (SOECs) and alkaline electrolysis.

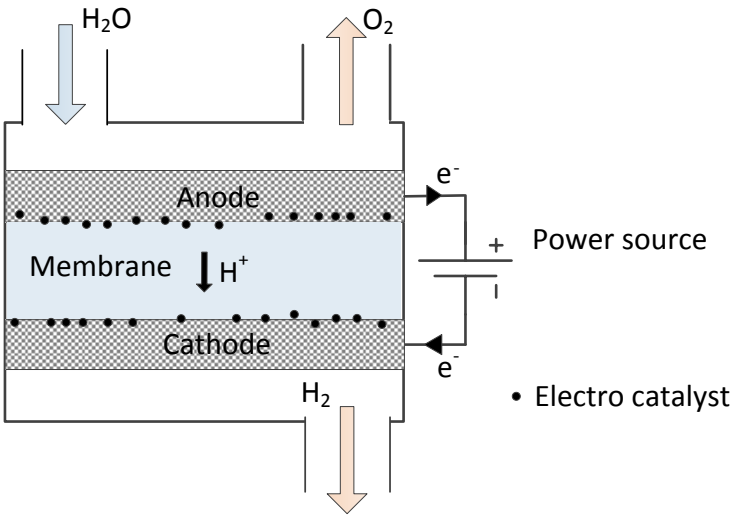

Figure 1.4: PEM Electrolysis cell: Protons are formed at the anode under water consumption, where the oxygen evolution reaction (OER) takes place. The protons migrate through the solid polymer electrolyte membrane to the cathode, where they are reduced into hydrogen.

1.2.1 *PEM Electrolysis cells*

Hydrogen production by water electrolysis follows a rather simple reaction. Electrical energy is used to split water into hydrogen and oxygen. In an acidic PEM- electrolysis cell, water splitting is performed according to the reactions shown by equations 1.1-1.3. Protons are formed at the anode under water consumption, where the oxygen evolution reaction (OER) takes place. The protons migrate through the solid polymer electrolyte (SPE) membrane to the cathode, where they are reduced into hydrogen.

$$\text{Anode}: \quad H_2O \rightarrow 1/2\, O_2 + 2\, H^+ + 2\, e^- \tag{1.1}$$

$$\text{Cathode}: \quad 2\, H^+ + 2\, e^- \rightarrow H_2 \tag{1.2}$$

$$\text{Total}: \quad H_2O \rightarrow H_2 + 1/2\, O_2 \tag{1.3}$$

Nafion is commonly used as proton conductor for PEM fuel cells and electrolyzers, because of its high proton conductivity and its chemical and mechanical stability. PEM electrolysis cells achieve high current densities already at low operational temperatures from 20 °C to 100 °C, i.e. Millet et al. demonstrated current densities of 2.0 $A\,cm^{-2}$ at a cell voltage of 1.86 V and a temperature of 90 °C [8]. Although this current density is considerably higher than that of the commercial alkaline electrolysers at similar conditions, PEM electrolysers are not utilized in market applications to the same extent as alkaline

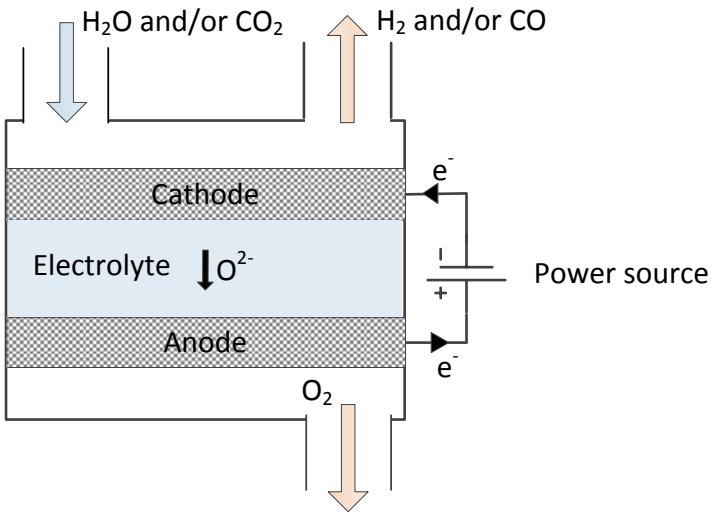

Figure 1.5: SOEC Electrolysis cell: Steam and/or CO_2 is fed to the cathode of the SOEC. Oxide ions (from H_2O or CO_2) are forced to migrate through the electrolyte from the cathode to the anode, where the OER takes place.

ones due to the high investment costs. The high investment costs occur mainly from the electro-catalysts, which are commonly platinum for the HER and iridium or ruthenium oxide for the OER.

1.2.2 *SOEC*

Water electrolysis by solid oxide electrolysis cells (SOECs) is principally performed at temperatures in between 700 °C and 1000 °C. The high temperature allows hydrogen production with significantly reduced electrical energy demand. This results in reduced hydrogen production costs especially in regions where waste heat is available or heat is easy to produce, for example in desertic areas by solar collectors. SOEC offers the possibility to perform so called co-electrolysis, where steam and CO_2 is converted to syngas (a CO and H_2 - mixture). Synthetic fuels can then be produced in another production step [5, 1]. The functionality of a SOEC is schematically shown in figure 1.5. Steam and/or CO_2 is fed to the cathode of the SOEC. Oxide ions (from H_2O or CO_2) are forced to migrate through the electrolyte from the cathode to the anode, where the OER takes place. The reactions are given by equations 1.4 - 1.8.

$$\text{Anode}: \quad O^{2-} \rightarrow 1/2\ O_2 + 2e^- \tag{1.4}$$

$$\text{Cathode}: \quad H_2O + 2e^- \rightarrow 2H_2 + O^{2-} \tag{1.5}$$

$$CO_2 + 2e^- \rightarrow CO + O^{2-} \tag{1.6}$$

$$\text{Total}: \quad H_2O \rightarrow H_2 + 1/2\ O_2 \tag{1.7}$$

$$CO_2 \rightarrow CO + 1/2\ O_2 \tag{1.8}$$

1.2.3 *Alkaline electrolysis*

Alkaline electrolysis is the only water electrolysis technology which is commercially available on a large scale at the moment. While PEM electrolyzers are available up to 160 kW, alkaline electrolyzers are available up to 3.4 MW rated power per unit. Very large hydrogen production facilities have for example been build in Egypt with a 160 MW facility at the Aswan fill dam [6]. The functionality of an alkaline electrolysis cell is described in chapter 2.

1.3 OBJECTIVE AND LAY-OUT OF THE THESIS

The objective of the PhD-study was to identify the potential for improving the efficiency and decreasing the costs associated with alkaline electrolysis by increasing the operation pressure and temperature of the electrolyser. New materials which are able to withstand the aggressive environment of an alkaline electrolysis cell under high temperature and pressure had to be identified. Furthermore, it was the aim of this project to find a new fabrication method for alkaline electrolysis cells.

The experimental activities during the PhD-study comprised the construction of test set-ups for the electrochemical characterization of alkaline electrolysis cells. Low temperature alkaline electrolysers with nickel based electrodes had to be characterized as a reference in the lower temperature range of up to 120 °C at atmospheric pressure. A special setup to allow electrochemical measurements under pressures of up to 100 bar and a temperature of 250 °C had to be constructed before durability and performance tests were performed. The electrolysis cells had to be characterized using scanning electron microscopy, both as fabricated and post mortem in order to identify degradation mechanisms.

The thesis is divided in 8 consecutive chapters which are divided into 4 parts. The introductory Part I (Introduction) comprises chapter 1 and gives an overview of hydrogen production technologies in general. Part II (Background) encloses chapter 2 and describes the functionality of an alkaline electrolysis cell and discusses the relevant thermodynamics. Part III (Experimental) contains chapter 3 and explains the constructed measurement systems. Part IV (Results) comprises chapters 4-8. The obtained results for high temperature and pressure alkaline electrolysis are presented in chapters 4-7 and

chapter 8 gives the overall discussion, conclusion and describes future plans. The chapters comprises in detail:

Chapter 1: The introduction chapter contains a brief description of the electrical energy supply system in the European Union and Denmark with a focus on the increasing amount of renewable energy. Furthermore it describes how the conversion of the electrical energy in times of energy excess can be stored electrochemically, i.e. in the form of hydrogen through water electrolysis. The objective and lay-out of the thesis are described in order to give an overview of the performed work.

Chapter 2: It is the aim of this chapter to give an overview of the thermodynamics and kinetics of alkaline electrolysers and alkaline fuel cells with main focus on electrolysis. Typical losses in the electrolyte and at the electrodes are discussed. The role of an appropriate electro-catalyst was explained and promising catalysts for the high temperature electrolysis are described. A literature review about the solubilities of oxygen and hydrogen as a function of temperature and pressure in potassium hydroxide is given.

Chapter 3: The Measurement systems to test the conductivity of aqueous and aqueous immobilized electrolytes and the performance of alkaline electrolysis cells are described in this chapter. Initial measurements in an atmospheric setup are presented here. A single atmosphere high temperature and pressure setup, which was build to determine the conductivity of aqueous and aqueous immobilized electrolytes and the performance of alkaline electrolysis cells is furthermore described. A measurement system to allow fully automatized measurements under high temperature and pressure and controllable gas composition is presented in this chapter as well.

Chapter 4: The conductivity of aqueous KOH at elevated temperatures and high concentrations was investigated using the van der Pauw method in combination with electrochemical impedance spectroscopy (EIS) and the results are presented in this chapter. Conductivity values for 35 wt%, 45 wt% and for 55 wt% concentrated aqueous solutions were measured at temperatures up to 200 °C. Micro- and nano-porous solid pellets were produced and used to immobilize aqueous KOH solutions. The conductivity of immobilized KOH has been determined by the same method in the same temperature and concentration range.

Chapter 5: A new type of alkaline electrolysis cells with nickel foam based gas diffusion electrodes and KOH (aq) immobilized in mesoporous $SrTiO_3$ have been developed and are presented in this chapter. The cells were tested at temperatures and pressures up to 250 °C and 42 bar, respectively. Current densities of 1.0 $A\,cm^{-2}$ have been measured at a cell voltage of 1.5 V without the use of expensive noble metal catalysts.

Chapter 6: The new type of alkaline electrolysis cells with nickel foam based gas diffusion electrodes and immobilized KOH (aq) was improved by the addition of cobalt oxide and molybdenum oxide as nano sized electro-catalysts. The cells were tested at temperatures of 150 °C, 200 °C and 250 °C at a pressure of 40 bar. Two cells have been characterized during a 270 h long test, using impedance spectroscopy, cyclic voltammetry and chronoamperometry. At a temperature of 250 °C current densities of 1.1 $A\,cm^{-2}$ and 2.3 $A\,cm^{-2}$ have been obtained at a cell voltages of 1.5 V and 1.75 V, respectively.

Chapter 7: Long term tests on a foam based electrolysis cell, similar to those described in chapter 6, with a duration of 350 h and constant current density of 640 $mA\,cm^{-2}$ was performed in this work at 250 °C and 40 bar. A similar cell was tested simultaneously by potentiostatic measurements at an applied cell voltage of 1.5 V for 80 h. Polarized electrochemical impedance spectroscopy measurements with an interval of 5 h show the development of the cell specific resistances. Scanning electron microscopy analysis before and after the tests was used in order to identify the degradation mechanism.

Chapter 8: Chapter 8 comprises an overall discussion and the conclusion. An outlook is given in which the possibilities of improving the cell characteristics even further are discussed.

Part II

BACKGROUND

2 ALKALINE ELECTROLYSIS

The aim of this chapter is to give an overview of the thermodynamics and kinetics of alkaline electrolysers and alkaline fuel cells with main focus on electrolysis. Parts of this chapter are also used in the following chapters as part of the introduction or discussion.

2.1 ALKALINE ELECTROLYSIS CELLS

An alkaline electrolysis cell consists of four major components; the electrolyte, which is commonly potassium hydroxide (KOH) in high concentrations (usually above 25 wt%), the cathode, the anode, and a solid barrier (diaphragm). The solid barrier is separating the produced gases to avoid recombination and contamination and furthermore needs to be permeable to hydroxide ions and water; it is used in all types of alkaline electrolysis cells (conventional, zero-gap, immersed cells, or gas-diffusion electrode type alkaline electrolysers) [9, 10]. Hydrogen evolution takes place at the cathode, where the electrons are provided for the decomposition of water. The hydroxide ions are decomposed at the anode, where oxygen evolution takes place under the formation of water. A basic schematic drawing of an alkaline electrolyser along with the most important components is shown in figure 2.1. The basic reactions of the decomposition of water in an alkaline electrolyser are given by equations (2.1)-(2.3).

$$\mathrm{Anode:}\ 2OH^- \rightarrow 1/2\ O_2 + H_2O + 2e^- \tag{2.1}$$

$$\mathrm{Cathode:}\ 2\ H_2O + 2e^- \rightarrow H_2 + 2\ OH^- \tag{2.2}$$

$$\mathrm{Total:}\ H_2O \rightarrow H_2 + 1/2\ O_2 \tag{2.3}$$

The cell voltage, U_{cell}, that has to be applied to produce hydrogen and oxygen with a given rate depends on the operating temperature [11] and pressure [12] as well as on a number of other factors such as the electro-catalyst material and microstructure, i.e. a high specific surface area [13]. Furthermore, the right choice of the electrolyte concentration for a specific temperature [14] and proper circulation of the electrolyte are important factors.

The losses which occur during the electrolysis process (the difference between the applied potential and the reversible cell voltage) cause a voltage drop which is defined as polarization. The polarization can furthermore be separated into the cathodic overvoltage, η_{H_2}, for the hydrogen evolution reaction, HER, the anodic overvoltage, η_{O_2}, for the oxygen evolution reaction, OER, and ohmic losses in the electrolyte. Ohmic losses in the electrodes are

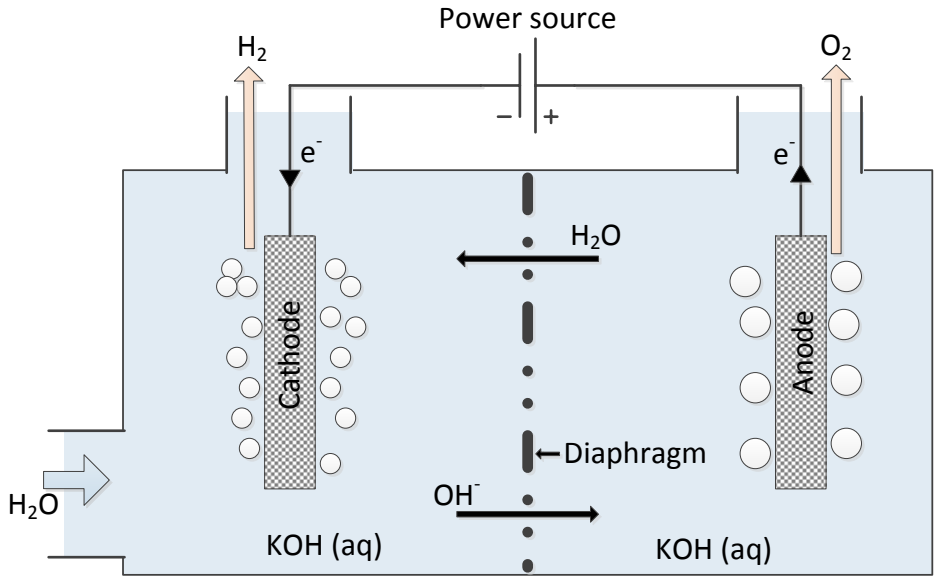

Figure 2.1: Schematic drawing of a traditional alkaline electrolysis cell: Hydrogen evolution takes place at the cathode, where the electrons are provided for the decomposition of water. The hydroxide ions are decomposed at the anode, where oxygen evolution takes place under the formation of water.

usually relatively small if compared to the HER, OER and ohmic losses in the electrolyte. The ohmic losses are relatively small at low current densities, but become significant at industrially relevant current densities (200 $mA\,cm^{-2}$ or more). Bubble formation affects also the polarization of the cell, especially at higher current densities, due to bubble formation, which partly blocks the transport of ions [15]. Since electrolysis is an endothermic reaction, part of the electrical losses that turn into heat are actually utilizable within the cell. The pronounced temperature dependence of the polarization can be seen in figure 2.2.

2.2 ELECTRODES

2.2.1 *Electrodes in aqueous electrolysers*

The first electrodes used for electrolysis purposes where plain metal electrodes as it is schematically drawn in figure 2.1. While the system was easy to handle and allowed hydrogen production with low efforts, the performance was bad especially at higher current densities due to the relatively large distance to the opposite electrode resulting in high ohmic losses in the electrolyte. The applicability as an electrode for an alkaline fuel cell was relatively bad, because only dissolved gases in the electrolyte could be used or the reactant gases had to be

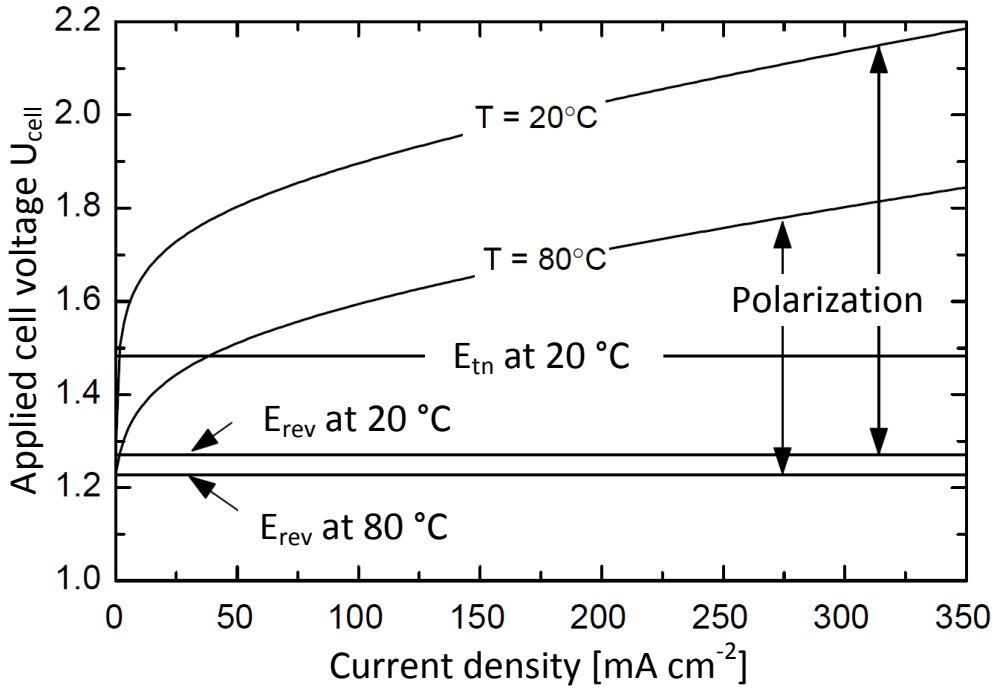

Figure 2.2: Polarization as a function of temperature and current density for temperatures of 20 °C and 80 °C, redrawn from [11].

flushed around the electrodes, leading to a high amount of unreacted gas (low fuel utilization).

2.2.2 *Zero-gap electrodes*

The so called zero-gap electrodes have been developed some decades ago and enhanced the performance of the electrolysis cells significantly [16]. The advantage is the design is that there is no gap between the electrodes and the diaphragm, which leads to a significant decrease of the ohmic losses. Disadvantageous is the higher possibility of trapped gas bubbles at the electrode-diaphragm interface which may block some pores and reaction sites. Since part of the surface of the diaphragm is covered with the electrode (compare figure 2.1 and figure 2.3), an uneven current distribution through the electrolyte will arise. The use of high porous structures like Raney-Nickel help to overcome this problem while at the same time they provide a high specific surface, which is along with the high catalytic activity of Ni the main reason for the great success of this material in alkaline electrolysis. Studies on the Raney type electrodes began in the late 70´s [17]. Great success was for example achieved with a 10 kW alkaline electrolyser for solar operation by Hug et al.[18].

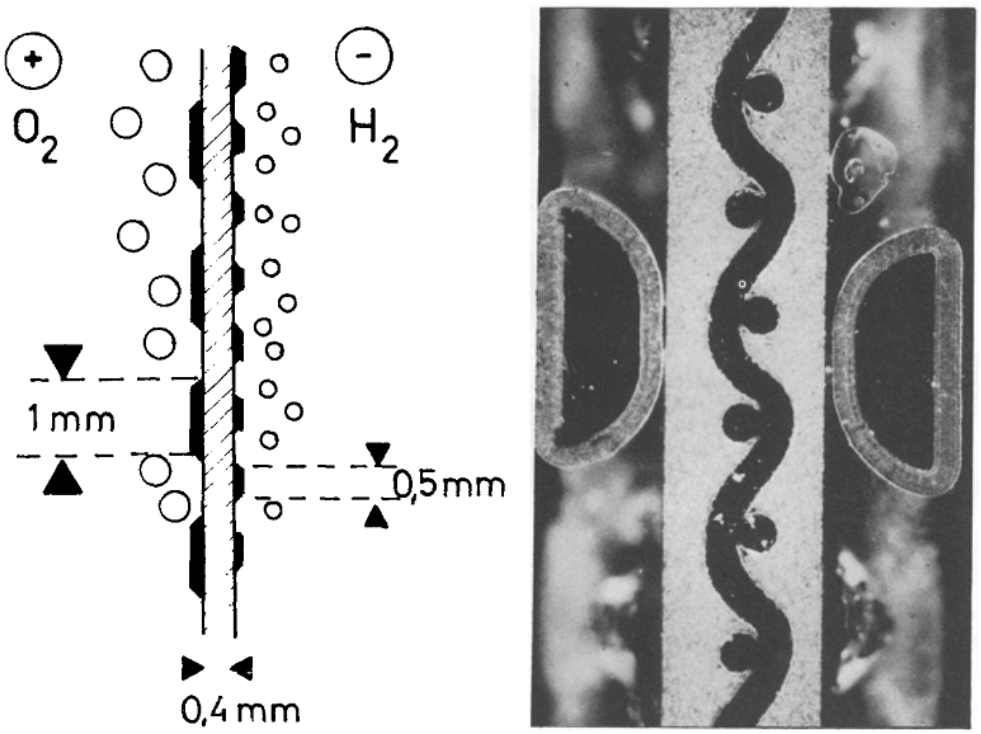

Figure 2.3: Left: Schematic drawing of a zero-gap electrolysis cell. Plane electrodes with a perforated structure were pressed to the diaphragm. The hole diameters of the perforated plates were found to be ideal with 1mm for the anode and 0.5 mm for the cathode [16]. Right: Image of a zero gap electrode setup in an alkaline electrolyser consisting of a NiO diaphragm and Raney-nickel electrodes. [19].

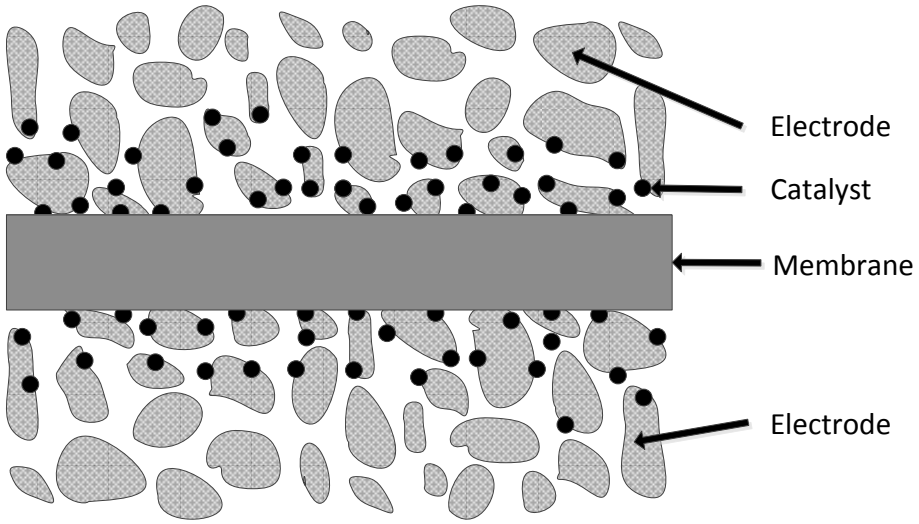

Figure 2.4: Gas diffusion electrode with an electrolyte (membrane) carrying porous structure, catalyst and gas diffusion layer.

2.2.3 *Gas diffusion electrodes*

As mentioned above, it is problematic to use solid electrodes immersed in aqueous solution for alkaline fuel cells because the gas transport to the electrode surface is very inefficient. Gas diffusion electrodes are therefore used in alkaline fuel cells. A typical membrane electrode assembly is shown in figure 2.4. The electrolyte is immobilized in or flushed through the diaphragm. The electrodes have to be porous to allow gas flow, but the pores must not be too small to avoid that capillary forces soak electrolyte through them, which would cause blocked pores.

It is furthermore important to have a large (surface wise) circular reaction zone, because this is the area of the highest possible current densities as it can be seen in figure 2.5. The design of a gas diffusion electrode, including the right choice and amount of the catalyst, the right structure, pore size and distribution and thickness is one of the major tasks when designing electrolysis cells.

2.3 THERMODYNAMICS OF WATER SPLITTING

The following section describes how the reversible cell voltage and the thermoneutral voltage behave as a function of temperature and pressure. Furthermore, methods to calculate these potentials are given that make it possible to calculate those without the necessity to use steam tables.

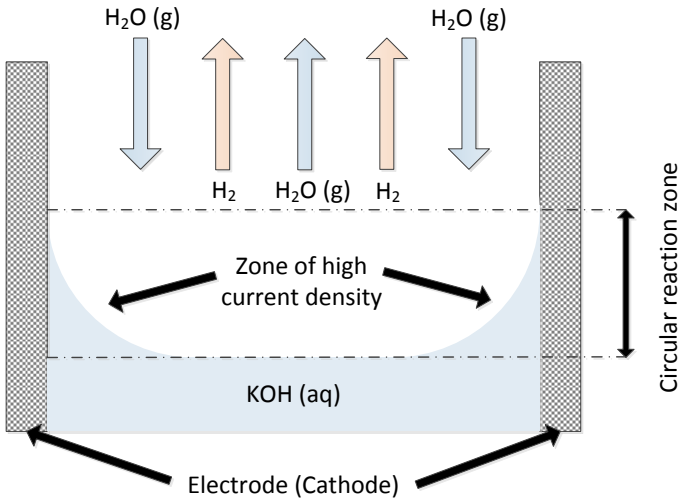

Figure 2.5: Single pore in a gas diffusion electrode (cathode) filled with electrolyte (KOH (aq)). The current density is highest close to the three phase boundary in the circular reaction zone. Steam flows towards the TPB, H_2 gas diffuses out of the reaction zone.

2.3.1 *Thermoneutral Voltage*

The Thermoneutral voltage E_{tn} describes the potential, at which the process in the electrolysis cell is neither endothermic nor exothermic; the electrical losses equal the heat required by the endothermic electrolysis process and describes the total energy demand for the reaction. It can be calculated by equation 2.4, with ΔH_f being the enthalpy of formation of water or steam, n is the number of electrons involved in the reaction, and F is Faraday's constant (96485 $C \cdot mol^{-1}$).

$$E_{tn} = \frac{-\Delta H_f}{nF} \tag{2.4}$$

The thermoneutral voltage $E_{tn,0}$ at standard temperature and pressure (STP, 25 °C, 101.325 kPa) is 1.481 V for $\Delta H_f^0 = -285.840\,kJ\,mol^{-1}$ [20]. The enthalpy for water splitting can be calculated using enthalpies from steam tables for temperatures above 25 °C. E_{tn} as a function of temperature can also be calculated by the empirical equation 2.5, valid for water in the temperature range 25 °C - 100 °C [21] with t being the temperature in [°C]:

$$E_{tn,25-100°C}[V] = 1.485 - 1.49\,10^{-4}t - 9.84\,10^{-8}\,t^2 \tag{2.5}$$

The influence of the temperature to the enthalpy of steam at atmospheric pressure can be calculated using the empirical equation 2.6 from the same authors [21], with $\triangle H^0_{f,H_2O(g)}$ ($-241.827\,kJ\,mol^{-1}$) being the enthalpy of formation of steam at STP.

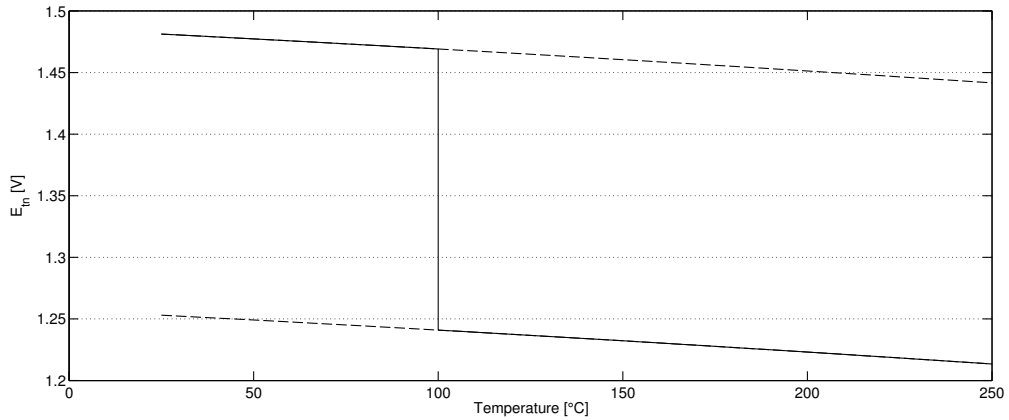

Figure 2.6: Thermoneutral voltage E_{tn} as a function of temperature at standard pressure calculated by empirical equations given from LeRoy et al. [21].

$$\triangle H_f - \triangle H^0_{f,H_2O(g)}[J\,mol^{-1}] = 730.68 - 28.752\,t - 0.01898\,t^2 \tag{2.6}$$

E_{tn} as a function of temperature at standard pressure can be calculated by the empirical equation 2.5 for water and by equations 2.6 and 2.4 for steam; this is shown in figure 2.6. It must be pointed out that parts of the figure are only theoretical, since water at standard pressure and temperatures above 100 °C becomes steam and steam will partly condensate to water below 100 °C, respectively. The theoretical values are therefore given as dashed lines. The influence of the pressure to the thermoneutral voltage is negligible for most practical applications. The numerical change is only 2.2 mV for a pressure change of 100 bar [12]. It will therefore not be calculated explicitly.

2.3.2 *Reversible cell voltage*

The reversible (or equilibrium) cell voltage, E_{rev}, is the minimal voltage at which electrolysis of H_2O is possible and can be calculated by equation (2.7), where ΔG_f is the Gibbs free energy of the reaction, n is the number of electrons involved in the reaction, and F is Faraday's constant. At standard conditions it is 1.229 V with $\Delta G^0_f = -237.178\,kJ\,mol^{-1}$ [20].

$$E_{rev} = \frac{-\Delta G_f}{nF} \tag{2.7}$$

A comparison of the electrical energy demand, the total energy demand and the heat demand for water electrolysis at standard pressure is shown in figure 2.7 with thermodynamic data obtained from FactSage [20]. It is shown that the electrical energy demand for water electrolysis decreases with increasing temperature, while heat demand rises and the total energy demand is almost constant both for the liquid and the gaseous phase.

As it is not common to perform electrolysis at standard conditions, it is necessary to know both the influence of pressure and temperature to the reversible

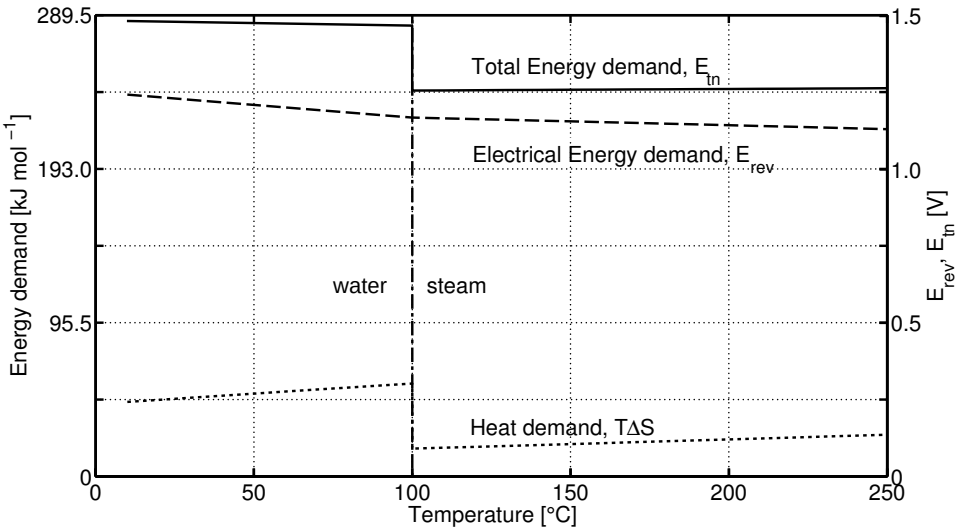

Figure 2.7: Temperature dependence of the total energy demand, ΔH_f (full line), the electrical energy demand, ΔG_f (dashed line), and the heat demand $T \cdot \Delta S_f$ (dotted) for water ($T \leqslant 100\,°C$) and steam ($T \geqslant 100\,°C$) electrolysis at 1 atm using data from FactSage [20].

cell voltage. The reversible cell voltage as a function of temperature and pressure, $E_{rev(T,p)}$, can be calculated by equation (2.8), where R is the Gas constant (8.3144621 J mol^{-1} K^{-1}), a_{H_2} is the hydrogen activity, a_{O_2} is the oxygen activity, a_{H_2O} is the activity of water and T is the temperature in Kelvin.

$$E_{rev(T,p)} = \frac{-\Delta G_f}{n \cdot F} = \frac{-\Delta G_f^0}{n \cdot F} + \frac{RT}{nF} \ln\left(\frac{a_{H_2} a_{O_2}^{\frac{1}{2}}}{a_{H_2O}}\right) \tag{2.8}$$

$E_{rev(T,p)}$ can also be obtained from steam tables or CALPHAD (Computer Coupling of Phase Diagrams and Thermochemistry) programs like FactSage [20] which include data for ΔG_f at elevated temperatures and pressures. A graph displaying the influence of the pressure and temperature on $E_{rev(T,p)}$ has been calculated by equation 2.7 with data from FactSage and is shown in figure 2.8. Important values are numerically extracted in table 2.1.

Furthermore, it should be noted that the reversible cell voltage of an alkaline electrochemical cell is also depending on the concentration of the electrolyte, as this will affect the activity of water incl. steam. Balej [22, 23] has provided expressions for computing the reversible cell voltage as a function of the concentration of the electrolyte, temperature and pressure, $E_{rev(t,p,m)}$, said to be valid for temperatures between $25\,°C - 200\,°C$ in the pressure range 1 bar - 200 bar. This expression is reproduced as equation 2.9, here where $E^0(t)$ is the standard equilibrium voltage of water electrolysis, calculated by the empirical equation 2.10, T is temperature in [K], $\ln \gamma_{O_2}$ and $\ln \gamma_{H_2}$ are fugacity coefficients for oxygen and hydrogen, calculated by equations 2.11 and 2.12,

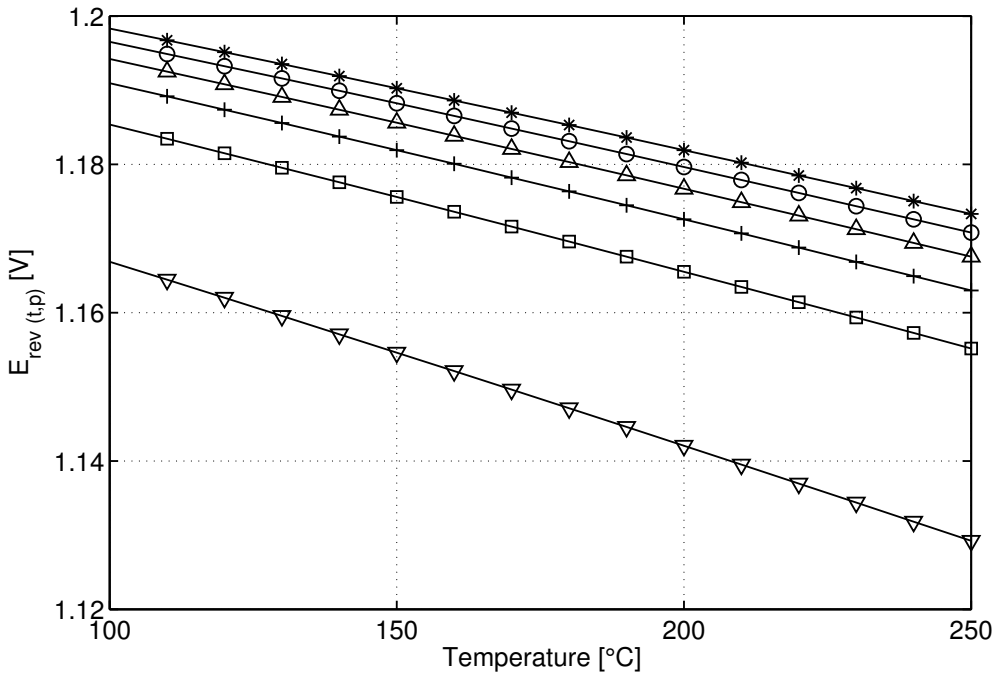

Figure 2.8: Reversible cell voltage $E_{rev(t,p)}$ as function of the temperature for steam electrolysis at pressures of 1 bar (▽), 10 bar (□), 20 bar (+), 30 bar (△), 40 bar (○) and 50 bar (⋆).

respectively, $p_{H_2O,m}$ is the water vapor partial pressure over aqueous KOH as a function of temperature and molality, as calculated by equation 2.13, P is the system pressure in [bar], $a_{H_2O,m}$ is the water activity as function of the molality and temperature over concentrated solutions of potassium hydroxide, calculated by equation 2.14, and m is the molality of the aqueous KOH.

$$\begin{aligned} E_{rev(t,p,m)} &= E^0(t) + 4.30851\,10^{-5} T(\ln(P - p_{H_2O,m})^{1.5} \\ &\quad +0.5\ln\gamma_{O_2} + \ln\gamma_{O_2} - 2.30259\log a_{H_2O,m}\ [V] \end{aligned} \tag{2.9}$$

$$\begin{aligned} E^0(t) &= 1.639 - (5.03824\,10^{-3} - 7.0467\,10^{-4}\ln T)T - 1.1700\,10^{-6}T^2 \\ &\quad +4.675\,10^{-10}T^3 - 4.016/T\ [V] \end{aligned} \tag{2.10}$$

$$\begin{aligned} \ln\gamma_{O_2} &= (42.6\,T - 17400)\,P/83.1447\,T^2) + (-2604\,T^2 + 61457\,T^{1.5} \\ &\quad -(42.6\,T - 17400)^2)\ P^2/(1.4009\,10^4\,T^4) \end{aligned} \tag{2.11}$$

$$\begin{aligned} \ln\gamma_{H_2} &= (20.5\,T - 1857)\,P/83.1447\,T^2) + (-351\,T^2 + 12760\,T^{1.5} \\ &\quad -(20.5\,T - 1857)^2)\ P^2/(1.4009\,10^4\,T^4) \end{aligned} \tag{2.12}$$

$$\begin{aligned} \log\left(\frac{p_{H_2O,m}}{1\,bar}\right) &= -0.01508m - 0.0016788m^2 + 2.2588710^{-5}m^3 + (1 - 0.0012062m) \\ &\quad +5.6024\cdot10^{-4}\cdot m^2 - 7.8228\cdot10^{-6}m^3)\cdot(35.4462 - \\ &\quad \frac{3343.93}{T} - 10.9\cdot\log T + 0.0041645\cdot T) \end{aligned} \tag{2.13}$$

$$\log a_{H_2O,m} = -0.02255\,m + 0.001434\,m^2 + (1.38\,m - 0.9254\,m^2)T^{-1} \quad (2.14)$$

The reversible cell voltage of 45 wt% KOH(aq), $E_{rev}(t,p,m)$, has been calculated for different temperatures and pressures and is displayed in table 2.1 (lower values). It can be seen that the $E_{rev(t,p,m)}$ is higher than $E_{rev(t,p)}$ for steam inside the validity range for $E_{rev(t,p,m)}$ (25 °C − 200 °C and 1 bar - 200 bar).

Table 2.1: Reversible cell voltage $E_{rev(t,p)}$ [V] for steam electrolysis as function of the system pressure and temperature calculated by equation 2.7 with data from FactSage (upper value) and reversible cell voltage of 45 wt% KOH(aq), $E_{rev}(t,p,m)$, as a function of the system temperature and pressure, calculated by equation 2.9 (lower value). Values in *italic* are outside the validity of the equation.

	System pressure [bar]					
Temperature [°C]	1	10	20	30	40	50
100	1.167	1.185	1.191	1.194	1.197	1.198
	1.176	1.240	1.257	1.267	1.274	1.280
150	1.155	1.176	1.182	1.186	1.188	1.190
	1.134	1.203	1.225	1.237	1.245	1.252
200	1.142	1.166	1.173	1.177	1.180	1.182
	1.156	1.149	1.187	1.204	1.215	1.223
250	1.129	1.155	1.163	1.168	1.171	1.173
	1.161	*1.132*	*1.112*	*1.157*	*1.176*	*1.188*

2.4 LOSSES IN ALKALINE ELECTROLYSIS

2.4.1 *Ohmic losses in the electrolyte*

Beside the overpotentials, ohmic losses are the main reason for decreased efficiency in fuel cells and electrolysis cells. While the ohmic losses in the wires from the power source to the cell are usually negligible if they are sufficiently big in diameter and if the interconnections are properly designed, ohmic losses in the electrolyte and the diaphragm are significant. It is therefore important to know the temperature and concentration dependence of the specific electrical conductivity of the electrolyte, σ, usually given in $S\,cm^{-1}$, in order to minimize the ohmic losses in an alkaline electrolyser though optimal design of the system. The conductivity of the commonly used aqueous potassium hydroxide (KOH) is well described from 0 to 100 °C and concentrations up to 45 wt%

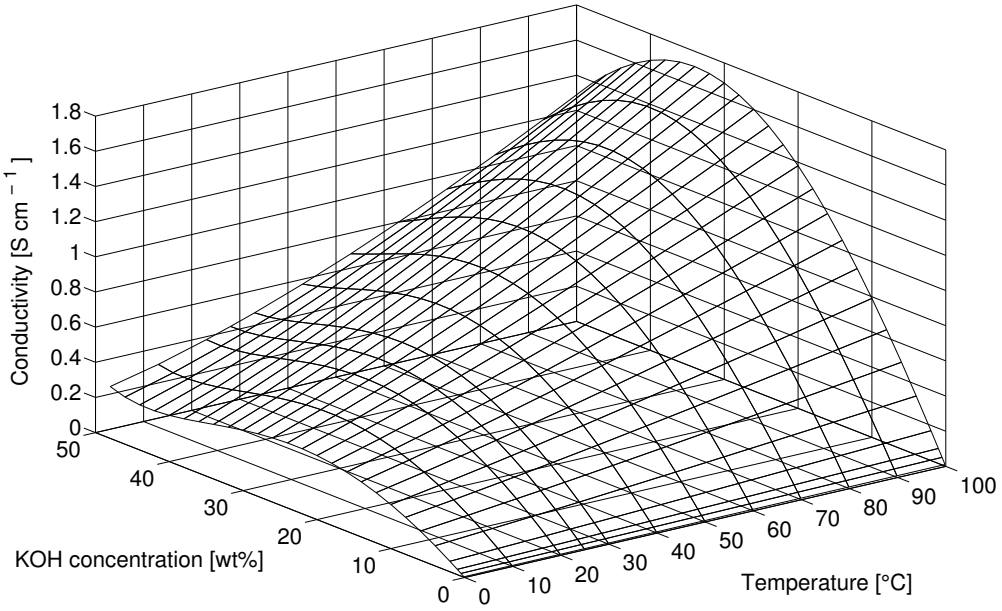

Figure 2.9: Concentration and temperature dependence of the conductivity of aqueous solutions of KOH, redrawn using the data of Gilliam et al [25].

[24]. Gilliam et al recently published a method to calculate the conductivity from 0 to 12 M KOH (0 to 48 wt%) in the temperature range 0 °C - 100 °C [25]. From these data, which are plotted in figure 2.9, it can be seen that at each temperature there exists a specific concentration at which the conductivity has a maximum; the higher the temperature, the higher the concentration at the conductivity peak.

Conductivity data for temperatures above 100 °C are scarce. One data set from Lown et al. extending to temperatures up to 200 °C and concentrations up to 37.5 wt% can be found in the literature [26], but following the trend of the conductivity peak shown in Figure 11, it can be expected that at temperatures above 100 °C, the conductivity maximum will be at concentrations higher than 37.5 wt%. This assumption is fortified by data from Yushkevich et al, who showed that the conductivity of aqueous KOH has a maximum at 45 wt% KOH at a temperature of 260 °C [27]. A method to determine the electrical conductivity of aqueous KOH and aqueous KOH immobilized in a porous structure using the van der Pauw technique [28] will be discussed in chapter 4 and has been published by the author of this work [29].

2.4.2 *Ohmic losses in the gas separation membrane*

Regardless of the electrolyser design, it is necessary to separate the produced gases by an electrolyte (diaphragm), which has to be gas-tight and ion-conductive. A porous structure in which the liquid electrolyte is immobilized by capillary forces can be used for that matter. In this case, the reduced free volume for

the liquid electrolyte is expected to result in a decrease in conductivity, and by that to an increase in ohmic losses. The determination of the conductivity of such structures is therefore important. The conductivity of immobilized KOH which has been achieved during measurements for this thesis is as high as 0.84 $S\,cm^{-1}$ for 45 wt% KOH at 200 °C as it will be discussed in detail in chapter 4. Zirfon is a commercially available diaphragm and used as the standard diaphragm in commercially available electrolysers. The measured conductivities of immobilized KOH as described in chapter 4 are slightly lower in direct comparison to Zirfon, which has also been used to immobilize KOH by Vermeiren et al [30]. They achieved an area specific resistance of 0.1 $\Omega\,cm^2$ at a temperature of 80 °C for a membrane of 600 μm in thickness. This corresponds to a conductivity of 0.6 $S\,cm^{-1}$ and by that almost twice as high as the values that have been achieved in this work at 80 °C, namely 0.33 $S\,cm^{-1}$. Assuming that it will be possible to use the porous structure down to thicknesses of 200 μm, or even thinner depending on the used support, the proposed method may achieve area specific resistances of 60 $m\Omega\,cm^2$ and by that reduce the ohmic losses in the electrolyte significantly. Furthermore, it is possible to use the proposed structure at temperatures like 200 °C or even higher, while commercial diaphragm are usually limited to 100 °C - 120 °C.

2.4.3 *Losses due to bubble formation*

In conventional electrolysers it is common to use a diaphragm in between the electrodes to allow gas separation. The distance between the diaphragm and the electrode is usually kept to a minimum in order to reduce losses in the electrolyte. Nevertheless, this configuration implies that there is an increased loss due to the formation of bubbles which reduce the active area on the electrodes as well as the free volume of the electrolyte. Fischer et al calculated that the formation of bubbles may lead to an increase in the total overvoltage of ca. 100 mV assuming that 50 % of the active electrodes are covered by bubbles [9] (exact conditions not given).

2.5 ELECTRODE ELECTROLYTE INTERFACE

The reaction rate as a function of the applied cell voltage U_{cell} in order to produce hydrogen or oxygen in an electrolysis cell depends strongly on the morphology of the electrode surface and the electrolyte facing the electrodes. A so called double layer is formed between the electrode and the electrolyte. This was first reported by Helmholtz who described the layer as a simple capacitor with an even distribution of the ions as shown in figure 2.10. Nowadays models of the double layer show a more ordered concentration of the ions in the region of the inner Helmholtz Plane, IHP, with some adsorbed ions at the metal surface, and less ordered ions with relatively smaller concentration be-

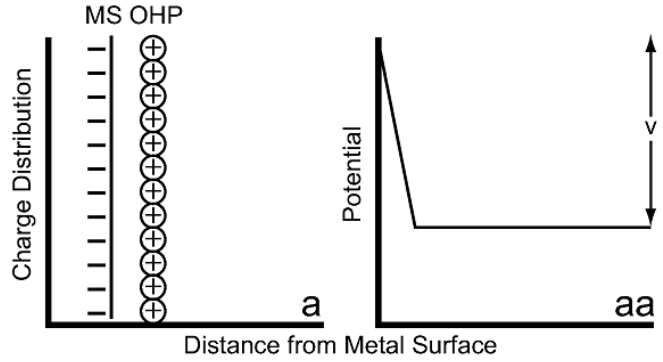

Figure 2.10: Helmholtz model of the electrochemical double layer of the metal surface MS and the outer Helmholtz Plane OHP, taken from [31].

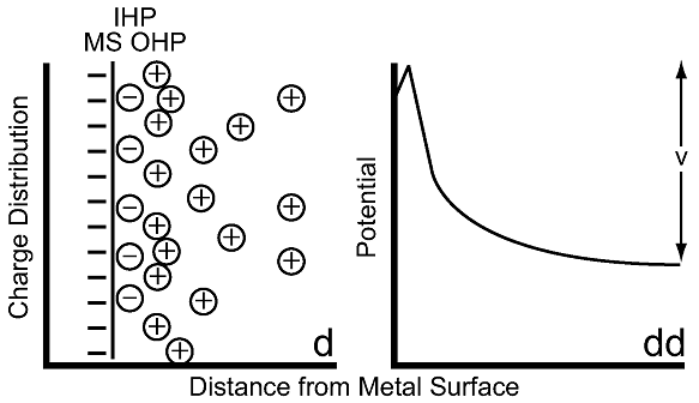

Figure 2.11: Esin and Markov, Grahame, and Devanathan model of the electrochemical double layer, taken from [31].

tween the two Outer Helmholtz Planes, OHP, of an electrode pair like shown in figure 2.11.

2.6 EXCHANGE CURRENT DENSITY

Experiments have shown that, under exclusion of mass transfer limitations, there is an exponential relationship between the reaction rate and the overpotential [32]. The overpotential η is defined as the difference between electrode potential E_i and the reversible (or equilibrium) potential E_{rev}.

$$\eta = E_i - E_{rev} \tag{2.15}$$

The influence of the overpotential on the corresponding current density can be calculated with the Butler-Volmer equation 2.16, where i is the current density in $[A\,cm^{-2}]$, i_0 the exchange current density in $[A\,cm^{-2}]$, α_a the anodic charge transfer coefficient and α_c is the cathodic charge transfer coefficient.

$$i = i_0 \left\{ e^{\left[\frac{\alpha_a n F}{RT}\eta\right]} - e^{\left[-\frac{\alpha_c n F}{RT}\eta\right]} \right\} \tag{2.16}$$

The resulting current density is a function of both, the exchange current density and the overpotential. For adequately high values of η, one of the exponential terms in equation 2.16 becomes rate determining and the current density can also be calculated by

$$i = i_0 e^{\left[\frac{\alpha_a n F}{RT}\eta\right]} \qquad \text{for} \qquad \frac{\alpha_a n F}{RT}\eta \gg 1 \tag{2.17}$$

or

$$i = -i_0 e^{\left[-\frac{\alpha_c n F}{RT}\eta\right]} \qquad \text{for} \qquad \left|\frac{\alpha_c n F}{RT}\eta\right| \gg 1 \tag{2.18}$$

The exchange current densities and charge transfer coefficients for different electrode materials at 90 °C have been determined by Wendt and Pizak [33]. The exchange current density of steel blasted nickel electrodes is $7.9\,10^{-7}$ A cm^{-2} for the OER and $7.1\,10^{-4}$ A cm^{-2} for the HER, respectively.

2.7 ELECTRO-CATALYSIS

In order to enhance the performance and efficiency of an electrochemical cell, it is necessary to reduce the overpotentials. The hydrogen and oxygen overpotentials, η_{H_2} and η_{O_2}, can be reduced by the use of proper electro-catalysts. The gas evolution reactions in alkaline electrolysis of water are multi-step reactions, where the hydrogen evolution reaction (HER) in the form of

$$2\,H_2O + 2e^- \rightarrow H_2 + 2\,OH^- \tag{2.19}$$

includes the rather fast established, and by that not rate determining, electrochemical adsorption of hydrogen atoms as shown by reaction 2.20.

$$H_2O + e^- \leftrightarrows H_{ads} + OH^- \qquad \textit{fast step} \tag{2.20}$$

This fast step is followed by a relatively slow, and with that rate determining step for the charge transfer in the Volmer step (reaction 2.21)

$$H_2O + H_{ads} + e^- \rightarrow H_2 + OH^- \qquad \textit{slow step} \tag{2.21}$$

or the Tafel step, as shown by reaction 2.22 [34].

$$H_{ads} + H_{ads} \rightarrow H_2 \qquad \textit{slow step} \tag{2.22}$$

The corresponding steps for the anodic Oxygen evolution reaction

$$4\,OH^- \rightarrow O_2 + 2\,H_2O + 4\,e^- \tag{2.23}$$

are known to be even more complicated and can be expressed as [35]:

$$OH^- \leftrightarrows OH_{ads} + e^- \tag{2.24}$$

$$OH_{ads} + OH^- \leftrightarrows O^-_{ads} + H_2O \tag{2.25}$$

$$O^-_{ads} \leftrightarrows O_{ads} + e^- \tag{2.26}$$

$$O_{ads} + O_{ads} \leftrightarrows O_2 \tag{2.27}$$

In these multi-step reactions, the electrochemical reaction rate is kinetically hindered and the corresponding exchange current densities are relatively small for certain electrode materials. The proper choice of the right catalyst for the oxygen and hydrogen evolution is one of the most important factors to reduce the overpotential for alkaline (and other) electrolysis cells.

2.7.1 *Hydrogen Overpotential and catalysts for the Hydrogen Evolution Reaction*

As mentioned above, the HER is rate determined by its second, relatively slow step of the hydrogen molecule formation from the adsorbed hydrogen atoms (compare equation 2.21). The exchange current densities on different metals as catalysts for the HER differ by several orders of magnitude, with Pt and platinum metals being the most active ones. Pt is unfortunately very expensive and therefore there is a high demand for alternative electrode materials. A comparison of experimental and computational values for the exchange current densities has been performed by Nørskov et al and is presented in table 2.2 as well as in the form of a volcano plot in figure 2.12. The exchange current density for each metal has been obtained at equilibrium potential.

A comparison of some well known and often used electro-catalysts for the HER (Ni, Raney-Ni, Raney-Ni/Co) in aqueous KOH at a temperature of 90 °C has been performed by Wendt and Plzak [33]. It was found that the (IR-free) calculated cell voltage for a RuO_2 anode and a Pt-black cathode would be as low as 1.66 V at 90 °C and 1.47 V at 160 °C and a current density of 1 $A\ cm^{-2}$. A symmetrical cell with Raney Ni-Co anode and cathode had only slightly higher values with 1.75 V at 90 °C and 1.51 V at 160 °C.

2.7.2 *Oxygen Overpotential and catalysts for the Oxygen Evolution Reaction*

It is experimentally proven that the the overpotential for the OER is significantly higher than for the cathodic HER, although equation 2.17 could indicate a lower overvoltage for a multi electron process (the exchange current density has to be taken into consideration at this point). Four electrons have to be transferred as shown by equation 2.23. Some of the best known and widely used catalyst for the OER are Co_3O_4 [44] and Raney-Co, other oxides like RuO_2 or IrO_2 [45] showed very good performance as well, but are too expensive

Table 2.2: "Calculated hydrogen adsorption energies $\triangle E_H$ and measured exchange current densities on different transition and noble materials with hydrogen chemisorption energies calculated for 0.25 and 1.0 monolayer (ML) coverage". Reprinted from Nørskov et al. [36].

	$\triangle E_H$ [eV] 0.25 ML	$\triangle E_H$ [eV] 1.00 ML	log $(i_0/A\,cm^{-2})$	Ref
Au(111)	0.21	0.39	26.6	[37]
Au (111)			26.8	[38]
Au			25.4	[39]
Ag(111)	0.27	0.34	25.0	[40]
Ag			27.85	[41]
Pd	20.38	20.33	23	[39]
Pd			23	[42]
Pt	20.33	20.27	23.1	[39]
Pt			22.63	[41]
Pt(111)			23.34	[43]
Rh	20.34	20.30	23.6	[39]
Rh			23.22	[41]
Ir	20.21	20.16	23.7	[39]
Ir			23.46	[41]
Ni	20.51	20.47	25.2	[39]
Ni			25.21	[41]
W	20.67a	20.83	25.9	[39]
W			25.9	[41]
Co	20.51	20.49	25.32	[41]
Cu	20.05	0.03	25.37	[41]
Mo	20.61a	20.77	27.07	[41]
Re	20.56	20.45	22.87	[41]
Nb	20.80a	20.80	26.8	[39]

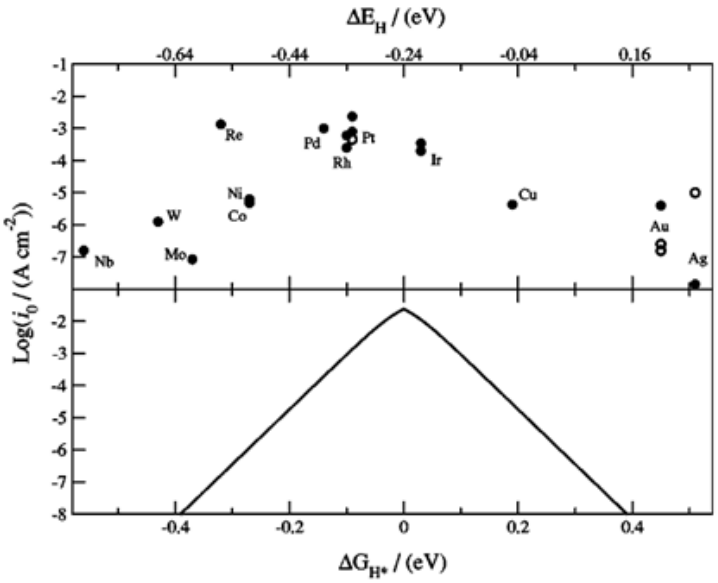

Figure 2.12: Upper graph: "Experimentally measured exchange current densities, $\log(i_0)$, at equilibrium potential for hydrogen evolution over different metal surfaces plotted as a function of the calculated hydrogen chemisorption energy per atom ($\triangle E_H$). Lower graph: Kinetic model as a function of the free energy for hydrogen adsorption ($\triangle G_{H^+}$)" [36].

for large scale hydrogen production. Ag is another promising candidate to enhance the OER [32].

Volcano plots for the anodic OER can be found in the literature similar to the one presented for the HER. A volcano plot for different types of metal oxides is shown in figure 2.13 [46, 47]. Perovskite oxides with the general formula ABO_3, where A is a cation of larger size than B, are widely used mixed metal catalyst. A volcano plot for these perovskite type materials with a fixed overpotential of 0.3 V is shown in figure 2.14 [48], where A was mainly La and A´ was mainly Sr, for example $La_{0.9}Sr_{0.1}CoO_3$, $La_{0.7}Sr_{0.3}FeO_3$ or $LaNiO_3$.

2.8 EFFICIENCY

The efficiency of an alkaline electrolyser is of high importance for the economical analysis of an energy storage system based on hydrogen. The electrical efficiency in relation to the Higher Heating Value (HHV) of an electrolysis cell, $\eta_{el_{HHV}}$, can be calculated by equation 2.28. It is 100 % if $U_{Cell} = E_{tn}$. If the cell voltage is below E_{tn}, the process is endothermic and the electrical efficiency is above 100 %. For cell voltages above E_{tn}, the process is exothermic and the efficiency is below 100 %.

$$\eta_{el_{HHV}} = \frac{E_{tn,0}}{U_{Cell}} = \frac{1.481\,V}{U_{Cell}} \tag{2.28}$$

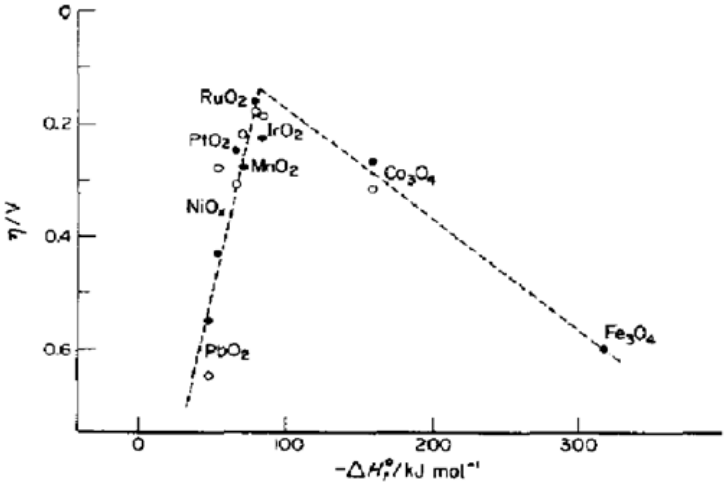

Figure 2.13: "Electro-catalytic activity in O2 evolution at various oxide electrodes as a function of the enthalpy of the lower → higher oxide transition. Alkaline (o) and acid (•) solutions are indicated" [46].

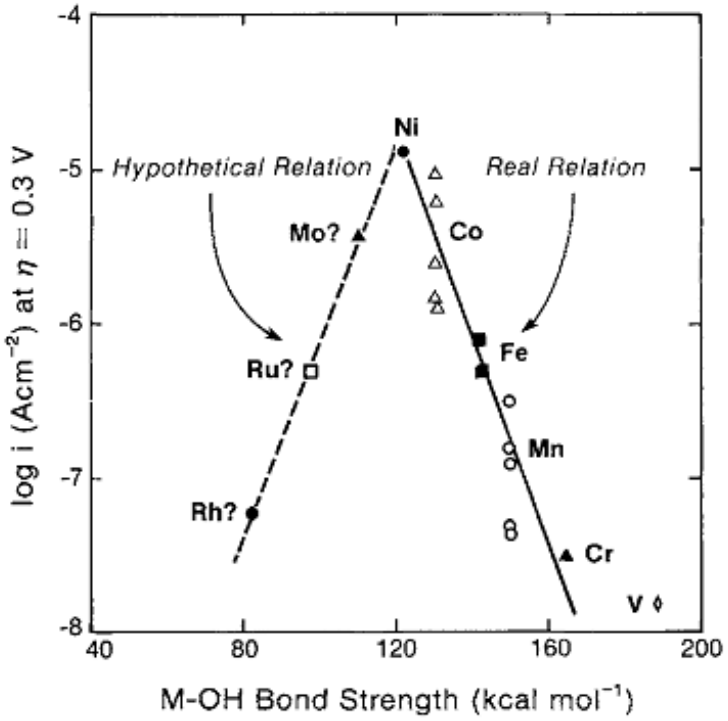

Figure 2.14: "Hypothetical volcano plot for oxygen evolution on perovskites with the structure ABO_3. Transition metal B ions in perovskites are indicated with different symbols. A was mainly La and A´ was mainly Sr, for example $La_{0.9}Sr_{0.1}CoO_3$" [48].

The efficiency $\eta_{el_{LHV}}$ of an electrolysis cell in relation to the lower heating value, LHV (241.827 kJ mol^{-1} at STP), can be calculated by equation 2.29.

$$\eta_{el_{LHV}} = \frac{LHV\, n^{-1}\, F^{-1}}{U_{Cell}} \tag{2.29}$$

It is common to calculate the efficiency against the reversible or thermoneutral voltages at STP, although the electrolysis temperature is higher and the system is pressurized. Unfortunately there is no common agreement how the cell efficiency should be calculated; a proposal on how to calculate the efficiency of an electrolysis system has recently been published by Zhang et al [49]. A more detailed discussion about the efficiency of an electrolysis cell at elevated temperatures and pressures will follow in chapter 5.

2.9 SOLUBILITY OF OXYGEN AND HYDROGEN

The oxygen and hydrogen solubility in the electrolyte is an important factor while designing alkaline electrolyser cells. A high oxygen solubility will result in diffusion of oxygen through the electrolyte to the hydrogen side, where it will be electrochemically reduced on the hydrogen electrode and would therefore reduce the faradaic efficiency of the electrolysis process. Similarly, a high hydrogen concentration will result in diffusion of hydrogen to the oxygen electrode, where the hydrogen will be electrochemically oxidized. Another issue is the corrosion aspect; a higher oxygen concentration will demand higher corrosion resistance of the used materials. Finally, the most important perhaps issue relates to the presence of O_2 impurities in the evolved H_2 gas (and the other way round), which has to be limited primarily for safety reasons.

2.9.1 *Solubility of oxygen in aqueous KOH and water*

Tromans [50] developed a formula to predict the oxygen solubility in different inorganic solutions. This formula is said to be feasible to predict the oxygen solubility in potassium hydroxide solutions in a wide range of pressures, temperatures and concentrations. The comparison of his formula with available data showed satisfying accuracy up to 100 °C, but for higher temperatures no data are available.

Figure 2.15 shows the variation of the oxygen solubility in potassium hydroxide solution as a function of the temperature and different concentrations of KOH (aq); an excerpt of some important numerical values are shown in table 2.3. It is seen that the solubility is decreasing strongly with increasing concentration. It is also seen that the solubility has a minimum at around 100 °C. The prediction was shown to be valid for temperatures up to the boiling point of the solution at ambient pressure. Comparison of Tromans formula with data for other solutions that he described in his work, i.e. NaOH, indicate that his formula is accurate and can be used also for temperatures above 100 °C.

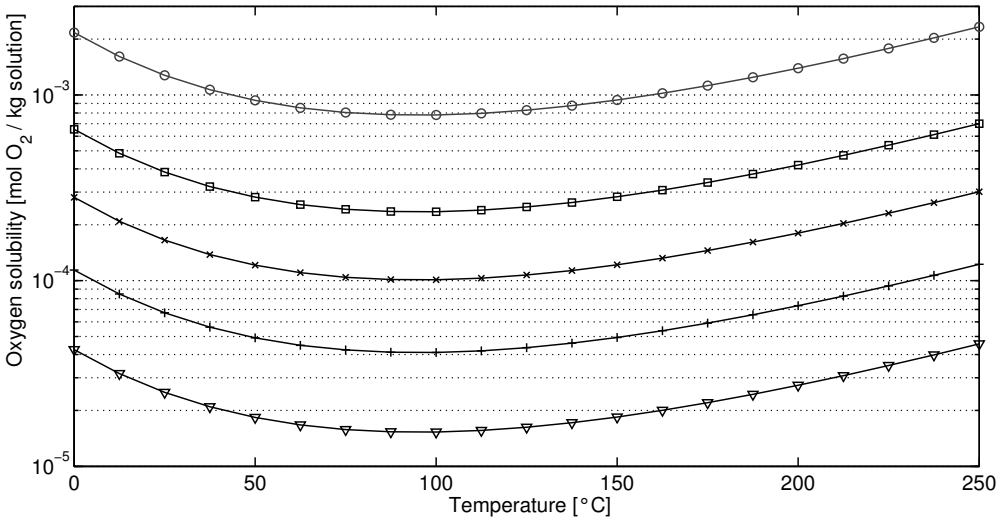

Figure 2.15: Oxygen solubility as a function of temperature in water (o) and aqueous solutions of KOH for a concentration of 15 wt% (□), 25 wt% (x), 35 wt% (+), and 45 wt% (∇). The solubilities were calculated after an empirical formula developed by Tromans [50].

Table 2.3: Oxygen solubility in concentrated aqueous solutions of KOH between 15 wt% and 45 wt% and water, given in [mol/ kg] solution. The solubilities were calculated after an empirical formula developed by Tromans [50].

Oxygen solubility in [mol/ kg]					
	KOH concentration [wt%]				
Temperature [°C]	0.0	15.0	25.0	35.0	45.0
0	2.17E-03	6.53E-04	2.81E-04	1.14E-04	4.25E-05
50	9.35E-04	2.82E-04	1.21E-04	4.92E-05	1.83E-05
100	7.81E-04	2.35E-04	1.01E-04	4.11E-05	1.53E-05
150	9.40E-04	2.83E-04	1.22E-04	4.94E-05	1.84E-05
200	1.39E-03	4.19E-04	1.80E-04	7.33E-05	2.73E-05
250	2.33E-03	7.01E-04	3.01E-04	1.22E-04	4.56E-05

2.9.2 *Solubility of hydrogen in aqueous KOH*

The hydrogen solubility in aqueous KOH solutions was measured by Ruetschi et al. [51] at 30 °C and ambient pressure. His results are displayed in comparison with calculated oxygen solubility data from Tromans in figure 2.16. It

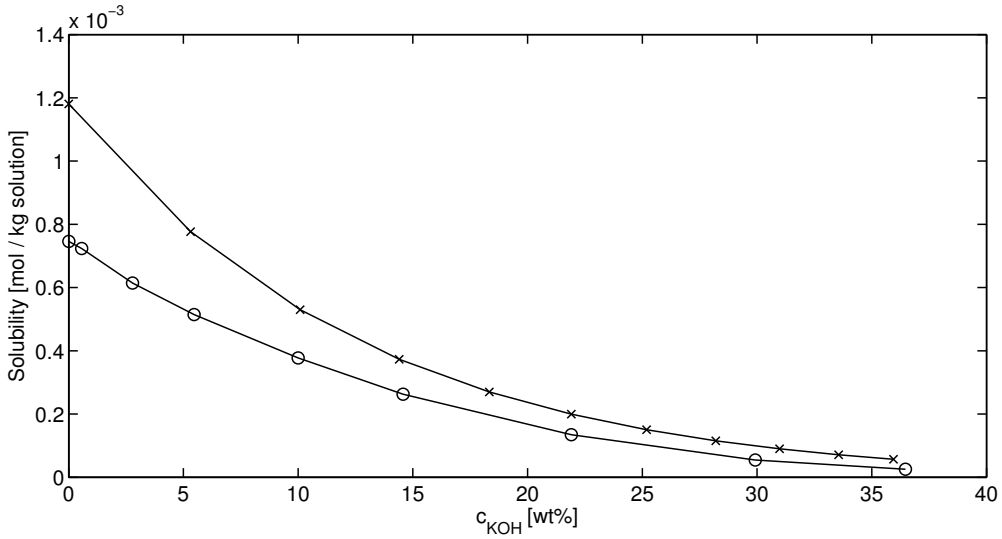

Figure 2.16: Hydrogen solubility (o) and oxygen solubility (x) as a function of the concentration of KOH (aq) at 30 °C with data from Ruetschi [51] for the hydrogen solubility and data from Tromans [50] for the oxygen solubility.

can be seen that the solubility of hydrogen (and oxygen) in aqueous potassium hydroxide is decreasing with increasing concentration of KOH.

Data of the solubility at elevated temperature and pressure is scarce, only one Russian paper was found in literature about the H_2 (and O_2) solubility as a function of temperature and KOH concentration from Knaster et al. [52]. The results are shown if figure 2.17 and listed in table 2.4; the hydrogen solubilities at 21 °C are in good compliance with the data from Ruetschi et al. [51] for the H_2 solubility and the O_2 data from Tromans [50] at 30 °C. In fact the data are, as expected, slightly higher at 21 °C.

Table 2.4: Hydrogen and oxygen solubility in water and aqueous solutions of KOH with a concentration of 5.3 wt%, 18.3 wt%, 28.3 wt% and 35.9 wt% at temperatures of 21 °C, 45 °C and 75 °C. Data obtained from Knaster et al. [52].

Oxygen and hydrogen solubility in [mol/ kg]						
		KOH concentration [wt%]				
Temperature [°C]		0.0	5.3	18.3	28.2	35.9
21.0	O_2	1.35E-03	8.97E-04	3.36E-04	1.02E-04	2.32E-05
	H_2	8.08E-04	6.32E-04	2.73E-04	1.12E-04	4.96E-05
45.0	O_2	9.82E-04	7.12E-04	2.88E-04	8.84E-05	2.04E-05
	H_2	7.28E-04	5.69E-04	2.39E-04	9.51E-05	3.61E-05
75.0	O_2	7.99E-04	5.97E-04	2.44E-04	8.13E-05	1.83E-05
	H_2	7.19E-04	5.42E-04	2.33E-04	8.84E-05	3.29E-05

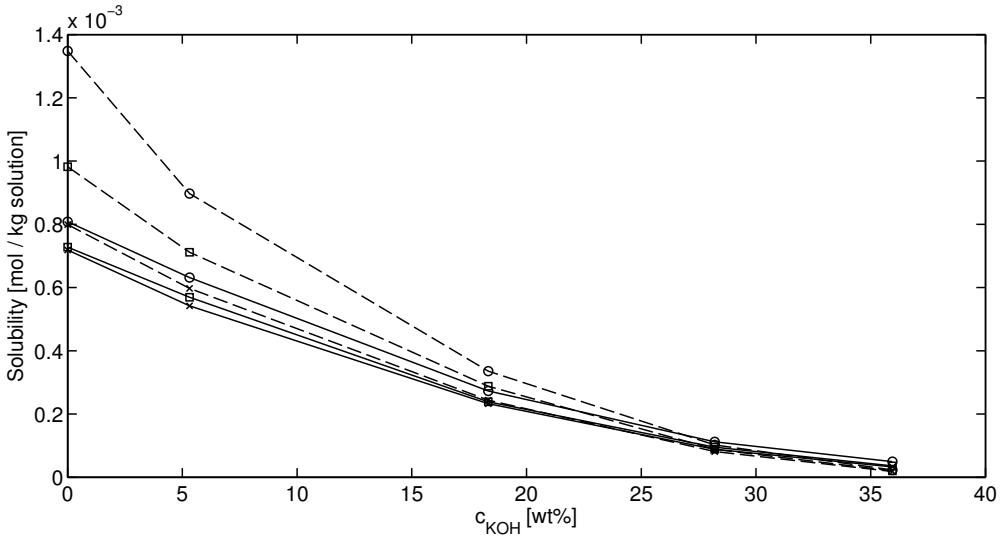

Figure 2.17: Hydrogen solubility (full line) and oxygen solubility (dashed line) as a function of the concentration of KOH (aq) at temperatures of 21 °C (o), 45 °C (□) and 75 °C (x) with data from Knaster et al. [52].

Pray et al. measured the H_2 solubility in water at elevated temperatures and high pressures, showing that the solubility has a similar behavior as this of O_2. The results can be seen in figure 2.18 [53].

2.9.3 *Pressure dependence of O_2 and H_2 solubility*

The pressure dependence of the O_2 and H_2 solubility follows the simple equation 2.30, where $c_{i(T,P_i)}$ is the solubility of the species i as a function of temperature and pressure, $c_{i(T)}$ is the solubility of the species i as a function of temperature, P_i is the partial pressure of the species i above the solution and $P_{i,0}$ is the pressure at which the data were obtained (the values given above are measured or calculated at a partial pressure of 1 bar).

$$c_{i(T,P_i)} = c_{i(T)}\, P_i\, P_{i,0}^{-1} \tag{2.30}$$

2.9.4 *Conclusion on O_2 and H_2 solubility*

Experiments have shown that the solubility of oxygen and hydrogen in aq. KOH as a function of the temperature have minimum around 100 °C, where the solubility is ca. 2 times lower than at 25 °C. At 250 °C it was shown that the solubility increases to values more or less 2 times higher than at 25 °C for the O_2 solubility in water and KOH solutions. The H_2 solubility in water is ca. 4 times higher at 250 °C than at 25 °C. The solubility of oxygen and hydrogen as a function of the KOH concentration decreases strongly with increasing

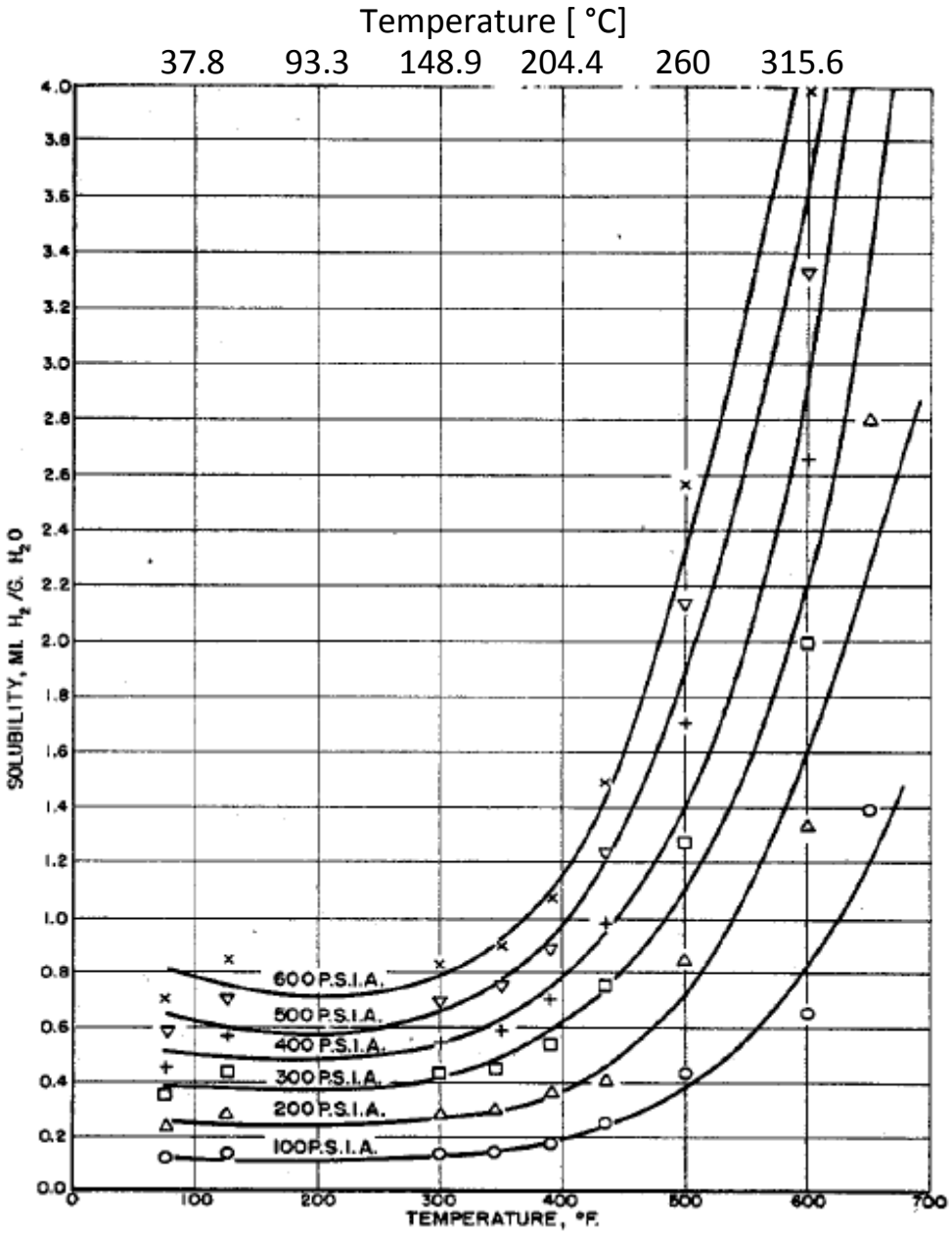

Figure 2.18: H_2 solubility in water at elevated temperatures and pressures [53].

concentration; the O_2 and H_2 solubility in 35 wt% KOH is ca. 21 and 30 times lower, respectively, than this of pure water (compare figure 2.16).

Since no experimental solubility data for O_2 and H_2 in KOH (aq) are available above 100 °C, the theoretical values must be taken with care until they are validated experimentally.

2.10 ALKALINE FUEL CELLS

Alkaline fuel cells AFC have been used for a long time and showed excellent performance and reliability. They were applied already in the 1960´s in space missions, i.e. the Apollo program. One of the great advantages of AFC is the possibility to use non-noble metal catalysts and their excellent efficiency even at low temperatures [54]. A main disadvantage is that AFC suffer from degradation due to the formation of carbonates if they are used with air as a feed gas for the oxygen reduction reaction ORR. Hence, it is necessary to supply pure oxygen, which leads to increased operational costs unless it has been produced as a by-product in alkaline electrolysis.

2.10.1 *Functionality*

In an alkaline fuel cell, hydrogen and hydroxyl ions react at the anode under the formation of water and the release of electrons. Oxygen and water is reduced at the cathode under the formation of hydroxyl ions. These reactions are summarized in equations 2.31 - 2.33. Figure 2.19 shows the ions, electrons and molecules pathway.

$$\text{Anode}: \; H_2 + 2\,OH^- \rightarrow 2\,H_2O + 2\,e^- \tag{2.31}$$

$$\text{Cathode}: \; 1/2\,O_2 + H_2O + 2e^- \rightarrow 2\,OH^- \tag{2.32}$$

$$\text{Total}: \; H_2 + 1/2\,O_2 \rightarrow H_2O \tag{2.33}$$

Some problems concerning AFCs are described in the literature. The most important problems are common with those of other fuel cell technologies, like preparation of the electrodes and the catalyst choice and application, costs and degradation. Some are more specific, like the necessity to use pure oxygen and corrosion problems because of the strongly alkaline media [55].

Anyway, AFCs still have the potential to play a major role in the future energy systems, especially for stationary applications where hydrogen and oxygen is produced by alkaline electrolysis as part of an energy storage system.

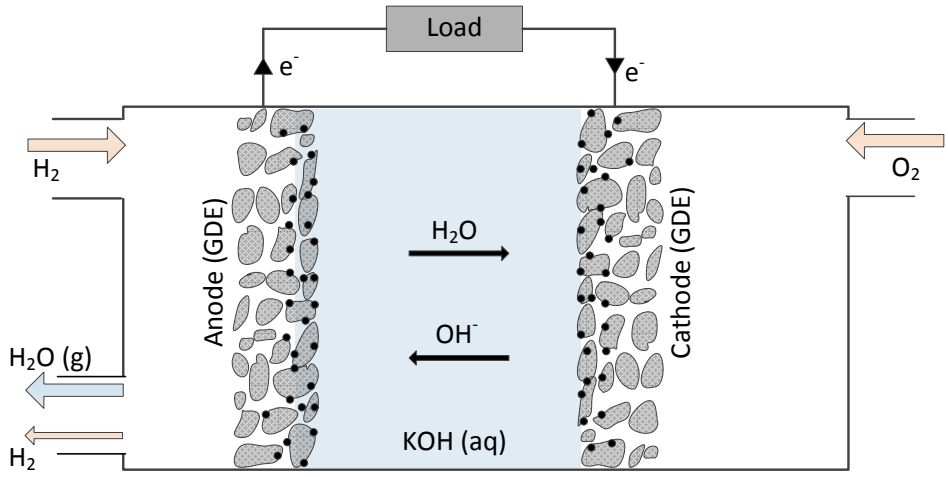

Figure 2.19: Basic functionality of an alkaline fuel cell. Hydrogen and hydroxyl ions react at the anode under the formation of water and the release of electrons. Oxygen and water is reduced at the cathode under the formation of hydroxyl ions.

Part III

EXPERIMENTAL

3 MEASUREMENT SYSTEMS AND TECHNIQUES

Measurement systems to test the conductivity of aqueous and aqueous immobilized electrolytes, and the performance of alkaline electrolysis cells were designed and constructed for this thesis. Initial measurements were performed in an atmospheric setup in order to test half cell reactions of alkaline electrolysis cells. A single atmosphere high temperature and pressure setup was build to determine the conductivity of aqueous electrolytes and aqueous electrolytes immobilized in porous structures. The same setup was modified in order to perform electrolysis measurements on alkaline electrolysis cells. A further measurement system to allow fully automatized measurements under high temperature and pressure and controllable gas composition was designed and built for long term measurements.

3.1 ATMOSPHERIC SETUP

3.1.1 *Introduction*

An introduction to alkaline electrolysis and fuel cells was given in chapter 2. Thermodynamic data of potassium hydroxide KOH was presented over a wide temperature and pressure range. In order to study half cell reactions of electrochemical cells it is common to use a so called 3 electrode setup which consists generally of a working electrode (WE), a reference electrode (RE) and a counter electrode (CE). The WE is the electrode of interest. It is important to perform measurements under a defined atmosphere; a sufficient amount of gas stream through the electrochemical cell is therefore necessary and can for example be realized as shown schematically in figure 3.1: Argon or air can be flushed through a beaker in order to wash and humidify the gas before it enters the electrochemical cell. Furthermore, continuous gas flow ensures that no explosive gas mixtures will occur in the cell beaker from hydrogen and oxygen evolution. The electrical contacts of the WE, RE and CE are connected to a potentiostat in order to perform electrochemical measurements like cyclic voltammetry (CV) or electrochemical impedance spectroscopy (EIS).

For measurements which can be compared with data from others, it is necessary to present the reaction potential relative to a certain reference potential. For CV measurements it is common to give the obtained results against the standard hydrogen electrode (SHE). Hence, it is necessary to transform data which have been measured against another type of reference electrode, for example the reversible hydrogen electrode (RHE). The transformation from RHE to SHE is based on equation 3.1, where E_{SHE} is the potential against the stan-

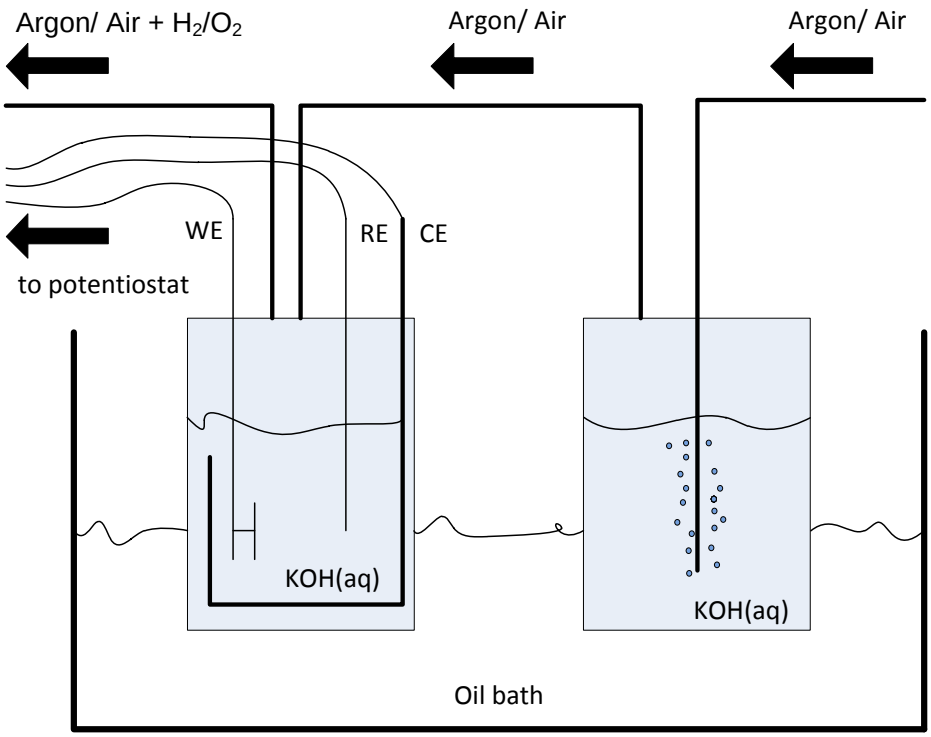

Figure 3.1: Schematic assembly of an atmospheric 3 electrode setup for electrochemical measurements in aqueous solutions. The working electrode (WE), the reference electrode (RE) and the counter electrode (CE) are connected to a potentiostat in order to perform electrochemical measurements. Argon or air can be flushed through a beaker (right beaker) in order to wash and humidify the gas before it enters the electrochemical cell (left beaker). A heated oil bath allows measurements at elevated temperatures.

dard hydrogen electrode, E_{RHE} is the potential against the reversible hydrogen electrode, F is Faradays constant (96485 $C \cdot mol^{-1}$), T is the temperature in [K], pH is the negative logarithmic value of the Hydrogen ion (H^+) concentration and R is the gas constant.

$$E_{SHE} = E_{RHE} - \frac{2.303\,R\,T}{F} pH \tag{3.1}$$

3.1.2 *Experimental*

A measurement setup which can be used for electrochemical measurements in aqueous KOH, under atmospheric pressure and temperatures as high as the boiling point of the solution, was designed and constructed. PTFE (Polytetrafluoroethylene or Teflon) is known to be one of the most resistant non-metal materials under caustic and acid conditions. PFA (Perfluoroalkoxy) shows similar resistance and is said to be inert towards KOH. Both fluoropolymers are suitable to work at temperatures up to 250 °C [56] and were therefore chosen as construction materials for the atmospheric setup.

Pictures of the developed measurement setup which was build on the basis of the schematic shown in figure 3.1 can be seen in figure 3.2. Two beakers, which are made from PFA, were used for the housing of the electrochemical cell and for the gas humidification. The PFA beakers are placed into a glass beaker filled with silicon oil which is heated on a common laboratory heating plate with a temperature controller. The counter electrode CE is produced from a nickel mesh and formed into a cylindrical shape as shown on the right picture of figure 3.2. The working electrode was placed in a gas diffusion electrode sample holder delivered by BANK IC [57], which was customized to withstand temperatures up to 250 °C and produced from PTFE. The reference electrode is a reversible hydrogen electrode bought from Gaskatel [58]. Cyclic voltammetry experiments on plain nickel and an experimental Raney-Nickel electrode delivered by Force Technology were performed with a Gamry 600 potentiostat. The concentration of the electrolyte varied from 1M to 10M and the temperature from 25 °C to 118 °C.

3.1.3 *Results*

3.1.3.1 *Cyclic voltammetry on plain nickel electrodes at different concentrations of KOH*

Cyclic voltammograms with a sweep rate of 50 $mV\ s^{-1}$ on plain nickel electrodes have been obtained at concentrations of 1 M (5.0 wt%), 5.5 M (23.5 wt%) and 10 M (36.0 wt%) KOH (aq) under argon atmosphere at a temperature of 25 °C. The results are presented in figure 3.3. The hydrogen evolution reaction HER vs. SHE started at a potential of ca. -1.05 V, -1.1 V and -1.1 V for the 1 M, 5.5 M and 10 M solution, respectively. The oxygen evolution started at

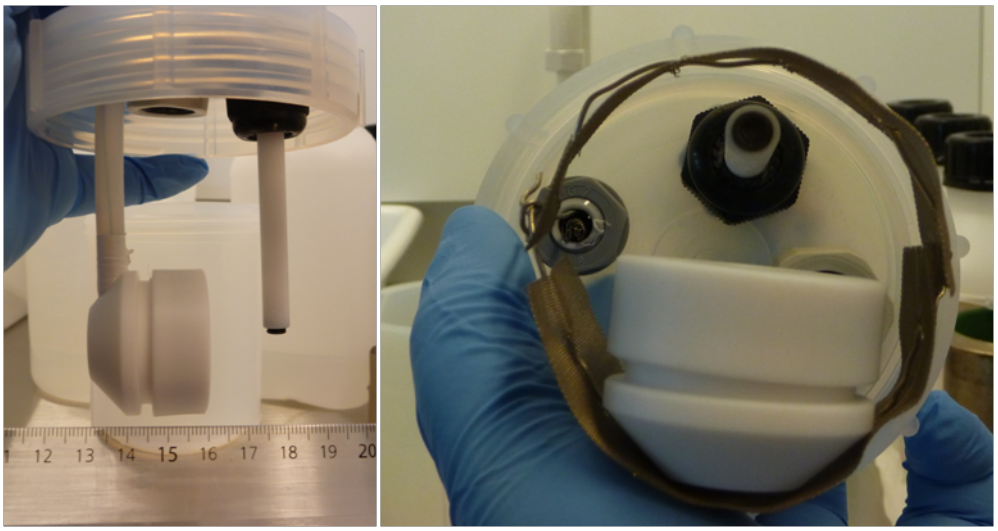

Figure 3.2: Front view (left) and bottom view (right) of the assembly of the atmospheric setup for electrochemical measurements in strong alkaline solutions.

0.68 V, 0.63 V and 0.63 V for the 1 M, 5.5 M and 10 M solution, respectively. The Tafel-slope during hydrogen and oxygen evolution is significantly higher in the higher concentrated solutions which is coincident with the higher conductivity of the electrolyte [25] at the given condition. All measurements were carried out without IR-compensation.

3.1.3.2 *Cyclic voltammetry on plain nickel electrodes at different temperatures*

To analyze the influence of temperature on a plain nickel electrode in aqueous solutions of KOH with a concentration of 5.5 M, cyclic voltammetry experiments were carried out at temperatures of 25 °C and 100 °C. The results are displayed in figure 3.4. The potential for the OER at a current density of 100 $mA\ cm^{-2}$ was 1.13 V and 0.51 V at temperatures of 25 °C and 100 °C, respectively. Hence, the polarization for the OER was reduced by 0.62 V. The HER started at -1.16 V for 25 °C and -1.22 V for 100 °C. The potential for the HER at a current density of 100 $mA\ cm^{-2}$ was found to be -1.5 V for both, 25 °C and 100 °C. All measurements have been carried out without IR-compensation.

3.1.3.3 *Cyclic voltammetry on Raney-nickel electrodes at different temperatures*

A Raney-nickel sample which has been delivered by Force-Technologies has been tested in the above described atmospheric measurement setup. After activation in 30 wt% KOH with 10% KNa-tartrate tetrahydrate at 80 °C for 24 hrs (Step1), the sample has been conditioned at $-10\ mA\ cm^{-2}$ for 2 hours (Step 2) and at $-200\ mA\ cm^{-2}$ for 14 hours (Step3) in 25 wt% KOH (aq) after instructions from Force Technologies.

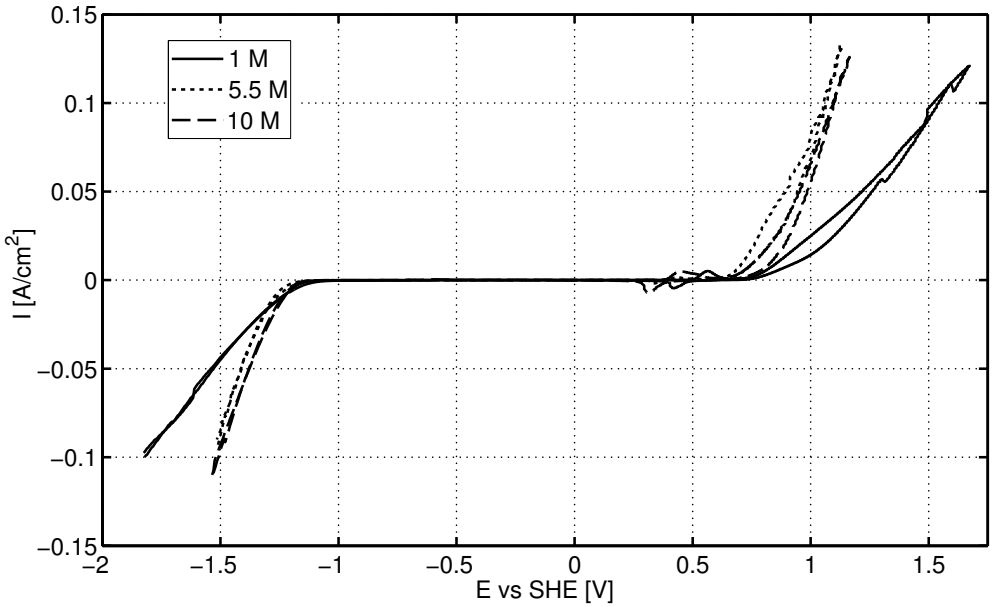

Figure 3.3: CV results of a plain nickel electrode in aqueous solutions of KOH with different concentrations at STP in argon atmosphere. The sweep rate was $50\,\mathrm{mV\,s^{-1}}$.

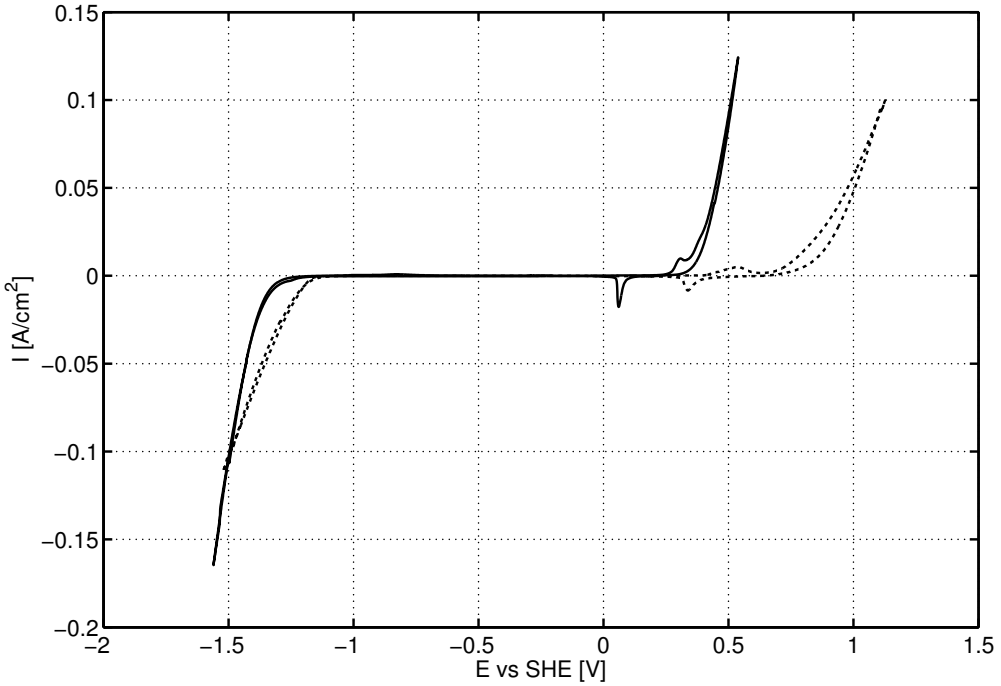

Figure 3.4: CV of a plain Nickel electrode in 5.5 M aqueous KOH at a temperature of 25 °C (dashed line) and 100 °C (full line). The sweep rate was $50\,\mathrm{mV\,s^{-1}}$.

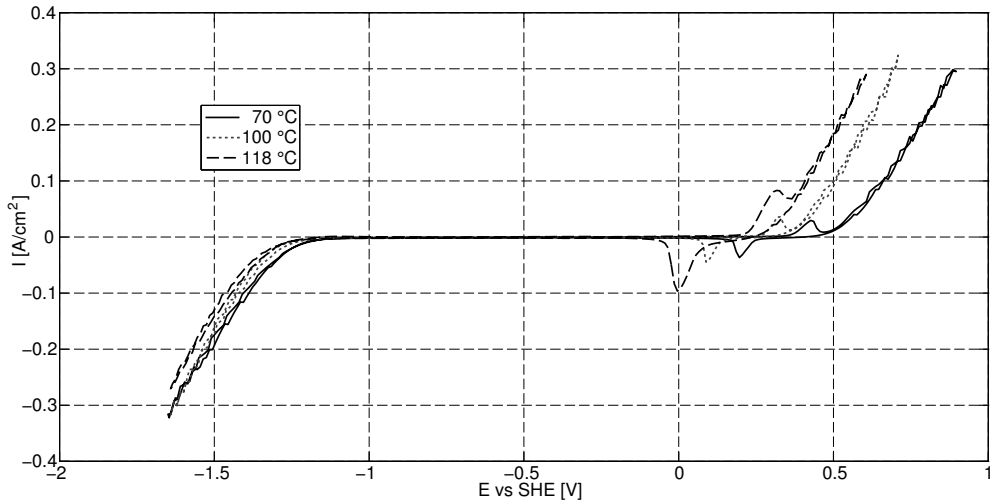

Figure 3.5: Cyclic Voltammograms of the Force Raney-nickel electrode under N_2 atmosphere at ambient pressure and temperatures from 70 °C to 118 °C in 10 M KOH (aq) measured with a sweep rate of 10 $mV\ s^{-1}$.

Cyclic voltammetry was applied to the activated and conditioned electrode at temperatures of 70 °C, 100 °C and 118 °C. The obtained results are shown in figure 3.5. The potential for the OER at a current density of 200 $mA\ cm^{-2}$ was found to be 0.77 V, 0.6 V and 0.51 V for temperatures of 70 °C, 100 °C and 118 °C, respectively. Hence, the anodic polarization was reduced by 260 mV through heating from 70 °C to 118 °C. The potential for the HER at a current density of $-200\ mA\ cm^{-2}$ was found to be -1.52 V, -1.54 V and -1.58 V for temperatures of 70 °C, 100 °C and 118 °C, respectively. All measurements have been carried out without IR-compensation.

3.1.3.4 *Discussion*

Cyclic voltammetry has been applied to pure plain nickel electrodes and a Raney-nickel electrode at different temperatures and concentrations of KOH. The Tafel-slopes improved significantly with increasing temperature on the plain nickel electrode while they were almost constant on the Raney-nickel electrode. Increasing the temperature lead to significantly reduced polarization losses, especially for the OER. It can be expected that the polarization losses at higher temperatures will be reduced even more. A system to perform measurements at higher temperatures requires the possibility to pressurize the system in order to avoid boiling and evaporation of the electrolyte.

Table 3.1: Technical specifications of the Parr autoclave.

Producer	Type	Vessel material	Volume	p_{max}	T_{max}	Liner	T_{max} with liner
Parr Instruments	4760	Inconel 600	600ml	200 bar	350 °C	PTFE	250 °C

3.2 SINGLE ATMOSPHERE HIGH TEMPERATURE AND PRESSURE SETUP

3.2.1 *Parr autoclave*

To perform measurements under high pressure and at elevated temperatures it was necessary to build a measurement system around an autoclave which could stand high temperatures up to 250 °C and pressures up to 95 bar as well as extremely caustic environments. PTFE and PFA would be feasible for the high temperatures, but not for the high pressures. A metallic autoclave had to be build or ordered after a careful selection of construction materials: Aluminum is heavily attacked in KOH [59] and should be avoided as a construction material. Also alumina, which is usually a highly corrosion resistant material, was strongly attacked by KOH at elevated temperatures of ca. 220 °C and a KOH concentration of 30 wt% [60]. A broad study of the corrosion behavior of stainless steels and nickel based alloys by Gras et al. [61] at temperatures of 120 °C, 150 °C and 180 °C under hydrogen and oxygen atmosphere in 28 wt% KOH recommended 310(L) SS and Alloy 800 as the most corrosion resistant alloys, but it was furthermore pointed out that non of the tested materials were sufficiently corrosion resistant under oxygen overpressure. Pure Nickel was found to be corrosion resistant under argon overpressure , but else similar conditions (180 °C, 28 wt% KOH) in earlier work [62]. Inconel alloy 600 is recommended for alkalies from the "Special Metals" corporation [63], but it is recommended to anneal the alloy if stress corrosion cracking is an issue. This was verified by Pement et al. [64], who furthermore recommended Inconel 690 if stress corrosion cracking is an issue. Anyway, Inconel 600, also called Alloy 600, showed the most promising resistances among the metals which are available for autoclave construction [56]. After comparing the variety of choices on the market and obtaining quotations from different suppliers, a Parr autoclave Type 4760 was ordered; technical specifications are listed in table 3.1.

3.2.2 *Autoclaves peripheries*

To perform electrochemical measurements, the autoclave had to be equipped with additional gas handling components and fittings as well as wire leadtroughs. The complete setup, how it was used for the measurements discussed in chapters 4 and 5 (with modified sample holders and connections to the potentiostat), is shown in figure 3.6: A gas bottle (here shown as nitrogen) is used

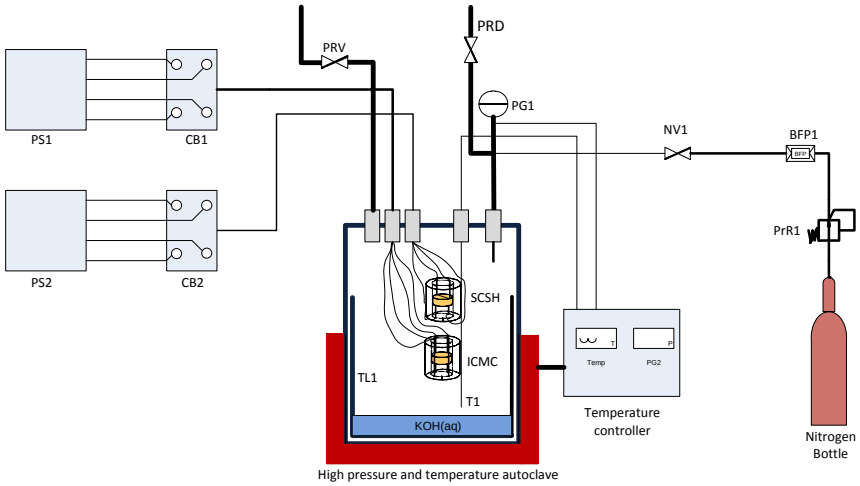

Figure 3.6: Schematic description of the measurement setup: PrR1= Pressure reducer, BFP1= Backflow protection, NV1= Needle valve, T1= J- Type thermo-well, PG2= Pressure gauge, TL1= Teflon liner, SCMC= Symmetrical Cell Sample Holder, ICMC= Immobilized conductivity measurement cell, CB1& CB2= Connection boxes, PS1 & PS2= Gamry Type 600 potentiostat.

for the pressurization of the autoclave. A pressure reduction valve PrR1 was installed to avoid too high pressure increase rates and over-pressurization of the system during initial pressurization. The back-flow protection valve BFP1 avoids the back-flow of hazardous gases in the gas bottle. The pressure is adjusted by manually stopping the flow of pressurized gas to the autoclave by needle valve NV1. The J-Type thermo-well T1 measures the Temperature in the autoclave. The pressure gauge PG1 displays the actual pressure analog in order to allow steady control, even if the electricity supply to the system fails, while another pressure gauge allows recording the pressure together with the temperature in the temperature controller unit. A Teflon liner TL1 protects the inner part of the autoclave from corrosion.

The sample holders, for example the aqueous conductivity measurement cell ACMC, was connected to the protection hood of the thermo-well by a PTFE shrinking tube in the center of the autoclave. The immobilized conductivity measurement cell ICMC was situated directly below and equally fixed. Other sample holders were fixed in a comparable way. The connection wires from each cell were put through to the outside of the autoclave by high pressure glands (the wire feedthroughs) and were then connected to the connection boxes CB1 or CB2. A Gamry Type 600 or 3000 potentiostat, PS1 and PS2, was used to perform the electrochemical measurements. An aqueous solution of potassium hydroxide with lower concentration of than the sample being measured, was placed at the bottom of the teflon liner to avoid drying of the samples during the measurements. A photograph of the complete setup can be seen in figure 3.7.

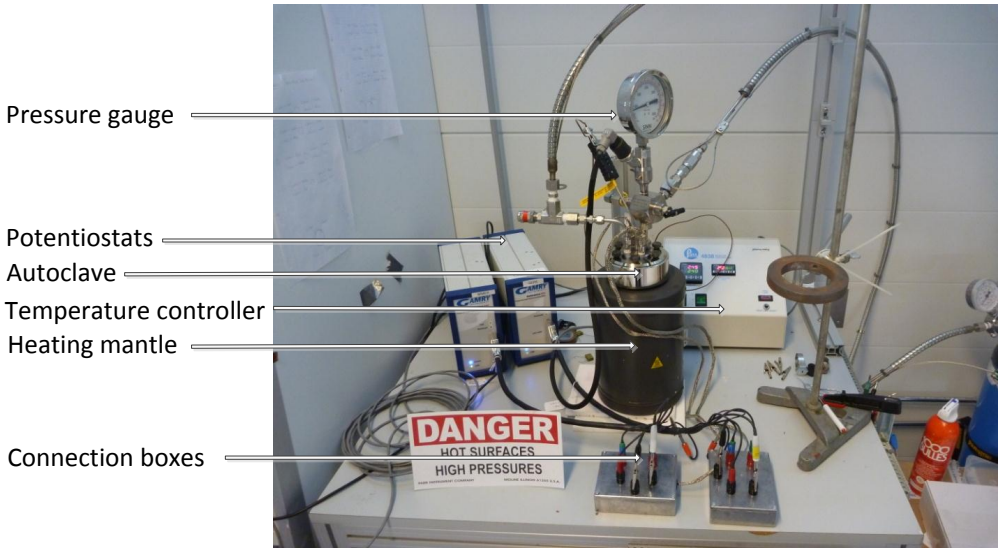

Figure 3.7: Photograph of the system used for the measurements discussed in chapter 4 and 5. Two potentiostats are connected to connections boxes which are further connected to the autoclave. The temperature controller unit regulates the autoclave temperature and records the temperature and pressure electronically.

3.3 CONDUCTIVITY MEASUREMENT SETUP

3.3.1 *Introduction*

The conductivity of the electrolyte is a very important parameter for the performance of an alkaline electrolysis or fuel cell in general. This was discussed earlier in chapter 2.4.1 and will also be discussed in chapter 4. This section will give an overview of the techniques and sample holders used to determine the conductivity of aqueous KOH and of aqueous KOH immobilized in porous pellets of $SrTiO_3$ for a broad range of concentrations and temperatures up to 250 °C. The measurement equipment was designed in a versatile way to allow similar measurements with other aqueous electrolytes. Parts of the equipment have been developed for and during a master thesis entitled "Immobilized K_2CO_3 Electrolyte for Low-Temperature CO_2 Electrolysis"[65].

3.3.2 *Measurement Methods: Resistance, conductance, resistivity and conductivity*

When it comes to the determination of the conductivity in DC driven circuits, it is important to distinguish between the resistance, conductance, resistivity and the conductivity. In AC driven circuits it is furthermore important to distinguish between the impedance and the admittance. The commonly used symbols and units are listed in table 3.2.

	Symbol	Unit	equal to
Resistance	R	Ω (Ohm)	1/S
Conductance	S	S (Siemens)	1/R
Resistivity	ρ	Ω m	R*l (length))
Conductivity	σ	$S\,m^{-1}$	1/ρ
Impedance	Z	Ω, Ohm	1/Y
Admittance	Y	S, Siemens	1/Z

Table 3.2: Basic relations of impedance related values

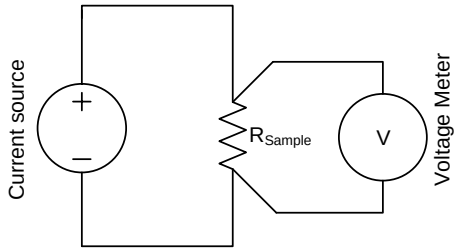

Figure 3.8: Ordinary four point measurement circuit.

To determine the resistance of any kind of electronic conductor, it is common to apply a current to this sample and to measure the voltage drop. It is beneficial to apply a constant current to the sample instead of a constant voltage because of the voltage drop that occurs in the connection wires may result in some calculation errors. This is even more important for the case that the resistance of the sample is in the same order of magnitude as the resistance of the wires. The described measurement method is called a four point measurement and is schematically drawn in figure 3.8. The resistance of the sample can be calculated by Ohms law. Further information can be found in the literature [66].

When it comes to area or length- specific determination of the resistivity or conductivity, it is very important to apply a linear current or ion-flow in the sample to archive high accuracies. A measurement cell which was used by Guanti et al [67] to measure the electrolytic conductivity in highly conducting solutions is shown in figure 3.9. A current which will be applied to the outer, black, electrodes will lead to a constant ion flow in the cell. The current density must be limited, since a too high current can cause bubble formation at the electrodes as well as unwanted heating of the electrolyte, which will both lead to inaccurate measurements. The conductivity of an aqueous electrolyte using this cell can be calculated by the use of equation 3.2, where $\sigma_{Electrolyte}$ is the conductivity of the electrolyte, $U_{lattice}$ is the measured voltage between the lattices, A is the area of the cross section of the sample and d is the distance between the inner electrodes (the lattices).

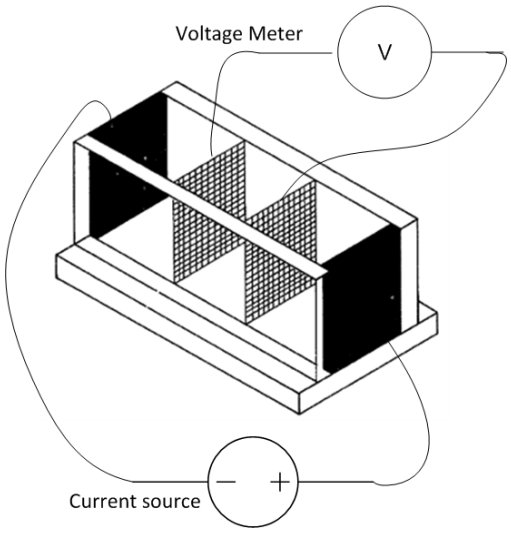

Figure 3.9: Cell to determine the conductivity of aqueous solutions [67].

$$\sigma_{Electrolyte}[S\,m^{-1}] = \frac{I\,d}{U_{lattice}\,A} \tag{3.2}$$

3.3.3 *The van der Pauw technique*

The previously described method is feasible for aqueous solutions and to some extend also for solid samples. To determine the conductivity of arbitrary shaped samples, the van der Pauw method is a well known and proven technique. In theory, it allows measurements on any kind of arbitrary shaped sample as long as the following preconditions are fulfilled [28]:

- The contacts must be at the circumference of the sample
- The contacts must be relatively small in comparison to the sample
- The sample is homogeneous in thickness
- The sample must not have any isolated holes and must be isotropic

Further details on the use of the van der Pauw technique can be found in chapter 4.

3.3.4 *Aqueous conductivity measurement setup*

A sample holder for aqueous electrolytes had to be developed and built in order to apply the van der Pauw theory for conductivity measurements. Figure 3.10 shows the sample holder for aqueous electrolytes. Platinum black coated platinum wires with a diameter of 0.5 mm were used as electrodes. They were

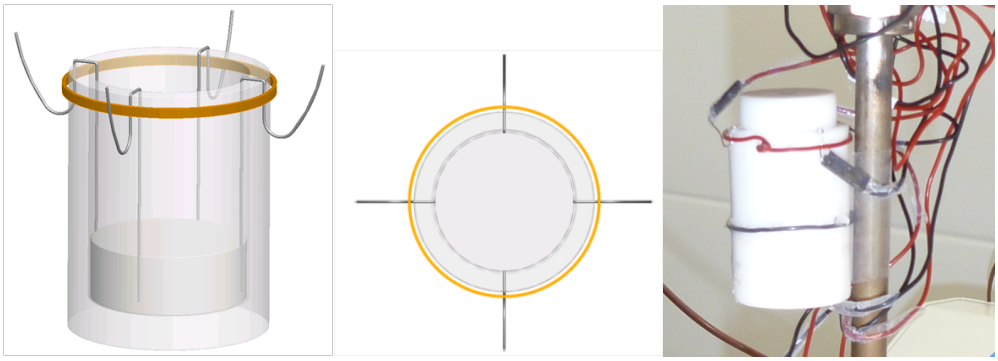

Figure 3.10: Illustration of the Teflon setup for the aqueous KOH solutions as a tilted view (left) and as a top view (middle) [65] and photograph of the sample holder for aqueous electrolytes.

placed on the sides of a Teflon beaker and stretched down by a Teflon pellet and fixed at the outer top of the sample holder by an insulated metal wire. figure 3.10 shows the sample holder during a measurement. A Teflon lid was placed on top to keep the height of solution in the sample holder constant and to avoid or minimize concentration changes through evaporation and condensation. A hole with a 3 mm winding in the middle of the lid allows exact positioning and avoids overpressure built up in the sample holder during heating.

3.3.5 *Immobilized conductivity measurement setup*

The sample holder which has been developed and built to determine the conductivity of immobilized electrolytes is shown in figure 3.11. The electrodes were built of 0.5 mm platinum black coated platinum wires. A Nickel ring at the outer part of the sample holder presses the electrodes onto the sample. A slit in the holder makes it somewhat flexible to be able to take samples with slightly varying diameter. The platinum electrodes are connected to Nickel-copper wires by cold welding a nickel tube which surrounds the interface. This interconnection can be seen on the right image of figure 3.11 together with the sample holder. The left and center image of figure 3.11 shows a 3D- and top view of the sample holder.

3.3.6 *Alkaline electrolysis cell sample holder*

Electrochemical measurements on alkaline electrolysis cells were performed in the previously described high temperature and pressure autoclave setup. The sample holder which was designed and built for the measurements on electrolysis cells is shown in figure 3.12. The cylindrical cell is mounted in the middle of the PTFE cylinder. The cell can be fixed by three M3 screws for easier mounting. A metal mesh was used to ensure uniform current distribution through the cell. Nickel springs with a platinized tip pressed the mesh with a

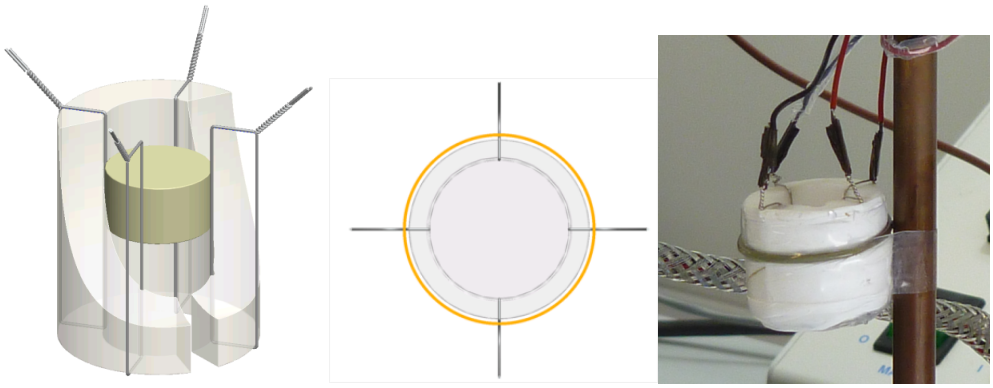

Figure 3.11: Illustration of the Teflon setup for the immobilized KOH solutions as a tilted view (left) and as a top view (middle) [65] and as a photograph (right).

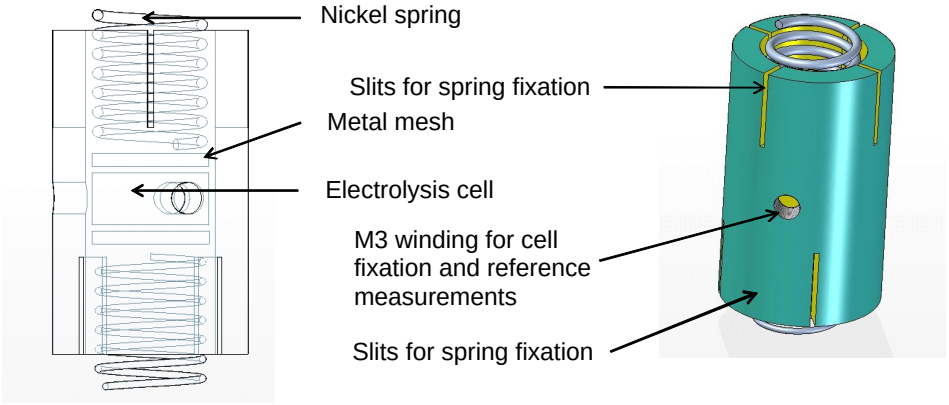

Figure 3.12: 3D- model of the symmetrical cell test holder.

constant force on the cells surface. The cables to the potentiostat/ measuring device were connected to the outer end of the springs. Slits in the side of the PTFE cylinder allowed fixation of the springs with a corrosion resistant wire. The springs were squeezed so that they were completely in the cylinder; the 45° angle between the slits on both ends of the cylinder prevented a shortcut between the two electrodes.

3.3.7 *Improved sample holder*

Since initial measurements with the first version of the cell holder as shown in figure 3.12 showed contact and handling problems, a new version of the cell holder was developed to allow electrochemical measurements. Figure 3.13 shows the cross section of the improved cell holder which was used for all measurements on electrolysis cells in chapter 5. Nitinol tension springs were used to apply a constant force between two Inconel tubes which acted as cur-

rent collectors. Inconel screws attached to the Inconel tube acted as corrosion resistant connection points as well as mounting points for the Nitinol spring. PTFE O-rings ensured electronic insulation between the Inconel screws and the Nitinol springs. The AEC was placed in between two metal foams acting as current collectors (Inconel foam on the cathode, nickel on the anode). The produced gases could evolve through the Inconel tubes to the autoclave vessel. 5 mm holes on the side of the PFA tube fitting (Swagelock type PFA-820-6) ensured that the cell would not dry out during the performed measurements and allowed to connect a platinum wire to the center of the cell (immobilized electrolyte) in order to perform measurements against a reference electrode. The working electrode (WE) and the working sense (WS) of the potentiostat terminals were connected to the anodic side of the sample holder while the counter electrode (CE) and the reference (Ref) terminals were connected to the cathodic side of the sample holder.

3.4 SAFETY ASPECTS

Hydrogen and oxygen will be produced by electrolysis during the experiments in the autoclave. The lower explosion limit LEL of Hydrogen in known to be around 4 % in air at atmospheric pressure and room temperature [68], but varies with temperature, pressure and gas composition. A literature and safety study was undertaken to retrieve the relevant data for the project. Furthermore, it was necessary to make sure that those values would not be exceeded during the experiments at any time.

3.4.1 *Explosion limits dependance on pressure*

As mentioned, the LEL of H_2 in air at STP is around 4.0 %. Schroeder et al [69] analyzed the LEL as a function of pressure and found that it increases slightly from 4.0 mol% at STP to 5.9 mol% at 200 bar in hydrogen-oxygen mixtures and from 4.3 mol% at STP to 5.6 mol% at 150 bar in hydrogen-air mixtures as displayed in figure 3.15.

3.4.2 *Explosion limits depending on temperature*

The LEL and HEL of H_2 in hydrogen-air mixtures decrease with increasing temperature [69]. The LEL decreases from 3.9 mol% at 20 °C to 1.5 mol% at 400 °C while the HEL increases from 75.2 mol% to 87.6 mol% like shown in figure 3.16. Values for the LEL and HEL as a function of temperature for hydrogen-oxygen mixtures could not be found.

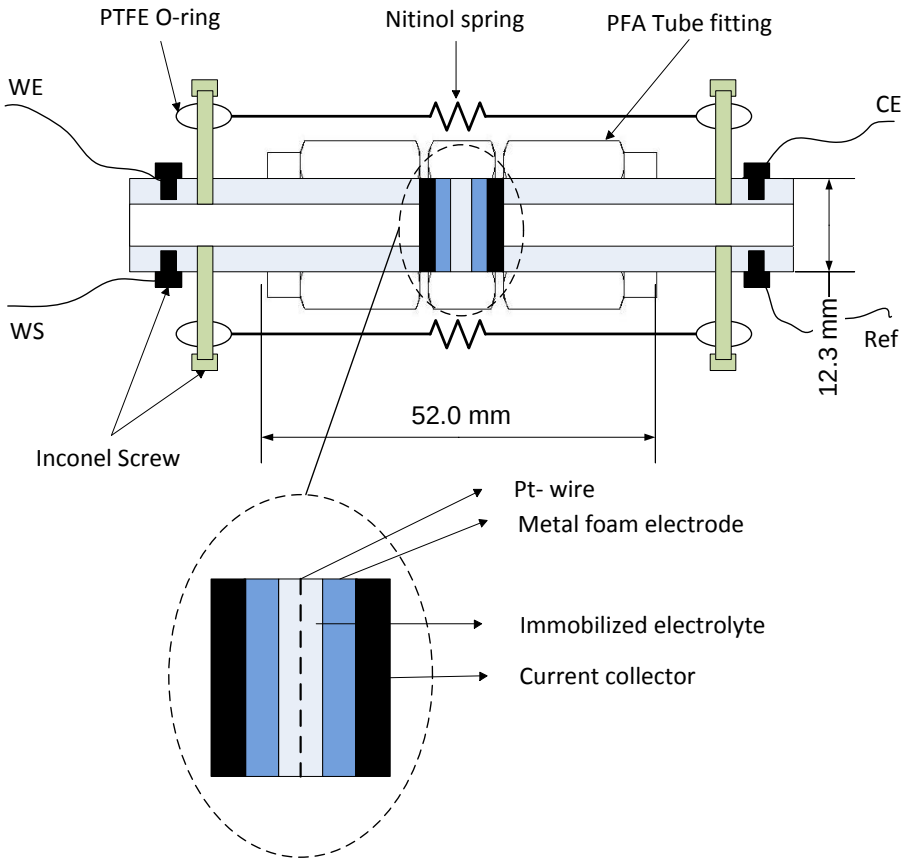

Figure 3.13: Principal cross section of the Alkaline Electrolysis Cell Holder (AECH): The electrolysis cell is centered in the sample holder. A piece of metal foam acts as current collector. The Inconel tubes press the foam against the active electrode of the electrolysis cell. Nitinol springs are assembled to provide constant force in order to avoid contacting problems. They are insulated against the screws by a PTFE O-ring. The wires WE, WS, CE and Ref indicate how the cell was connected to the potentiostat. The Pt-wire acts as reference electrode in the three electrode setup.

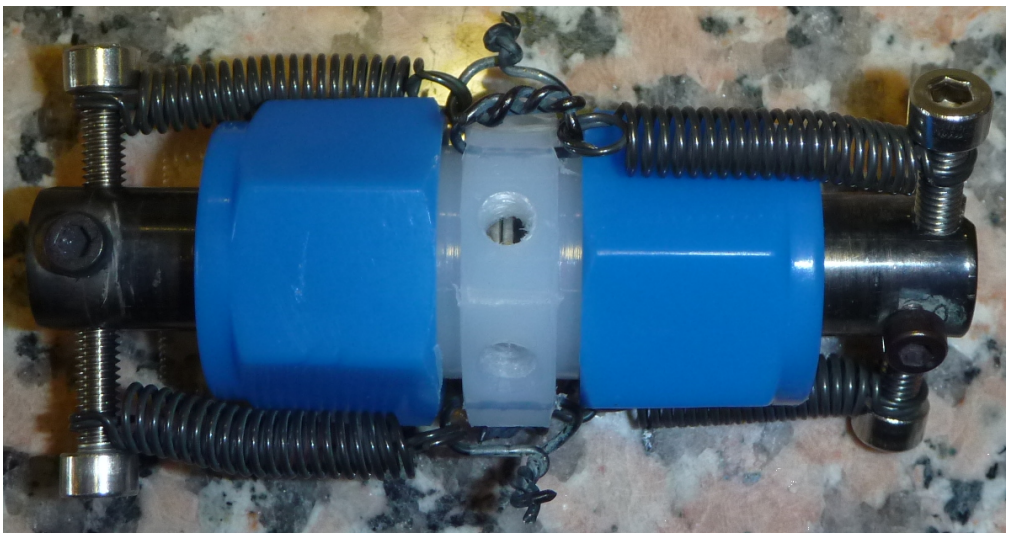

Figure 3.14: Picture of the cell holder used for electrochemical measurements on electrolysis cells.

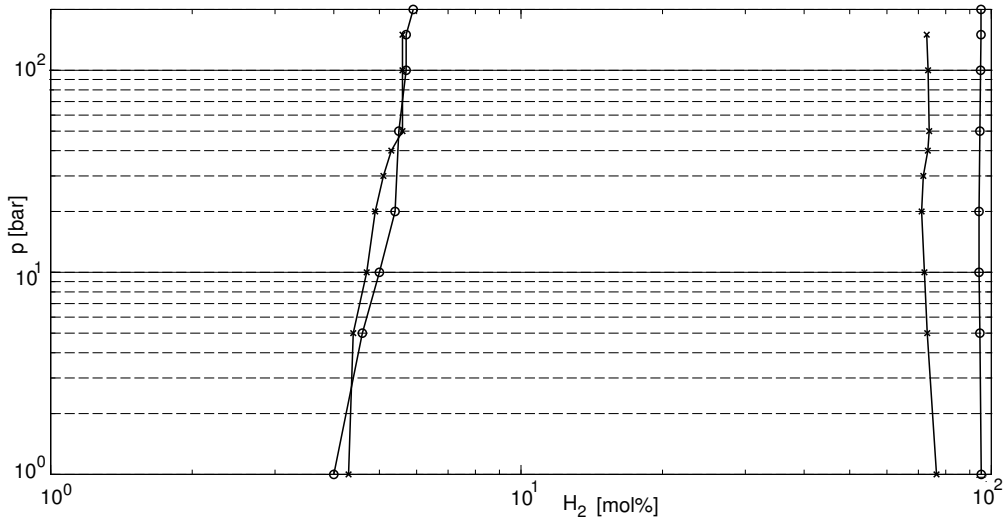

Figure 3.15: Influence of the pressure on the lower (LEL) and higher (HEL) explosion limit of hydrogen-air (x) and hydrogen-oxygen (o) gas mixtures.

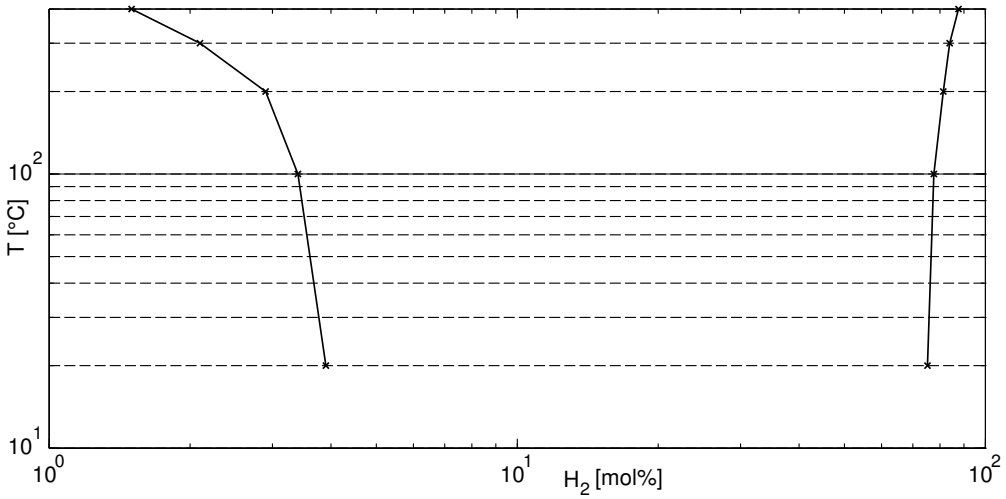

Figure 3.16: Influence of the temperature on the LEL and HEL of hydrogen-air (x) gas mixtures.

3.4.3 *Time limited experiments*

The lower explosion limit should never be reached during experiments in the measurement setup. To ensure that the maximal allowable concentration was set to 10 % of the LEL. A simple method to avoid an explosive atmosphere in the autoclave is to limit the experiments duration at a certain hydrogen production rate. Assumed that the pressure vessel of the autoclave is filled with inert gas of a specific pressure, the total amount of gas can be calculated by equation 3.3, where n_{inert} is the amount of inert gas in [mol], R is the gas constant, T is the temperature in [K], V is the volume of the autoclave (0.6 l, tubing neglected) and p is the partial pressure of the inert gas.

$$n_{inert} = \frac{p\,V}{R\,T} \tag{3.3}$$

The maximum amount of produced gas is limited by the potentiostat, which can provide 3000 mA, and can be calculated by equation 3.4, where $\dot{n}$ is the gas production rate in $[mol\,s^{-1}]$ and I is the applied current.

$$\begin{aligned} \dot{n} &= \frac{I}{z\,F} \qquad (3.4)\\ with& \\ \dot{n} &= Amount\ of\ produced\ gas\ [mol\,s^{-1}] \\ I &= Current\ [A] \end{aligned}$$

The maximum electrolysis time at a certain applied electrolysis current until 10 % of the LEL (4 %) are reached can then be calculated to:

$$
\begin{aligned}
t_{max} &= 0.1 \cdot 0.04 \frac{n_{inert}}{\dot{n}} \qquad (3.5)\\
&with \\
t_{max} &= maximum\ electrolysis\ time\ [s]
\end{aligned}
$$

3.5 AUTOMATIZED HIGH TEMPERATURE AND PRESSURE SETUP

3.5.1 *Autoclave and gas handling cabinet*

The measurements which were performed in the Parr autoclave as described above were time limited to avoid the formation of explosive gas mixtures in the reaction chamber. In order to perform measurements over an extended period of time it was necessary to construct a system which is able to supply the reaction chamber with a continuous flow of H_2, O_2, N_2 and steam. Since it was desired to have an automated operation of the system at temperatures of up to 300 °C and pressures of up to 95 bar, a number of safety issues had to be considered. The design and construction work were done by specialized employees in order to fulfill the safety demands. The completed system with the internal identification name "Rig 28" is shown in figure 3.17 along with the external gas supply panel, "Rig 29" (a similar system) and the mobile unit for data acquisition. Rig 28 was used for the measurements discussed in chapter 6 and 7.

An inside view of the gas handling cabinet (GHC) of rig 28 is shown in figure 3.18 A. The gas sensors in the upper left corner monitor the partials pressures of O_2, H_2 and CO to ensure that they remain within safety limits. The autoclave will be evacuated in the case that a critical concentration is measured and the gas flow will be interrupted. The gas control panels comprise mass flow controllers (MFC), magnetic valves (MV) and pressure control valves (PCV) in order to control the gas flow of O_2, N_2 and CO_2 (gas control panel 1) and H_2 (gas control panel 2) to the autoclave. The safety box controls and monitors all system parameters. Figure 3.18 B shows the autoclave used in the GHC. The setup allowed electrochemical tests in a temperature range of 25 °C – 250 °C and a pressure range of 1 – 100 bara. The main vessel of the autoclave is made from steel. Two heating elements in direct contact with the autoclave body are used to heat the autoclave. The temperature is computer controlled using a Eurotherm controller. Alumina wool insulates the reaction chamber of the autoclave from the surroundings and ensures even temperature distribution inside. A titanium liner inside the autoclave offers improved corrosion resistance towards the highly corrosive KOH and other hazardous chemicals. Furthermore, an additional teflon liner has been placed inside the vessel for even higher corrosion resistance. Two Inconel lids are placed at the top and the bottom of the autoclave; they are sealed with Teflon or titanium O-rings and a number of bolts. Wire feedthroughs allow electrical connection to the

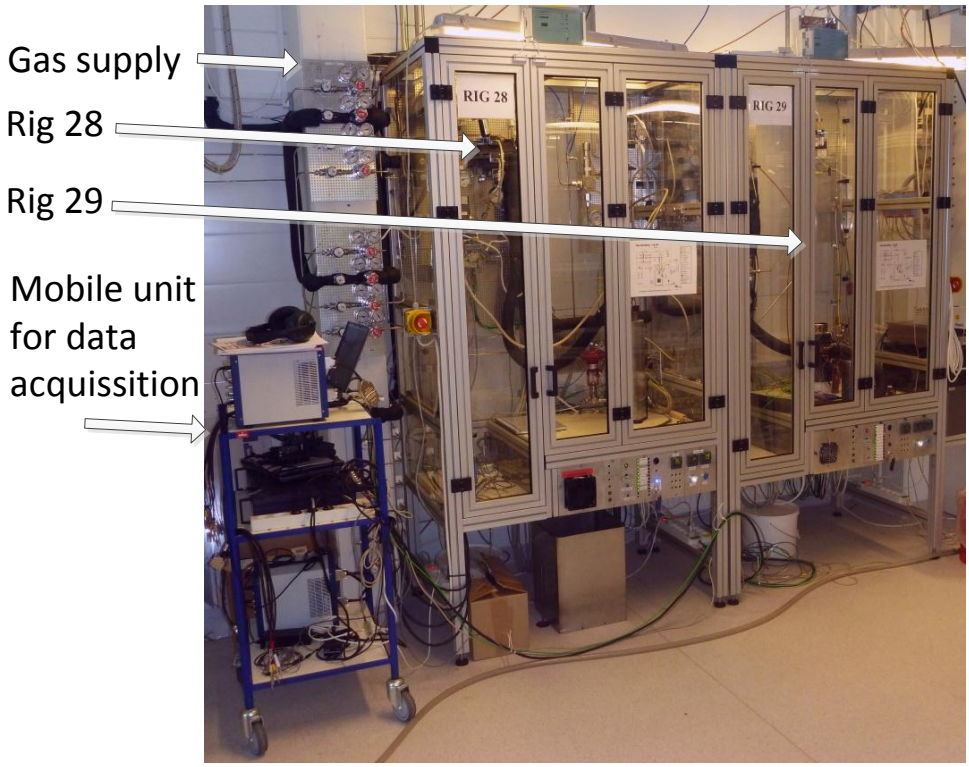

Figure 3.17: Test rigs 28 and 29 for automatized electrochemical tests in the temperature range from room temperature to 250 °C and pressures up to 95 bar. The mobile unit for data acquisition consists of two Gamry type 3000 potentiostats, a 8 channel multiplexer and a personal laptop computer.

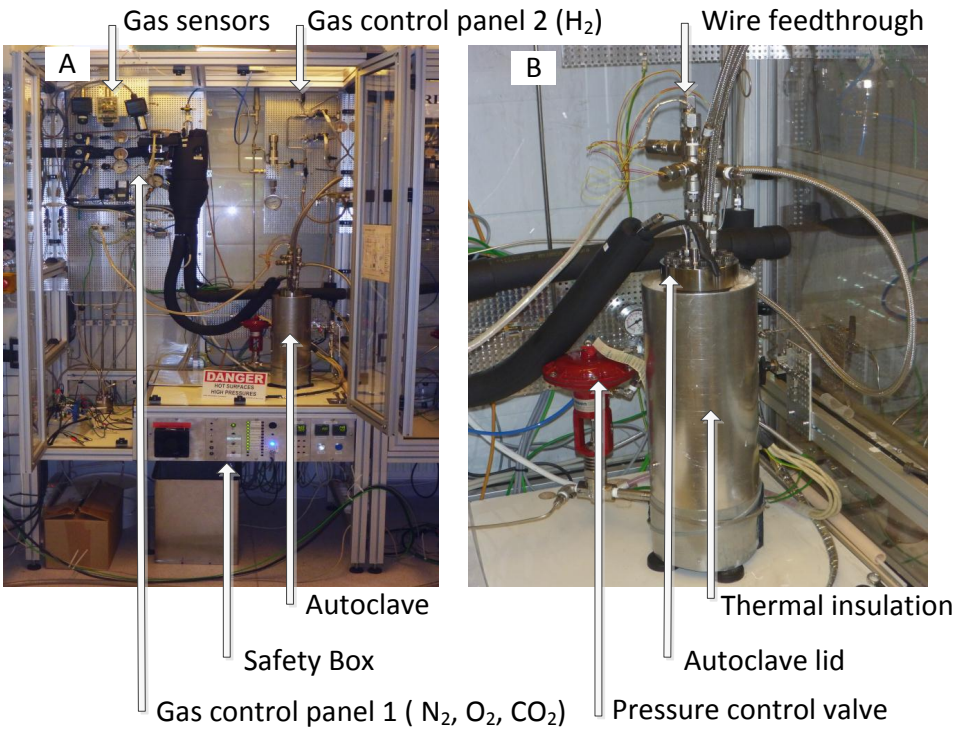

Figure 3.18: A: Test rig 28 with the inner gas handling system and the safety box. B: High temperature and pressure autoclave for the electrochemical cell tests in rig 28.

interior of the autoclave for temperature and electrochemical measurements. The pressure in the reaction chamber is controlled by a pressure control valve.

A detailed flow plan comprising the used actuators is shown in figure 3.19: The gases enter the autoclave through the inlets 3, 5 and 7 in figure 3.19. N_2, CO_2 and O_2 are fed through one tube (inlet 3) and H_2 is fed through inlet 7 to the catalytic burner (CB). The CB comprises a honeycomb structured ceramic body with a catalyst to allow steam generation by H_2 and O_2 combustion in the autoclave with a known flow rate, controlled by mass flow controllers. An excess of H_2 or O_2 can be programmed for the case that measurements should be performed in reducing or oxidizing atmosphere. A second catalytic burner placed right below the cell holder and before the outlet of the autoclave, ensures that the H_2 and O_2 produced by electrolysis will recombine into H_2O before exiting the autoclave. The shown mass spectrometer (MS) and the heated CO_2 tubes are used for other projects and are not further discussed in this thesis.

3.5.2 *Sample holder*

The sample holder used to test the produced electrolysis cells is schematically shown in figure 3.20 (left image) along with a picture of it and the holder for

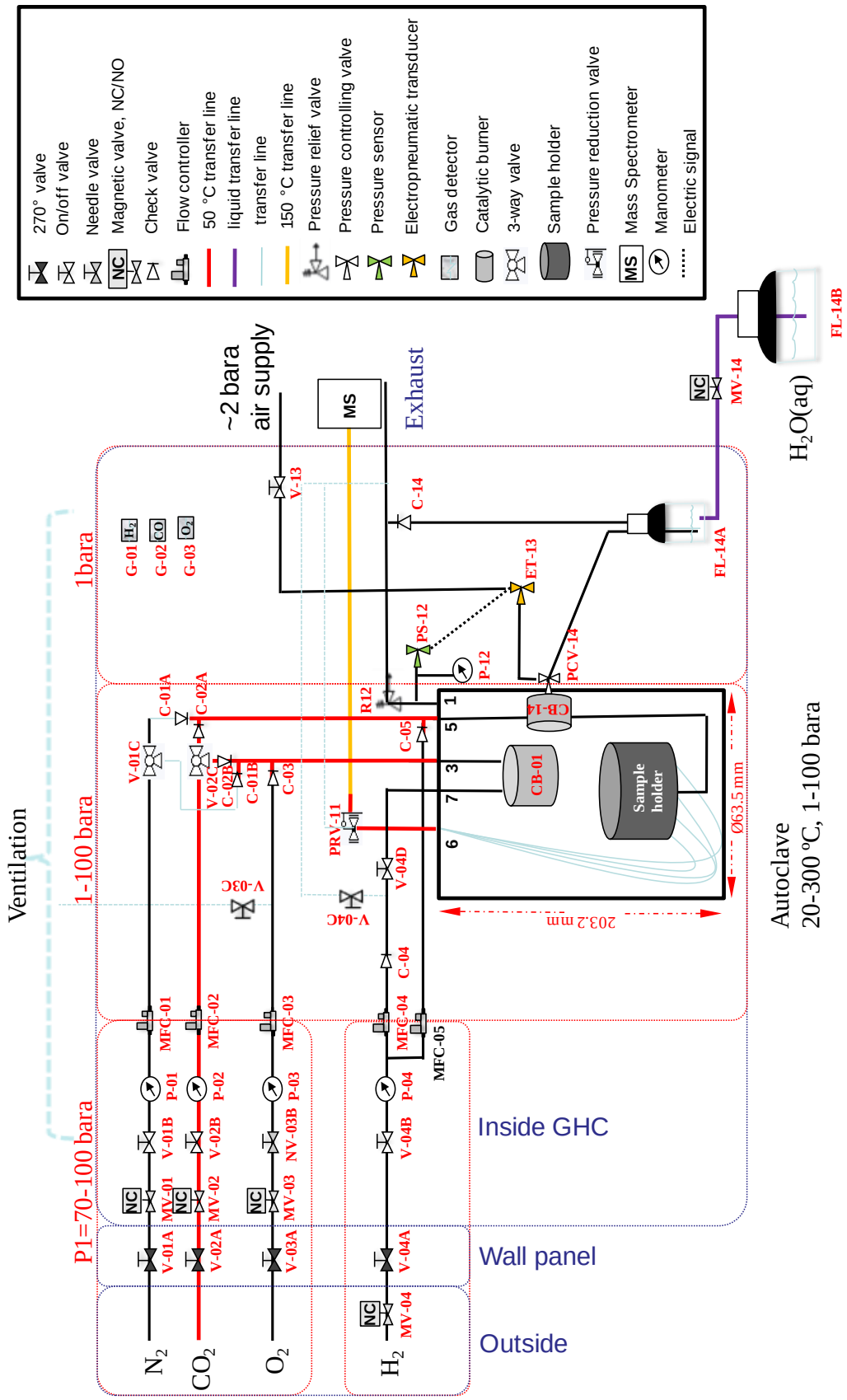

Figure 3.19: Rig 28 gas handling system.

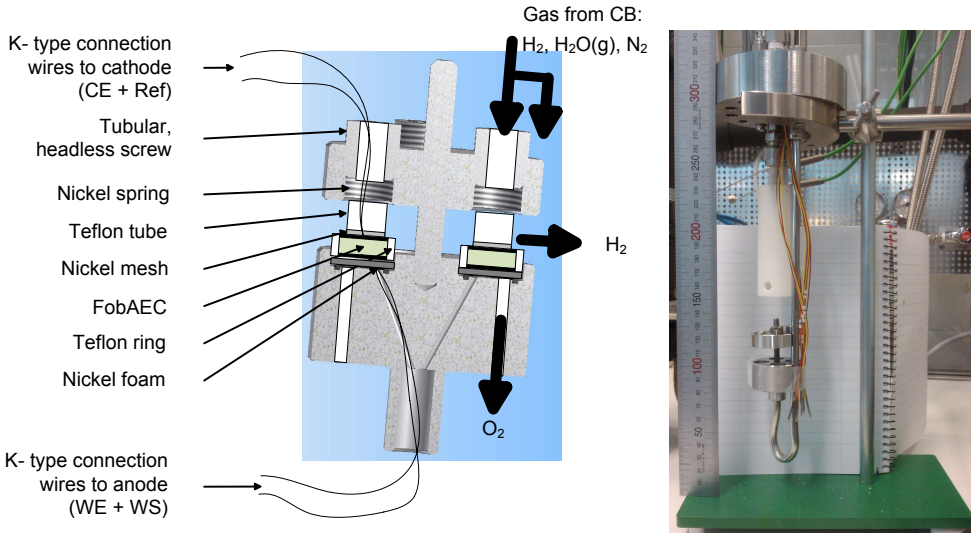

Figure 3.20: Illustration of the sample holder used in the autoclave to test the electrolysis cells, with mounted sample and simplified demonstration of the gas flow (left image) and picture of the sampleholder and holder for the catalytic burner (white ceramic body) (right image).

the catalytic burner on the right image of the same figure (the ceramic zirconia (YSZ) body has been replaced by a stainless steel body at a later stage).

A K-type thermocouple is used to connect the cathode of the FobAEC to the counter electrode (CE) and reference input (Ref) of the potentiostat multiplexer. A tubular, headless screw is used to fix the setup initially. A nickel spring ensures that the nickel mesh, which is wrapped around a teflon tube, is pressed to the cathode during the measurements. A teflon ring has been placed around the FobAEC to avoid gas mixing. A layer of nickel foam is used as current collector at the anodic side of the FobAEC. Another K-type thermocouple is connected to the nickel foam current collector on the sample bottom. It is connected to the working electrode (WE) and the working sense (WS) of the potentiostat. The same connections were used on the right sample shown in figure 3.20, but have not been drawn for clarity reasons.

The gas mixture from the catalytic burner CB at the gas inlet (in the experiments discussed later on a mixture of H_2, H_2O and N_2) flows partly to the cathode of the FobAEC and further through the autoclave. The oxygen produced at the anode of the FobAEC escapes the sampleholder through a tubular hole, where it will mix with the other gases and react to form steam at the CB placed at the autoclave outlet. A pressure control valve is placed at the outlet stream of the autoclave to set the gas pressure to the desired value.

Part IV

RESULTS

4

ELECTRICAL CONDUCTIVITY MEASUREMENTS OF AQUEOUS AND IMMOBILIZED POTASSIUM HYDROXIDE[1]

4.1 ABSTRACT

It is important to know the conductivity of the electrolyte of an alkaline electrolysis cell at a given temperature and concentration so as to reduce the ohmic loss during electrolysis through optimal cell and system design. The conductivity of aqueous KOH at elevated temperatures and high concentrations was investigated using the van der Pauw method in combination with electrochemical impedance spectroscopy (EIS). Conductivity values as high as 2.7 S cm^{-1} for 35 wt%, 2.9 S cm^{-1} for 45 wt%, and 2.8 S cm^{-1} for 55 wt% concentrated aqueous solutions were measured at 200 °C. Micro- and nano-porous solid pellets were produced and used to immobilize aqueous KOH solutions. These are intended to operate as ion-conductive diaphragms (electrolytes) in alkaline electrolysis cells, offering high conductivity and corrosion resistance. The conductivity of immobilized KOH has been determined by the same method in the same temperature and concentration range. Conductivity values as high as 0.67 S cm^{-1} for 35 wt%, 0.84 S cm^{-1} for 45 wt%, and 0.73 S cm^{-1} for 55 wt% concentrated immobilized aqueous solutions were determined at 200 °C. Furthermore, phase transition lines between the aqueous and aqueous + gaseous phase fields of the KOH/H_2O system were calculated as a function of temperature, concentration and pressure in the temperature range of 100°C - 350 °C, for concentrations of 0 wt% - 60 wt% and at pressures between 1 and 100 bar.

4.2 INTRODUCTION

Renewable energies have become an important part of the energy supply system. Among a number of advantages, like CO_2-free or neutral energy production, some indisputable disadvantages have to be overcome towards a sustainable energy supply system. The permanent fluctuation of the wind speed and solar radiation, for example, leads to periods with excess or deficits of available energy. It is therefore necessary to develop energy storage systems with a high efficiency, and reliability, as well as low cost. The production of hydrogen in times of energy excess through electrolysis of water and the combustion or re-electrification of the produced hydrogen in periods of energy deficit is one promising attempt [4]. Alkaline electrolysis has proven to be reliable and

1 Published as: "Frank Allebrod, Christodoulos Chatzichristodoulou, Pia Lolk Mollerup, and Mogens B. Mogensen. Electrical conductivity measurements of aqueous and immobilized potassium hydroxide. International Journal of Hydrogen Energy, 37(21):16505- 16514, 2012.

efficient [19], but further cost reduction along with increased efficiency is still necessary in order for it to become commercially attractive. A significant reduction of the investment costs can be achieved by increasing the operational pressure of the electrolyser, as this would result in the production of pressurized hydrogen (and oxygen), thereby eliminating the need of a compressor for pressurization. Furthermore, it has been estimated that the energy demand for pressurization by the electrolyser is ca. 5 % less than this for pressurization by common compressors [12]. A substantial step towards higher efficiencies can be made by increasing the operational temperature from the industrial standard of ~100 °C to temperatures as high as 264 °C, where a cell voltage of 1.43 V has been demonstrated at a current density of 200 mA cm^{-2} [70]. Anyway, the main losses in common alkaline electrolysis cells are ohmic losses in the electrolyte, the oxygen electrode overpotential, and the hydrogen electrode overpotential. The ohmic losses are relatively small at low current densities, but become significant at industrially relevant current densities of 200 mA cm^{-2} or more, and even more significant if the effect of bubble formation is taken into account [15].

It is important to know the temperature and concentration dependence of the specific electrical conductivity of the electrolyte, σ, usually given in S cm^{-1}, in order to minimize the ohmic losses in an alkaline electrolyser through optimal design of the system. The conductivity of the commonly used potassium hydroxide (KOH) is well described from 0 to 100 °C and concentrations up to 45 wt% [24]. Gilliam et al recently published an expression to calculate the conductivity from 0 to 12 M KOH, 0 to 48 wt% respectively, in the temperature range 0 to 100 °C [25]. A formula to convert between molar and weight specific concentration was presented in the same work. From these data, which are plotted in figure 4.1, it can be seen that each temperature has a specific concentration at which the conductivity has a maximum; the higher the temperature, the higher the concentration at the conductivity peak. All concentrations below will be given in wt% because the molar concentration changes with temperature due to the varying density of the aqueous solution.

Two conductivity data sets for temperatures above 100 °C have been found in the literature. One data set from Lown et al. [26] extend to temperatures up to 200 °C and concentrations up to 37.5 wt%, but following the trend of the conductivity peak shown in figure 4.1, it can be expected that at temperatures above 100 °C, the conductivity maximum will be at concentrations higher than 37.5 wt%. This assumption was confirmed by data from Yushkevich et al, who showed that the conductivity of aqueous KOH has a maximum at 45 wt% KOH at a temperature of 260 °C [27].

For all types of alkaline electrolysis cells (conventional, zero-gap, immersed cells, or gas-diffusion electrode type alkaline electrolysers) [71, 9], it is necessary to separate the produced gases by an electrolyte (diaphragm), which has to be gas-tight and ion-conductive. A porous structure in which the liquid electrolyte is immobilized by capillary forces can be used for that matter. In this case, the reduced free volume for the liquid electrolyte is expected to result

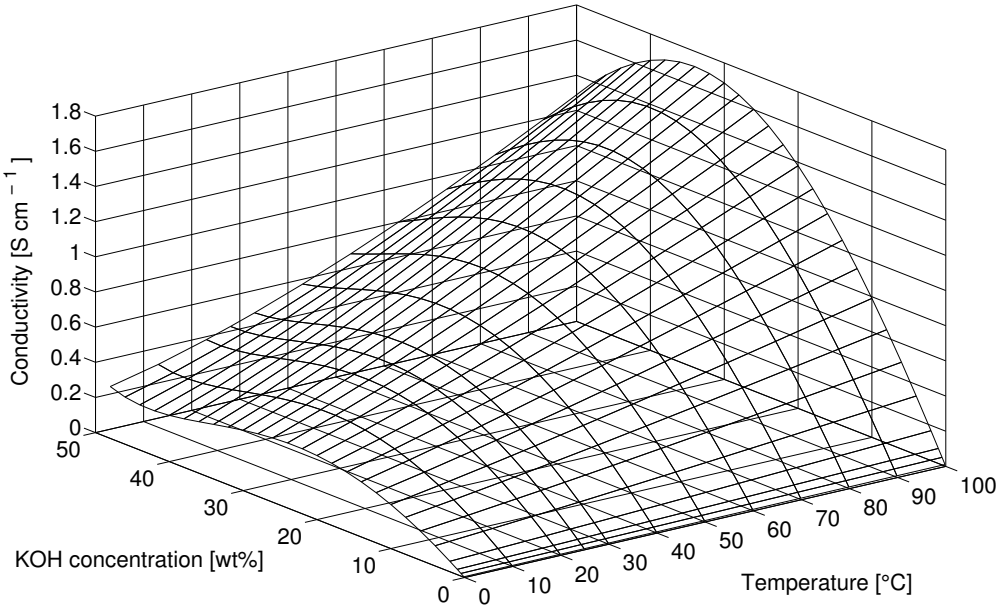

Figure 4.1: 3D plot of the conductivity of aqueous solutions of KOH as a function of temperature and concentration using the data of Gilliam et al for a temperature range of 0 °C - 100 °C and a concentration range of 0 wt% KOH - 50 wt% KOH.

in a decrease in conductivity, and by that to an increase in ohmic losses. The determination of the conductivity of such structures is therefore important.

4.2.1 *The van der Pauw technique*

The van der Pauw method is a well known and proven technique that allows one to determine the electrical conductivity of arbitrary shaped samples, as long as the following conditions are fulfilled [28]:

- The contacts must be at the circumference of the sample
- The contacts must be relatively small in comparison to the sample
- The sample is homogeneous in thickness
- The sample must not have any isolated holes and must be isotropic

The resistivity of an isotropic sample with a homogenous thickness, as displayed in figure 4.2, can be determined by equation 4.1. The index AB and CD describes where the specific value is determined. $R_{AB,CD}$ is the resistance which is determined while applying a current to electrodes A and B while the potential is measured between the electrodes C and D.

$$\rho = \frac{\pi h}{\ln 2} \frac{(R_{AB,CD} + R_{CA,DB})}{2} \tag{4.1}$$

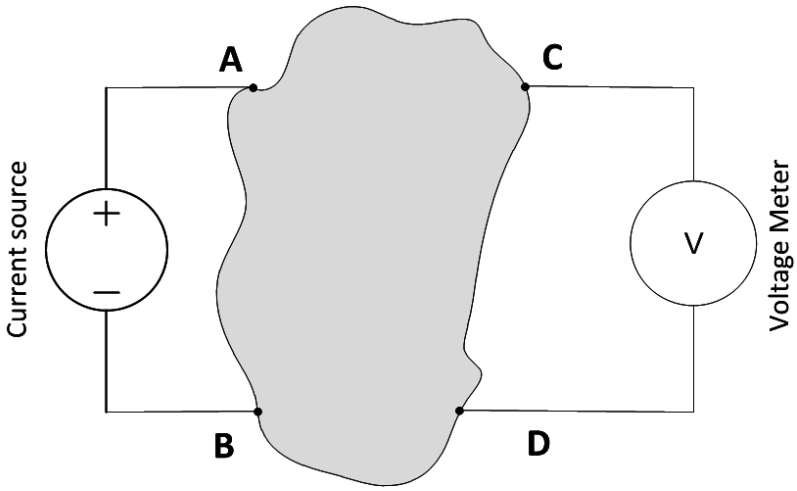

Figure 4.2: Application of the van der Pauw technique for sample where $R_{AB,CD} \neq R_{CA,DB}$.

where h = thickness of the sample, ρ = resistivity of the sample.

Equation 4.1 is valid within an error of 1 % if the ratio of the lower to the higher resistance is closer to 1 than 0.75. For irregulary shaped samples with greater asymmetry it is possible to use equation 4.2 to obtain the resistivity [28].

$$\exp\left(\frac{-\pi h R_{AB,CD}}{\rho}\right) + \exp\left(\frac{-\pi h R_{CA,DB}}{\rho}\right) = 1 \tag{4.2}$$

4.2.2 *Determination of conductivity upon DC and AC polarization*

Applying a DC current to an aqueous KOH electrolyte will result in the establishment of a gradient in the chemical potential of K^+, due to the fact that the electrodes are blocking with respect to K^+ (it is assumed in the following that the electrode potential is far below what would be required for electrodeposition of K):

$$i_{K^+} = \frac{\sigma_{K^+}}{F}\nabla\eta_{K^+} = 0 \Rightarrow \nabla\mu_{K^+} = -F\nabla\varphi \tag{4.3}$$

where i_{K^+} is the partial current density, σ_{K^+} the partial conductivity, η_{K^+} the electrochemical potential, and μ_{K^+} the chemical potential of K^+ ions. F is Faraday´s constant, and φ the inner or Galvani potential. Due to local charge neutrality:

$$\nabla\mu_{OH^-} = \nabla\mu_{K^+} = -F\nabla\varphi \tag{4.4}$$

where μ_{OH^-} is the chemical potential of OH^- ions. In effect the application of a DC current will generate a concentration gradient within the electrolyte. The established OH^- chemical potential gradient favors the transport of OH^-

species, which appear as if migrating with double their partial conductivity (at steady state):

$$i_{OH^-} = i = -\frac{\sigma_{OH^-}}{F}\nabla\eta_{OH^-} = -\frac{\sigma_{OH^-}}{F}\left(\nabla\mu_{OH^-} - F\nabla\varphi\right) = 2\sigma_{OH^-}\nabla\varphi \quad (4.5)$$

The conductivity measured under the application of a DC current doesn't reflect the total conductivity of the starting electrolyte solution. It corresponds to double the average partial conductivity of the OH^- ions within the established concentration gradient. As such, it offers a means of separating the partial conductivity of the OH^- ions from the total conductivity of an aqueous KOH solution. It should be stressed though that the partial conductivity of the OH^- ions determined upon application of a DC current does not correspond to a homogeneous solution with the starting concentration, but rather represents a spatial average corresponding to the established concentration profile (which will be non-linear, unless a very small DC current is applied) between the DC voltage probes. The established concentration gradient will depend on the magnitude of the applied DC current. Combining equations 4.4 and 4.5 we have:

$$\nabla\mu_{OH^-} = -\frac{iF}{2\sigma_{OH^-}} \Rightarrow \frac{d\ln a_{OH^-}}{dx} = -\frac{iF}{2RT\sigma_{OH^-}} \quad (4.6)$$

where R is the gas constant and T the temperature. Increasing current density, i, will result in the establishment of a larger concentration gradient.

In order to determine the total conductivity of an aqueous KOH electrolyte having a homogeneous composition, AC current has to be used. It may not be sufficient to apply an AC current of a single frequency, as the result may be influenced by capacitive and/or inductive contributions. It is important to determine the impedance of the circuit over a broad range of frequencies. By comparing the results to equivalent circuits, it is possible to determine a number of properties of the measured circuits.

4.3 EXPERIMENTAL

4.3.1 *Autoclave*

A Parr autoclave Type 4760 with 600 ml volume and a PTFE liner was used to perform measurements under high pressure and at elevated temperatures. The autoclave was made of Inconel 600, which can withstand high temperatures and pressures as well as extremely caustic environments [64]. To perform electrochemical measurements, the autoclave was equipped with additional gas handling components and wire throughputs. Nitrogen from a 200 bar pressurized bottle was used for the pressurization of the Autoclave. The pressure in the autoclave was regulated with a needle valve. A J-Type thermowell was used to measure the temperature in the autoclave while a pressure

gauge displayed the actual pressure. An additional digital pressure gauge allowed recording the pressure. The autoclave was insulated to avoid temperature gradients during the measurements.

The measurement cell used for the measurement of the aqueous electrolyte conductivity (ACMC) was connected mechanically to the protection hood of the thermo-well by a PTFE shrinking tube in the center of the autoclave. The cell employed for the measurement of the immobilized electrolyte conductivity (ICMC) was situated directly below and equally fixed. In order to avoid drying out of the samples due to evaporation of water during the conductivity measurements, approximately 8 ml of a bath solution (an aqueous solution of KOH having a 2 wt% lower concentration than the solution under investigation) was placed at the bottom of the autoclave, as shown in figure 4.3.

4.3.2 *Conductivity measurement setup*

Figure 4.4 shows the measurement cell used for electrical conductivity measurements of aqueous electrolytes. Platinum black coated platinum wires with a diameter of 0.5 mm were used as electrodes. They were placed on the sides of a Teflon beaker and kept in place by a Teflon pellet at the bottom of the sample holder and an insulated metal wire at the outer top of the sample holder. A lid, having a hole with a 3 mm orifice in the center, was applied to keep the height of solution in the sample holder constant to a value of ca. 10 mm and to avoid or minimize evaporation or condensation of H_2O which would influence the concentration of the electrolyte.

The impedance measurements were performed using a Gamry reference 600 or 3000 potentiostat in the "Galvanostatic impedance spectroscopy" mode. The amplitude of the applied AC current was 1 mA over a frequency range starting at 100 kHz going down to 1 kHz. The terminals marked working electrode WE, counter electrode CE, reference electrode RE and the sense of the working electrode WSE of the potentiostat/impedance response analyser are connected to the sample holder as shown in figure 4.5.

The obtained data at room temperature and atmospheric pressure were analyzed using equation 4.7, where the correction factor f has been neglected due to the symmetry of the measurement cell as discussed in the introduction. The validity of the applied method has been proven by [72]. The value for $Z_{CA,DB}$ was determined at the beginning of a measurement sequence, and the ratio $Z_{CA,DB\_STP}/Z_{AB,CD\_STP}$, which was assumed temperature independent, was used to calculate the conductivity over the entire temperature range without further electrode rotation, by making use of equation 4.8, where h = sample height [cm], ff = conductivity $\left[\mathrm{S\,cm^{-1}}\right]$, $Z_{AB,CD}$ = determined impedance between point A and B, $Z_{CA,DB}$ = determined impedance between point C and A, Z_{AB,CD_STP} = Impedance between A and B at room temperature and atmospheric pressure and Z_{CA,DB_STP} = Impedance between C and A at room temperature and atmospheric pressure.

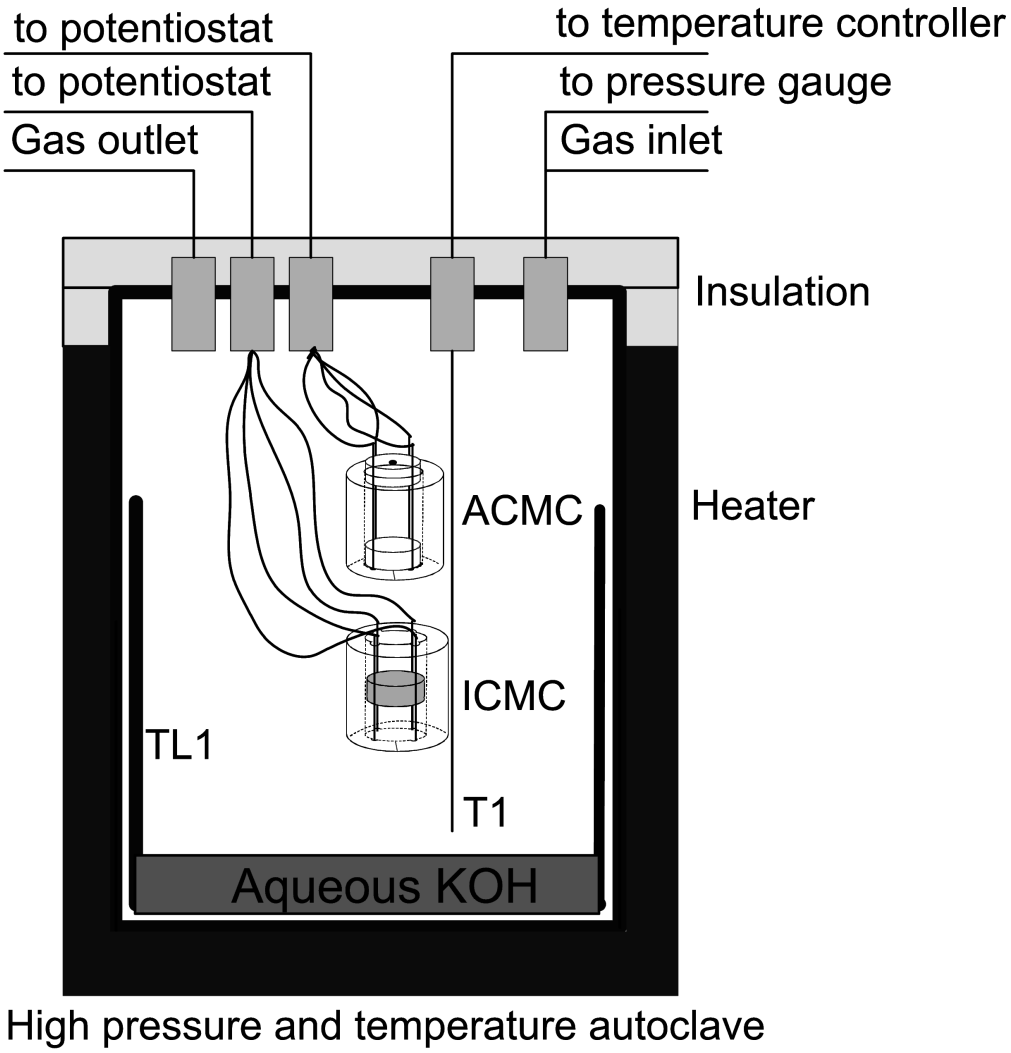

Figure 4.3: Schematic description of the autoclave setup including heater and top insulation: T1 = J- Type thermo-well, TL1 = Teflon liner, ACMC = Aqueous electrolyte conductivity measurement cell, ICMC = Immobilized electrolyte conductivity measurement cell. The diluted aq. KOH solution used to humidify the autoclave atmosphere is also shown.

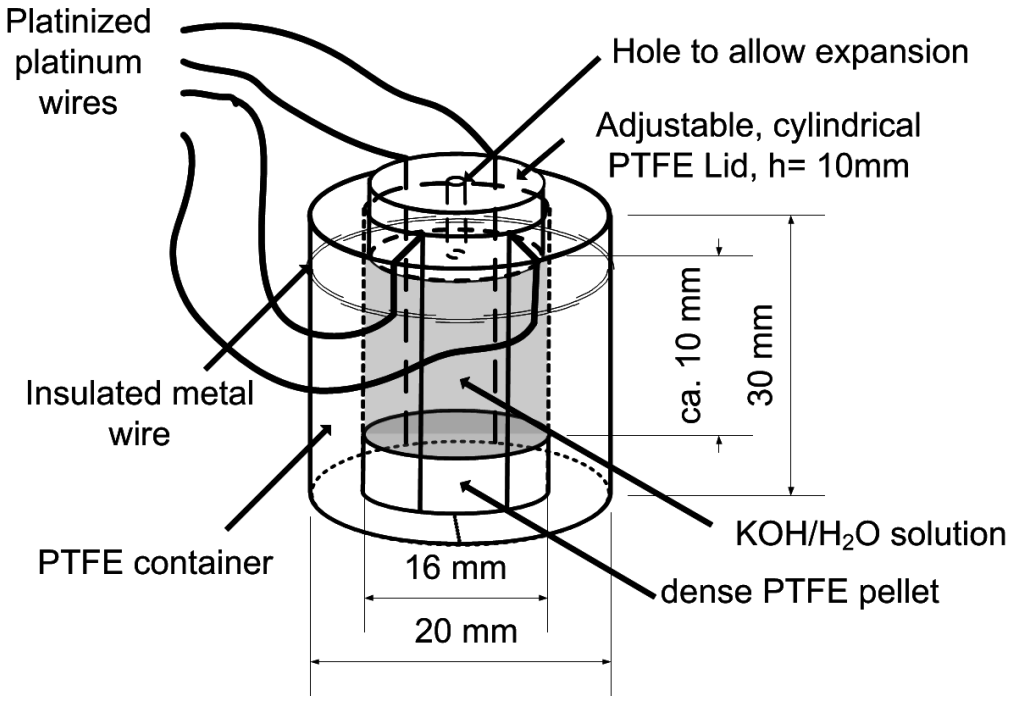

Figure 4.4: Illustration of the cell used for the measurement of the electrical conductivity of aqueous KOH solutions with the van der Pauw technique. The grey shaded area is filled with KOH/H_2O solution. A PTFE lid keeps the height of the solution to ca. 10 mm. Four platinized platinum wires are used as electrodes.

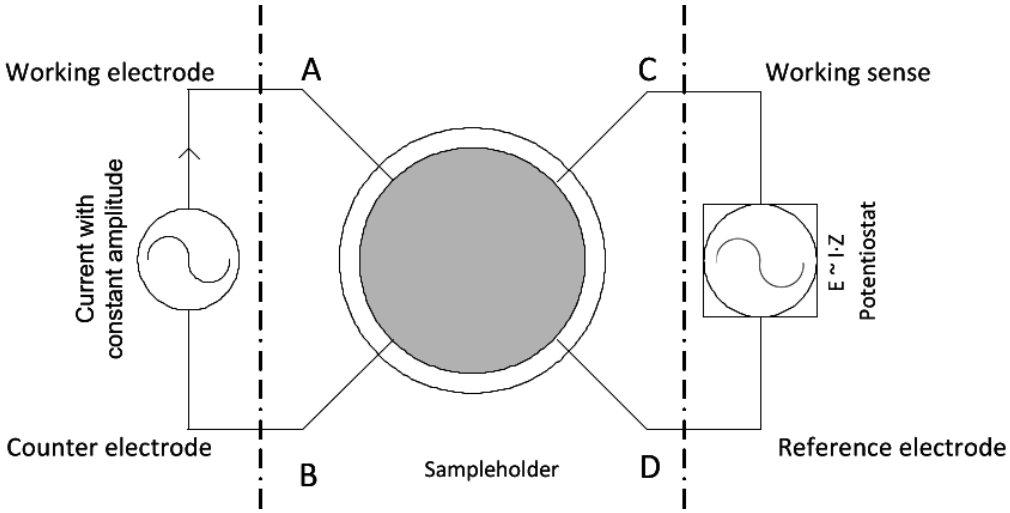

Figure 4.5: Connection of the potentiostat/impedance response analyser to the sample holder to determine the impedance $Z_{AB,CD}$. Current with a constant amplitude of 1 mA is supplied through the electrodes A (working electrode) and B (counter electrode) while the potential is measured between C (working sense) and D (reference electrode).

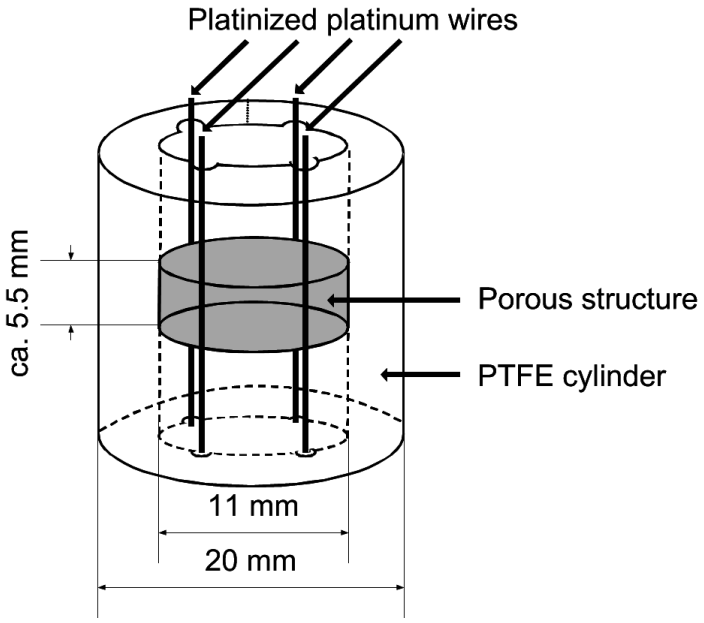

Figure 4.6: Illustration of the cell used for the measurement of the electrical conductivity of immobilized aqueous KOH solutions with the van der Pauw technique. The porous structure is mounted in the middle of a PTFE cylinder which is open to the autoclave atmosphere from both sides. Four platinized platinum wires are used as electrodes.

$$\sigma = \frac{\ln 2}{\pi h} \frac{2}{(Z_{AB,CD} + Z_{CA,DB})} \tag{4.7}$$

$$\sigma = \frac{\ln 2}{\pi h} \frac{2}{(Z_{AB,CD} \left(1 + \frac{Z_{CA,DB\_STP}}{Z_{AB,CD\_STP}}\right)} \tag{4.8}$$

The sample holder which was developed and built to determine the conductivity of immobilized electrolytes is shown in figure 4.6.

The electrodes were platinum black coated platinum wires of a thickness of 0.5 mm. The platinum electrodes are connected to Nickel-copper wires by cold welding a nickel tube. A slit in the holder makes it somewhat flexible to be able to take samples with slightly varying diameter. The pellets were soaked in aqueous KOH of the desired concentration for at least two hours prior to the conductivity measurements. Pellets with a diameter of ca. 12 mm and a height of ca. 5.5 mm were pressed out of a suitable powder to obtain a nano-porous structure. Evaporation and condensation problems have been minimized by placing a lid on top of the conductivity cell for the aqueous measurements and by wrapping the ICMC with Teflon-tape since it is open to the autoclave atmosphere. Mercury porosimetry was conducted to a sample pellet using a Micrometrics Autopore IV Hg Porosimeter to obtain the pore size distribution and total porosity of the produced pellets.

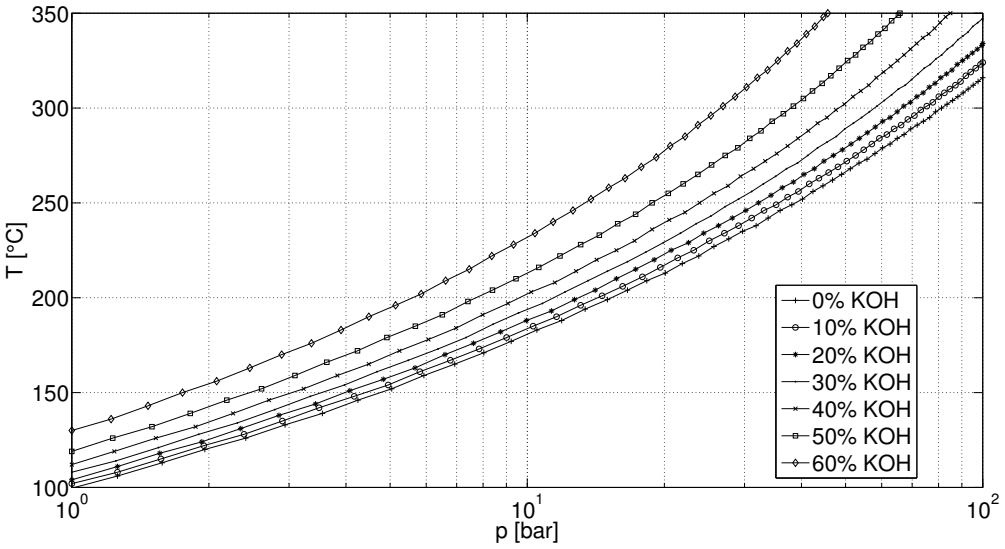

Figure 4.7: Phase transition lines between the aqueous (area below the line) and the gaseous + aqueous (area above the line) phase fields of the KOH/H_2O system in the concentration range 0 - 60 wt% KOH.

4.4 RESULTS

4.4.1 *Phase transition lines of KOH*

To determine the conductivity of liquid electrolytes at temperatures above their boiling point at atmospheric pressure, it is important to find the phase transition lines between the aqueous and the aqueous + gaseous phase for the solution and make sure that the solution concentration will not vary due to evaporation of H_2O during the measurements. For this purpose, the phase transition lines for KOH aqueous solutions with concentrations from 0 wt% KOH (pure water) to 60 wt% KOH have been calculated using FactSage, Version 5.5 [20]. The results are displayed in figure 4.7 where the aqueous phase field is represented by the area below the transition line for a specific concentration. The phase transition line for a specific pressure is shifted towards higher temperatures with increasing concentration. At a pressure of 1 bar the phase transition temperature for pure water is naturally 100 °C, for 50 wt% KOH it is 120 °C and it increases to 130 °C for 60 wt%. It is obvious, that the pressure has to be increased from atmospheric pressure to perform measurements at temperatures around 200 °C. Conductivity measurements on 45 wt% KOH at 200 °C can be performed at 10 bar, but since the pressure itself has a negligible influence on the conductivity [26], the measurements for the conductivity have been performed at pressures above 25 bar.

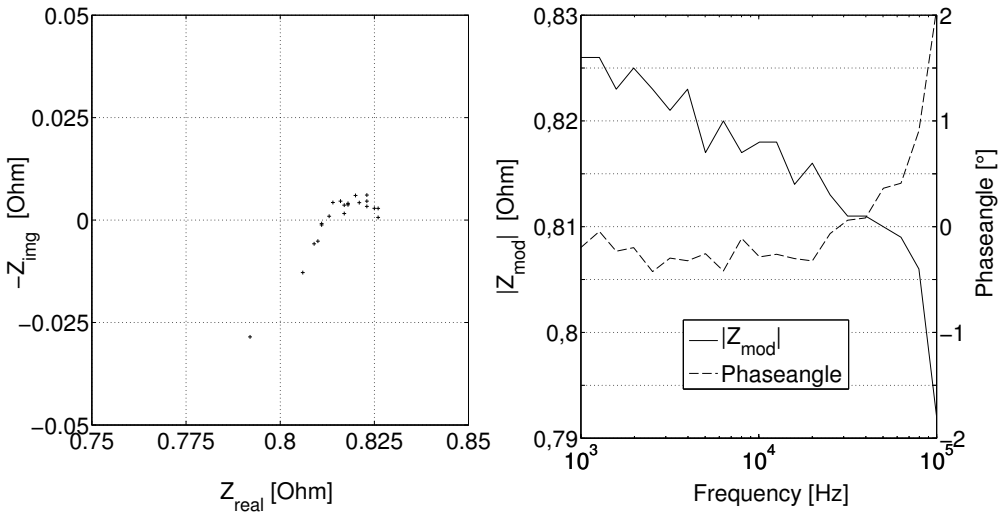

Figure 4.8: Nyquist (left) and Bode (right) plot for a typical EIS measurement in the frequency range from 100 kHz to 1 kHz measured in the galvanostatic mode with an amplitude of 1 mA.

4.4.2 *Uncertainties for the conductivity measurements*

The uncertainties in the performed measurements are primarily due to temperature differences between the measured and the actual sample temperature, and due to dilution or concentration of the solution by condensation or evaporation of H_2O. The temperature variation in the autoclave was less than 5 K, which results in a relative uncertainty of less than 4.3 % for the conductivity of the 45 wt% aqueous solution. The uncertainty of the potentiostat/impedance response analyser is less than ±1 % in the impedance mode. Figure 4.8 shows a typical impedance measurement. The real part of the impedance drifts by 4.4 % from 0.79 Ω to 0.83 Ω in the frequency range from 100 kHz to 1 kHz. The data obtained at 10 kHz were used for the calculation of the conductivity, as the phase angle appeared to be closest to zero at this frequency in all data sets; inductive or capacitive contributions to the measured impedance could therefore be excluded. The total uncertainty according to the root-mean-square sum is 6.2 %. It should be noted though that this is a somewhat overestimated value of the uncertainty, as the observed impedance drift of 4.4 % (in the worst case) includes the uncertainties of the potentiostat, temperature drift and uncertainties due to evaporation/condensation during the measurement.

4.4.3 *Conductivity of aqueous KOH*

The results from three independent measurement series to determine the aqueous conductivity of a 35 wt% aqueous KOH solution are displayed in figure 4.9 A. The conductivity slope from room temperature to 150 °C is rather constant while above this temperature a slight decrease of the slope occurs, which

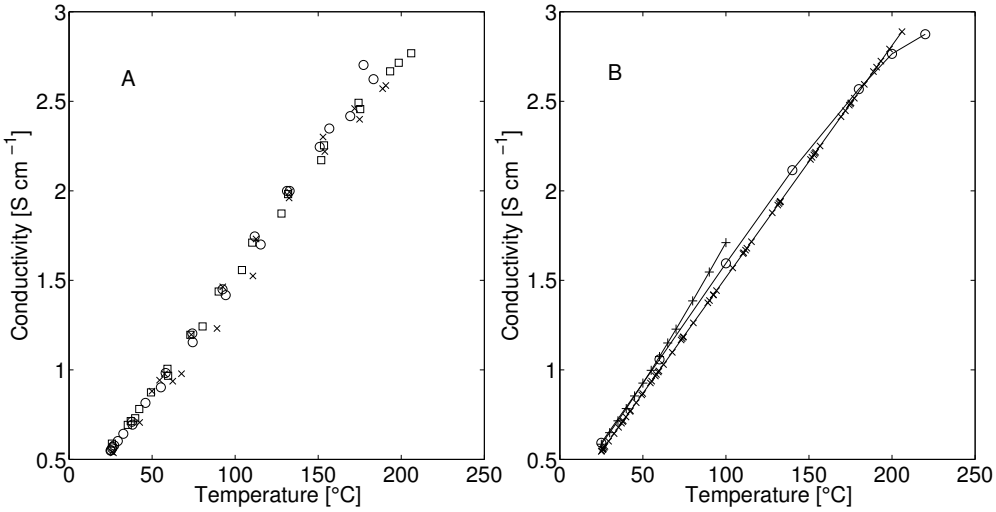

Figure 4.9: A: Three measurements (x, o, □) of the conductivity of 35 wt% aqueous KOH as a function of temperature at pressures from 25 bar to 40 bar. B: Comparison of the linear regression analysis (x) of the measurements in figure 4.9 A to conductivity data from [27] (o), and calculated conductivity data from [25] (+).

has also been reported in the literature and seems to be more pronounced at lower concentrations [26]. The conductivity at 25 °C is 0.55 S cm^{-1} and reaches a maximum of 2.8 S cm^{-1} at 206 °C. Figure 4.9 B shows a linear regression of the measured data together with literature values from Yushkevich et al [27] and calculated values from Gilliam et al [25]; the coincedence is satisfying over the entire temperature range.

The same measurement series as described above has also been performed for concentrations of 45 and 55 wt% KOH. All measurement points with the corresponding conductivity at a specific temperature are displayed in figure 4.10. A cubic fit of the measured data showed the best agreement for both, the aqueous and the immobilized conductivity data. The conductivity of the 35 wt% aqueous KOH at 25 °C has the highest value, while at 200 °C the 45 wt% solution has the highest conductivity.

4.4.4 *Pellet characterization*

The porosity of the pellets used for immobilization of the aqueous KOH was characterized by Hg porosimetry and are shown in figure 4.11. The mean pore size was found to be 59 nm. Weight measurements of the dry and wetted pellets have shown that the pellets fill up to 70 - 85 % of their pores with aqueous KOH at room temperature and pressure, which allows the assumption that 15 - 30 vol% of the pores are not completely filled with the electrolyte. A comparison of weight, dimensions, relative density and the percentage of pore-filling

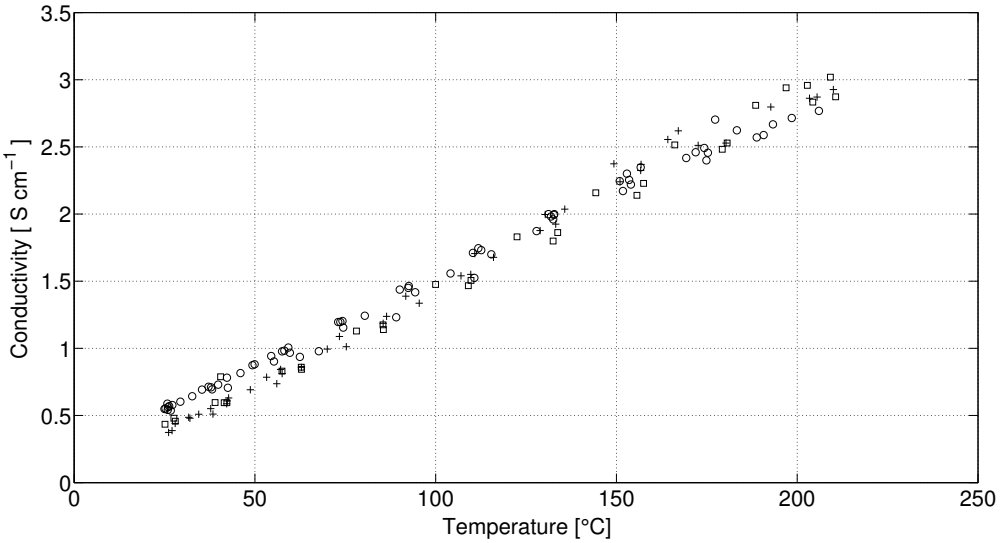

Figure 4.10: Measured conductivity as a function of temperature for 35 wt% (o), 45 wt% (□) and 55 wt% (+) KOH (aq).

can be found in table 4.1 for three representative pellets, which were used in the measurements.

Table 4.1: Comparison of the weight, dimensions, relative density and percentage of filled pores of three pellets used for the measurements.

KOH Concentration	Dry weight [g]	Wet weight [g]	Diameter [mm]	Height [mm]	Relative density pellet [%]	Specific density KOH at 25°C [g/cm3]	Pores filled [%]
35 wt%	1.321	1.652	11.2	5.0	52	1.34	84
45 wt%	1.361	1.669	11.2	5.4	51	1.45	81
55 wt%	1.412	1.684	11.1	5.2	51	1.56	73

4.4.5 *Conductivity of immobilized aqueous KOH*

The measured conductivity values of 35 wt% KOH immobilized in the porous pellets over temperature are shown in figure 4.12. Conductivities from 0.13 S cm^{-1} at 24 °C up to 0.68 S cm^{-1} at 221 °C were achieved in these measurements. It can also be seen in figure 4.12 that the conductivity seems to reach a maximum around 202 °C.

All measured data for the immobilized KOH can be found in figure 4.13 along with the cubic fittings. The slope of the conductivity of the pellet with 45 wt% KOH seems to increase at higher temperatures, while the slope of the

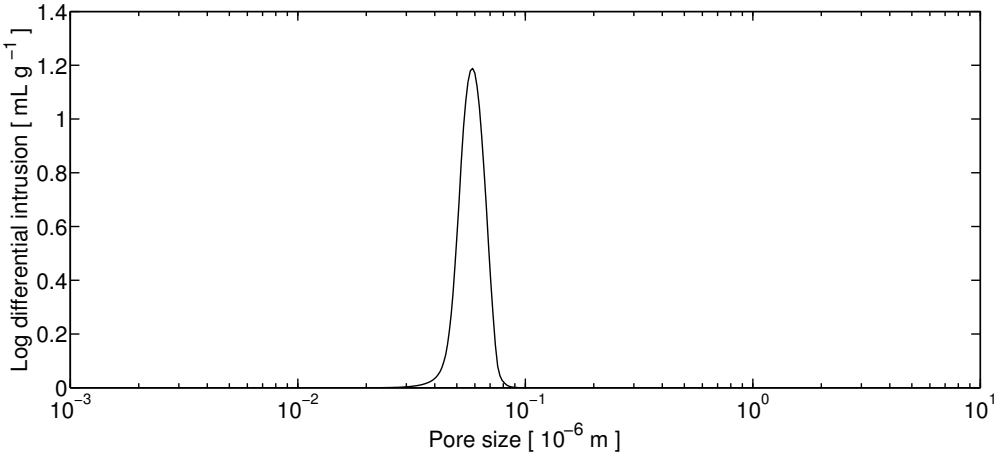

Figure 4.11: Porosimetry results of the pellets used for the immobilization of the aqueous KOH solution showing a mean pore size of 59 nm.

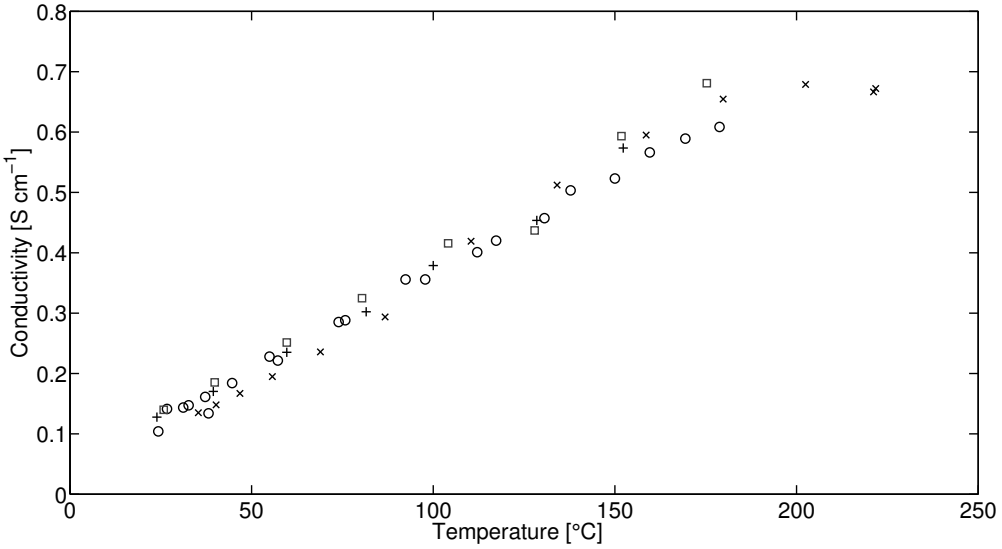

Figure 4.12: Measured conductivity of immobilized KOH (35 wt%) versus temperature with p = const = 30 bar (x, o) and pressure increasing with temperature (□, +) (p = 25 - 40 bar). The porous structure was mounted in the ICMC.

55 wt% is constant and this of the 35 wt% pellets decreases above 160 °C. The coefficients for the cubic fittings are listed in table 4.2; the conductivity can thereby be calculated in S cm^{-1} from equation 4.9. It should be stressed that the coefficients obtained from the fitting don´t carry any physical meaning and that equation may only be trusted to reproduce the experimentally determined conductivity values in the temperature range 25 - 200 ˚C.

$$\begin{aligned} \sigma(T) &= C1 \cdot T^3 + C2 \cdot T^2 + C3 \cdot T + C4 \\ \text{with :} \quad T &= \text{Temperature } [^\circ C] \\ C1, C2, C3, C4 &= \text{Coefficients} \end{aligned} \tag{4.9}$$

Table 4.2: Coefficients of the cubic fitting to the conductivity.

Conductivity type	Concentration [wt%]	C1	C2	C3	C4
aqueous	35	-2.15E-07	6.44E-05	0.007675	0.3299
immobilized	35	-9.26E-08	2.85E-05	0.000902	0.0888
aqueous	45	-1.78E-07	7.04E-05	0.005973	0.2706
immobilized	45	7.11E-08	-2.14E-05	0.005747	-0.0276
aqueous	55	-3.30E-07	1.06E-04	0.005205	0.2105
immobilized	55	-2.52E-08	8.77E-06	0.002775	0.0283

4.5 DISCUSSION

4.5.1 *Literature values for aqueous conductivity*

All measurements for the aqueous conductivity are in good accordance with the available literature values, as shown in figure 4.14. The measured values for the 35 and 45 wt% solution are slightly lower than those reported by Yushkevich [27]. The measured conductivity for the 55 wt% solution is slightly higher than this reported by Vogel et al [73] as shown in figure 4.14 C.

4.5.2 *Conductivity of immobilized KOH*

The conductivity of the immobilized KOH, achieved in this study, is as high as 0.84 S cm^{-1} for 45 wt% KOH at 200 °C. Weight measurements (table 4.1) have shown that the pores of the structure are not filled completely, so that improved

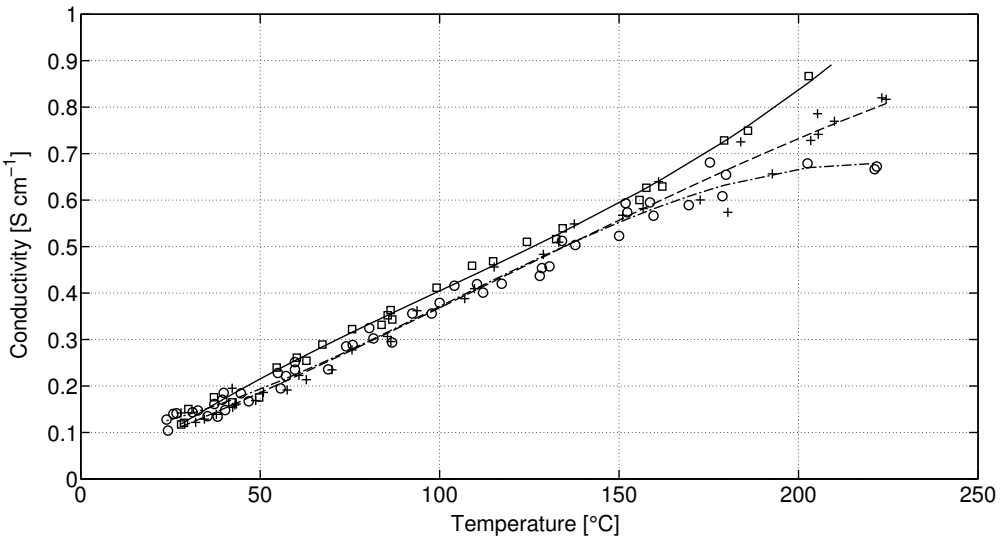

Figure 4.13: Measured conductivity and cubic regression analysis for 35 wt% (o = measured, dash-dotted line = regression), 45 wt% (□= measured, full line = regression) and 55 wt% (+ = measured, dashed line = regression) immobilized KOH (aq) as a function of temperature and a pressure of 25 - 40 bar.

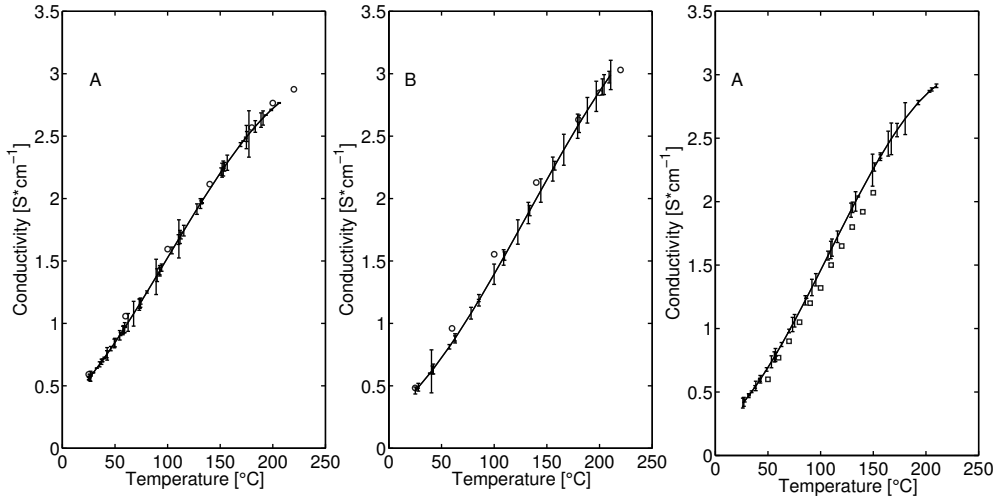

Figure 4.14: Comparison between literature values from [27] (o) and [73] (□) and the cubic fitting (line) of the measured conductivity for 35 wt% (A), 45 wt% (B) and 55 wt% (C) aqueous KOH with the corresponding error-bars.

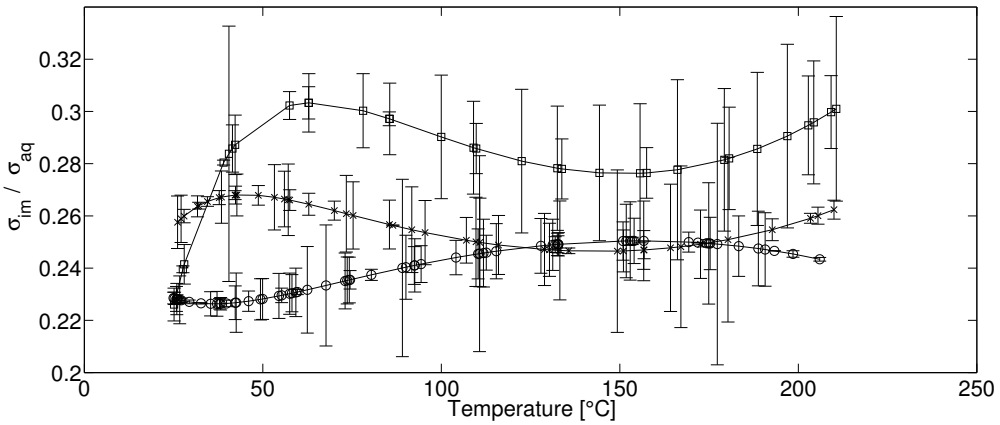

Figure 4.15: Ratio of the conductivity of immobilized aqueous KOH, σ_{im}, to the conductivity of aqueous KOH, σ_{aq}, for concentrations of 35 wt% (o), 45 wt% (□) and 55 wt% (x) , derived from equation 4.9.

wetting procedures may lead to even higher conductivities if the unfilled pores are not closed. The measured conductivities are lower in direct comparison to Zirfon, a commercially available diaphragm with a porosity of 44 - 59 % [74] which has also been used to immobilize KOH by Vermeiren et al [30]. They achieved an area specific resistance of 0.1 Ω cm^2 at a temperature of 80 °C for a membrane of 600 μm in thickness. This corresponds to a conductivity of 0.6 S cm^{-1} which is almost twice that achieved in this work, namely 0.33 S cm^{-1}, at this specific temperature. Assuming that it will be possible to use the porous structure down to thicknesses of 200 μm, or even thinner depending on the used support, we may achieve area specific resistances of 60 mΩ cm^2 and by that reduce the ohmic losses in the electrolyte significantly. Furthermore, it is possible to use the proposed structure at temperatures like 200 °C or higher, while the commercial Zirfon diaphragm is limited to 120 °C.

4.5.3 *Comparison between aqueous and immobilized electrolyte conductivity*

The ratio between the conductivity of a certain concentration immobilized in a pellet to the aqueous one is shown in figure 4.15. In an ideal case this value should be identical to the porosity of the pellet used for the measurements (~48 %), but the tortuosity of the pores limits the conductivity as well as the fact that there is a possibility of closed pores or gas bubbles caught inside the pellet. Furthermore, weight measurements have shown that the pores of the pellets are not completely filled with the electrolyte.

4.6 CONCLUSIONS

The electrical conductivity of aqueous solutions of potassium hydroxide with a concentration of 35, 45 and 55 wt% KOH was measured over a wide tem-

perature range by the van der Pauw method. The 45 wt% solution showed the highest conductivity at high temperatures; a conductivity of 3.0 S cm^{-1} was measured at a temperature of 209 °C. A cubic regression was found to be adequate to describe the temperature dependence of the conductivity in the temperature range of 25 °C - 200 °C and concentrations of 35, 45 and 55 wt%. Furthermore, the conductivity of aqueous potassium hydroxide, immobilized in a nano-porous structure, was measured for the same concentrations. The conductivity of the 45 wt% immobilized solution at ca. 200 °C was 0.84 S cm^{-1}, higher than those of 35 wt% and 55 wt% with values of 0.67 S cm^{-1} and 0.73 S cm^{-1}, respectively.

4.7 ACKNOWLEDGMENTS

The financial support from the 2nd generation alkaline electrolysis project, EUDP 63011-0200, is gratefully acknowledged. The authors are also thankful for additional financial support from the “Catalysis for Sustainable Energy initiative”, funded by the Danish Ministry of Science, Technology and Innovation. The worthy contributions from Ane Sælland Christiansen to the implementation of the van der Pauw technique as part of her MSc project are also appreciated.

5

ALKALINE ELECTROLYSIS CELL AT HIGH TEMPERATURE AND PRESSURE OF 250 °C AND 42 BAR[1]

5.1 ABSTRACT

A new type of alkaline electrolysis cells with nickel foam based gas diffusion electrodes and KOH (aq) immobilized in mesoporous $SrTiO_3$ have been developed and tested at temperatures and pressures up to 250 °C and 42 bar, respectively. Current densities of 1.0 $A\,cm^{-2}$ have been measured at a cell voltage of 1.5 V without the use of expensive noble metal catalysts. The high electrical efficiency and current density combined with relatively small production costs can lead to both reduced investment and operating costs for hydrogen and oxygen production.

5.2 INTRODUCTION

Energy from renewable sources is becoming an increasingly important part of the energy supply system worldwide. Besides the obvious advantages of renewable energy sources, like CO_2 free or neutral energy production, some indisputable disadvantages have to be overcome towards a sustainable energy supply system [75]. The fluctuation of the wind speed and solar radiation, for example, leads to periods with excess or deficit of available energy. It is therefore necessary to develop energy storage systems with high efficiency and reliability, as well as low cost. The production of hydrogen by means of electrolysis of water during times of energy excess, followed by conversion of the produced hydrogen to electricity during periods of energy deficit is a promising possibility [4]. Alkaline electrolysis has proven to be reliable and efficient some decades ago [19], but further cost reduction along with increased efficiency is still necessary in order to make it commercially attractive. A significant reduction of the investment costs may be achieved by increasing the operational pressure of the electrolyser as this will result in the production of pressurized hydrogen (and oxygen), thereby eliminating or reducing the cost of the compressor. Furthermore, it has been estimated that the energy demand for pressurization by the electrolyser is ca. 5 % less than for pressurization by common compressors, leading to reduced operation cost for the system [12].

A substantial step towards higher efficiencies can be made by increasing the operational temperature from the conventionally used temperature of about

1 Published as: "Frank Allebrod, Christodoulos Chatzichristodoulou, Mogens B. Mogensen. Alkaline Electrolysis Cell at High Temperature and Pressure of 250 °C and 42 bar. Journal of Power Sources, 229: 22- 31, 2013"

100 °C to temperatures as high as 264 °C, where a current density of 200 $mA\,cm^{-2}$ has been demonstrated at a cell voltage of 1.43 V [70]. Another substantial step forward has been made by Divisek et al. by the use of Raney activated electrodes and zero gap electrodes, thereby achieving a current density of 400 $mA\,cm^{-2}$ at a cell voltage of ca. 1.55 V at 100 °C and pressures between 1 and 5 bar [19].

5.2.1 *Alkaline electrolysis*

An alkaline electrolysis cell consists of four major components; the electrolyte, which is commonly potassium hydroxide (KOH) in high concentrations (usually above 25 wt%), the cathode, the anode, and a solid barrier (diaphragm). The solid barrier is separating the produced gases to avoid recombination and furthermore needs to be permeable to hydroxide ions and water; it is used in all types of alkaline electrolysis cells (conventional, zero-gap, immersed cells, or gas-diffusion electrode type alkaline electrolysers) [9, 10]. Hydrogen evolution takes place at the cathode, where the electrons are provided for the decomposition of water. The hydroxide ions are decomposed at the anode, where oxygen evolution takes place under the formation of water. The basic reactions of the decomposition of water in an alkaline electrolyser are given by equations (5.1)-(5.3).

$$\mathrm{Anode:}\ 2OH^- \rightarrow {}^1/_2O_2 + H_2O + 2e^- \tag{5.1}$$

$$\mathrm{Cathode:}\ 2H_2O + 2e^- \rightarrow H_2 + 2OH^- \tag{5.2}$$

$$\mathrm{Total:}\ H_2O \rightarrow H_2 + {}^1/_2O_2 \tag{5.3}$$

The cell voltage, U_{cell}, that has to be applied to produce hydrogen and oxygen with a given rate depends on the operating temperature [11] and pressure [12] as well as on a number of other factors such as the electrocatalyst material and microstructure [13]. Furthermore, the right choice of electrolyte concentration for a specific temperature [14], and a high specific surface area of the electrodes are important factors. Major losses are defined as cathodic overvoltage, η_{H_2}, for the hydrogen evolution reaction, HER, the anodic overvoltage, η_{O_2}, for the oxygen evolution reaction, OER, and ohmic losses in the electrolyte. The ohmic losses are relatively small at low current densities, but become significant at industrially relevant current densities of 200 $mA\,cm^{-2}$ or more, especially if significant bubble formation takes place [15].

5.2.2 *Thermodynamic Considerations*

The reversible (or equilibrium) cell voltage, E_{rev}, is the minimal voltage at which electrolysis of H_2O is possible and can be calculated by equation (5.4), where ΔG_f is the Gibbs free energy of the reaction, n is the number of electrons involved in the reaction, and F is Faraday's constant ($96485\ C \cdot mol^{-1}$). At

standard conditions it is 1.229 V with the Gibbs free energy of formation at standard conditions $\Delta G_f^0 = -237.178\,\mathrm{kJ\,mol^{-1}}$ [20].

$$E_{rev} = \frac{-\Delta G_f}{nF} \tag{5.4}$$

The total energy demand for the reaction corresponds to the thermoneutral voltage, E_{tn}, and can be calculated from the enthalpy of formation, ΔH_f, as shown by equation 5.5. The thermoneutral voltage $E_{tn,0}$ at standard temperature and pressure (STP, 25 °C, 101.325 kPa) is 1.481 V with the standard enthalpy of formation $\Delta H_f^0 = -285.840\ \mathrm{kJ\,mol^{-1}}$ [20].

$$E_{tn} = \frac{-\Delta H_f}{nF} \tag{5.5}$$

A comparison of the electrical energy demand, the total energy demand and the heat demand for water electrolysis at standard pressure is shown in figure 5.1 with thermodynamic data obtained from FactSage [20]. It is shown that the electrical energy demand for water electrolysis decreases with increasing temperature, while heat demand rises and the total energy demand is almost constant (but different) both for the liquid and the gaseous phase.

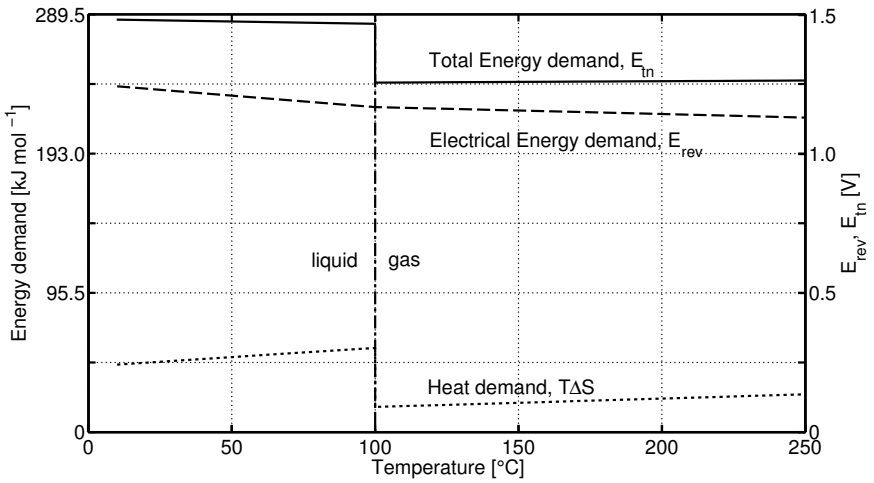

Figure 5.1: Temperature dependence of the total energy demand, ΔH_f (full line), the electrical energy demand, ΔG_f (dashed line), and the heat demand $T \cdot \Delta S_f$ (dotted) for water ($T \leqslant 100\,°C$) and steam ($T \geqslant 100\,°C$) electrolysis at 1 bar using data from FactSage [20].

As it is not common to perform electrolysis at standard conditions, it is necessary to know both the influence of pressure and temperature to the reversible cell voltage. The reversible cell voltage as a function of temperature and pressure, $E_{rev(t,p)}$, can be calculated by equation (5.6), where R is the Gas constant (8.3144621 J mol^{-1} K^{-1}), a_{H_2} is the hydrogen activity, a_{O_2} is the oxygen activity, a_{H_2O} is the activity of water and T is the temperature in Kelvin.

$$E_{rev(t,p)} = \frac{-\Delta G_f}{n \cdot F} = \frac{-\Delta G_f^0}{n \cdot F} + \frac{RT}{nF} \ln\left(\frac{a_{H_2} a_{O_2}^{\frac{1}{2}}}{a_{H_2O}}\right) \tag{5.6}$$

$E_{rev(t,p)}$ can also be obtained from steam tables or CALPHAD (Computer Coupling of Phase Diagrams and Thermochemistry) programs like FactSage [20] which include data for ΔG_f at elevated temperatures and pressures. A graph displaying the influence of the pressure and temperature to $E_{rev(t,p)}$ has been calculated by equation 5.4 with data from FactSage and is shown in figure 5.2 (the partial pressure of H_2, O_2 and H_2O is assumed equal to the total pressure in this calculation). Important values are numerically extracted in table 5.1. Furthermore, it should be noted that the reversible cell voltage of an alkaline electrochemical cell is also depending on the concentration of the electrolyte. Balej [22, 23] has provided expressions for computing a_i and the reversible cell voltage as a function of the concentration, temperature and pressure of the electrolyte, said to be valid for temperatures between 25 °C – 200 °C. Since reliable data sets above 200 °C are not available, we have neglected the influence of the electrolyte concentration here.

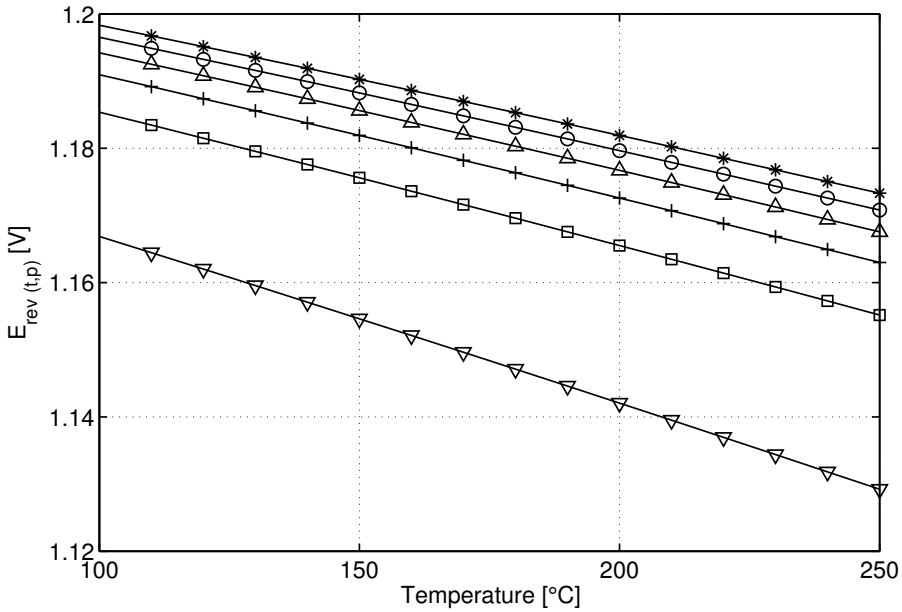

Figure 5.2: Reversible cell voltage $E_{rev(t,p)}$ as function of the temperature for steam electrolysis at pressures of 1 bar (∇), 10 bar (□), 20 bar (+), 30 bar (△), 40 bar (○) and 50 bar (⋆) (the partial pressure of H_2, O_2 and H_2O is assumed equal to the total pressure in this calculation).

Table 5.1: Reversible cell voltage $E_{rev(t,p)}$ for steam electrolysis as function of the system pressure and temperature calculated by equation 5.4 with data from FactSage

Temperature [°C]	System pressure [bar]					
	1	10	20	30	40	50
100	1.167	1.185	1.191	1.194	1.197	1.198
150	1.155	1.176	1.182	1.186	1.188	1.190
200	1.142	1.166	1.173	1.177	1.180	1.182
250	1.129	1.155	1.163	1.168	1.171	1.173

5.2.3 *Immobilization of electrolytes and gas diffusion electrodes*

A porous structure in which the liquid electrolyte is immobilized by capillary forces can be used as a combination of diaphragm and electrolyte. In this case, the reduced free volume for the liquid electrolyte and the tortuosity of the porous structure are expected to result in a decrease in conductivity, and by that to an increase in ohmic losses. Nevertheless, the ohmic losses can be reduced by reducing the thickness of the porous structure. The determination of the conductivity of such structures is therefore important and can be measured with the van der Pauw technique as demonstrated by the authors [14]. A great advantage of immobilizing the electrolyte is the possibility to use gas diffusion electrodes (GDEs) for steam electrolysis at temperatures well above the boiling point of water, i.e. up to 250 °C in the work presented here, while the electrolyte remains in the liquid phase due to the higher boiling point of concentrated KOH (aq). At any given temperature, it is important to operate within an appropriate pressure range since too high pressures could cause condensation of steam (and thereby dilute the electrolyte or flood the GDE) while too low pressures could cause evaporation of the electrolyte (through which ohmic losses would increase). Further consequences of electrolyte evaporation could be disconnection of the circuit or the formation of open gas channels between cathode and anode. Phase transition lines between the liquid and liquid + gas phase for water and KOH solutions as a function of temperature and pressure have been presented in previous work [14].

Gas diffusion electrodes, similar to those used in high temperature solid oxide fuel cells (SOFC) and solid oxide electrolysis cells (SOEC) [76] allow electrolysis without the formation of bubbles. Bubble formation usually leads to increased ohmic losses due to area reduction and increased anodic and cathodic overpotentials due to reduced available electrode area in a traditional alkaline electrolyser [77]. GDEs have to be highly electronic conductive to minimize ohmic losses, and porous to allow the produced gases to escape while steam flows into the cell towards the triple phase boundary, TPB, as shown in figure

5.3. Since the electrochemical reactions take place at the TPB, it is important that the TPB-length is as long as possible [78]. Nickel is known to be corrosion resistant in alkaline media and electro-catalytically active, hence it is often used as a base material for electrodes in alkaline electrolysis cells. Electro-catalysts for the OER [44, 46] and HER [36, 79] have been extensively studied for alkaline electrolysis. They are optimally placed at the TPB in order to achieve low overpotentials. Silver is known to be an excellent catalyst for the oxygen reduction reaction ORR in alkaline fuel cells [80, 81] and can be considered as catalyst for the OER reaction as well. Co_3O_4 and Co- based spinel oxides are also known to be good electro-catalysts for the OER [82], while Raney-nickel and molybdenum [83] are preferred electro-catalysts for the HER. The anodic overpotential caused by the OER is usually dominating over the cathodic overpotential caused by the HER.

Nickel foams are widely used [84] and have already been shown to work as a gas diffusion electrode for the oxygen reduction reaction ORR in an alkaline fuel cell [85]. More advanced metal foams have recently been developed from Alantum Europe GmbH, where metal alloy foams are obtained by a powder metallurgical process. Important material parameters, i.e final composition, the specific surface area, and the pore size of the foam can be customized to the application [86].

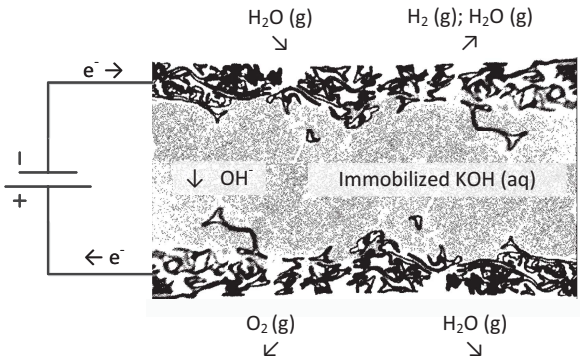

Figure 5.3: Illustration of an alkaline electrolysis cell with KOH (aq) electrolyte immobilized in a porous matrix and gas diffusion electrodes.

5.3 EXPERIMENTAL

5.3.1 *FobAEC - Foam based alkaline electrolysis cells*

A new type alkaline electrolysis cell and method to produce them has been developed [87]. Foam based alkaline electrochemical cells (FobAEC) are produced from metal foams delivered by Alantum Europe GmbH. Circular foam pieces with a diameter of 12 mm are stamped out of the foam sheets with a

thickness of 1.0 mm for nickel foam, and 1.6 mm for Inconel 625 foam (Inconel 625 alloy composition is for example in wt%: Cr, 21.32; Mo, 8.58; Nb, 3.73; Al, 0.18; Ti, 0.16; Fe, 0.11; Si, 0.09; C, 0.053; Mn, 0.04; Mg, 0.01; Balance Ni. [88]). The circular foam pieces were cleaned in ethanol; beside that, the foams were used as delivered. One or two foam layers are placed in an uni-axial press and 0.25 - 1.5 g $SrTiO_3$ powder is placed on top of the foam. One drop of an appropriate binder, i.e. MEK in 33 % ethanol, has been mixed to 100 mg of the perovskite $SrTiO_3$ powder to obtain better adhesion of the powder particles during processing and sintering. Another one or two layers of foam is placed on top of the powder. The whole structure is pressed for 30 s with a pressure of 13.0 kN/cm^2. The cells have then been sintered in air at 450 °C for 2 h with a heating ramp of 100 K h^{-1} followed by a second sintering step in 9 % H_2/ Ar at 1000 °C for 6 h with a heating and cooling ramp of 50 K h^{-1}.

Mercury porosimetry analysis has been performed with an AutoPore IV 9500 porosimetry analyzer, since the porosity and pore size distribution of the $SrTiO_3$ structure is of high interest for the immobilization of the electrolyte. A sample for the pore size measurements has been produced similar to the FobAECs, but without the foams pressed to the surfaces.

Electrodeposition of silver has been performed to some of the cells in order to improve the performance of the anode for the OER after preparing the cells as described above. The electrodeposition was performed with a 0.1 M $AgNO_3$+ 1 M KNO_3 solution under N_2 atmosphere and stirring. Pulsed deposition with pulse/pause relation of 1s/1s and a potential difference of −3.0 V (vs a platinised Pt counter electrode) has been used to deposit the Ag particles on the foam with a Gamry type 600 or 3000 potentiostat. Scanning electron microscopy SEM has been used to analyze the surface and cross section of the FobAEC before and after measurements. Analysis of the impedance and voltammetry data was partly performed using the software Ravdav [89].

5.3.2 *High temperature and pressure autoclave*

A Parr autoclave Type 4760 with 600 ml volume and a PTFE (Polytetrafluoroethylene) liner was used to perform measurements under high pressure and at elevated temperatures as shown in figure 5.4. The autoclave was made of Inconel 600, which can withstand high temperatures and pressures as well as extremely caustic environments [90]. To perform electrochemical measurements, the autoclave was equipped with additional gas handling components and wire through-puts. Nitrogen from a 200 bar pressurized bottle was used for the pressurization of the Autoclave. The pressure in the autoclave was regulated with a needle valve. A J-Type thermo-well was used to measure the temperature in the autoclave while a pressure gauge displayed the actual pressure. An additional digital pressure gauge allowed recording the pressure. The autoclave was insulated to avoid temperature gradients during the measurements.

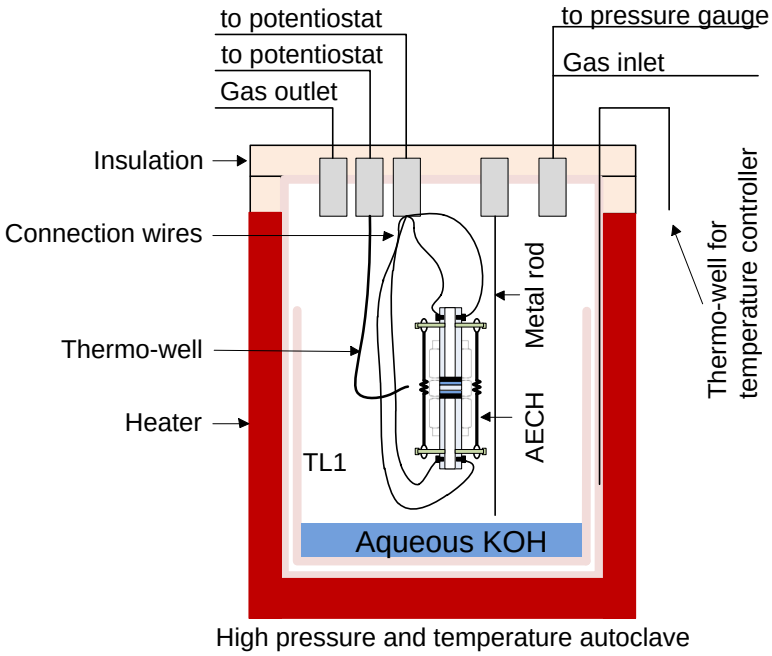

Figure 5.4: Schematic description of the autoclave setup including heater and top insulation. A teflon liner TL1 protects the autoclave from the caustic environment. The alkaline electrochemical cell holder (AECH) is connected to a metal rod by an insulated wire (not shown). The diluted aq. KOH solution used to humidify the autoclave atmosphere is also shown. The temperature controller is connected to a thermo-well placed in between the heater and the autoclave.

5.3.3 *Electrochemical measurements*

Electrochemical measurements have been performed with a Gamry type 600 or 3000 potentiostat. Electrochemical impedance spectroscopy (EIS) has been used to determine the cell characteristics under polarization and at open circuit voltage (OCV). Cyclic voltammograms have been recorded to analyze the cell performance as a function of the applied cell voltage.

A cell holder was developed to allow electrochemical characterization of the FobAECs. It is important that the materials used for the tests will not suffer from severe corrosion or degradation due to the harsh conditions in the autoclave. Inconel was chosen where low electrical resistance was needed, PFA (Perfluoroalkoxy) or PTFE where insulating properties and chemical resistance was an issue. Figure 5.5 shows the cross section of the cell holder that was used during the measurements. Nitinol (a nickel-titanium alloy) tension Springs were used to apply a constant force between two Inconel tubes which acted as current collectors. Inconel screws attached to the Inconel tube acted as

corrosion resistant connection points as well as mounting points for the Nitinol spring. PTFE O-rings ensured electronic insulation between the Inconel screws and the Nitinol springs. The FobAEC was placed in between two metal foams acting as current collectors (Inconel foam on the cathode, nickel on the anode). The produced gases could evolve through the Inconel tubes to the autoclave vessel. 5 mm holes on the side of the PFA tube fitting (Swagelock type PFA-820-6) ensured that the cell would not dry out during the performed measurements and allowed to connect a platinum wire to the center of the cell (immobilized electrolyte) in order to perform measurements against this reference electrode (compare section 5.3.4). The working electrode (WE) and the working sense (WS) of the potentiostat terminals were connected to the anodic side of the sample holder while the counter electrode (CE) and the reference (Ref) terminals were connected to the cathodic side of the sample holder.

The main intention of the presented work was to obtain performance data of the produced cells at temperatures close to 250 °C, but measurements at 100 °C and 200 °C have also been performed to analyze the influence of temperature. The cells have been kept in the aqueous electrolyte for at least two hours prior to the measurements in order to soak up the electrolyte; the concentration was 45 *wt*% for all cells. Humidification of the autoclave atmosphere to prevent the cells from drying was realized by filling the reaction chamber in which the sample holder was mounted with 22.5 ml of a 22.5 *wt*% KOH solution as shown in figure 5.4. The autoclave was filled with 10 bar N_2, supplied from a gas bottle, before heating. Further pressurization occurred through thermal expansion of the embedded gases and evaporation of part of the solution in the bottom during heating.

5.3.4 *Three electrode setup*

A reference electrode was attached to the middle of the FobAEC to determine the oxygen and hydrogen evolution overpotentials η_{O_2} and η_{H_2} as shown in figure 5.5. The hydrogen evolution overpotential was measured in safety gas (9 % H_2 in N_2) and the oxygen evolution overpotential in technical air (20 % O_2, 80 % N_2).

The reaction that takes place at the $H_2/Pt/KOH(aq)$ reference electrode is given in equation 5.7 with a standard potential E_C^0 of -0.828 V vs the standard hydrogen electrode, SHE [91].

$$2OH^-(aq) + H_2(g) \leftrightarrow 2H_2O(g) + 2e^- \tag{5.7}$$

The equilibrium electrode potential vs the SHE for the HER (reaction 5.7) E_C^{eq}, under measurement conditions can be calculated from equation 5.8, where a_i are activities of species i. For 240 °C and 40 bar it was calculated to be -844 mV under the experimental conditions employed here.

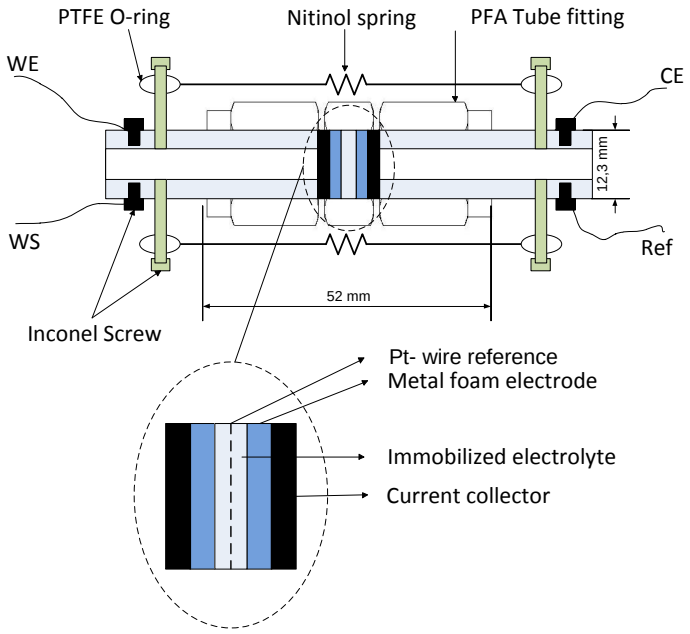

Figure 5.5: Principal cross section of the Alkaline Electrolysis Cell Holder (AECH): The electrolysis cell is centered in the sample holder. A piece of metal foam acts as current collector. The Inconel tubes press the foam against the active electrode of the electrolysis cell. Nitinol springs are assembled to provide constant force in order to avoid contacting problems. They are insulated against the screws by a PTFE O-ring. The wires WE, WS, CE and Ref indicate how the cell was connected to the potentiostat (see text). The Pt-wire acts as reference electrode in the three electrode setup.

$$E_C^{eq} = E_C^0 + \frac{RT}{2F} \ln\left(\frac{a_{H_2O}^2}{a_{H_2} a_{OH^-}^2}\right) \tag{5.8}$$

The reaction that takes place at the $O_2/Pt/KOH(aq)$ reference electrode is given in equation 5.9 with a standard potential E_A^0 of 0.4 V vs the SHE[91].

$$4OH^-(aq) \leftrightarrow O_2(g) + 2H_2O(g) + 4e^- \tag{5.9}$$

The equilibrium electrode potential vs the SHE for the OER (reaction 5.9) E_A^{eq}, under measurement conditions can be calculated from equation 5.10. For 240 °C and 40 bar it was calculated to be 352 mV under the experimental conditions employed here.

$$E_A^{eq} = E_A^0 + \frac{RT}{2F} \ln\left(\frac{a_{O_2} a_{H_2O}^2}{a_{OH^-}^4}\right) \tag{5.10}$$

5.4 RESULTS

5.4.1 *Porosimetry analysis*

The porosity and pore size distribution of the pellets used for immobilization of the aqueous KOH was characterized by Hg porosimetry and is shown in figure 5.6; the mean pore size was found to be 63 nm with a porosity of 48.0 %.

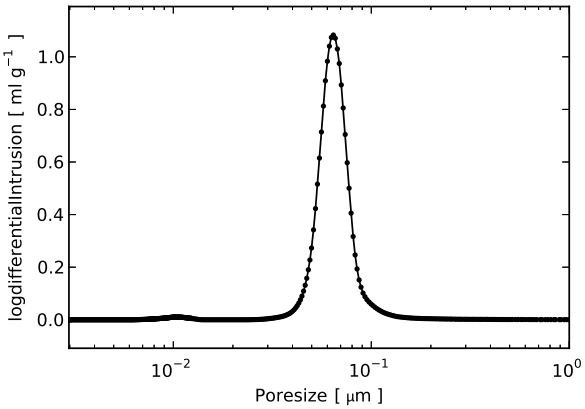

Figure 5.6: Results of the mercury intrusion porosimetry of the electrolyte supporting porous $SrTiO_3$ structure showing a mean pore size of 63 nm.

5.4.2 *Scanning electrode microscopy*

5.4.2.1 *Untreated Foam*

SEM (Scanning electron microscopy) images of the untreated foam are shown in figure 5.7. The pore size of the nickel and Inconel foam is ca. 450 µm with a porosity of 95 % for the nickel foam and $>$ 91 % for the Inconel foam according to the manufacturers specification. It can be seen that the surface of the nickel foam is relatively smooth compared to this of the Inconel foam. The coarse layer on the Inconel foam shows the Inconel layer, which has been coated on a nickel foam, similar to those seen on the left part of the figure.

5.4.2.2 *Surface analysis of the FobAECs anode*

The porosity of the foam is significantly reduced after pressing of the whole cell body in the uni-axial press. The typical pore size diameter is reduced to values in the order of 150 µm $\pm$ 50 µm with an even distribution. The shape is naturally changed to a more flat form instead of being ball-like, as it can be seen in figure 5.8, left image. The highly porous $SrTiO_3$ structure sticks out of the nickel foam at several places up to the surface of the cell. It can be seen that the nickel foam can act as a current collector as well as the active electrode. The right image of figure 5.8 shows the interface of the $SrTiO_3$ and the nickel foam,

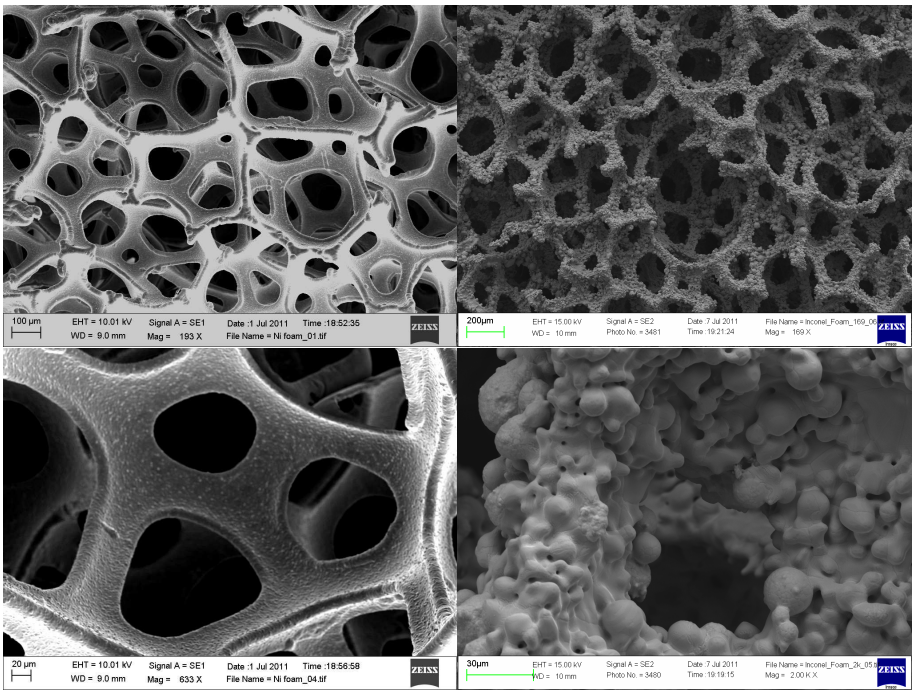

Figure 5.7: SEM picture of an untreated nickel foam (upper-left and lower-left) and Inconel foam (upper-right and lower-right). Note: the magnifications are different as indicated by the scale bars.

which will act as the TPB after immersion of the cell into liquid electrolyte. The $SrTiO_3$ has a tendency to form clusters on the surface which have a size of ca. $2 - 10\ \mu m$ while the pore size is mainly distributed around 63 nm as shown in figure 5.6.

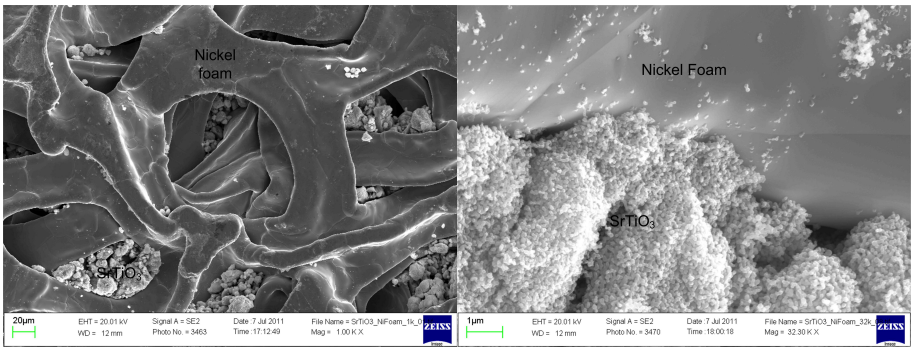

Figure 5.8: SEM picture of the surface of the nickel foam anode of a FobAEC at low (left), and high magnification (see scale bar) showing the interface between the nickel foam and the $SrTiO_3$ (right).

5.4.2.3 *Surface analysis of the silver deposited anode of the FobAECs*

Silver electro-deposition was successfully applied to the nickel foam anode as shown in figure 5.9. The left image shows the foam with silver crystals

of a particle size in the region of $10 - 20\ \mu m$ and nano sized silver particles distributed all over the foams surface. The right image shows the interface of the same sample at higher magnification where a relatively large silver particle of $7.5\ \mu m$ can be seen in the upper left part with well distributed nano sized particles in the range of $50 - 500\ nm$.

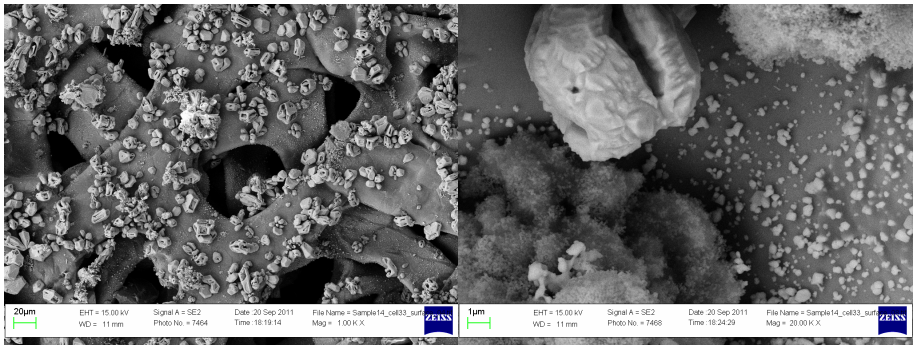

Figure 5.9: SEM picture of the surface of the nickel foam after Ag electrodeposition of the anode of a FobAEC at low (left) and high magnification (see scale bar) (right) showing the interface between the nickel foam and $SrTiO_3$ as well as the nano sized Ag particles.

5.4.2.4 *Cross section analysis of the FobAECs*

The results of the cross section analysis are shown in figure 5.10. The brightest structure indicates the metal foams, light gray is the porous $SrTiO_3$ structure and dark gray is the surrounding epoxy coating for the SEM analysis. Both electrodes are pressed out of two layers of the corresponding metal foam. The Inconel foam is less compressed than the nickel foam and shows a higher specific surface area than the pure nickel. It can also be seen that it will be sufficient to use only one layer of Inconel foam, but 2 layers of nickel foam are needed in order to obtain a good distribution of gas channels in combination with the ability of the foam to work as a current collector and active electrode.

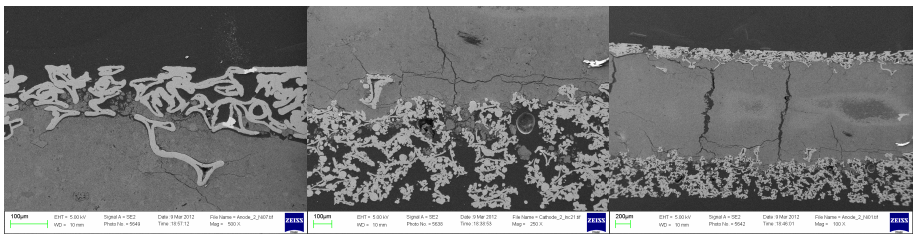

Figure 5.10: SEM picture of the cross section of a FobAEC with two layers of nickel and two layers of Inconel foam showing the nickel anode (left), the Inconel cathode (center) and the full cell (right).

Table 5.2: Comparison of the cell performance for different compositions of the FobAEC at around 240 °C and 40 bar

Cell	Anode	Cathode	Temperature [°C]/Pressure [bar]	I [mA cm^{-2}] at 1.5 V (uncomp.)	I [mA cm^{-2}] at 1.75 V (uncomp.)	Rs [mΩ cm^2] at 1.4 V polarization	U_{cell} [V] at 0.5 A cm^{-2} (comp.)
Cell 1a	2 layer Ni foam	2 layer Inc foam	240/38	466	1130	148	1.441
Cell 1b	2 layer Ni foam	2 layer Inc foam	237/36	528	1378	140	1.419
Cell 2	1 layer Ni foam	1 layer Inc foam	240/39	679	1570	112	1.388
Cell 3a	1 layer Ni foam + Ag deposition	1 layer Inc foam	240/37	1000	1918	119	1.291
Cell 3b	1 layer Ni foam + Ag deposition	1 layer Inc foam	247/42	903	1978	124	1.337

5.4.3 *Cell performance at high temperatures*

Cell performance tests have mainly been performed at temperatures in the region of 250 °C and pressures around 40 bar. Cyclic voltammograms of different compositions of the FobAECs are shown in figure 5.11. The current density at a polarization of $U_{cell} = 1.5$ V (uncompensated for ohmic resistance) reached from 466 mA cm^{-2} at 240 °C and 38 bar (for a cell with 2 layers of nickel foam as anode and two layers of Inconel foam as cathode), to 1000 mA cm^{-2} at 240 °C and 37 bar (for a cell with 1 layer of nickel foam with Ag- deposition as anode and one layer of Inconel 625 foam as cathode). Additional performance data for further cell compositions are shown in table 5.2. The serial resistance R_s has been measured with EIS under polarization of 1.4 V.

5.4.4 *Ag- deposited nickel anode with Inconel cathode*

The Ag- activated cells have shown the best performance as shown in table 5.2. Impedance analysis have generally been performed at a polarization voltage of 1.4 V. Figure 5.12 shows the cyclic voltammogram for a Ag- activated cell along with polarized impedance measurements before and after recording the voltammogram at polarization voltages of 1.4 V and 1.5 V. The serial resistance R_s decreased slightly after recording the voltammogram from 133 mΩ cm^2 to 125 mΩ cm^2 at 1.4 V polarization, while the area specific resistance of the cell, ASR_{cell}, decreased from 335 mΩ cm^2 before, to 319 mΩ cm^2 after recording the voltammogram. The R_s at 1.5 V was equal to this at 1.4 V (125 mΩ cm^2),

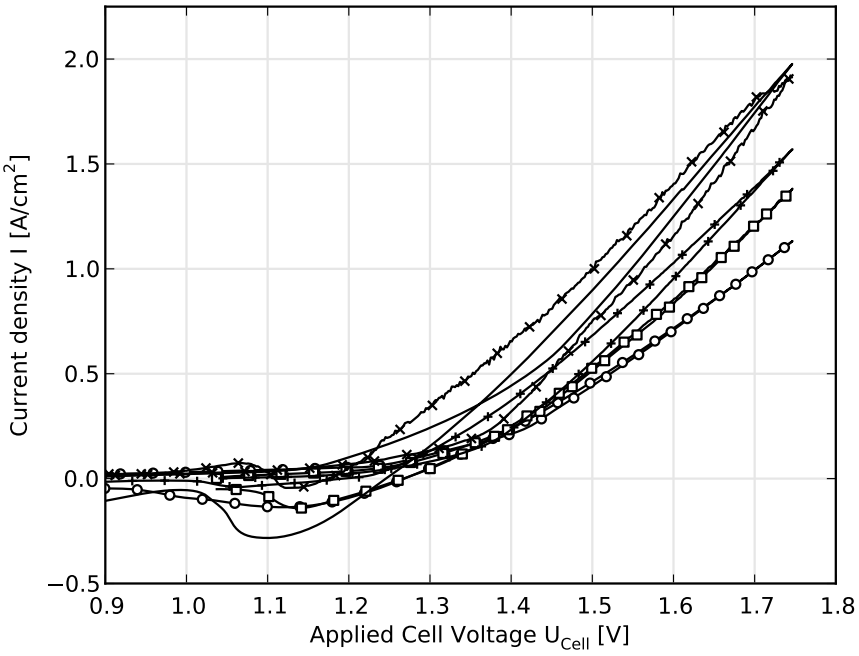

Figure 5.11: iV- curves of different cells at temperatures around 240 °C and pressures around 40 bar, i.e.: Cell 3a (x) and Cell 3b (full line) with 1 layer Ag- deposited nickel anode and 1 layer Inconel as cathode; Cell 2 (+) with 1 layer nickel foam anode and 1 layer Inconel as cathode; Cell 1b (□) with 2 layers nickel foam anode and 2 layers Inconel as cathode; Cell 1a (o) with 2 layers nickel foam anode and 2 layers Inconel as cathode.

whereas the ASR_{cell} reduced to 250 $m\Omega\,cm^2$. The main change is associated with the low frequency part of the spectrum.

5.4.5 *Influence of the temperature*

The performance of a FobAEC with Ag- deposited anode and Inconel cathode at 240 °C and 37 bar, 202 °C and 27 bar and 108 °C and 15 bar in comparison with the corresponding impedance measurements can be seen in figure 5.13. The investigated cell showed current densities of 1000 $mA\,cm^{-2}$ at 240 °C, 640 $mA\,cm^{-2}$ at 202 °C and 85 $mA\,cm^{-2}$ at 108 °C at a cell voltage of 1.5 V (during decreasing the cell voltage). The current densities at 1.75 V were 200 $mA\,cm^{-2}$, 1440 $mA\,cm^{-2}$ and 1940 $mA\,cm^{-2}$ at temperatures of 108 °C, 202 °C and 240 °C, respectively. The results are not R_s - compensated. The impedance plots at a polarization voltage of 1.4 V show that R_s improved from 164 $m\Omega\,cm^2$ to 128 $m\Omega\,cm^2$ and more significantly ASR_{cell} improved from 508 $m\Omega\,cm^2$ to 361 $m\Omega\,cm^2$ with increasing temperature from 202 °C to 240 °C as sown in the lower part of figure 5.13. The impedance curve shows significant scattering at low frequencies; a Kramers - Kronig test showed an error

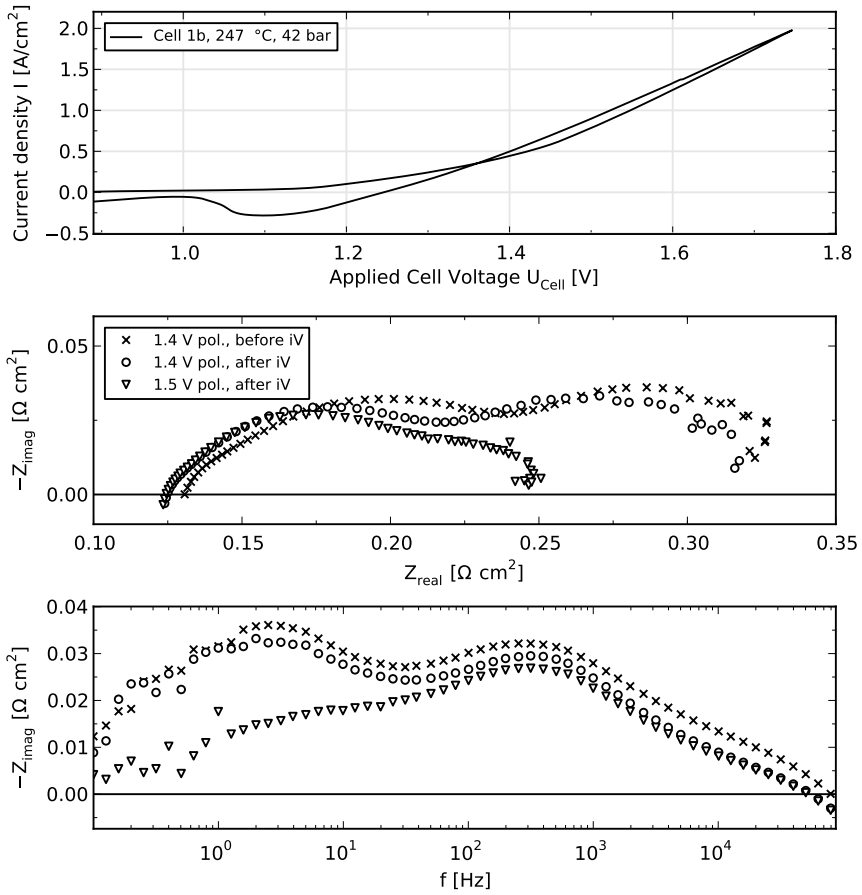

Figure 5.12: Cyclic voltammogram (upper figure) of a FobAEC with Ag- deposited anode and Inconel cathode at 247 °C and 43 bar in comparison with the corresponding impedance analysis (central figure) at polarization voltages of 1.4 V before (x) and 1.4 V (o) and 1.5 V (∇) after the cyclic voltammetry test.

above 1 % (up to $\pm$ 4.5 %) at frequencies below 10 Hz with random distribution around zero.

5.4.6 *Determination of the hydrogen evolution overpotential*

The overpotential of the Inconel cathode has been studied with the use of the sample holder as shown in figure 5.5. The reference of the potentiostat has been connected to the Pt- wire in the center of the FobAEC, as shown in figure 5.5 as well, which acts as a reference electrode. The analysis of the hydrogen evolution reaction HER has been performed in safety gas ($9\,\%\,H_2$ in N_2) with the results for the cyclic sweep voltammogram shown in figure 5.14. At a current density of 100 $mA\,cm^{-2}$ the overpotential was -40 mV and at 1000 $mA\,cm^{-2}$ it was -131 mV , resulting in a Tafel-slope of 91 mV/dec. The uncompensated overpotential for a current density of 1 $A\,cm^{-2}$ was -0.28 V.

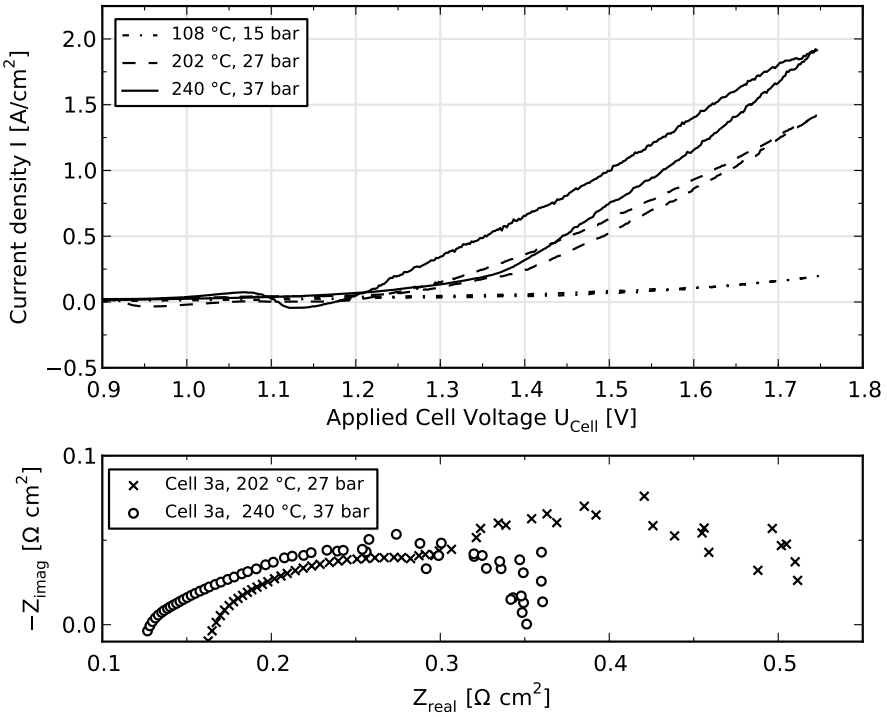

Figure 5.13: Cyclic voltammogram (upper figure) of a FobAEC (Cell 3a) with Ag- deposited anode and Inconel cathode at 240 °C and 37 bar (full line), 202 °C and 27 bar (dashed line) and 108 °C and 15 bar (dash-dot) along with the corresponding impedance analysis (lower figure) from data achieved at a polarization of 1.4 V.

The iR- corrected results (η_{H_2}) correspond to the difference of the cathode potential vs the equilibrium potential of the reference electrode E_C^{eq}. The cathode potential vs the SHE ($E_{C,SHE}$) is displayed on the second ordinate of figure 5.14 (compare chapter 5.3.4).

5.4.7 *Determination of the oxygen evolution overpotential*

The oxygen overpotential has been measured for cells with and without the Ag catalyst in technical air (20 % O_2, 80 % N_2) with the results shown in figure 5.15. The obtained current density for low overpotentials between 50 mV and 150 mV is higher for the not Ag activated cell, which has not generally been the case (compare figure 5.11). At higher overpotentials the situation changes and the current density of the Ag activated anode is higher than that of the pure nickel foam anode, i.e. at a current density of 90 $mA\,cm^{-2}$ the overpotentials are 250 mV and 220 mV, while at 900 $mA\,cm^{-2}$ they are 360 mV and 380 mV for the Ag activated anode and the nickel anode, respectively. The Tafel slope for the not activated cell is 160 $mV/decade$ while the Ag- activated anode im-

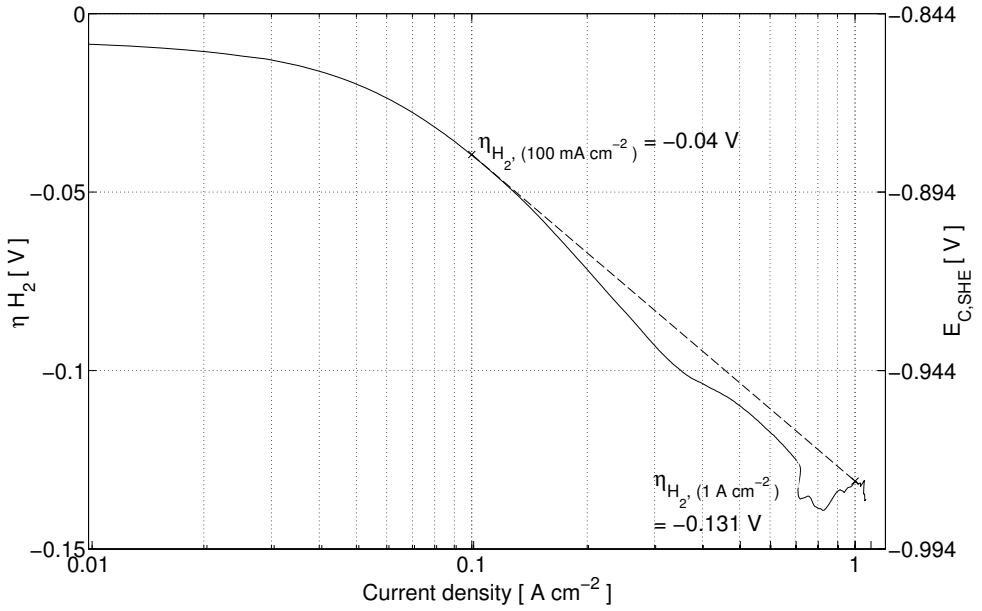

Figure 5.14: Cyclic voltammogram for the hydrogen evolution overpotential of the Inconel cathode with a sweep rate of 20 mV/s at 42.1 bar and 248 °C. The full line shows the R_s - compensated applied cell voltage; the dashed line shows the graphical estimation of the tafel slope between 100 $mA\,cm^{-2}$ and 1 $A\,cm^{-2}$.

proved to 130 $mV/decade$ between 90 $mA\,cm^{-2}$ and 900 $mA\,cm^{-2}$. The slope appears to be highly nonlinear.

The iR- corrected results (η_{O_2}) correspond to the difference of the cathode potential vs the equilibrium potential of the reference electrode E_A^{eq}. The anode potential vs the SHE ($E_{A,SHE}$) is displayed on the second ordinate of figure 5.15 (compare chapter 5.3.4).

5.5 DISCUSSION

5.5.1 *Cell performance*

The obtained current densities of 1.0 $A\,cm^{-2}$ at 1.5 V and 2.0 $A\,cm^{-2}$ at 1.75 V show that the proposed FobAEC cell design is able to compete with the state of the art PEM (Proton Exchange Membrane) electrolysis cells, but offers cost effective production since no expensive catalysts are needed. High performance has been achieved by increasing the temperature up to 250 °C at pressures up to 42 bar. The FobAEC can in principle be used in fuel cell mode as well, but this remains to be proven in future measurements along with long term measurements to determine the stability of the cell.

The overpotential for the HER after iR correction was as low as -40 mV for the Inconel foam at a current density of 100 $mA\,cm^{-2}$and−84 mV at a current

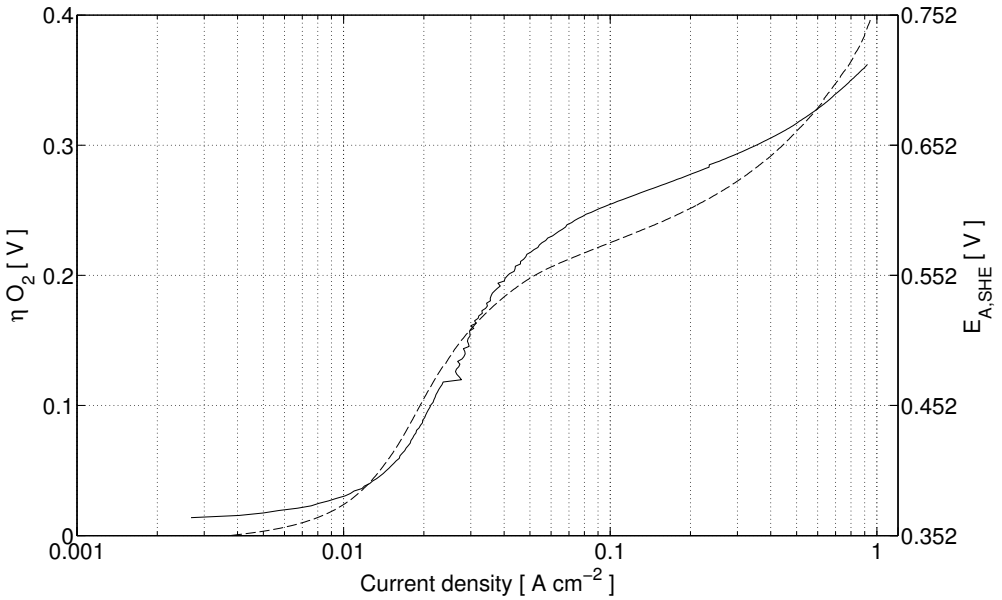

Figure 5.15: iV curve of a Ag loaded anode at 43.3 bar and 248 °C (full line) in comparison with an iV- curve of a pure nickel anode (dashed) at 42 bar 250 °C, both recorded with a sweep rate of 50 mV/s and compensated for R_s.

density of 250 $mA\,cm^{-2}$ as shown in figure 5.14. A recent review by Zeng and Zang [15] reported values between −58.0 mV and −489 mV for nickel alloys at the same current density of 250 $mA\,cm^{-2}$, but lower temperature (70 °C).

Overpotentials for the OER of 224, 235, 250, 270 and 300 mV at a current density of 100 $mA\,cm^{-2}$ have been reported by Zeng and Zang [15] for Ni + La doped Co_3O_4, Ni + Spinel type Co_3O_4, $La_{0.5}Sr_{0.5}CoO_3$, $Ni_{0.2}Co_{0.8}LaO_3$ and pure nickel electrodes, respectively, at temperatures between 25 °C and 90 °C. These values are similar with the overvoltage measured here at the same current density for the nickel foam anode (225 mV) and the Ag deposited nickel foam anode (254 mV), as shown in figure 5.15. Ag deposition on the anode leads to reduction of the overpotential at elevated current densities.

5.5.2 *Cell efficiency*

The calculation of the efficiency for water or steam electrolysis can be done in several ways, which may lead to confusion when results are compared. The electrical efficiency is often calculated by equation 5.11, where $HHV_{H_2,STP}$ is the Higher Heating Value of Hydrogen at standard temperature and pressure, STP; $E_{tn,0}$ is the thermoneutral voltage at STP and U_{Cell} is the applied cell voltage. This can lead to electrical efficiencies greater than 100 % since electrolysis is possible at lower voltages starting from 1.23 V at STP as calculated with equation 5.6. The energy efficiency is of course below 100 %, since the supply of heat is necessary in this case.

$$\eta_{electric} = \frac{HHV_{H_2,STP}\, n^{-1}\, F^{-1}}{Electricity\ demand} = \frac{E_{tn,0}}{U_{Cell}} = \frac{1.481\,V}{U_{Cell}} \tag{5.11}$$

Since water electrolysis is usually performed at elevated temperatures, it is more precise to take heat demands into consideration and calculate the efficiency by equation 5.12, where η_{HHV} is the efficiency correlated to the HHV, $HHV_{H_2,T}$ is the HHV for H_2 at a specific temperature.

$$\eta_{HHV} = \frac{HHV_{H_2,T}\, n^{-1}\, F^{-1}}{Electricity\ demand} = \frac{E_{tn,T}}{U_{Cell}} \tag{5.12}$$

The efficiency correlated to the HHV of cell 1a, which reached 1.0 A cm^{-2} at 240 °C and 37 bar, could, if further losses are said to be zero, be calculated to 84.3 %. The electric efficiency would be 98.7 % at this point.

It is also common to calculate the efficiency against the lower heating value LHV of hydrogen, i.e the US department of Energy DOE recommends the use of the LHV. Reservations against the use of the LHV have been expressed stating that it is not possible to obtain a efficiency of 100 %, although the cell might operate below the thermoneutral voltage, where ohmic losses compensate for the heat demand of the endothermic electrolysis reaction [92]. Anyway, it is of interest to compare the achieved efficiencies against the LHV, as calculated from equation 5.13, with the target from the DOE for 2017, which is 74 % cell efficiency. The here obtained efficiency η_{LHV} at a current density of 2.0 A cm^{-2} is 70 %, while it is 74 % at a current density of 1.6 A cm^{-2}.

$$\eta_{LHV} = \frac{\Delta G_f^0\, n^{-1}\, F^{-1}}{Electricity\ demand} = \frac{1.229\,V}{U_{Cell}} \tag{5.13}$$

The influence of the pressure on the reversible cell voltage E_{rev} was discussed in section 5.2.2. $E_{rev(t,p)}$ decreases with increasing temperature, but increases with increasing electrolysis pressure, as shown in figure 5.2. The efficiency against $E_{rev(t,p)}$, can be calculated by equation 5.14 where $\eta_{E_{rev}(t,p)}$ is the efficiency against the reversible cell voltage $E_{rev(t,p)}$. It is obvious that equation 5.14 is the only one taking the system pressure into account (compare figure 5.2) and allows for comparison of cells operated at elevated pressures, although the same restrictions as discussed for η_{LHV} are valid for $\eta_{E_{rev}(t,p)}$.

$$\eta_{E_{rev}(t,p)} = \frac{E_{rev(t,p)}}{U_{Cell}} \tag{5.14}$$

Furthermore it should be stressed that none of the given equations is utilizable to compare the performance of a cell unless the current density is also given. The efficiency of the measured cells have been calculated in comparison with cells from the literature at relevant current densities and are shown in table 5.3. The differences between the calculated efficiencies by equation 5.11 - 5.14 are up to 25 % for the same data-set (compare Cell 1a at 240 °C and 37 bar).

Table 5.3: Efficiencies of the measured cells at relevant current densities in comparison with available literature data.

Cell/ type	Temperature [°C]/ Pressure [bar]	I [$mA\,cm^{-2}$]	Ucell [V]	$\eta_{electric}$	η_{LHV}	η_{HHV}	$\eta_{E_{rev}(t,p)}$
Cell 1a; Ag deposited Ni foam anode, Inconel cathode	108/15	100	1.57	94.3	78.3	80.1	75.6
		200	1.75	84.6	70.2	71.9	67.8
	202/27	100	1.27	116.6	96.8	99.4	92.5
		200	1.33	111.4	92.4	94.9	88.4
		500	1.45	102.1	84.8	87.1	81.1
		1000	1.62	91.4	75.9	77.9	72.5
	240/37	100	1.22	121.4	100.7	103.6	96.0
		200	1.25	118.5	98.3	101.1	93.7
		500	1.35	109.7	91.0	93.6	86.8
		1000	1.5	98.7	81.9	84.3	78.1
		2000	1.76	84.1	69.8	71.8	66.6
Raney nickel cell [19]	100/4	400	1.55	95.5	79.3	94.8	75.3
Anode: $NiFe(OH)_2$ layer. Cathode: Pt coated SS [93]	58/ atmospheric	1000	2.12	69.9	58.0	69.3	55.0
Polished nickel electrodes in 50 wt% KOH [70]	264/15.5	500	1.55 (iR-corrected)	95.5	79.3	81.6	74.7
		1000	1.65 (iR-corrected)	89.8	74.5	76.7	70.1

5.5.3 *System costs*

No precious materials are used in the cell, and metal foams are widely used in industrial processes. Thus, it is possible to produce FobAECs at raw material prices under 1310 US$ m^{-2}, equal to 88 US$ kW_{el}^{-1} if operated at 1.0 A cm^{-2} and no further electro-catalysts are used. Ag is expensive material, but if it is used as a catalyst only with a small load, it would not raise the cost very much, especially if compared to some of the best known catalysts for the OER (RuO_2 or IrO_2) [45]. Lab-scale prices for Ag, RuO_2 and IrO_2 are 5.00 US$ g^{-1}, 34.40 US$ g^{-1} and 91.40 US$ g^{-1}, respectively (Alfa Aesar, October 2012). The price of silver on the stock market is ca. 1 US$ g^{-1} as of October 2012, whereas platinum cost about 50 US$ g^{-1}. The additional investment costs of an electrolysis system using FobAECs due to the high temperature and pressure will be compensated by the fact that the systems can be build much smaller if compared to standard alkaline electrolysis systems at the same production rate due to the high current densities and a high electrical efficiency. Also the costs of pressurized hydrogen (and oxygen) will be reduced.

5.6 CONCLUSION

A new type of alkaline electrochemical cell has been developed and tested. Current densities of almost 1.0 A cm^{-2} at 240 °C and 37 bar have been reached at the thermoneutral voltage for water splitting (1.481 V at STP), thereby achieving an electrical efficiency of 98.7 % at this current density. At the industrial more relevant cell voltage of 1.75 V (industrial electrolysis systems are usually operated at or above this voltage, compare table 5 from [15]), corresponding to an electrical efficiency of 84.5 %, the current density reached 2.0 A cm^{-2} and is thereby better than the targets of the US Department of Energy DOE for 2017.

5.7 ACKNOWLEDGMENTS

The financial support from the 2nd generation alkaline electrolysis project, EUDP 63011-0200, is gratefully acknowledged. The authors are also thankful for additional financial support from the “Catalysis for Sustainable Energy initiative”, funded by the Danish Ministry of Science, Technology and Innovation. Furthermore we are thankful for the supply of metal foams by Alantum Germany GmbH. Johan Hjelm is acknowledged for valuable consultation during the electrodeposition experiments. For valuable discussions along the way, we are very thankful to Jonathan Hallinder. We also appreciate the consultations from Sune D. Ebbesen and Ane Sælland Christiansen.

6

TEMPERATURE DEPENDENCE OF COBALT AND MOLYBDENUM ACTIVATED ELECTRODES IN FOAM BASED ALKALINE ELECTROLYSIS CELLS

6.1 ABSTRACT

A new type of alkaline electrolysis cells with nickel foam based gas diffusion electrodes and KOH (aq) immobilized in mesoporous $SrTiO_3$ has been developed and tested at temperatures of 150 °C, 200 °C and 250 °C at a pressure of 40 bar. Two cells have been characterized during the 270 h long test, using impedance spectroscopy, cyclic voltammetry and chronoamperometry at an applied cell voltage of 1.5 V, 1.625 V and 1.75 V. The performance of the electrolysis cells was improved by the addition of cobalt oxide and molybdenum oxide as nano sized electro-catalysts. At a temperature of 250 °C current densities of 1.1 $A\,cm^{-2}$ and 2.3 $A\,cm^{-2}$ have been obtained at a cell voltages of 1.5 V and 1.75 V, respectively.

6.2 INTRODUCTION

6.2.1 *Alkaline electrolysis*

The political decision to change the energy supply system from fossil fuels towards renewable energies in many European countries, specially Denmark and Germany with very ambitious goals, rises the demand for effective, ecologic and economic energy storage systems. Hydrogen produced by renewable energy through water electrolysis can fulfill those demands [4]. For some decades, alkaline electrolysis has proven to be reliable and efficient [19], but both production and investment costs needs to be reduced, i.e. by pressurized electrolysis in order to reduce compression costs [12]. Higher operational temperatures can improve the electrical efficiency and with that the electricity costs significantly, as it has been described in chapter 5.

The principal functionality of an alkaline electrolysis cell is well described in literature [94, 95, 15] and has also been discussed in chapter 2 and in the introduction of chapter 5. The cell voltage, U_{cell}, at a certain current density, I, depends mainly on the operation temperature [11] and pressure [12], the electrolyte concentration (conductivity)[14], the right choice of the electro-catalyst and its concentration [13] and a high specific surface area of the electrodes. Major losses are the cathodic overvoltage, η_{H_2}, the anodic overvoltage, η_{O_2}, and ohmic losses in the electrolyte.

A new type of an electrolysis cell has been described in chapter 5; a porous structure in which the liquid electrolyte is immobilized by capillary forces can be used as a combination of diaphragm and electrolyte. The hydrogen evolution reaction, HER, and the oxygen evolution reaction, OER, takes place at gas diffusion electrodes (GDEs), similar to those used in high temperature solid oxide fuel cells (SOFC) and solid oxide electrolysis cells (SOEC) [76] with the aim of reducing or eliminating bubble formation. GDEs have to be highly electronic conductive to minimize ohmic losses, and porous to allow the produced gases to escape while steam flows into the cell towards the triple phase boundary, TPB, as shown in figure 6.1. Since the electrochemical reactions take place at the TPB, it is important that the TPB-length is as long as possible [78].

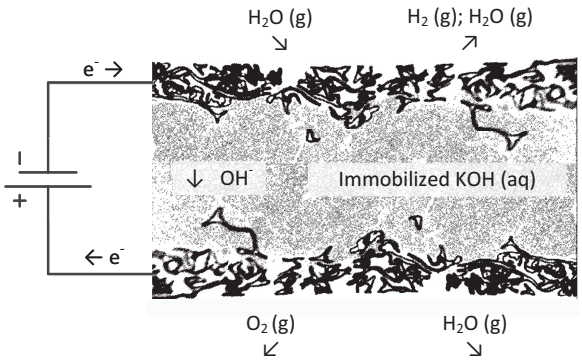

Figure 6.1: Illustration of an alkaline electrolysis cell with gas diffusion electrodes and KOH (aq) electrolyte immobilized in a porous matrix. The provided steam, $H_2O(g)$, is reduced at the cathode (upper GDE), where the produced H_2 leaves the GDE with the excess steam. Oxygen evolution takes place at the anode (lower GDE).

6.2.2 *Electro-catalysts for the OER and HER*

Electro-catalysts for the OER [44, 46] and HER [36, 79] have been extensively studied for alkaline electrolysis. Co_3O_4 and Co- based spinel oxides are known to be among the best electro-catalysts for the OER in alkaline media. An in situ activation process, where $Co(NO_3)_2$ was mixed to the electrolyte (KOH) of a traditional, immersed electrolysis cell to form Co_3O_4 by anodic deposition during electrolysis, showed a reduction of the electrode overpotential η_{O_2} by $80 - 140\,mV$ at $1\,A\,cm^{-2}$ and a temperature of $120\,^{\circ}C$ [96, figure 3]. Other utilized preparation methods, with catalyst deposition prior to operation (ex situ) are for example thermal decomposition, spray pyrolysis, electrostatic spray deposition, sol-gel, precipitation, electro-spinning, anodic oxidation of alloys, rheological phase reaction and pyrolysis, gel hydrothermal oxi-

dation, and electrodeposition techniques. A review of the named methods to produce Co-oxide coatings has recently been published by Hamdani et al [82].

Although the anodic overpotential caused by the OER is usually dominating over the cathodic overpotential caused by the HER, it is still relevant to identify corrosion resistant and economically attractive catalysts for the HER. Raney-nickel and molybdenum [83] are preferred electro-catalysts for the HER. A combination of the advantageous properties of Raney nickel and Mo as electro-catalyst lead to a reduction of η_{H_2} by 360 mV from -430 mV to -70 mV at a current density of 1 $A\,cm^{-2}$ and a temperature 70 °C by applying the vacuum plasma spraying process [97].

Nickel foams are widely used and versatile for many purposes [84] and have already been shown to work as a gas diffusion electrode for the oxygen reduction reaction ORR in an alkaline fuel cell [85]. Very recent data of an alkaline electrolysis cell with nickel foam electrodes and $NiCo_2O_4$ electro-catalyst, deposited with a direct combustion preparation procedure, for low temperature applications (120 °C) have been presented at the World Hydrogen Energy Conference 2012 in Toronto from Bouzek et al [98].

More advanced metal foams have recently been developed from Alantum Europe GmbH, where metal alloy foams are obtained by a powder metallurgical process. Important material parameters, i.e final composition, the specific surface area, and the pore size of the foam can be customized to the application [86].

6.3 EXPERIMENTAL

6.3.1 *Production of electrolysis cells*

The cells analyzed in this part are a new type of alkaline electrolysis cells [87]. A similar version has been shown to operate at 250 °C and 42 bar in chapter 5. The Foam based alkaline electrochemical cells (FobAEC) are produced from metal foams, $SrTiO_3$ as porous matrix to immobilize the aqueous electrolyte (45 wt % KOH) and a cobalt- or molybdenum $SrTiO_3$ mixture as electro-catalyst. The production method is illustrated in figure 6.2: Circular foam pieces with a diameter of 10 mm are stamped out of the foam sheets with a thickness of 1.0 mm for nickel foam, and 1.5 mm for Inconel foam. One layer of nickel foam is placed in an uni-axial press and pressed with a pressure of approximately 50 $N\,cm^{-2}$. Another layer of unpressed nickel foam is placed on top. Circa 30 mg of a mixture of 50 wt% Cobalt(II) hydroxide (99.9% (metals basis), Alfa Aesar product number 012524) and 50 wt% $SrTiO_3$ was placed on top of the foam. Another layer of 200 mg pure $SrTiO_3$ powder was added before 30 mg of a mixture of 30 wt% Molybdenum(VI) oxide (99.95% (metals basis) Alfa Aesar product number 011837), and 70 wt% $SrTiO_3$ was placed on top. One drop of an appropriate binder, i.e. MEK in 33 % ethanol, has been mixed to 100 mg of the perovskite $SrTiO_3$ powder to obtain better adhesion of the powder

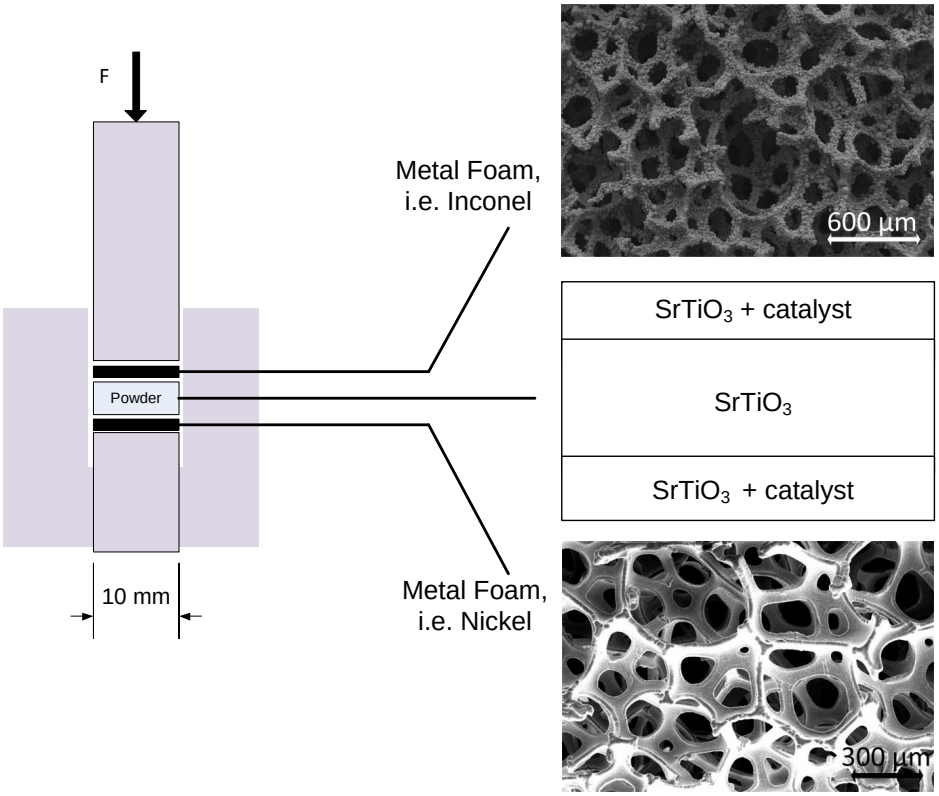

Figure 6.2: Schematic description of the production method: Nickel foam is placed in an uni-axial press. $SrTiO_3$ powder is placed between two layers of a $SrTiO_3$-electrocatalyst mixture. Inconel foam is placed on top before it is pressed and sintered (sintering not shown).

particles during processing and sintering. One layer of Inconel foam is placed on top of the powder-sandwich.

The whole structure is pressed for 30 s with a pressure of 13.0 kN cm^{-2}. The cells have then been sintered in air at 450 °C for 2 h with a heating ramp of 100 K h^{-1} followed by a second sintering step in 9 % H_2/ Ar at 1000 °C for 6 h with a heating and cooling ramp of 50 K h^{-1}.

The produced cells had a diameter of ca. 10 mm with a total height of 1.75 mm, the cathode, anode, and electrolyte thickness were ca. 300 µm , 150 µm and 1300 µm , respectively. The heights have been measured by SEM on a similar cell and may vary by roughly 100 µm since the foam electrodes may stick deeper or less deep into the electrolyte structure at some points.

6.3.2 *Electrochemical measurements*

Two similar cells were produced as described above. Electrochemical measurements, i.e. electrochemical impedance spectroscopy (EIS), cyclic voltamme-

try (CV), and chronoamperometry (potentiostatic measurements) have been performed in order to determine the cell characteristics during operation. A *Gamry Reference 3000* potentiostat connected to a 8 channel *ECM 8 Electrochemical Multiplexer* were used to conduct the measurements. Cyclic voltammograms or iV-curves were recorded with a sweep rate of 50 mV/s starting from OCV increasing to 1.75 V, then going back to OCV. EIS has been performed at open circuit voltage (OCV) and under polarization of 1.5 V. The area specific resistance ASR $[m\Omega\,cm^2]$ and the serial resistance R_s $[m\Omega\,cm^2]$ of the cells were determined from the polarized impedance measurements without further inductance corrections. The polarization resistance R_p $[m\Omega\,cm^2]$ was calculated by equation 6.1.

$$R_p = ASR - R_s \tag{6.1}$$

The programmed sequence for EIS and CV measurements was a repeating loop of 3 EIS measurements at OCV, prior to polarized EIS, followed by a CV. The channel of the multiplexer was changed after each step. The sequence was timed to allow hourly CV recordings for each channel.

Chronoamperometry were performed for both cells at temperatures of 200 °C and 250 °C in order to determine the steady state characteristics of the cell at an applied cell voltage of 1.5 V, 1.625 V and 1.75 V. The step time has been varied from 2 min to 100 h; high current densities at the elevated cell voltages made a limited testing time necessary in order to avoid strong degradation at an early stage.

6.3.3 *Automatized cell test setup*

An automatized setup to allow electrochemical tests in a temperature range of 25 °C − 250 °C and a pressure range of 1 − 100 bar in an autoclave has been constructed. The main vessel of the autoclave is made from steel. A titanium liner inside the autoclave offers improved corrosion resistance towards the highly corrosive KOH and other hazardous chemicals. Furthermore, an additional teflon liner has been placed inside the vessel for even higher corrosion resistance. Two heating elements in direct contact with the autoclave body are used to heat the autoclave. The temperature is computer controlled using a Eurotherm controller. Alumina wool insulates the reaction chamber from the surroundings. Two Inconel lids are placed at the top and the bottom of the autoclave; they are sealed with Teflon or titanium O-rings and a number of bolts.

Five NPT-type (National Pipe Thread) windings are installed on the top lid of the autoclave for gas supply and wire fead-throughs. An additional winding at the bottom lid of the autoclave is used as gas outlet. A holder for a catalytic burner (CB) has been mounted under the top lid (white ceramic body at 200 mm, right picture of figure 6.3; the ceramic zirconia (8YSZ) body has been replaced by a stainless steel body in the work presented in this chapter). The

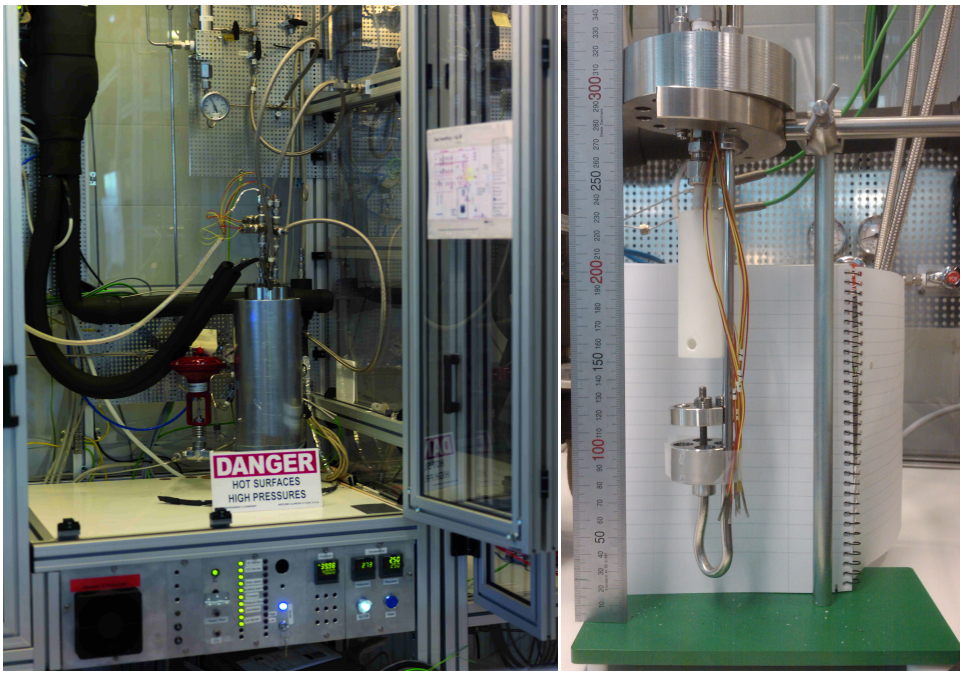

Figure 6.3: Picture of the autoclave in the automated test setup (left), picture of the sampleholder and holder for the catalytic burner (white ceramic body) (right).

CB comprises a honeycomb structured ceramic body with a catalyst to allow steam generation by H_2 and O_2 combustion in the autoclave with a known flow rate, controlled by mass flow controllers. An excess of H_2 or O_2 can be programmed for the case that measurements should be performed in reducing or oxidizing atmosphere.

The sample holder used to test the produced electrolysis cells is shown in figure 6.4. K-type thermocouple wire were used to connect the cathode of the FobAEC to the counter electrode (CE) and reference input (Ref) of the potentiostat multiplexer. A tubular, headless screw is used to fix the setup initially. A nickel spring ensures that the nickel mesh, which is wrapped around a teflon tube, is pressed to the cathode during the measurements. The mesh is more specifically placed at the cathode facing part of the teflon tube. A teflon ring has been placed around the FobAEC to avoid gas mixing. A layer of nickel foam is used as current collector at the anodic side of the FobAEC. Another K-type thermocouple is connected to the nickel foam current collector on the sample bottom. It is connected to the working electrode (WE) and the working sense (WS) of the potentiostat. The same connections were used on the right sample shown in figure 6.4, but have not been drawn for clarity reasons.

The gas mixture from the catalytic burner CB at the gas inlet (in the here shown experiments a mixture of H_2, H_2O and N_2) flows partly to the cathode of the FobAEC and further through the autoclave. The oxygen produced at the anode of the FobAEC escapes the sampleholder through a tubular hole, where

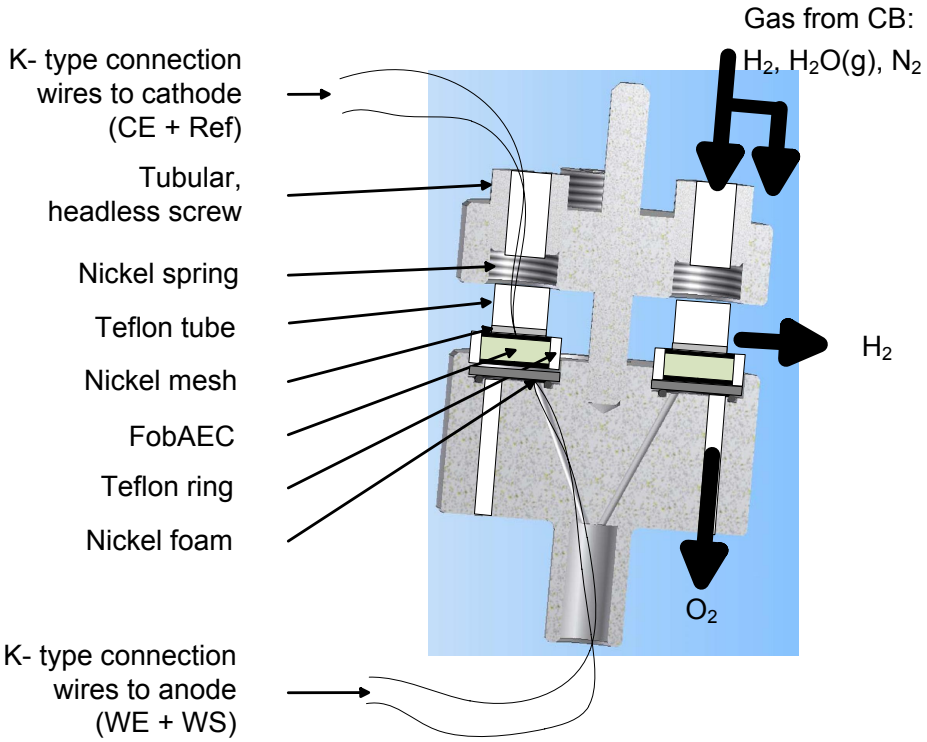

Figure 6.4: Illustration of the sample holder used in the autoclave to test the electrolysis cells, with mounted sample and simplified demonstration of the gas flow.

it will mix with the other gases and react to form steam at the CB placed at the autoclave outlet. It was not possible to supply a steady flow of O_2 to the anode for technical reasons. A pressure control valve is placed at the outlet stream of the autoclave to set the gas pressure to the desired value.

6.3.4 *Temperature, gas flow profile and partial pressures during testing*

The temperature and gas flow profile used for the electrochemical testing of the produced cells is shown in figure 6.5, with the gas flow on the left ordinate and the autoclaves temperature on the right ordinate. The electrochemical measurements were started at some time after t_0 + x hours, where t_0 indicates the starting point of the measurement and x is the time that passed after t_0, for example heating from 150 °C to 200 °C started at t_0 + 60 h.

H_2, N_2 and $H_2O_{(g)}$(steam) was supplied to the autoclaves chamber; in fact O_2 was also supplied, but it is completely converted to steam in the catalytic burner with part of the supplied H_2. The gas flow shown in figure 6.5 represents the gas composition after the catalytic burner.

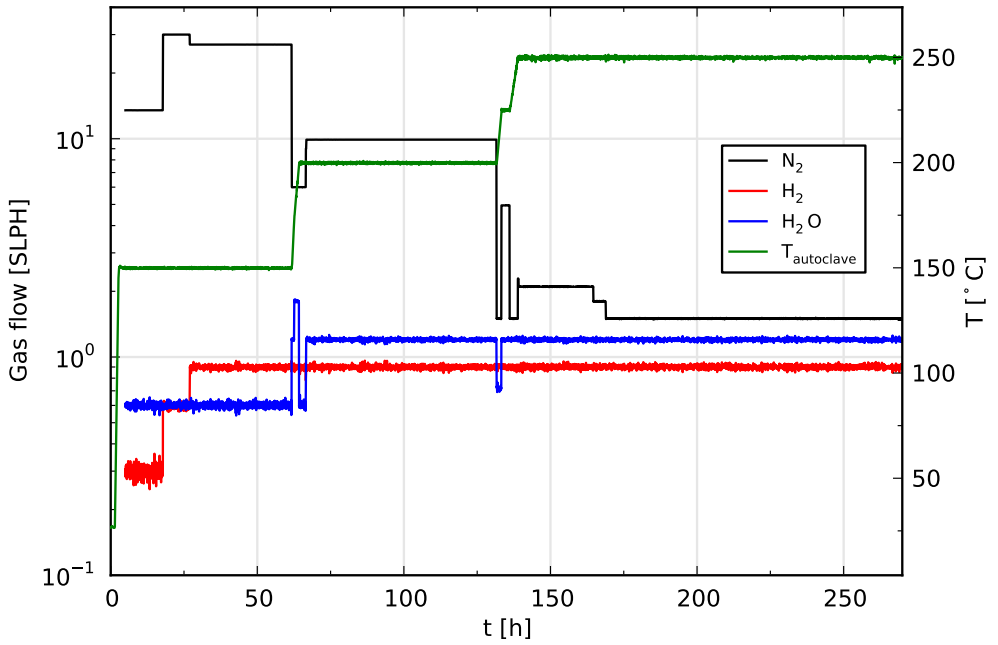

Figure 6.5: Gas flow profile of the supplied gases H_2(red), N_2(black) and $H_2O_{(g)}$(blue) over the entire measurement given in standard liters h^{-1} along with the temperature of the autoclave (green).

The maximal conversion rate of steam by the electrolysis cell during experiments, $H_2O_{conv,max}$, can be calculated with equation 6.2, where I_{Cell} is the electrolysis current, F is Faradays constant and $1.2417\,10^{-5} mol\ s^{-1}$ is equivalent to a gas flow rate of 1 standard liter per hour (SLPH). The steam flow rate has been set to 0.61 SLPH for the measurements at 150 °C (until t_0 + 60 h) and to 1.22 SLPH for measurements at 200 °C ($t_0 + 65\,h \rightarrow t_0 + 131\,h$) and 250 °C ($t_0 + 139\,h \rightarrow t_0 + 270\,h$). The maximal conversion rate is limited by the installed multiplexer with a maximal current of 2.0 A, equivalent to 2.55 $A\,cm^{-2}$ for the investigated cells; this corresponds to a $H_2O_{conv,max}$ of 1.29 SLPH. With the given steam flow rates of 0.61 SLPH at 150 °C, I_{Cell} must not exceed 1.21 $A\,cm^{-2}$ in order to prevent that more steam is used than provided.

$$H_2O_{conv,max}[SLPH] = \frac{I_{cell}}{2F}\frac{1}{1.2417\,10^{-5}} \tag{6.2}$$

In order to avoid evaporation or boiling of the immobilized electrolyte, it is necessary to keep the system pressure (40 bar for the entire measurement period) above the water vapor partial pressure of the electrolyte; this means that some small amounts of inert gas (N_2) are necessary; a higher pH_2 would be feasible as well, but would increase safety risks while testing. The equilibrium water vapor partial pressure over aqueous potassium hydroxide solutions, $p_{W,KOH}$, has been described by Balej [22], who showed that the empirical equation (6.3) can be used to calculate the water vapor partial pressures

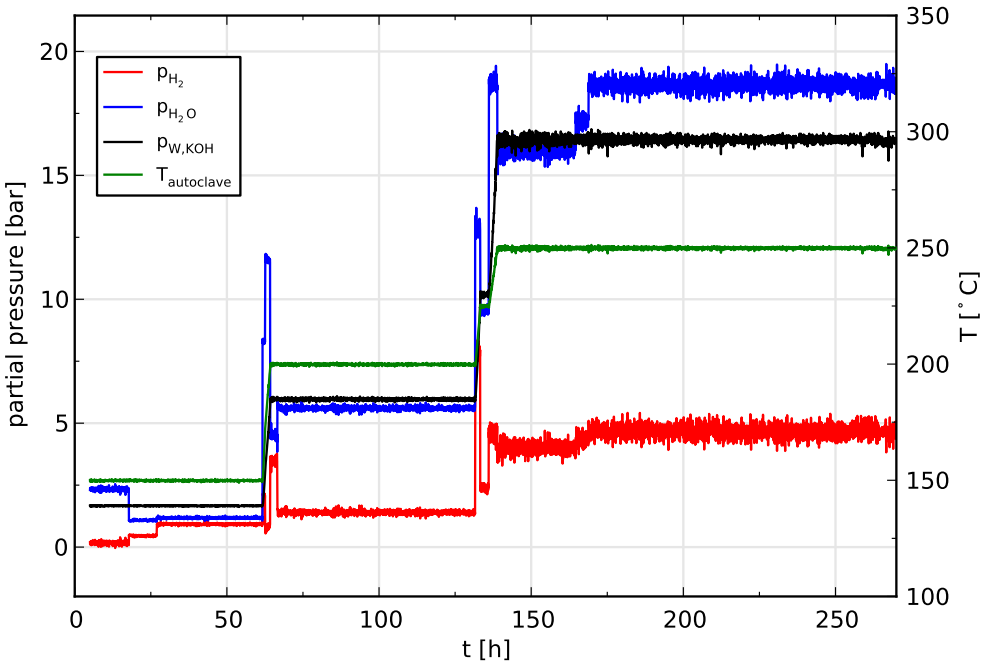

Figure 6.6: Partial pressures profile of H_2(red) and $H_2O_{(g)}$(blue) over the entire measurement period along with the equilibrium water vapor partial pressure over 45 wt% KOH (aq) (black) corresponding to the temperature in the autoclave (green).

in a temperature range of $0-300\,^{\circ}C$ and potassium hydroxide (KOH) concentrations for a molality of $0-18$ m, where $p_{W,KOH}$ is the water vapor partial pressure as a function of temperature T [K] and molality m. For a KOH concentration of 45 $wt\%$ and temperatures of 150 °C, 200 °C and 250 °C, $p_{W,KOH}$ has been calculated to be 1.67 bar, 5.98 bar and 16.47 bar, respectively.

$$\begin{aligned}\log\left(\frac{p_{W,KOH}}{1\,bar}\right) &= -0.01508m - 0.0016788m^2 + 2.2588710^{-5}m^3 + (1 - 0.0012062m) \\ &\quad +5.6024\cdot10^{-4}\cdot m^2 - 7.8228\cdot10^{-6}m^3)\cdot(35.4462 - \\ &\quad \frac{3343.93}{T} - 10.9\cdot\log T + 0.0041645\cdot T)\end{aligned} \tag{6.3}$$

Figure 6.6 shows the partial pressures of H_2 (pH_2), steam (pH_2O) as well as $p_{W,KOH}$ on the left ordinate along with the temperature of the autoclave on the right ordinate over the entire measurement period. The steam partial pressure was kept close to $p_{W,KOH}$ to avoid dilution or drying of the electrolyte. In order to compensate for the steam used for the electrolysis process, pH_2O was adjusted to 17.3 bar at t_0 + 164 h and to 18.7 bar at t_0 + 169 h by reducing the N_2 - flow rate and by that also pN_2 (the system pressure was constant during the entire measurement).

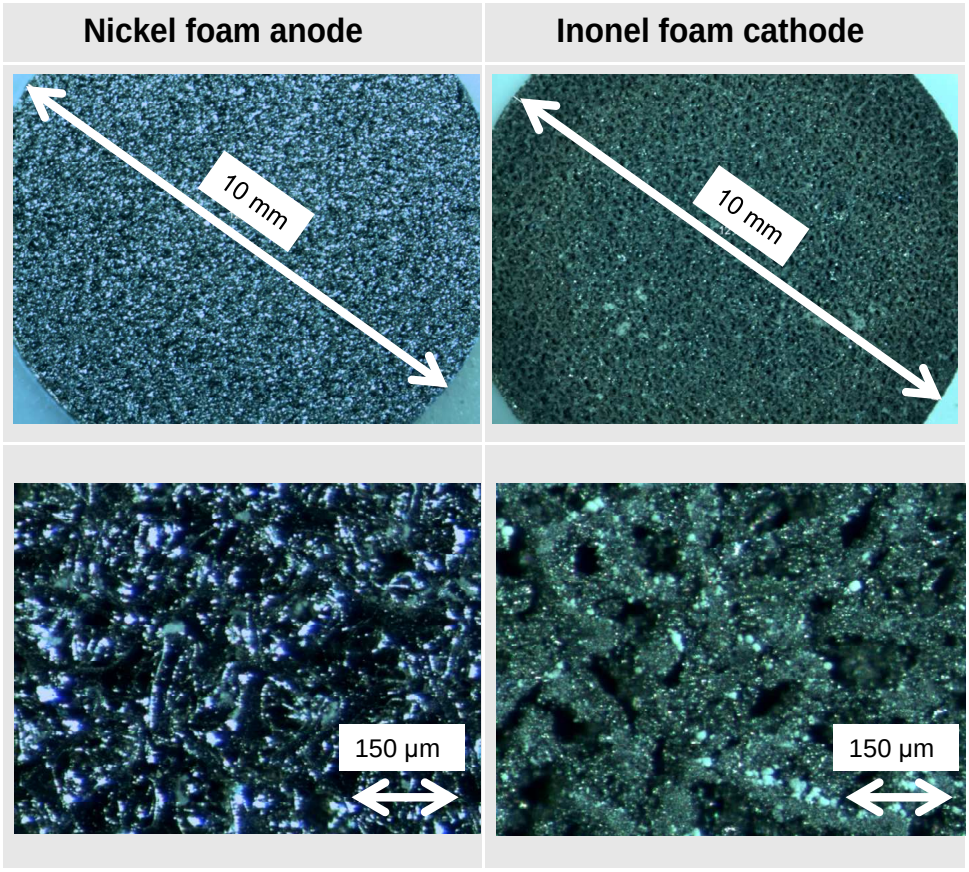

Figure 6.7: Optical micrographs of the electrodes of a FobAEC showing the nickel anode (left) and Inconel cathode (right) . The foam structure is well distributed over the entire electrode without regions that significantly differ from others. Also the porosity seems well distributed over the entire electrode with pore sizes in between 50 µm - 100 µm.

6.4 RESULTS

6.4.1 *Physical structure of the produced cells*

After pressing and sintering, the FobAECs were analyzed under the optical microscope . Pictures of the nickel foam side (anode) and the Inconel foam side (cathode) are shown in figure 6.7. The diameter before and after sintering was ca. 10 mm, the height of both cells was ca. 1.75 mm after sintering. The pore size of the foams was in between 50 and 100 µm.

6.4.2 *Electrode- electrolyte interface*

Scanning electron microscopy (SEM) images of the electrodes and the electrode-electrolyte interface are shown in figure 6.8, with the nickel electrode on the left column and Inconel on the right column. A cross section of the cell in the

upper images shows the nickel foam (light gray, upper left image) and the Inconel foam (light gray, upper right image) facing the porous $SrTiO_3$ structure (dark gray). The purpose of the porous $SrTiO_3$ structure (from now on called *electrolyte structure*) is to immobilize the aqueous KOH during operation. Both electrodes bonds well with the electrolyte structure, offering a long three phase boundary (TPB), although the nickel electrode sticks deeper into the electrolyte structure, where the electrolyte and the electrodes have no connection to the gas phase. A significant difference between the Inconel and nickel foam electrode is the tortuosity; while the gases can enter or leave the electrodes rather easily on the Inconel side, the higher tortuosity of the nickel foam may lead to gas diffusion limitations at higher current densities. This is a result of the pressing procedure, where the softer nickel foam is pressed to be more flat than the stiffer Inconel foam.

The images in the center of figure 6.8 are top views of the same electrodes. It can be seen that the electrolyte structure faces the top of the cell well distributed over the cell for the nickel electrode (left) while the Inconel electrode shows foam only. Furthermore it can be seen that the Inconel foams structure is rougher than the nickel one, thereby offering a higher specific surface.

A detailed picture of the electrode electrolyte interface is shown on the lower images. The highly porous $SrTiO_3$ electrolyte structure (light gray) with a mean pore size of 63 nm (compare chapter 5.4.1) faces the electrodes (dark gray). On the lower right picture it can also be seen that some of the molybdenum seems to agglomerate on the rough Inconel surface (similar to snow covered mountain peaks).

6.4.3 *Activated electrolyte structure*

6.4.3.1 *Cathode*

The $SrTiO_3$ powder facing the Inconel cathode has been mixed with molybdenum oxide powder as described in section 6.3.1. In figure 6.9 it can be seen that molybdenum particles (Mo) are well distributed in the electrolyte structure (S) with a particle size between 100 nm and 200 nm. The molybdenum has a tendency to agglomerate on the surface of the Inconel foam (Inc). E is epoxy for microscopy purposes and not of relevance.

6.4.3.2 *Anode*

Also the $SrTiO_3$ powder facing the nickel anode has been mixed with cobalt oxide powder as described in section 6.3.1. In figure 6.10 it can be seen that the cobalt particles (white) are distributed in the electrolyte structure (dark gray) with a pore size around 50 - 200 nm. There is no tendency for the Co particles to agglomerate at the nickel surface as it was seen in figure 6.9 for molybdenum on the Inconel foam.

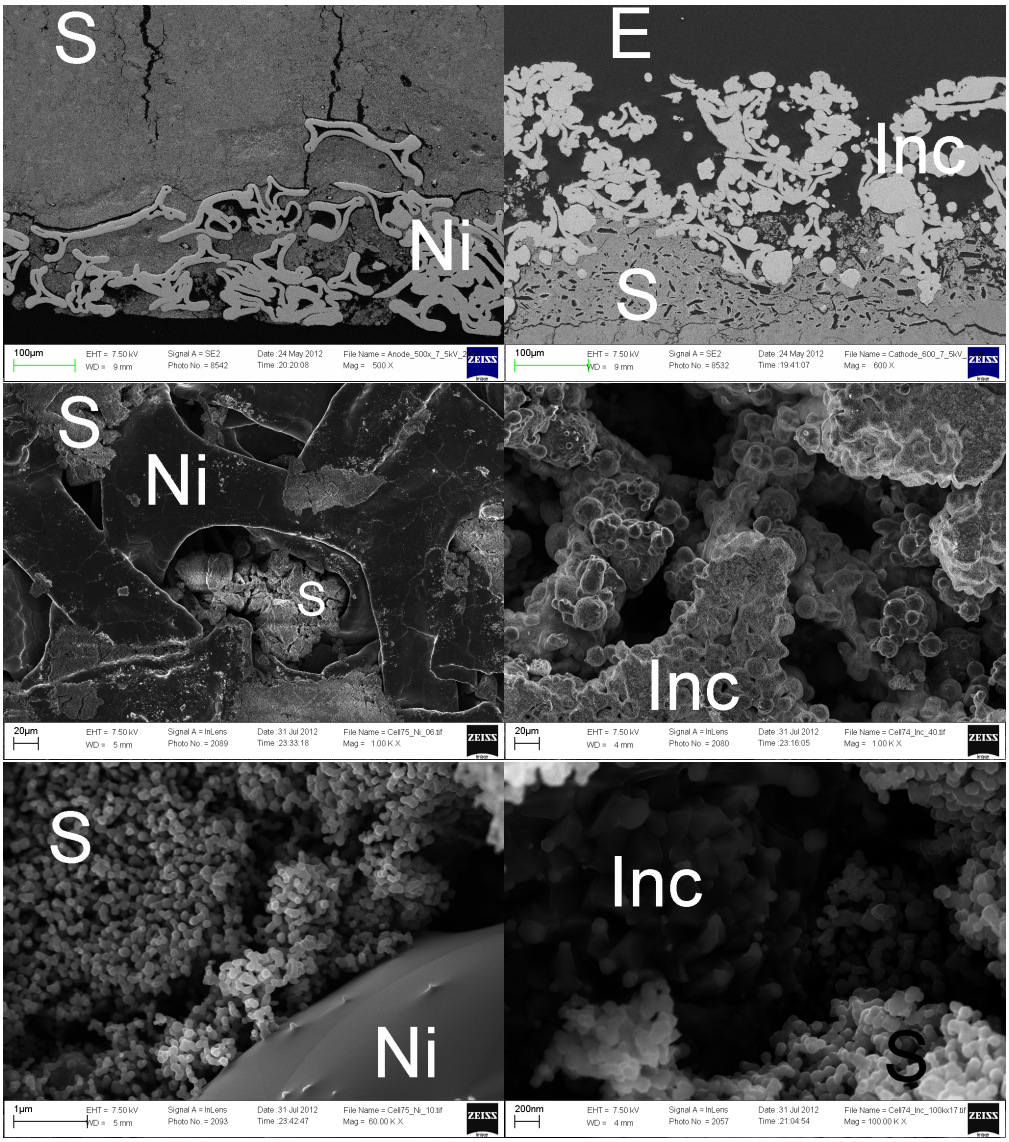

Figure 6.8: SEM images of the the nickel (Ni), Inconel (Inc) and $SrTiO_3$ (S) interface. Upper row: Cross-section of the electrodes of a FobAEC showing the nickel foam and the Inconel structure in contact with SrTiO3 (The dark structure E shows epoxy used for sample fixation in the microscope). Middle row: top view of the nickel foam anode (left) facing the electrolyte structure and the Inconel foam cathode (right). Lower row: detailed picture of the electrode electrolyte interface before soaking in KOH (aq) of the nickel foam (left) and the Inconel foam (right).

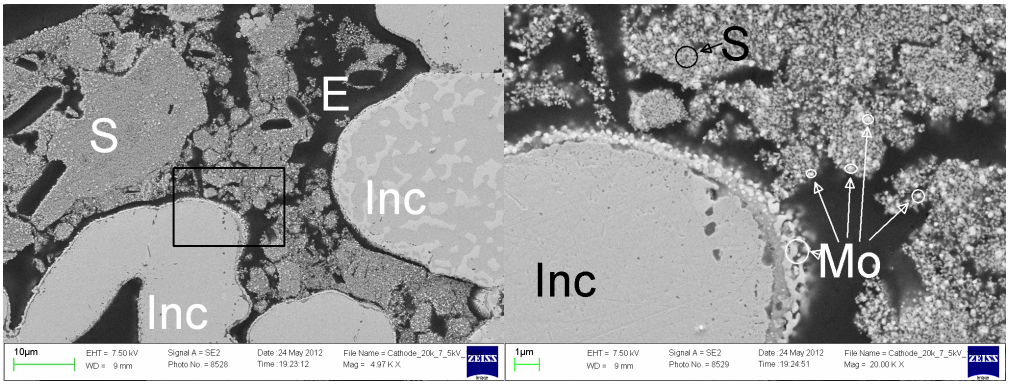

Figure 6.9: SEM picture of the cross section of the FobAECs cathode showing the interface between the Inconel foam (Inc) and the $SrTiO_3$ (S) structure with Mo particles with a size of 100 nm - 200 nm and Mo layers distributed along the TPB. E is epoxy for microscopy purposes and not of relevance.

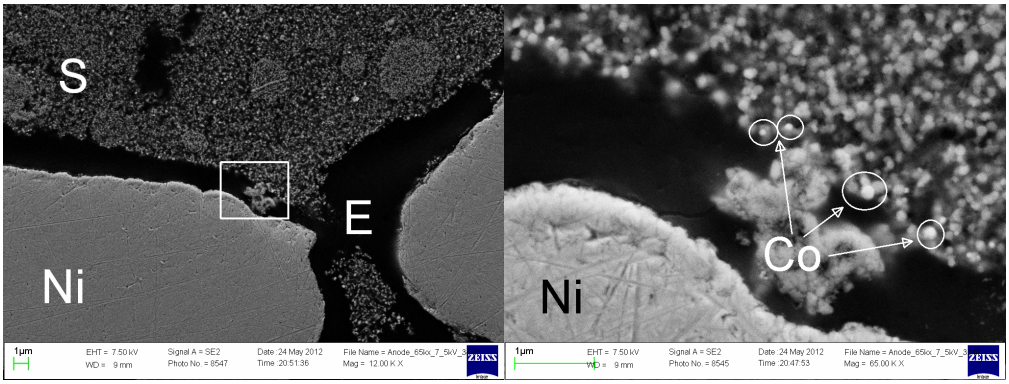

Figure 6.10: SEM picture of the interface between the cross section of the FobAECs anode showing the nickel foam (Ni) and the $SrTiO_3$ structure with Co particles distributed along the TPB.

6.4.4 *Cell performance at 150 °C*

Impedance plots that have been obtained from t_0 + 3h until t_0 + 21 h at 150 °C are shown in figure 6.11 for two similar cells produced after the method described in the experimental section (6.3.1). The cell performance obtained after heating the autoclave to 150 °C and a pressure of 40 bar showed an initial serial resistance R_s of 220 $m\Omega\,cm^2$ for the first of the investigated cells (cell 68) and 221 $m\Omega\,cm^2$ for the second (cell 69). It increased to 244 $m\Omega\,cm^2$ after a measurement time of 18h for cell 68 and to 276 $m\Omega\,cm^2$ for cell 69. The area specific resistance ASR increased more drastically from 534 $m\Omega\,cm^2$ and 431 $m\Omega\,cm^2$ to 919 $m\Omega\,cm^2$ and 858 $m\Omega\,cm^2$ for cell 68 and 69, respectively. Furthermore it can be seen that the degradation was faster in the first 10 h than thereafter. The iV-curves taken at t_0 + 4h, t_0 + 12 h and t_0 +20 h are shown in figure 6.12.

The current densities obtained at 1.75 V from the cyclic voltammetry measurements started at 725 $mA\,cm^{-2}$ and 920 $mA\,cm^{-2}$ at the beginning of the measurements (t_0 + 4 h) for cell 68 and cell 69, respectively. For cell 68 it decreased to 545 $mA\,cm^{-2}$ at t_0 + 12h and to 490 $mA\,cm^{-2}$ at t_0 + 20 h. For cell 69 it decreased from 595 $mA\,cm^{-2}$ to 570 $mA\,cm^{-2}$ in the same interval as can be seen in figure 6.12. The same figure indicates that the OCV decreased from 955 mV at the beginning of the measurements to 334 mV for cell 68 and 339 mV for cell 69.

The relatively fast degradation which occurred for both cells until t_0 +21 h of the measurement at 150 °C, stabilized at t_0 +24 h of measurement time. The R_s stabilized at 237 $m\Omega\,cm^2$ for cell 68 and 263 $m\Omega\,cm^2$ for cell 69 while the ASR stabilized at 793 $m\Omega\,cm^2$ for cell 68 and 815 $m\Omega\,cm^2$ for cell 69 as can be seen in figure 6.13. It should be noted that the gas composition was changed at t_0 +18 h towards a more reducing atmosphere and a higher inert gas flow rate (compare figure 6.5 and figure 6.6).

Figure 6.14 shows the iV curves recorded in the period t_0+24 h to t_0+38 h. Cell 68 showed stable current density of 590 $mA\,cm^{-2}$ at 1.75 V while for cell 69 the current density at 1.75 V decreased from 690 $mA\,cm^{-2}$ at t_0+24 h to 633 $mA\,cm^{-2}$ at t_0+38 h after the measurement started. The OCP increased during this time from 800 mV to 885 mV for cell 68 and from 792 mV to 885 mV for cell 69. The gas composition was changed at t_0 +27 h again towards a more reducing atmosphere (compare figure 6.5 and figure 6.6).

6.4.5 *Cell performance at 200 °C*

6.4.5.1 *Heating from 150 °C to 200 °C*

The development of the impedance during heating from 150 °C to 200 °C can be seen in figure 6.15. The R_s decreased from 237 $m\Omega\,cm^2$ to 189 $m\Omega\,cm^2$ after heating to 200 °C for cell 68 and decreased from 270 $m\Omega\,cm^2$ to 174 $m\Omega\,cm^2$

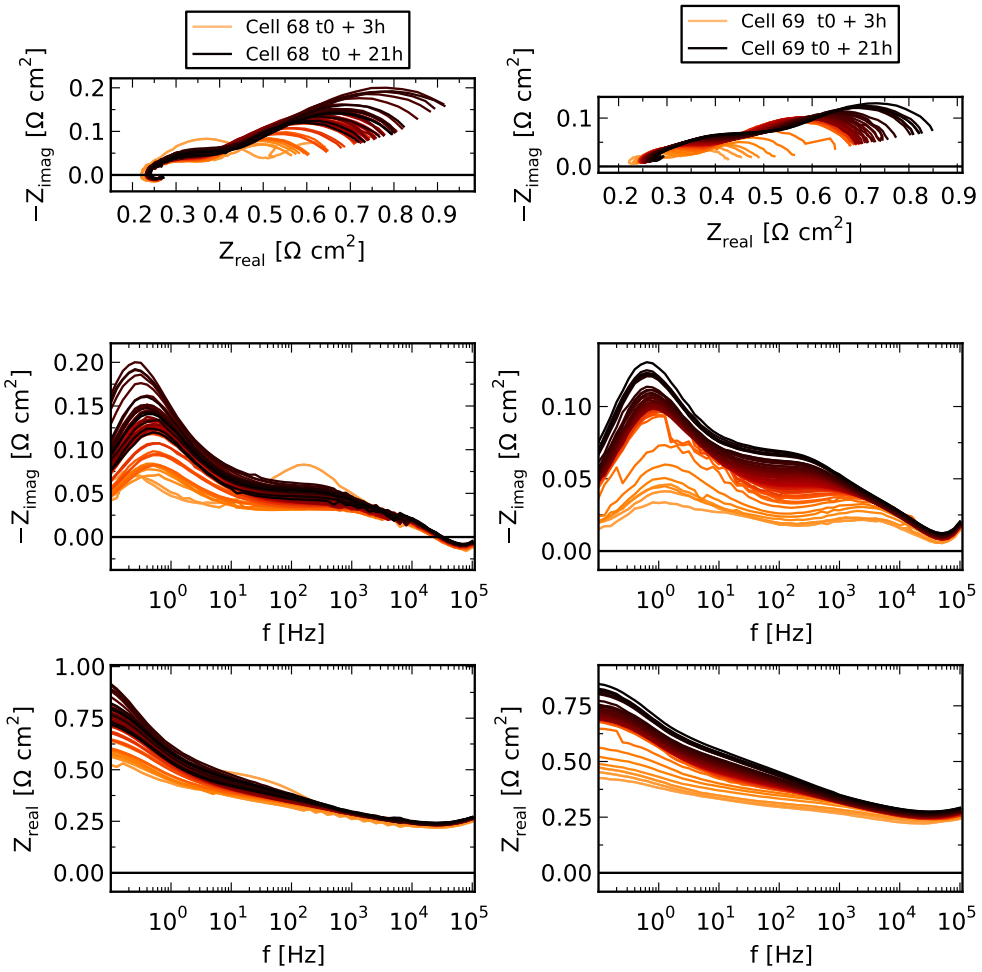

Figure 6.11: EIS curves at a polarization of 1.5 V of cell 68 (left) and cell 69 (right) showing the impedance in the Nyquist plot (top), $-Z_{img}$ vs. f (middle) and Z_{real} vs. f (bottom) during the first 18 h at 150 °C. The measurement interval was 20 min for each cell.

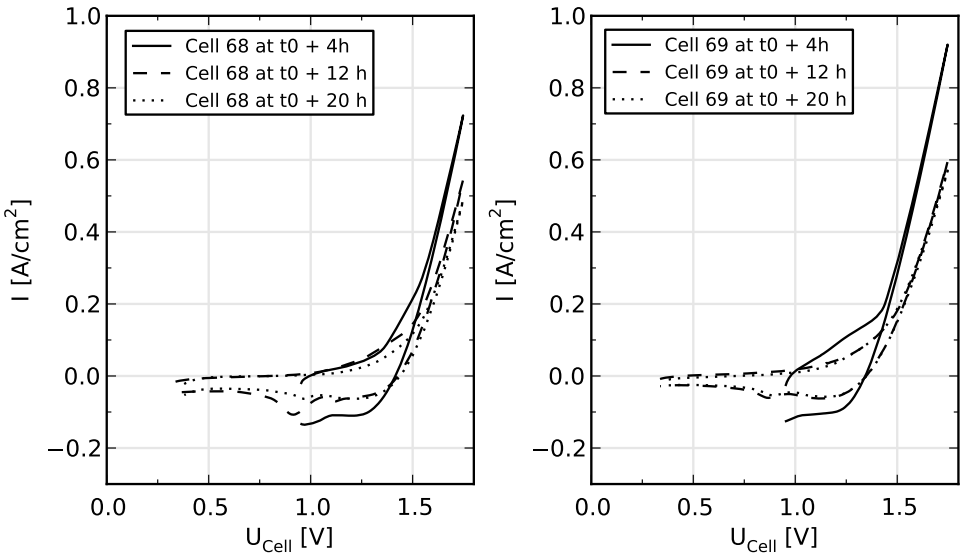

Figure 6.12: iV-curves of cell 68 (left) and cell 69 (right) after 4 h, 12 h and 20 h at 150 °C.

for cell 69. The ASR increased from 725 $m\Omega\,cm^2$ before heating to 900 $m\Omega\,cm^2$, but improved to 421 $m\Omega\,cm^2$ after heating to 200 °C for cell 68. Cell 69 showed a comparable behavior; ASR increased from 670 $m\Omega\,cm^2$ before heating to 770 $m\Omega\,cm^2$, but improved to 372 $m\Omega\,cm^2$ after heating .

Performance at 200 °C

Impedance measurements at a constant temperature of 200 °C and a pressure of 40 bar are shown in figure 6.16. The measurement sequence was started at t_0 + 73 h and was performed for 12 h. The results during this period was rather stable, the R_s increased from 202 $m\Omega\,cm^2$ to 212 $m\Omega\,cm^2$ for cell 68 and from 179 $m\Omega\,cm^2$ to 192 $m\Omega\,cm^2$ for cell 69. The ASR of cell 68 varied between 431 $m\Omega\,cm^2$ and 478 $m\Omega\,cm^2$ with no obvious trend while it increased from 390 $m\Omega\,cm^2$ to 418 $m\Omega\,cm^2$ for cell 69.

Figure 6.17 shows the iV curves that were recorded during the same period (t_0+73 h - t_0+85 h) at 200 °C. The obtained current density for cell 68 decreased slightly from 985 $mA\,cm^{-2}$ to 960 $mA\,cm^{-2}$ at 1.75 V while for cell 69 it decreased from 1069 $mA\,cm^{-2}$ to 1029 $mA\,cm^{-2}$. The OCV increased during this time from 1010 mV to 1045 mV for both cells.

6.4.6 *Cell performance at 250 °C*

After potentiostatic tests at a temperature of 200 °C, as shown later in section 6.4.7.1, impedance measurements at a constant temperature of 250 °C and a pressure of 40 bar were performed and are shown in figure 6.18. The measurement sequence was started 145 h after the entire measurement started

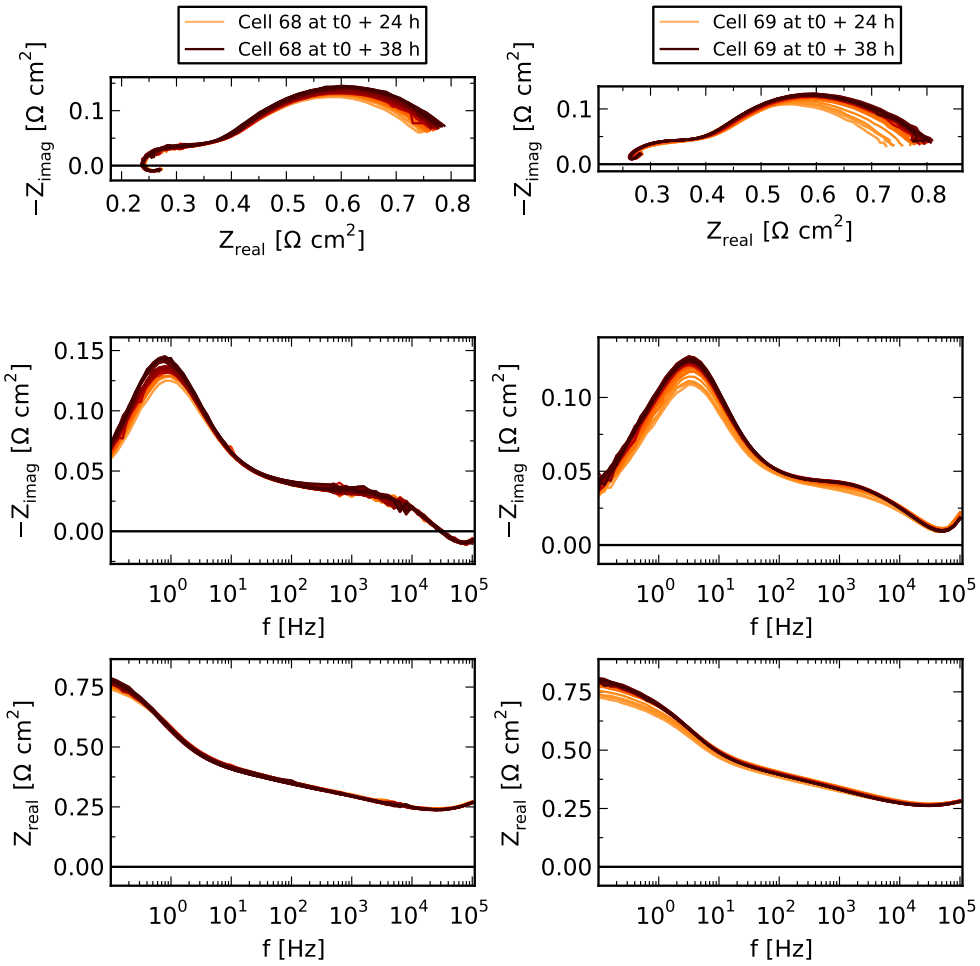

Figure 6.13: EIS curves of cell 68 (left) and cell 69 (right) at a polarization of 1.5 V, showing the impedance in the Nyquist plot (top), $-Z_{img}$ vs. f (middle) and Z_{real} vs. f (bottom) during 14 h at 150 °C, started at t_0+24 h and ending at t_0+38 h. The measurement interval was 20 min for each cell.

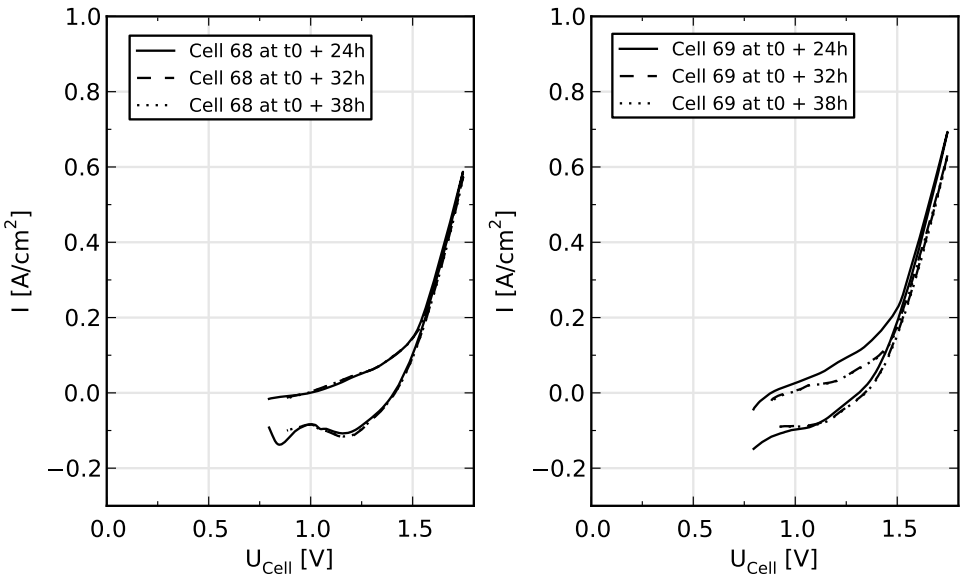

Figure 6.14: iV curves of cell 68 (left) and cell 69 (right) during 14 h at 150 °C and 40 bar, started at t_0+24 h and ending at t_0+38 h.

and was performed for 9 h. The R_s decreased initially from 150 mΩ cm^2 to 133 mΩ cm^2, before it increased again to 153 mΩ cm^2 for cell 68. For cell 69 R_s increased from 130 mΩ cm^2 to 191 mΩ cm^2. The ASR for cell 68 varied between 215 mΩ cm^2 and 234 mΩ cm^2, while it increased from 236 mΩ cm^2 to 327 mΩ cm^2 for cell 69.

Figure 6.19 shows the current densities recorded at 250 °C at t_0+147 h, t_0+150 h and t_0+153 h. The obtained current density for cell 68 decreased from a value of 2.29 A cm^{-2} to 2.03 A cm^{-2} at 1.75 V. It can also be seen that a second peak occurred at 520 mV for the iV curve of cell 68 147 h after t_0. The peak reduced its current density from 900 mA cm^{-2} to 825 mA cm^{-2} to 518 mA cm^{-2} while the peak voltages was reduced from 512 mV to 480 mV to 418 mV for the time of 147 h, 150 h, and 153 h after t_0, respectively. Cell 69 showed 2.23 A cm^{-2} at the beginning of the sequence with a relatively fast degradation resulting in a reduced current density of 1.51 A cm^{-2} 6 h after the sequence started. The OCV increased from 50 mV to 70 mV for cell 68 as well as for cell 69.

6.4.7 *Potentiostatic tests*

6.4.7.1 *Chronoamperometry at 200 °C*

Figure 6.20 shows the results of a potentiostatic step function started 70 h after t_0 for cell 68 (left image) and 71.5 h after t_0 for cell 69 (right image) with applied cell voltages of 1.5 V, 1.625 V and 1.75 V and a step time of 20 min at each cell voltage. Cell 68 showed a relatively stable current density of 322 mA cm^{-2}, 582 mA cm^{-2} and 830 mA cm^{-2} at 1.5 V, 1.625 V and 1.75 V, respectively, after an initial deactivation as can be seen in the upper left image of figure 6.20.

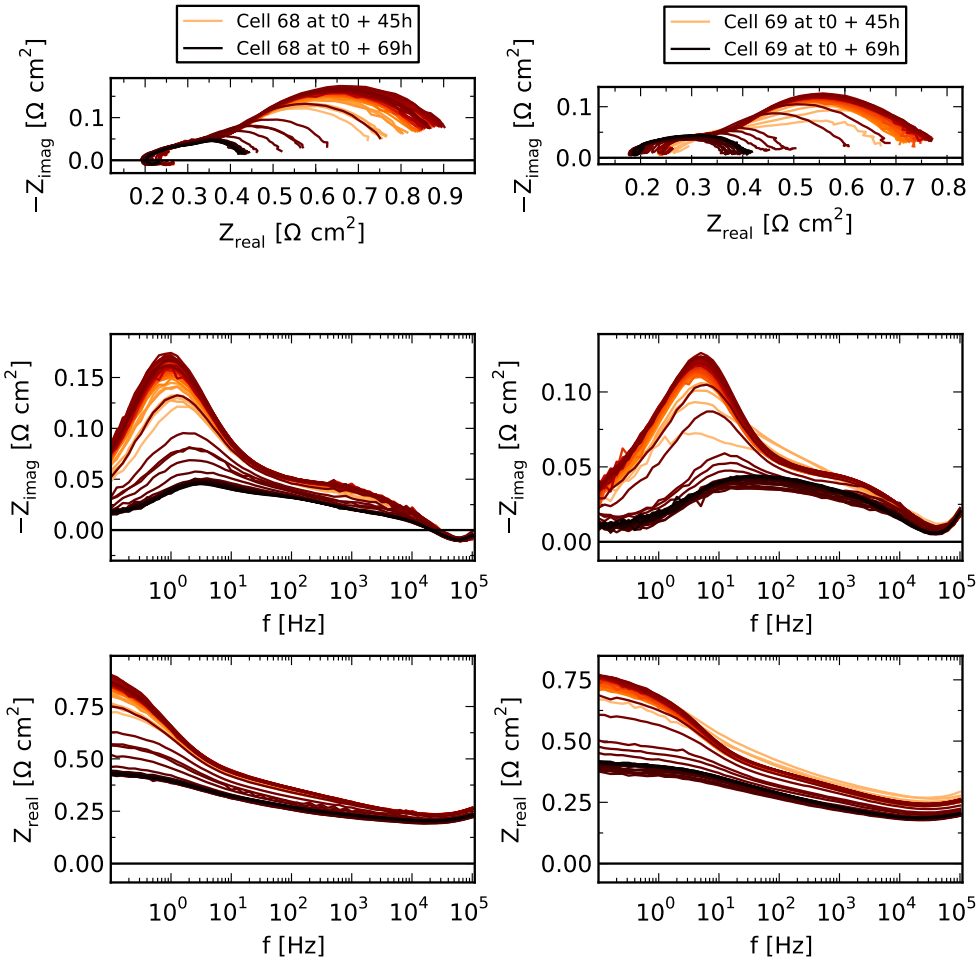

Figure 6.15: EIS curves of the two tested cells at a polarization of 1.5 V during heating from 150 °C to 200 °C started at t_0+45 h and ending at t_0+69 h. The measurement interval was 20 min for each cell.

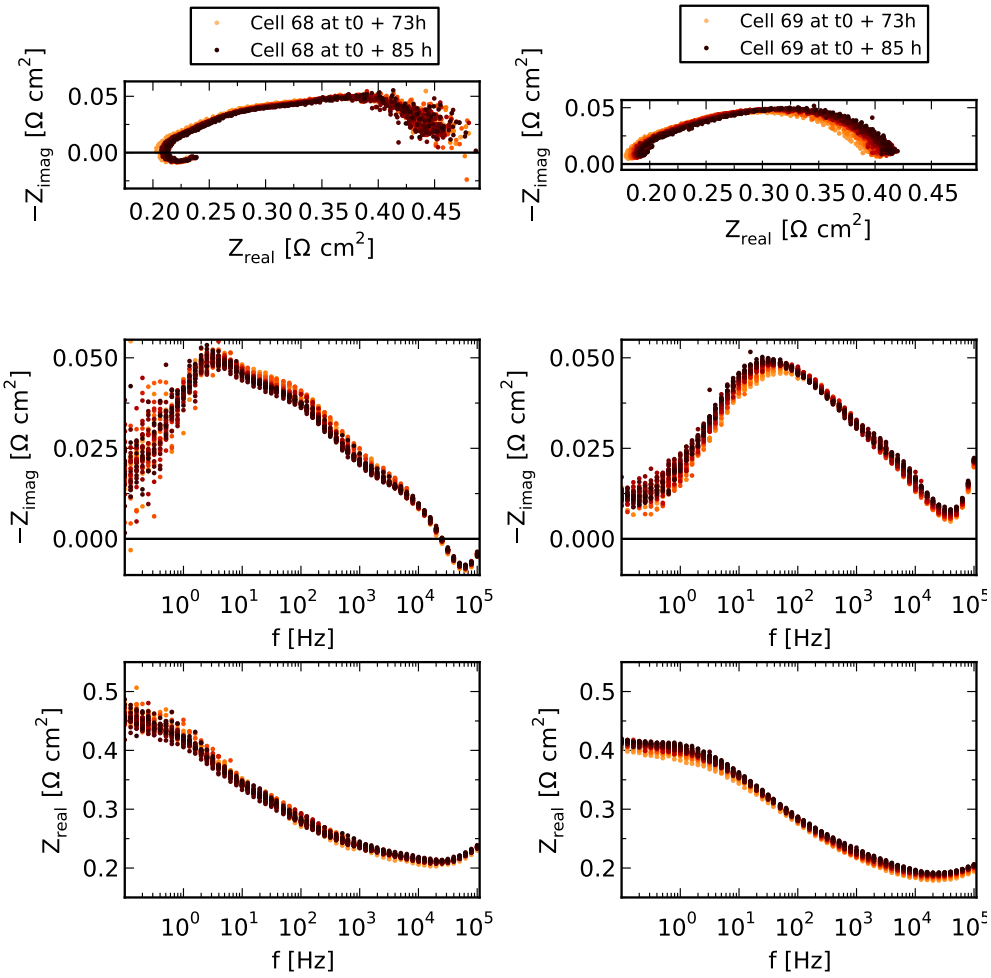

Figure 6.16: EIS curves at a polarization of 1.5 V of the two tested cells at 200 °C, started at t_0+73 h and ending at t_0+85 h. The measurement interval was 20 min for each cell.

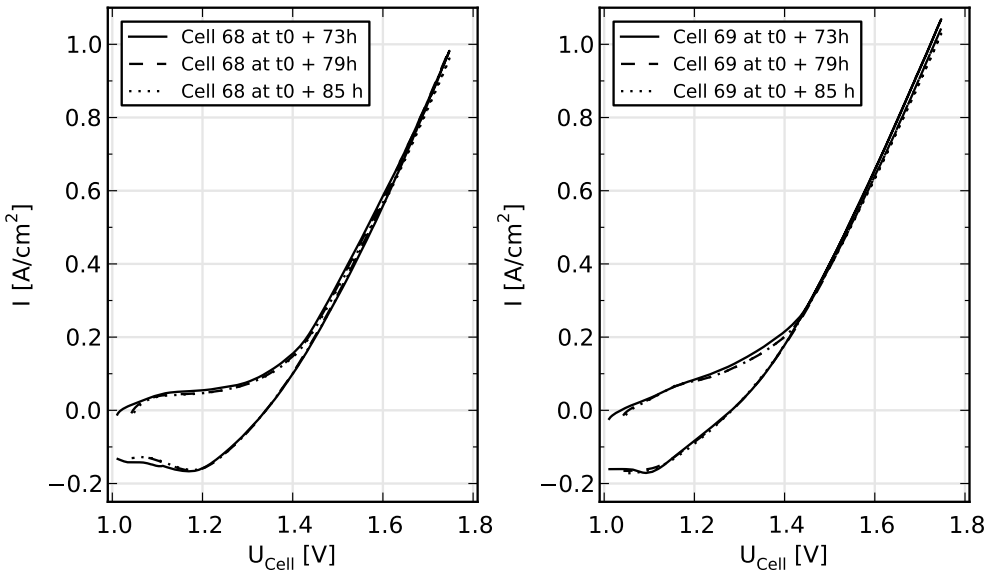

Figure 6.17: iV curves of the two tested cells at 200 °C and 40 bar, started at t_0+73 h and ending at t_0+85 h.

Cell 69 showed slightly higher values of 379 mA cm^{-2}, 625 mA cm^{-2} and 943 mA cm^{-2} at 1.5 V, 1.625 V and 1.75 V, respectively, as can be seen in the upper right image of figure 6.20.

A Nyquist plot of the impedance of cell 68 and cell 69 is shown on the lower left and lower right image of figure 6.20, respectively, recorded at a polarization of 1.75 V directly before (o) and after (x) the potentiostatic test. The R_s increased from 200 mΩ cm^2 to 220 mΩ cm^2 for cell 68 and from 194 mΩ cm^2 to 212 mΩ cm^2 for cell 69. The area specific resistance ASR increased from 335 mΩ cm^2 to 385 mΩ cm^2 for cell 68 and from 332 mΩ cm^2 to 351 mΩ cm^2 for cell 69.

The open circuit voltage OCV after the chronoamperometric measurement shown in figure 6.20, recorded directly after the last step of the step function, is shown in figure 6.21. The OCV decreased within 120 s from 1.35 V to 1.2 V for cell 68 and from 1.29 V to 0.80 V for cell 69. It should be mentioned here that there was no continuous O_2 support to the anode and reduction of the OCV is natural. The reduction of the OCV will be further analyzed in the discussion.

6.4.7.2 *Chronoamperometry for 24 h at 200 °C*

A following chronoamperometric measurement on cell 68 started at t_0 + 85 h for 24 h at 1.5 V and 20 min at 1.625 V and 1.75 V. The potentiostatic measurement at 1.5 V applied cell voltage, as shown in the upper part of figure 6.22, showed a stable current density of ca. 320 mA cm^{-2}, the current densities at 1.625 V and 1.75 V were 568 mA cm^{-2} and 848 mA cm^{-2}, respectively, at the end of the 20 min lasting steps. The R_s increased from 210 mΩ cm^2 to

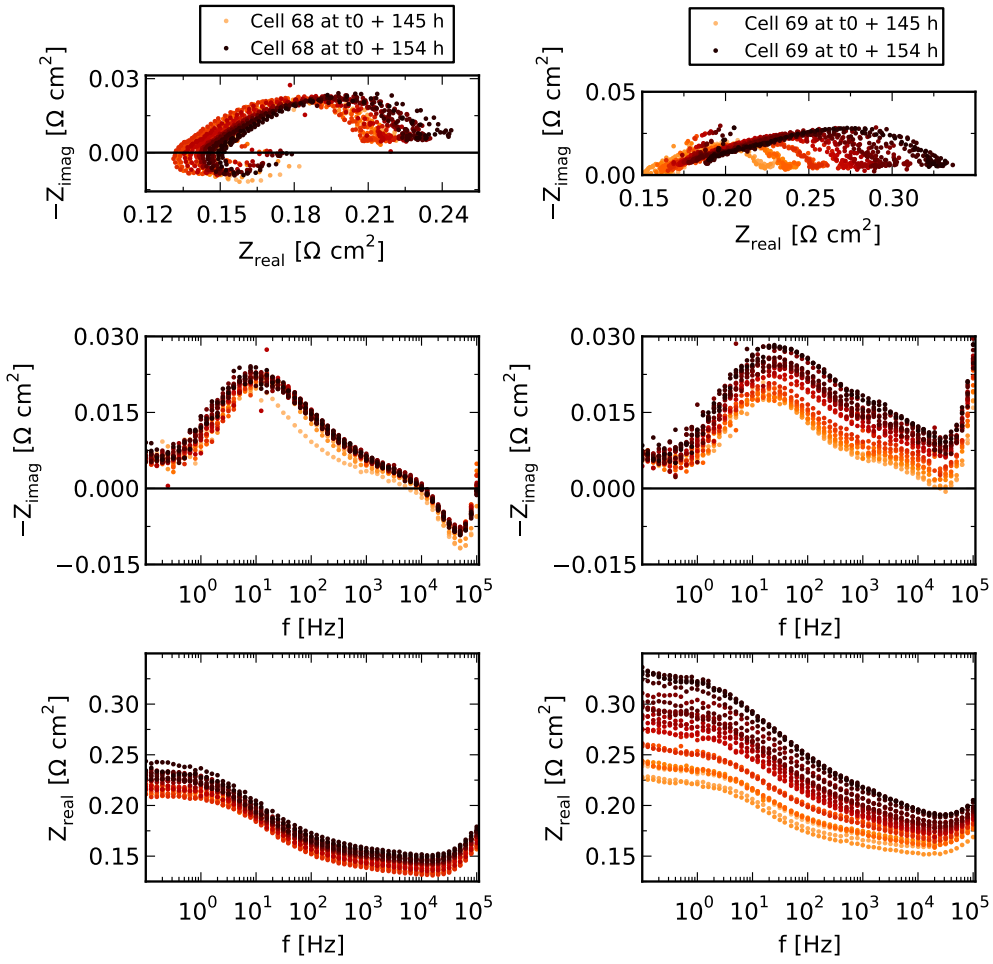

Figure 6.18: EIS curves of the two tested cells at 250 °C, started at t_0+145 h and ending at t_0+153 h. The measurement interval was 20 min for each cell.

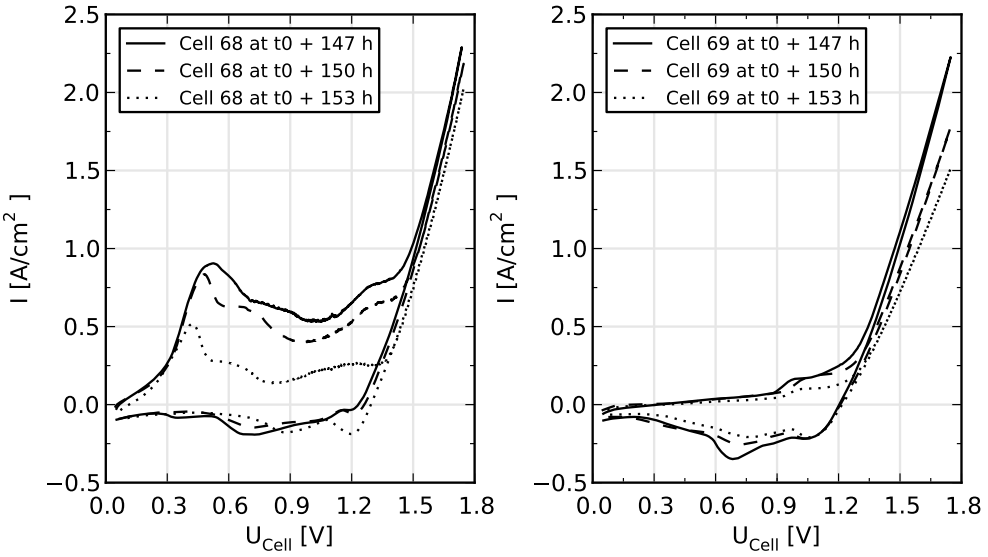

Figure 6.19: iV curves of the two tested cells at 250 °C started at t_0+147 h and ending at t_0+153 h.

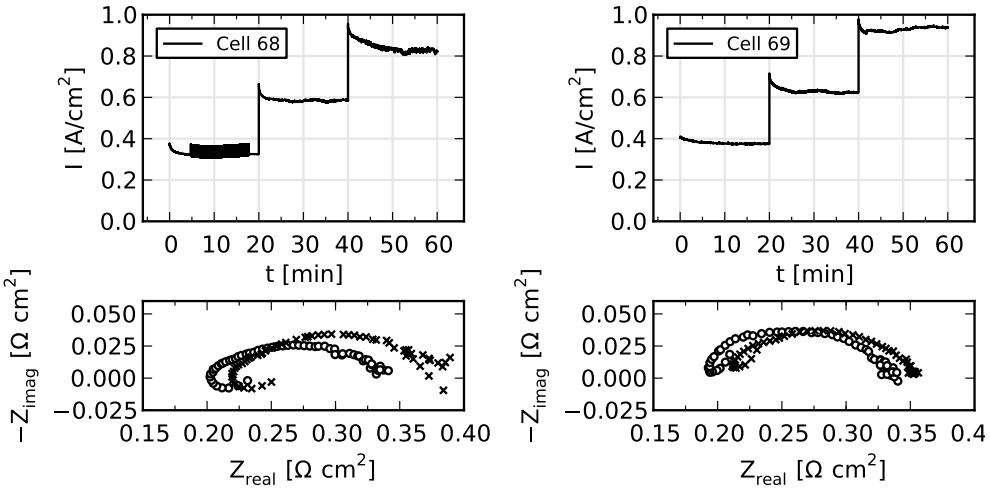

Figure 6.20: Chronoamperometric scan of cell 68 (left) and cell 69 (right) at 200 °C and 40 bar and a step function for the applied cell voltage of 1.5V, 1.625 V and 1.75 V for a time of 20 min/ step started at t_0 +70 h (upper left) and t_0 + 71.5 h (upper right) with the corresponding impedance plots at a polarization of 1.75 V before and after the chronoamperometric scan below.

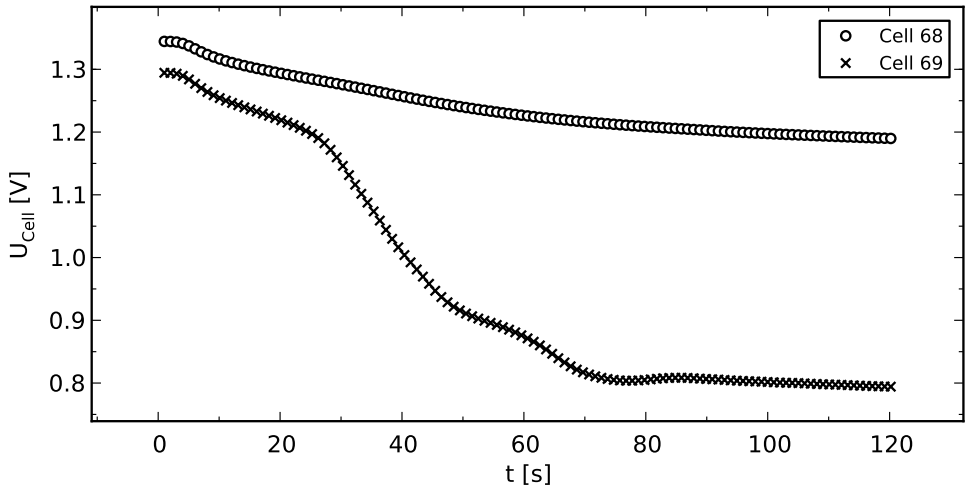

Figure 6.21: Open circuit voltage recorded after the chronoamperometric measurement shown in figure 6.20 for cell 68 (o) and cell 69 (x).

237 mΩ cm^2, and the ASR from 457 mΩ cm^2 to 512 mΩ cm^2 before (o) and after (x) the measurement as shown in the lower part of figure 6.22.

6.4.7.3 *Chronoamperometry at 250 °C and 40 bar*

Further chronoamperometric scans were performed at 250 °C and 40 bar for cell 68 and cell 69 as shown in figure 6.23. The applied cell voltage was 1.5 V, 1.625 V and 1.75 V with a step time of 60 min at 1.5 V and 2 min for 1.625 V and 1.75 V. The measurement started at t_0 +142 h for cell 68 (upper left image) at t_0+144 h for cell 69 (upper right image). Cell 68 showed slightly increasing current density from 720 mA cm^{-2} to 814 mA cm^{-2} at 1.5 V. At 1.625 V an initial peak of 1.43 A cm^{-2} was observed before the current stabilized at 1.34 A cm^{-2}. At 1.75 V only an initial peak of 2.02 A cm^{-2} was measured due to a current overload protection in the potentiostat which stopped the measurement on this cell.

Cell 69 showed slightly increasing current density from 950 mA cm^{-2} to 1.05 A cm^{-2} after an initial peak of 1.11 A cm^{-2} at 1.5 V. At 1.625 V an initial peak of 1.67 A cm^{-2} was measured, decreasing to 1.52 A cm^{-2} while at 1.75 V an initial peak current of 2.13 A cm^{-2} was measured, decreasing to 1.98 A cm^{-2}.

The impedance plot of cell 68 is shown in the lower left image of figure 6.23 recorded at a polarization of 1.5 V directly before and after the potentiostatic test. The R_s improved from 157 mΩ cm^2 to 153 mΩ cm^2, and the ASR was found to be constant at 241 mΩ cm^2. Thus, the R_p increased from 84 mΩ cm^2 to 88 mΩ cm^2.

The impedance analysis of cell 69 is shown on the lower right image of figure 6.23 recorded at a polarization of 1.5 V directly before and after the potentiostatic test. The R_s increased from 156 mΩ cm^2 to 162 mΩ cm^2, and the ASR

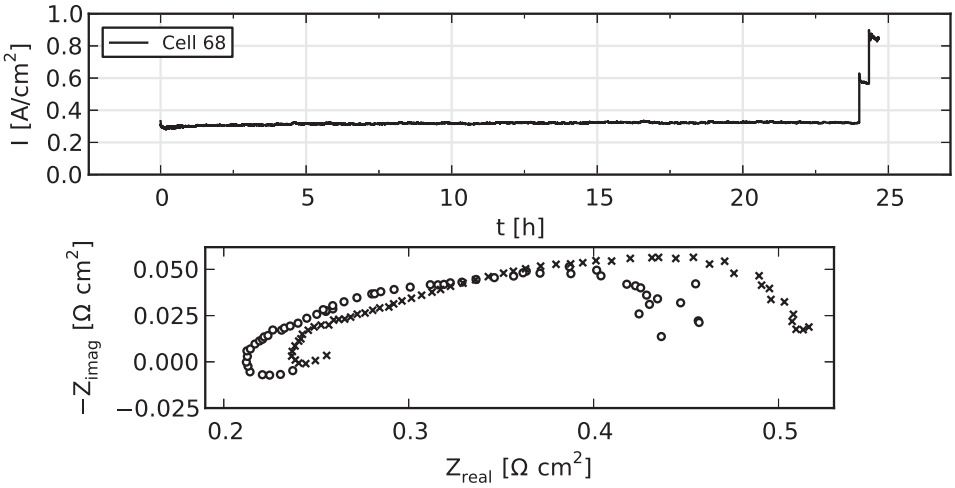

Figure 6.22: Chronoamperometric scan of cell 68 at 200 °C and 40 bar and a step function for the applied cell voltage of 1.5 V, 1.625 V and 1.75 V for a time of 24 h at 1.5 V and 20 min/ step at 1.625 V and 1.75 V started at t_0 +85 h with the corresponding impedance plots at a polarization of 1.5 V before (o) and after (x) the chronoamperometric scan.

was found to be 227 $m\Omega\,cm^2$ before and 242 $m\Omega\,cm^2$ after the measurement, so the R_p increased from 71 $m\Omega\,cm^2$ to 80 $m\Omega\,cm^2$.

The open circuit voltage OCV for the chronoamperometric measurement shown in figure 6.23, recorded directly after the last step of the step function, is shown in figure 6.24. The OCV fell within 120 s from 1.27 V to 1.02 V for cell 68 and from 1.24 V to 0.97 V for cell 69.

6.4.7.4 *Chronoamperometry for 100 h at 250 °C and 40 bar*

A 100 h lasting chronoamperometric scan was performed at t_0 + 155 h, at an applied cell voltage of 1.5 V on cell 69. Results are presented in the upper part of figure 6.25. The current density was 670 $mA\,cm^{-2}$ at the beginning of the measurement, decreased rapidly to 520 $mA\,cm^{-2}$ within 5h (30 $mA\,cm^{-2}\,h^{-1}$).The current density reduced by 5 $mA\,cm^{-2}\,h^{-1}$ to 450 $mA\,cm^{-2}$ during the following 9.0 h. After 14 h of measurement time, at t_0 + 169 h, the degradation stopped for a period of 6 h after increasing pH_2O to 18.7 bar (compare figure 7.1), but resumed to degrade with reduced degradation rate (2.2 $mA\,cm^{-2}\,h^{-1}$) to 304 $mA\,cm^{-2}$ after 100 h.

Impedance measurements have been performed before and after the chronoamperometric test and are shown in figure 6.25 in the Nyquist (center) and Bode plane (lower). The R_s increased from 190 $m\Omega\,cm^2$ to 572 $m\Omega\,cm^2$, and the ASR was found to be 350 $m\Omega\,cm^2$ before and 1.2 $\Omega\,cm^2$ after the measurement, so the R_p increased from 160 $m\Omega\,cm^2$ to 628 $m\Omega\,cm^2$.

The open circuit voltage OCV for the chronoamperometric measurement shown in figure 6.25, recorded directly after the last step of the step function, is

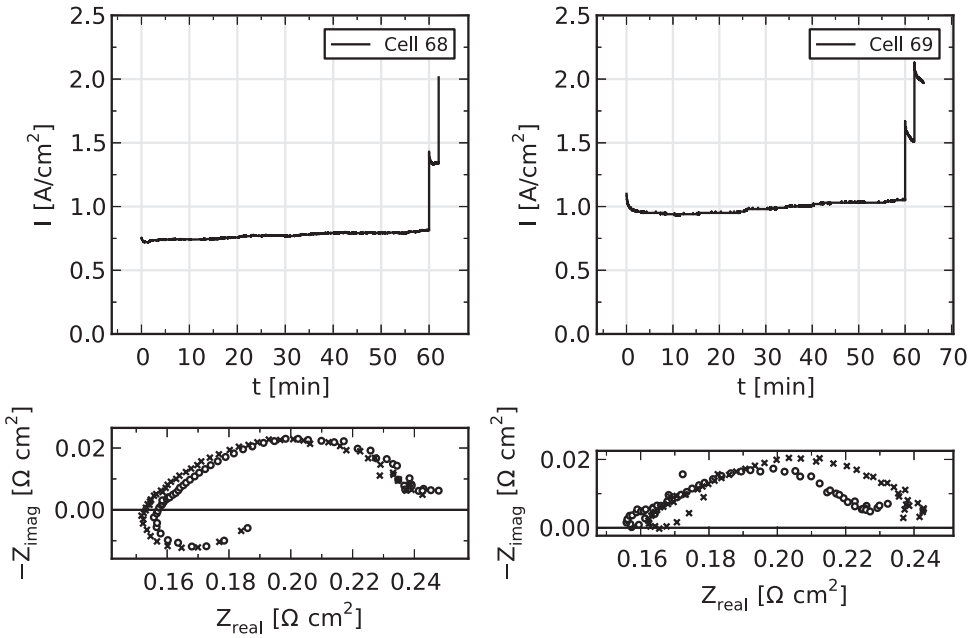

Figure 6.23: Chronoamperometric scan of Cell 68 started at t_0+142 h (left) and cell 69 started at t_0+144 h (right) at 250 °C and 40 bar at 1.5 V for 60 min, 1.625 and 1.75 V for 2 min/ step with the corresponding impedance plots at a polarization of 1.5 V before (o) and after (x) the chronoamperometric scan below.

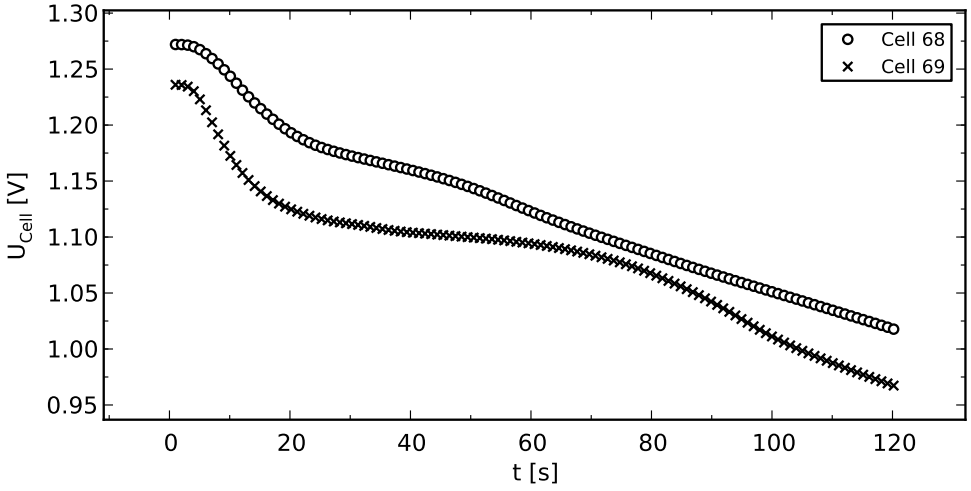

Figure 6.24: Open circuit voltage recorded after the chronoamperometric measurement shown in figure 6.23 for cell 68 (o) and cell 69 (x).

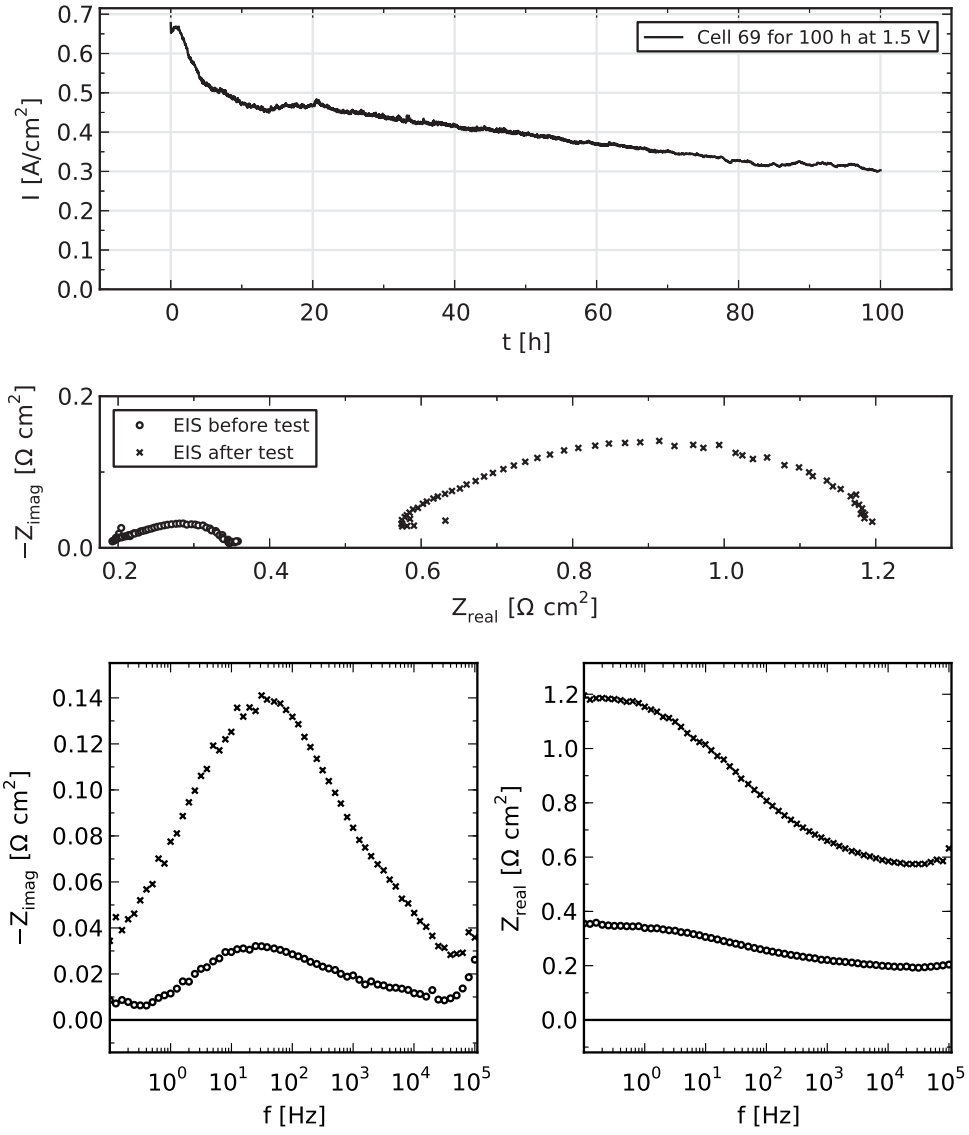

Figure 6.25: Chronoamperometric scan of Cell 69 at 250 °C and 40 bar at an applied cell voltage of 1.5 V for 100 h started at t_0+155 h (upper figure) with the corresponding impedance plots at a polarization of 1.5 V before (o) and after (x) the chronoamperometric scan in the Nyquist (middle) and Bode (lower) view.

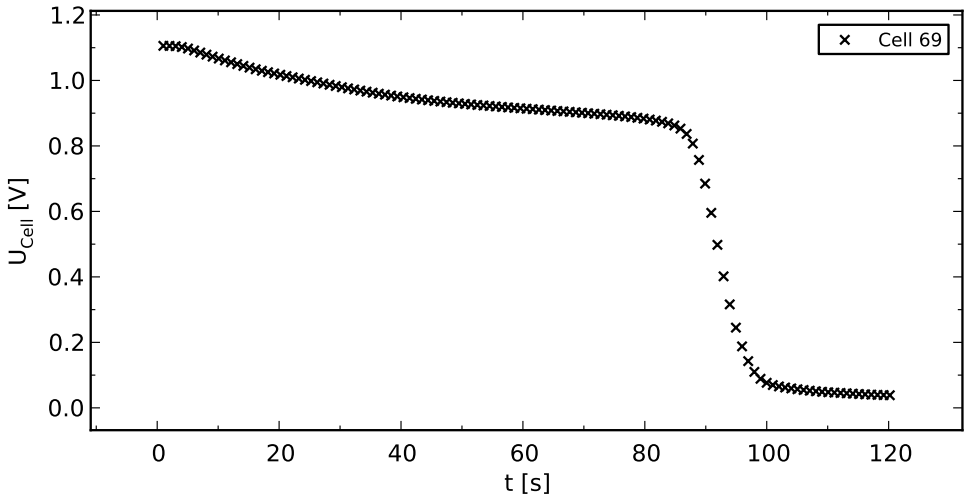

Figure 6.26: Open circuit voltage recorded after the chronoamperometric measurement shown in figure 6.25 for cell 69.

shown in figure 6.26. The OCV dropped non-linearly within 120 s from 1.11 V to 0.04 V; after a period of 85 s the OCV dropped from 0.87 V to 0.08 V within 14 s. The fast decrease of the OCV will be further analyzed in the discussion.

6.4.7.5 *Chronoamperometry for 1 h at 250 °C and 40 bar*

After the 100 h long chronoamperometric scan on cell 69, another chronoamperometric scan was started on cell 68 to examine its performance 258 h after t_0 at an applied cell voltage of 1.5 V, 1.625 V and 1.75 V with a step time of 20 min . The results of this measurement are presented in the upper part of figure 6.27. The current density increased continuously after an initial decrease at every potential step. At 1.5 V it increased from 308 $mA\,cm^{-2}$ to 508 $mA\,cm^{-2}$, at 1.625 V it increased from 728 $mA\,cm^{-2}$ to 1.25 $A\,cm^{-2}$ and at 1.75 V it increased from 1.63 $A\,cm^{-2}$ to 1.81 $A\,cm^{-2}$.

Impedance measurements were performed before and after the chronoamperometric test and are shown in figure 6.27 in the Nyquist (center) and and Bode plane (lower). The R_s decreased strongly from from 334 $m\Omega\,cm^2$ to 192 $m\Omega\,cm^2$, the ASR was found to be 600 $m\Omega\,cm^2$ before and 300 $m\Omega\,cm^2$ after the measurement, ant the R_p improved from 294 $m\Omega\,cm^2$ to 108 $m\Omega\,cm^2$.

The open circuit voltage OCV for the chronoamperometric measurement shown in figure 6.27, recorded directly after the last step of the step function, is shown in figure 6.28. The OCV decreased within 120 s from 1.17 V to 0.44 V.

6.4.7.6 *Chronoamperometry for 3 h at 250 °C and 40 bar*

Another test was initiated on cell 68 to see how the performance develops. The test was initiated 264 h after t_0 at an applied cell voltage of 1.5 V for 3 h, and at 1.625 V and 1.75 V for a step time of 2 min. The results of this measurement are presented in the upper part of figure 6.29. After the regularly observed

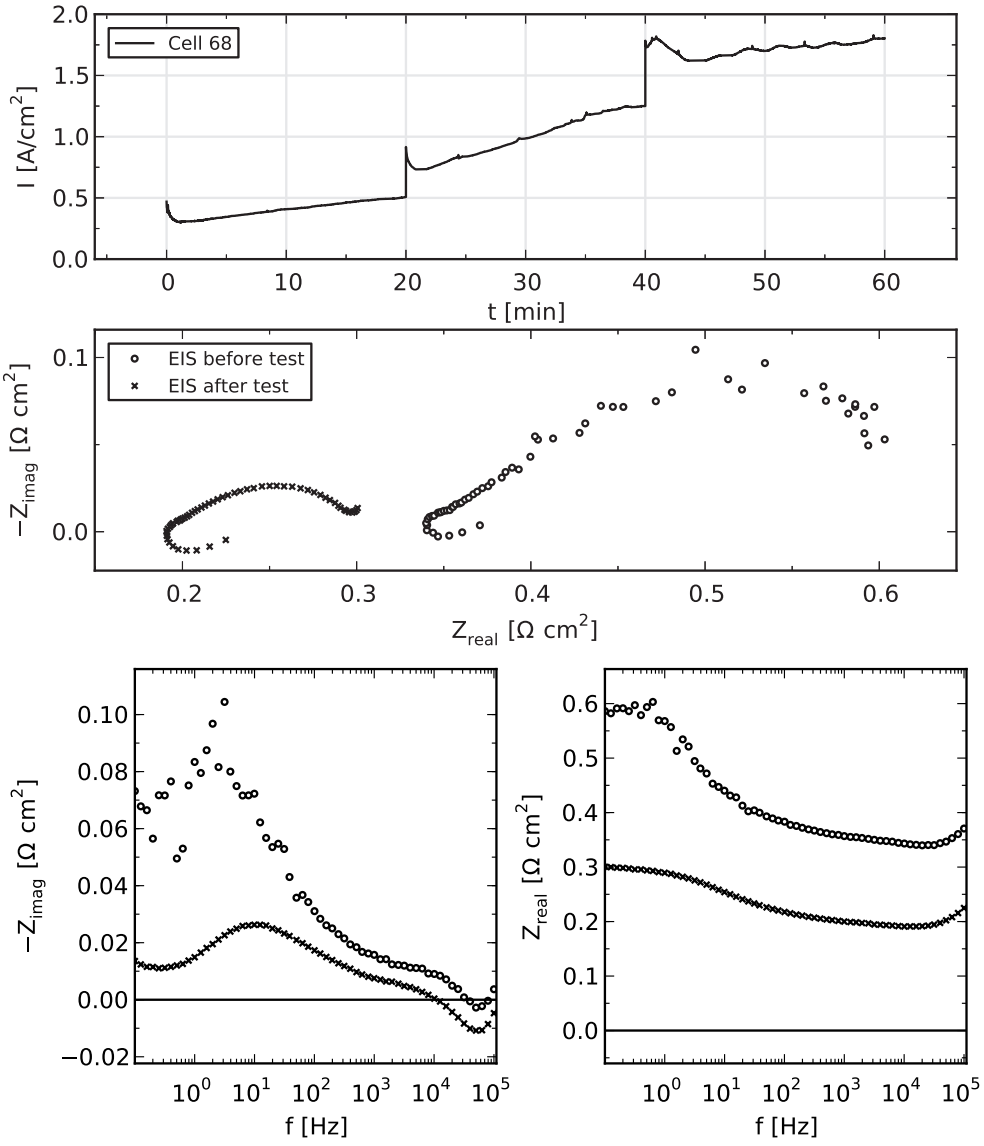

Figure 6.27: Chronoamperometric scan of Cell 68 at 250 °C and 40 bar at an applied cell voltage of 1.5 V, 1.625 V and 1.75 V for a time of 20 min/step, started at t_0+258 h (upper figure) with the corresponding impedance plots at a polarization of 1.5 V before (o) and after (x) the chronoamperometric scan in the Nyquist (middle) and Bode (lower) view.

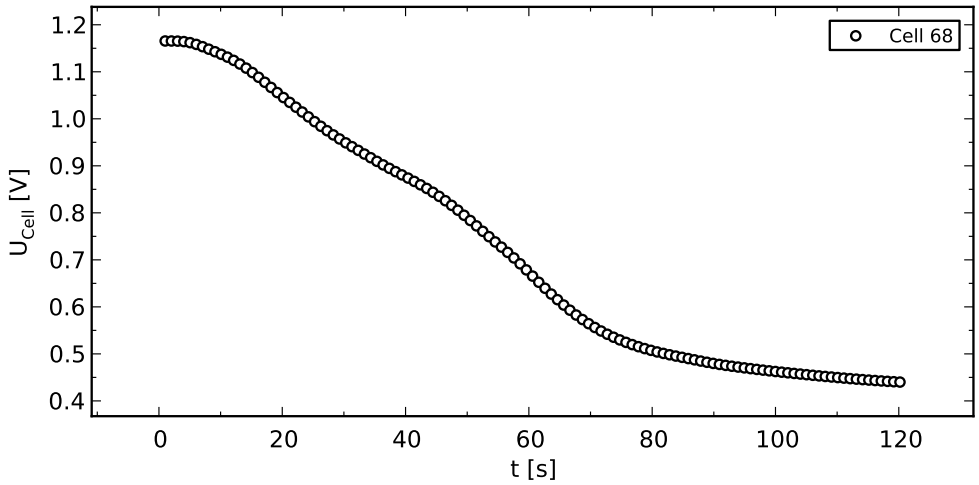

Figure 6.28: Open circuit voltage recorded after the chronoamperometric measurement shown in figure 6.27 for cell 68.

initial decrease, the current density increased at 1.5 V from 675 mA cm^{-2} to 1.05 A cm^{-2}, at 1.625 V it was around 1.60 A cm^{-2} and at 1.75 V it reached a value of 2.30 A cm^{-2}.

Impedance measurements performed before and after the chronoamperometric test are shown in figure 6.29 in the Nyquist (center) and Bode plane (lower). The R_s increased slightly from 191 mΩ cm^2 to 188 mΩ cm^2, the ASR was found to be 297 mΩ cm^2 before and 268 mΩ cm^2 after the measurement, and the R_p improved from 106 mΩ cm^2 to 80 mΩ cm^2.

The open circuit voltage OCV recorded directly after the last step of the chronoamperometric measurement shown in figure 6.29, is shown in figure 6.30. The OCV dropped within during 120 s from 1.21 V to 0.57 V.

6.5 DISCUSSION

6.5.1 *Conductivity of the electrolyte*

The serial resistance R_s decreased with increasing temperature. The corresponding conductivity of the electrolyte, σ_{Cell}, can be calculated by equation 6.4, where $h_{Electrolyte}$ is the thickness of the electrolyte matrix and A_{Cell} is the two dimensional surface area of the cell. In table 6.1 it can be seen how R_s and σ_{Cell} developed with temperature, where $R_{S,min}$ is the minimal value, $R_{S,mean}$ the averaged value for the given period and $R_{S,max}$ is the highest measured value. It should be noted that only the values from the EIS measurements under steady conditions (data from figures 6.13, 6.16 and 6.19) were taken into consideration for the values given in table 6.1. The corresponding conductivities are given in the same table in comparison with the conductivity in a porous matrix, $\sigma_{Cell,ref}$, which is similar to the one used for the immobi-

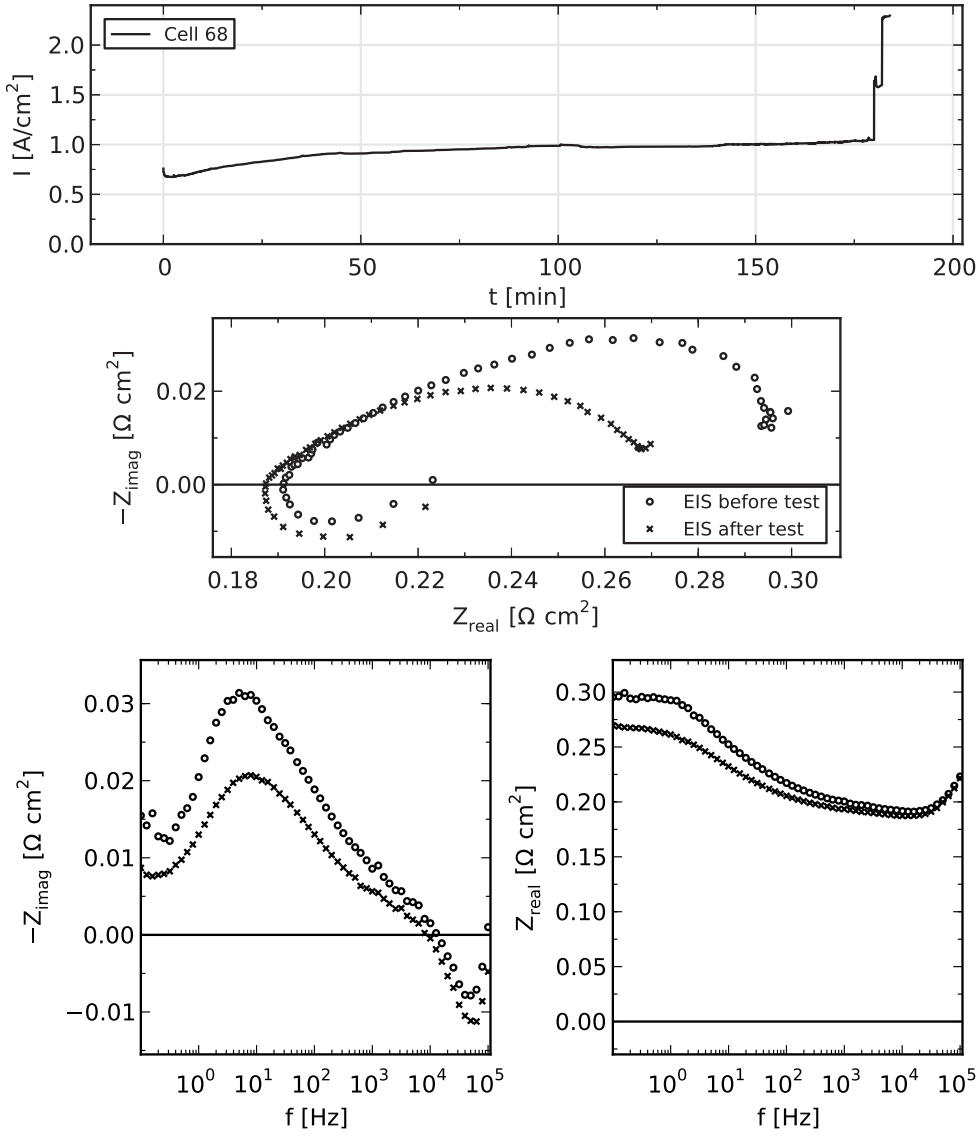

Figure 6.29: Chronoamperometric scan of Cell 68 at 250 °C and 40 bar at 1.5 V for 180 min, 1.625 and 1.75 V for of 2 min/ step, started at t_0+264 h. The corresponding impedance plots at a polarization of 1.5 V before (o) and after (x) the chronoamperometric scan in the Nyquist (middle) and Bode (lower) view.

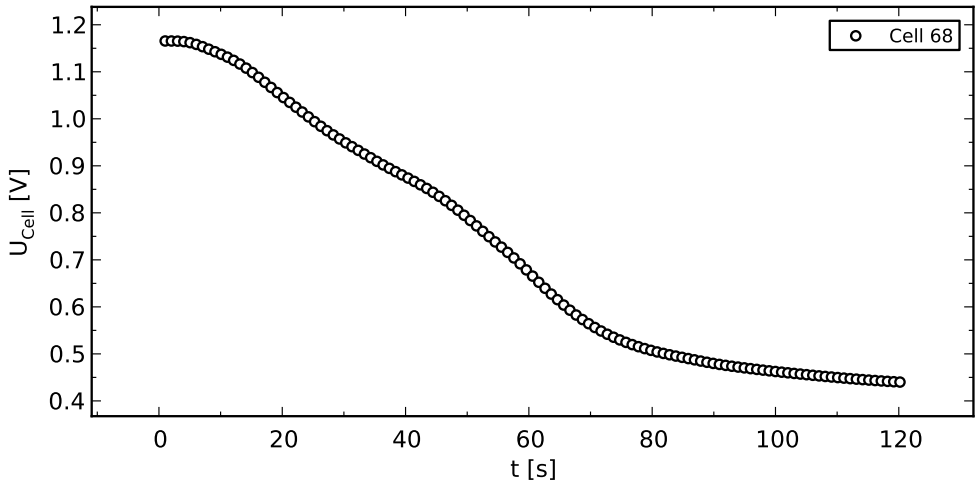

Figure 6.30: Open circuit voltage recorded after the chronoamperometric measurement shown in figure 6.29 for cell 68.

lization of the electrolyte in the here described cells [14]. Since the empirical equation from [14] which is used to calculate the conductivity is said to be valid only up to 200 °C, $\sigma_{Cell,ref}$ at 250 °C should be treated with caution. The here measured conductivities are in fair accordance with the expected values. Variances can occur from dilution or drying of the electrolyte as well as from contact problems in the setup, for example through oxidation of the Ni foam at the oxygen electrode.

$$\sigma_{Cell} = \frac{h_{Electrolyte}}{R_s A_{Cell}} \tag{6.4}$$

Table 6.1: Comparison of the minimal ($R_{S,min}$), averaged ($R_{S,mean}$) and highest ($R_{S,max}$) measured serial resistance during steady periods along with the corresponding conductivities $\sigma_{Cell,max}$, $\sigma_{Cell,mean}$ and $\sigma_{Cell,min}$ and a reference value obtained from previous work [14]. Data from figures 6.13, 6.16 and 6.19 were taken into account.

Temp. [°C]	time span t_0+ (start-end)	$R_{S,min}$ [mΩ cm²] Cell 68/69	$R_{S,mean}$ [mΩ cm²] Cell 68/69	$R_{S,max}$ [mΩ cm²] Cell 68/69	$\sigma_{Cell,max}$ [S cm^{-1}] Cell 68/69	$\sigma_{Cell,mean}$ [S cm^{-1}] Cell 68/69	$\sigma_{Cell,min}$ [S cm^{-1}] Cell 68/69	$\sigma_{Cell,ref}$ [S cm^{-1}] [14]
150	3-22	220 / 221	234 / 252	244 / 276	0.75 / 0.75	0.71 / 0.66	0.68 / 0.60	0.59
200	73-86	201 / 179	210 / 187	214 / 192	0.82 / 0.93	0.79 / 0.89	0.77 / 0.86	0.84
250	145-153	131 / 130	143 / 171	153 / 191	1.26 / 1.27	1.16 / 0.97	1.08 / 0.87	(1.18)

6.5.2 *Peak performance of the cells at 150, 200 and 250 °C*

Impedance and performance data have been obtained at temperatures of 150 °C, 200 °C and 250 °C. The best values after stabilization at the specific temperature have been extracted from the results and are shown in table 6.2. As discussed before a significant reduction of R_S has been measured with increasing temperature; it reduced by a factor of 1.83 for cell 68 and by a factor of 1.77 for cell 69 from 150 °C to 250 °C as it could be expected from previous work (compare chapter 4). An even more significant reduction has been obtained for R_p which has been reduced by a factor of 6.45 for cell 68 and by a factor of 6.00 for cell 69 from 150 °C to 250 °C.

Table 6.2: Peak performance data of the measured cells at temperatures of 150 °C, 200 °C and 250 °C.

Temp. [°C]	time t_0+ (Cell 68/69)	R_S $[m\Omega\,cm^2]$ Cell 68/69	ASR $[m\Omega\,cm^2]$ Cell 68/69	R_p $[m\Omega\,cm^2]$ Cell 68/69	I_{Cell} $[A\,cm^{-2}]$ at U_{Cell} = 1.5 V Cell 68/69	I_{Cell} $[A\,cm^{-2}]$ at U_{Cell} = 1.75 V Cell 68/69
150	24 / 24	240 / 268	737 / 730	497 / 462	0.14 / 0.23	0.59 / 0.69
200	112 / 117	213 / 204	480 / 451	267 / 247	0.31 / 0.36	0.90 / 0.86
250	150 / 148	131 / 151	208 / 228	77 / 77	1.05 / 1.11	2.3 / 2.23

6.5.3 *Activation energies*

The activation energy for the measured resistances R_s, R_p and ASR as well of the obtained current densities I_{Cell} at 1.5 V and 1.75 V as a function of the absolute temperature T [K] have been calculated using the Arrhenius equation in the form of equation 6.5. The rate constant k was substituted by either R_s, R_p, ASR or I_{Cell}. A is the the pre-exponential factor and E_a is the activation energy.

$$k = A\, e^{-E_a/RT} \tag{6.5}$$

A plot of $\ln(k)$ as a function of T^{-1} will have the slope $-E_a\, R^{-1}$. The calculated activation energies from the measurements on cell 68 and cell 69 with the data listed in table 6.2 are shown in table 6.3. E_a for R_s, R_p and ASR were calculated with the reciprocal value of the specific resistances. Figures 6.31 and 6.32 shows an Arrhenius plot of the mentioned data for cell 68 and 69, respectively. Literature values for the activation energy for the HER were determined to be between 17.3 and 20.0 kJ mol^{-1} for platinized electrodes [99, 100] and ca. 71 kJ mol^{-1} for the OER on a $NiCo_2O_4$-anode in 30 wt% KOH [101]. Wendt and Plzak reported typical values from 48.0 kJ mol^{-1} to 120.0 kJ mol^{-1} for the OER and 37.0 kJ mol^{-1} to 54.0 kJ mol^{-1} for the HER [33].

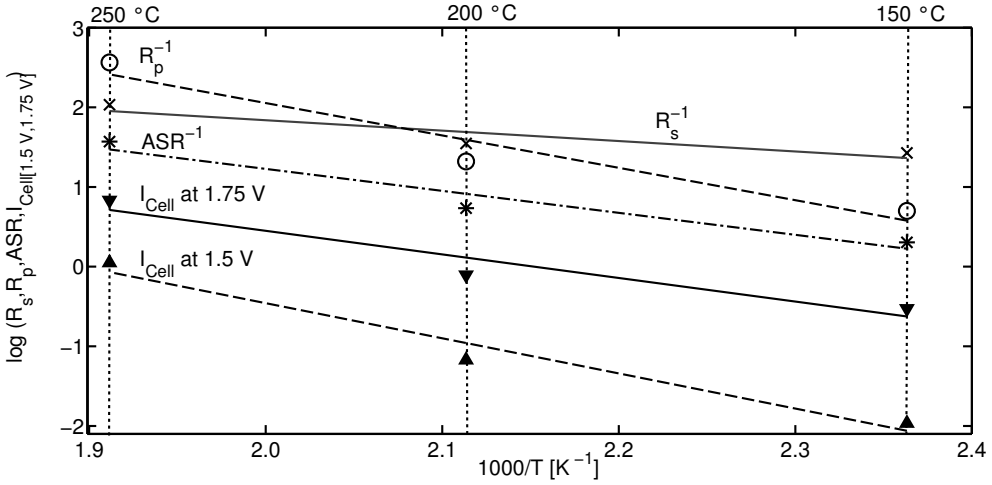

Figure 6.31: Arrhenius plot from the data of cell 68 showing $\ln(k)$ where k is either R_s (x), R_p (o), ASR (*) or I_{Cell} at 1.5 V ($\triangle$) or at 1.75 V (∇) as a function of 1000/T.

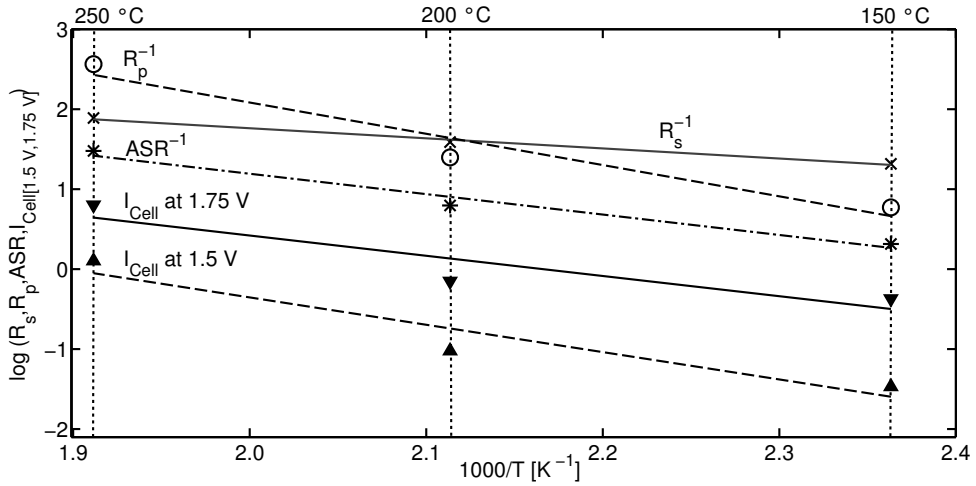

Figure 6.32: Arrhenius plot from the data of cell 69 showing $\ln(k)$ where k is either R_s (x), R_p (o), ASR (*) or I_{Cell} at 1.5 V ($\triangle$) or at 1.75 V (∇) as a function of 1000/T.

Table 6.3: Activation energies $E_a(R_s^{-1})$, $E_a(R_p^{-1})$, $E_a(ASR^{-1})$, $E_a(1.5\ V)$ and $E_a(1.75\ V)$ in $[kJ\ mol^{-1}]$ for R_s, R_p, ASR and I_{Cell} at 1.5 V and 1.75 V, respectively.

	$E_a(R_s^{-1})$ Cell 68/69	$E_a(R_p^{-1})$ Cell 68/69	$E_a(ASR^{-1})$ Cell 68/69	$E_a(1.5\ V)$ Cell 68/69	$E_a(1.75\ V)$ Cell 68/69
$E_a\ [kJ\ mol^{-1}]$	10.9 / 10.5	33.8 / 32.5	22.9 / 21.2	36.7 / 28.4	24.6 / 21.0
$E_a\ [eV]$	0.11 / 0.11	0.35 / 0.34	0.24 / 0.22	0.38 / 0.29	0.26 / 0.22

6.5.4 *Development of the OCV*

An interesting phenomena was measured in relation to the open circuit voltage. The OCV at 150 °C was measured to be relatively high at the beginning of the cyclic voltammetry measurements, but decreased from 955 mV to ca. 340 mV from t_0 + 4 h to t_0 + 20 h (compare figure 6.12). The OCV measured before CV measurements at 150 °C from t_0 + 24h to t_0 + 38 h (compare figure 6.14) showed an increasing OCV from ca. 800 to 880 mV. A comparable behavior was shown for the OCV measured before CV measurements at 200 °C from t_0 + 73 h to t_0 + 85 h (compare figure 6.17), where the OCV increased from 1.01 V to 1.05 V. A surprisingly low OCV was measured at 250 °C (compare figure **??**) from t_0 + 123 h to t_0 + 129 h with a value between 50 mV and 70 mV only.

A possible explanation can be found in the gas composition in the autoclave as shown in figure 6.6. The pH_2 was relatively low at temperatures of 150 °C with 0.2 bar from t_0 + 4 h to t_0 + 18 h, 0.5 bar from t_0 + 18 h to t_0 + 26 h and 0.94 bar from t_0 + 26 h to t_0 + 60 h. At a temperature of 200 °C it was set to 1.4 bar from t_0 + 67 h to t_0 + 131 h whereas pH_2 was between 4.0 bar and 5.0 bar from t_0 + 135 h to t_0 + 270 h. The higher pH_2 will most likely lead to a higher diffusion of the hydrogen gas from the autoclaves atmosphere to the cells anode as long as the cell is not in operation, thereby reducing the OCV. A faster diffusion path for H_2 can occur through the cell if there is an open channel, i.e. if the electrolyte has dried out and the gas can diffuse directly from the cathode to the anode.

In order to estimate the effect of the diffusion to the OCP and to determine which process is most likely it is necessary to determine the time constant for the two diffusion pathways (open path through the cell and diffusion through the sample holder). The diffusion coefficient D of H_2 gas at elevated pressures and temperatures can be estimated using equation 6.6, derived from the Chapman Enskog theory [102]. T is the Temperature [K], M_1 and M_2 are the molar masses [g/mol] of gas 1 and 2, p is the pressure [atm] and Ω is a temperature-dependent collision integral, usually of order 1 . σ_{12} determines the average collision diameter [Å] from tabulated values and can be calculated by equation 6.7, σ_{H_2} is 2.47 Å and σ_{N_2} is 4.3 Å [103].

$$D = \frac{1.858 10^{-3} T^{3/2} \sqrt{1/M_1 + 1/M_2}}{p \sigma_{12}^2 \Omega} \tag{6.6}$$

$$\sigma_{12} = \frac{1}{2}(\sigma_1 + \sigma_2) \tag{6.7}$$

The diffusion coefficient for the H_2 and N_2 mixture in the autoclave at 250 °C and 40 bar, $D_{250C,40bar}$ was calculated to be 3.52 10^{-2} cm^2 s^{-1} with $\Omega = 1$. The time constant for diffusion of H_2 through the sample holder (τ_{SH}) can then be calculated by equation 6.8, where x is the length of the diffusion path ($\approx$ 3 cm for the sample holder path). At a pressure of 40 bar it has been calculated to be 176 s, 149 s and 128 s at 150 °C, 200 °C and 250 °C, respectively, in the here given case.

$$\tau_{SH} = \frac{x^2}{2D} \tag{6.8}$$

For a porous structure, like the electrolyte structure in the measured cell, it is necessary to calculate the effective diffusion coefficient by equation 6.9, where ε_{STO} is the porosity of the structure ($\approx$ 0.5 in the given case) and τ_{STO} is the tortuosity of the given structure ($\approx$ 2.0 in the given case).

$$D_{eff} = \frac{D \varepsilon_{STO}}{\tau_{STO}} \tag{6.9}$$

The time constant for diffusion of H_2 through the electrolyte structure (τ_{STO}) can then be calculated by equation 6.10, where x is the length of the diffusion path ($\approx$ 2 mm for the electrolyte structure path). At a pressure of 40 bar it has been calculated to be 3.1 s, 2.6 s and 2.3 s at 150 °C, 200 °C and 250 °C, respectively,in the here given case.

$$\tau_{STO} = \frac{x^2}{2D_{eff}} \tag{6.10}$$

It should be mentioned that there is also a convective component of the H2 flow that will contribute to the reduction of the OCV through the sample holder path, due to the system design. Neglecting this and comparing the calculated time constants to the OCV measurements after the potentiostatic tests (compare figures 6.21, 6.24, 6.26, 6.28 and 6.30), it is most likely that the reduction of the OCV is due to diffusion through the sample holder path and the occurrence of open paths through the electrolyte structure can be excluded for most of the cases. Only the OCV measurement which was performed directly after the potentiostatic measurement for 100 h (compare figure 6.26) indicates a perhaps dried cell with an open path for gas diffusion where τ_{STO} is dominating.

6.5.5 *Chronoamperometric measurements*

Chronoamperometric measurements were performed at 200 °C and 250 °C. Most measurements showed an initial degradation for a short time after apply-

ing a specific voltage. For the first step it can partly be explained by the oxidation of the nickel anode, which was most likely reduced due to H_2 diffusion to the anode and through the fact that the system is not in steady state directly after incrementing the voltage. The obtained current density at 200 °C is in good accordance with the value obtained by cyclic voltammetry. The maximum measured current density with cyclic voltammetry at 1.5 V was 310 $mA\ cm^{-2}$, while the chronoamperometric measurements showed 322 $mA\ cm^{-2}$ at the same applied cell voltage of 1.5 V as seen in figure 6.20. An initial passivation was observed for the first 1 - 10 min after applying a specific cell voltage, but no further passivation or degradation occurred during the 24 h lasting test at 1.5 V. Nevertheless, the R_s and the R_p were increased by 27 $m\Omega\ cm^2$ and 55 $m\Omega\ cm^2$, respectively (compare lower right image of figure 6.20) at the end of the measurement. This is probably associated with the higher current density while applying higher cell voltages at the end of the chronoamperometric measurement.

The chronoamperometric measurements performed at 250 °C showed also stable or even activating performance at a cell voltage of 1.5 V, although the performance has not been as good as measured by cyclic voltammetry for cell 68 for which 814 $mA\ cm^{-2}$ was obtained (compare upper left image of figure 6.23) by chronoamperometry and 1.05 $A\ cm^{-2}$ by cyclic voltammetry. This is expected since the cell is measured in a steady stade condition during the potentiostatic measurements, which is not the case for CV at 50mV/s. Nevertheless, cell 69 was in very good accordance with 1.05 $A\ cm^{-2}$ (compare upper right image of figure 6.23) obtained by chronoamperometry and 1.11 $A\ cm^{-2}$ by cyclic voltammetry.

Although the cells showed some degradation during the cyclic voltammetry measurements, as shown in figure **??**, an extended chronoamperometric measurement for cell 69 was initiated for a time of 100 h at a cell voltage of 1.5 V (compare figure 6.25). Both R_s and R_p increased strongly during the measurement with the consequence that the performance of the cell reduced from 670 $mA\ cm^{-2}$ to 304 $mA\ cm^{-2}$. SEM analysis of another similar cell, as described in the following chapter 7, indicates corrosion of the anodic nickel foam electrode and the current collector. That could be the cause for the decreased performance.

Cell 68 has been left without further measurement during the 100 h test of cell 69, before a chronoamperometric measurement with a step function of 1.5 V, 1.625 V and 1.75 V and a step time of 20 min was performed. The cell performance improved significantly during this time as it can be seen in figure 6.27. A possible explanation could be condensed steam which flooded the anode or cathode partly during the passive time, but evaporated again during operation. Since the cell was passive for 100 h, the electrolyte could furthermore have been diluted to values slightly below 45 wt% KOH since the steam partial pressure in the autoclave was set to approximately 18.7 bar, while $p_{W,KOH}$ is 16.5 bar for 45 wt % KOH (if $p_{W,KOH}$ is 18.7 bar, the electrolyte concentration would be 42 wt % according to equation (6.3)). The electrolyte is concentrating

again during operation, the conductivity raises and the performance improves (compare figure 6.27). It should be mentioned here that this minor change in concentration alone could not explain the decreased initial performance since the conductivity would be almost equal. Furthermore it is possible that the possibly flooded electrodes dried again and resumed to work as gas diffusion electrodes, and not as conventional electrodes with bubble formation as they would if they were flooded.

In a following chronoamperometric measurement of the same cell (cell 68) for 3 h, further activation took place until the initial performance of 1.05 $A\,cm^{-2}$ at 1.5 V applied cell voltage was measured (compare figure 6.29). Impedance measurements after this measurement confirmed that the cell did not suffer from strong degradation since R_s was 188 $m\Omega\,cm^2$ and with that only 37 $m\Omega\,cm^2$ higher than the best measured value for that cell. Even more stable values was obtained for R_p, which was 80 $m\Omega\,cm^2$ and with that only 3 $m\Omega\,cm^2$ higher than the best measured value shown in table 6.2.

6.6 CONCLUSION

Two similar electrolysis cells with foam based electrodes and the aqueous KOH electrolyte immobilized in a porous matrix of $SrTiO_3$ were measured at 150 °C, 200 °C and 250 °C and a pressure of 40 bar. The performance of the cell increased with increasing temperature. At an applied cell voltage of 1.5 V current densities of 0.23 $A\,cm^{-2}$, 0.36 $A\,cm^{-2}$ and 1.11 $A\,cm^{-2}$ were obtained at 150 °C, 200 °C and 250 °C, respectively. The current densities obtained at an applied cell voltage of 1.75 V were as high as 0.69 $A\,cm^{-2}$, 0.9 $A\,cm^{-2}$ and 2.3 $A\,cm^{-2}$ at 150 °C, 200 °C and 250 °C, respectively. The conductivity of the immobilized electrolyte (45 wt% KOH) at 150 °C, 200 °C and 250 °C was 0.75 $S\,cm^{-1}$, 0.93 $S\,cm^{-1}$ and 1.27 $S\,cm^{-1}$. An initial passivation, which stabilized after 24 h was observed for both cells at the beginning of the investigation at 150 °C. The measurements at 200 °C showed stable values, among others a 24 h potentiostatic measurement at 1.5 V showed a constant current density of ca. 320 $mA\,cm^{-2}$. Activation and passivation processes were observed at 250 °C; i.e. one cell degraded strongly during a 100 h lasting test, while the other recovered its initial performance during this time, thereby indicating that at least one of the indicated passivation processes is reversible. Possible degradation mechanism could be oxidation and corrosion processes at the anodic current collector or the anode itself, enforced through H_2 diffusion to the anode, concentration changes in the electrolyte or electrode flooding or drying.

7

LONG TERM MEASUREMENTS OF COBALT AND MOLYBDENUM ACTIVATED FOAM BASED ALKALINE ELECTROLYSIS CELLS

7.1 ABSTRACT

Alkaline electrolysis cells based on a new technology were developed. The aqueous electrolyte of the cells is immobilized in a mesoporous structure. Metal foam based gas diffusion electrodes are used with enhanced active surface area and three phase boundary length. The cells have been shown to operate at temperatures up to 250 °C and pressures of 42 bar. Cobalt and molybdenum were used as electro-catalysts in order to reduce the oxygen and hydrogen evolution overpotential, respectively.

Long term tests on those foam based electrolysis cells with a duration of 350 h and constant current density of 640 $mA\,cm^{-2}$ were performed in this work at 250 °C and 40 bar simultaneous with potentiostatic measurements at an applied cell voltage of 1.5 V for the first 80 h. Polarized electrochemical impedance spectroscopy measurements with an interval of 5 h show the development of the cell specific resistances. Scanning electron microscopy analysis before and after the tests was used in order to identify the degradation mechanism.

7.2 INTRODUCTION

In order to develop an electrolyser which should operate in a sustainable energy supply system based on renewable energies, it is important to lower the hydrogen (and oxygen) production costs through reduced electricity demand and to reduce the investment costs by increased performance without the need of expensive noble metal catalysts. High temperature and high pressure alkaline electrolysis is a promising attempt to reduce the electricity demand for hydrogen and oxygen production [104]. In chapter 5 and 6 it was demonstrated that an alkaline electrolysis cell is able to operate at temperatures of 250 °C and a system pressure of ca. 40 bar. The developed foam based alkaline electrolysis cells (FobAECs) were tested (with and without further activation with electro-deposited Ag catalyst) (compare chapter 5). The obtained current densities were as high as 1.0 $A\,cm^{-2}$ at an applied cell voltage of 1.5 V and 2.0 $A\,cm^{-2}$ at 1.75 V for the cells with Ag activated anodes. In chapter 6 the cells were enhanced by Mo activated cathodes and Co activated anodes. The obtained current densities were 1.1 $A\,cm^{-2}$ at an applied cell voltage of 1.5 V and 2.3 $A\,cm^{-2}$ at 1.75 V.

The performance of those cells is among the very best known from literature, but in order to be used in an alkaline electrolyser it is necessary to test their long term stability. Although it is a known fact that the used electrolyte, potassium hydroxide in most applications, is very aggressive against numerous materials [56], commercial alkaline electrolysers have been shown to operate for as long as 20 years without drastic degradation, or have a predicted lifetime of 60,000 h [105].

7.3 EXPERIMENTAL

7.3.1 *Production of electrolysis cells*

The FobAECs are produced from metal foams, $SrTiO_3$as porous matrix to immobilize the aqueous electrolyte (45 wt% KOH) and a cobalt- or molybdenum-$SrTiO_3$mixture as electro-catalyst. The production method has been described in detail in chapter 6.3.1.

7.3.2 *Temperature, gas flow profile and partial pressures during testing*

H_2, N_2 and $H_2O_{(g)}$(steam) has been supplied to the autoclave chamber; the steam was produced by supplying O_2 together with H_2. The O_2 was converted by 100 % in the catalytic burner. The temperature and gas partial pressure profile for the electrochemical tests over the entire measurement period is shown in figure 7.1, with the partial pressures on the left ordinate and the autoclaves temperature on the right ordinate. The electrochemical measurements were started at $t_{el} = 0\,h$. After the heating period (ended at $t_{el} = -8\,h$) the gas flow was fixed to 2.1 SLPH (standard liter per hour) H_2, 2.3 SLPH N_2 and to 0.84 SLPH O_2 for the entire measurement period.

The maximal conversion rate of the supplied steam by the electrolysis cell during the experiments, $H_2O_{conv,max}$, can be calculated from equation 6.2 in chapter 6.3.4. The steam flow rate has been set to 1.68 SLPH for the entire measurement at 250 °C, so $\sum I_{Cell}$ must not exceed 3.32 $A\,cm^{-2}$ in order to prevent that more steam is used than provided.

In order to avoid evaporation of the immobilized electrolyte, it is necessary to keep the system pressure (40 bar for the entire measurement period) above the water vapor partial pressure of the electrolyte. The water vapor partial pressure over aqueous potassium hydroxide solutions, $p_{W,KOH}$, has been described in chapter 6.3.4. For a KOH concentration of 45 *wt*% and a temperature of 250 °C, $p_{W,KOH}$ has been calculated to be 16.47 bar.

7.3.3 *Electrochemical measurements*

Two similar cells, cells 70 and 71, were produced as described above. Electrochemical measurements, i.e. electrochemical impedance spectroscopy (EIS),

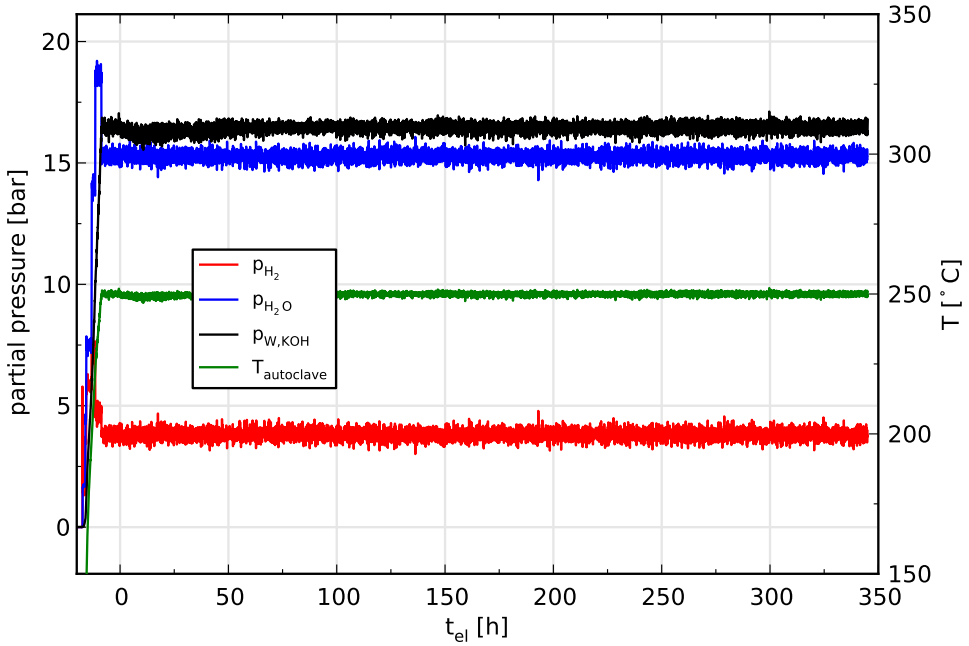

Figure 7.1: Partial pressures profile of H_2(red) and $H_2O_{(g)}$(blue) over the entire measurement along with the water vapor partial pressure over 45 wt% KOH(aq) (black) as a function of the temperature in the autoclave (gray).

chrono-amperometry (potentiostatic measurements) and chrono-potentiometry (galvanostatic measurements) have been performed. Two *Gamry Reference 3000* potentiostats were used to record the measurements simultaneously. Since it was the aim of the here described analysis to determine the long term performance of the developed cells under polarization, measurements which would require interruptions of the current flow, i.e. cyclic voltammetry and EIS at open circuit voltage, have been avoided.

Cell 71 was used to determine the cell characteristics under potentiostatic conditions with an applied cell voltage U_{cell} of 1.5 V. EIS measurements for cell 71 were performed every 5 h under the same polarization of 1.5 V. Cell 70 was used to determine the cell characteristics under galvanostatic conditions with an applied current of 500 mA, equivalent to a current density of 640 mA cm^{-2}. EIS measurements for cell 70 were performed every 5 h under the same load of 640 mA cm^{-2}.

7.3.4 *SEM analysis*

Scanning electron microscopy was performed using a Zeiss Supra 35 microscope. The cells used for the electrolysis measurements were fixed in Epoxy after the measurements and cut in order to analyze the cross section. Similarly produced cells that have not been used for electrolysis or other electrochemical

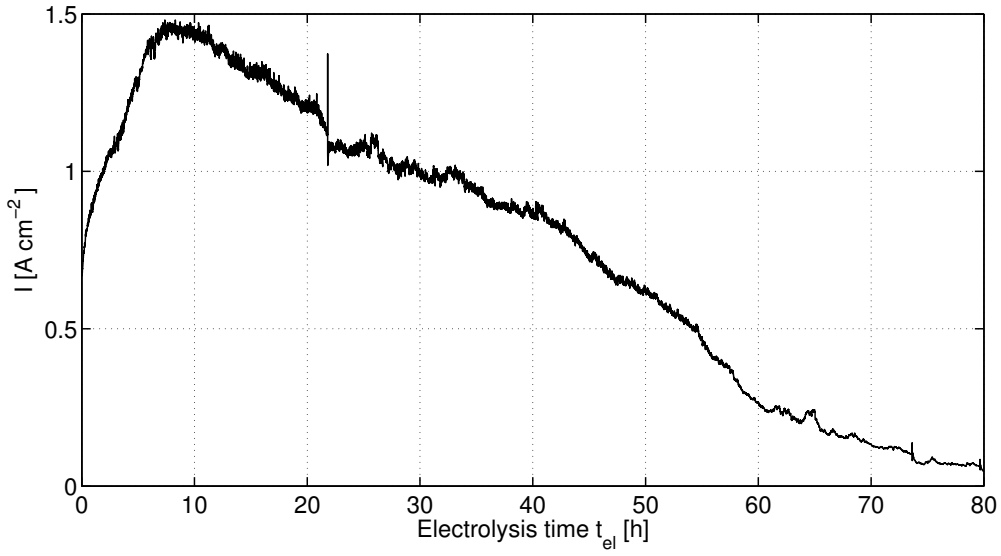

Figure 7.2: Current density as a function of time over the entire measurement period of 80 hours under an applied cell voltage of 1.5 V, at 250 °C and 40 bar.

measurements were also imaged to show the difference of an unused cell to the cells used for electrolysis.

7.4 RESULTS

7.4.1 *Potentiostatic measurements*

A chronoamperometric (potentiostatic) measurement was performed on cell 71 in order to determine the long time performance. The applied cell voltage, U_{Cell}, was 1.5 V over the entire measurement period, for both, chronoamperometry and polarized EIS measurements. The measured current density of the CAS measurement is displayed in figure 7.2. The current density at $t_{el} = 0\,h$ was 671 $mA\,cm^{-2}$, increasing to a peak with 1.48 $A\,cm^{-2}$ at $t_{el} = 7.4\,h$. After this activation period, a strong degradation took place and the current density reduced from 1.43 $A\,cm^{-2}$ at $t_{el} = 10\,h$, to 1.22 $A\,cm^{-2}$ at $t_{el} = 20\,h$, 870 $mA\,cm^{-2}$ at $t_{el} = 40\,h$, 260 $mA\,cm^{-2}$ at $t_{el} = 60\,h$ and 51 $mA\,cm^{-2}$ at $t_{el} = 80\,h$. The measurement was stopped at this point because impedance measurements were interrupted by the potentiostat since too many invalid measurement points occurred.

EIS measurements were performed every 5h in between the chronoamperometric measurement. Nyquist plots of the impedance during the first 20 h are displayed in figure 7.3 A. While the serial resistance R_s and the area specific resistance ASR were 190 $m\Omega\,cm^2$ and 291 $m\Omega\,cm^2$ at $t_{el} = 0\,h$, they developed to 152 $m\Omega\,cm^2$ and 228 $m\Omega\,cm^2$ at $t_{el} = 5\,h$, 159 $m\Omega\,cm^2$ and 212 $m\Omega\,cm^2$ at $t_{el} = 10\,h$, 175 $m\Omega\,cm^2$ and 235 $m\Omega\,cm^2$ at $t_{el} = 15\,h$ and 185 $m\Omega\,cm^2$ and 248 $m\Omega\,cm^2$ at $t_{el} = 20\,h$, respectively. Figure 7.3 shows how the impedance

developed in the Nyquist (B) and Bode plane (C+D) until $t_{el} = 60$ h. Beside the already given values at $t_{el} = 0$ h and $t_{el} = 20$ h, the R_s and the ASR were 226 mΩ cm^2 and 326 mΩ cm^2 at $t_{el} = 40$ h and 593 mΩ cm^2 and 1015 mΩ cm^2 at $t_{el} = 60$ h. Figure 7.3 A and B were not merged in order to keep the readability for the early impedance plots in figure 7.3 A.

7.4.2 *Galvanostatic measurements*

Galvanostatic measurements were performed on cell 70 in order to determine the long time performance under constant current. The current density of the cell was kept constant at 500 mA, equivalent to 640 mA cm^{-2}. The results from the galvanostatic measurements measurement over a period of 350 h is displayed in figure 7.4. The measured cell voltage U_{cell} at $t_{el} = 0$ h was 1.49 V, decreasing to 1.44 V at $t_{el} = 5$ h. After this activation period, degradation took place. Cell voltage peaks occurred from $t_{el} = 28$ h with increasing repetition rate and intensity. The highest peak was measured at $t_{el} = 279$ h with a peak voltage of 2.91 V.

Some of the peaks that occurred are shown more detailed in figure 7.5 beside a "peak free" measurement period of 5 h duration starting at $t_{el} = 0$ h. The peak in figure 7.5 B shows the typical shape of the peaks that occurred; the increasing part is typically not so steep as the falling edge and the cell voltage falls further down as before the peak. More specific: the peak has its positive edge at $t_{el} = 62$ h with $U_{cell} = 1.54$ V, it increases to 2.0 V at $t_{el} = 63.7$ h before it falls to 1.54 V at $t_{el} = 64$ h. Figure 7.5 C-F shows how the shape and intensity of the curves developed during the measurement. The lowest and highest voltages in the shown periods for image C, D, E and F are 1.52 V and 2.02 V, 1.51 V and 2.13 V, 1.53 V and 2.39 V and 1.56 V and 2.16 V, respectively. It is also worth noting that the lowest cell voltage at $t_{el} = 64$ h with 1.54 V is only 20 mV lower than this at $t_{el} = 323.5$ h with 1.56 V.

Polarized galvanostatic impedance measurements, with the same current density as used for the CPS measurements (640 mA cm^{-2}), were performed before each of the analyzed measurements shown in figure 7.5. The results of the EIS measurements are shown in figure 7.6 in the Nyquist and Bode plane. The R_s and the ASR developed from 182 mΩ cm^2 and 360 mΩ cm^2 at $t_{el} = 0$ h, to 228 mΩ cm^2 and 422 mΩ cm^2 at $t_{el} = 60$ h, 371 mΩ cm^2 and 925 mΩ cm^2 at $t_{el} = 120$ h, 320 mΩ cm^2 and 515 mΩ cm^2 at $t_{el} = 185$ h, 251 mΩ cm^2 and 741 mΩ cm^2 at $t_{el} = 250$ h to 286 mΩ cm^2 and 981 mΩ cm^2 at $t_{el} = 320$ h, respectively. ASR values above 600 mΩ cm^2 were not displayed in the Nyquist plane in order to enhance readability.

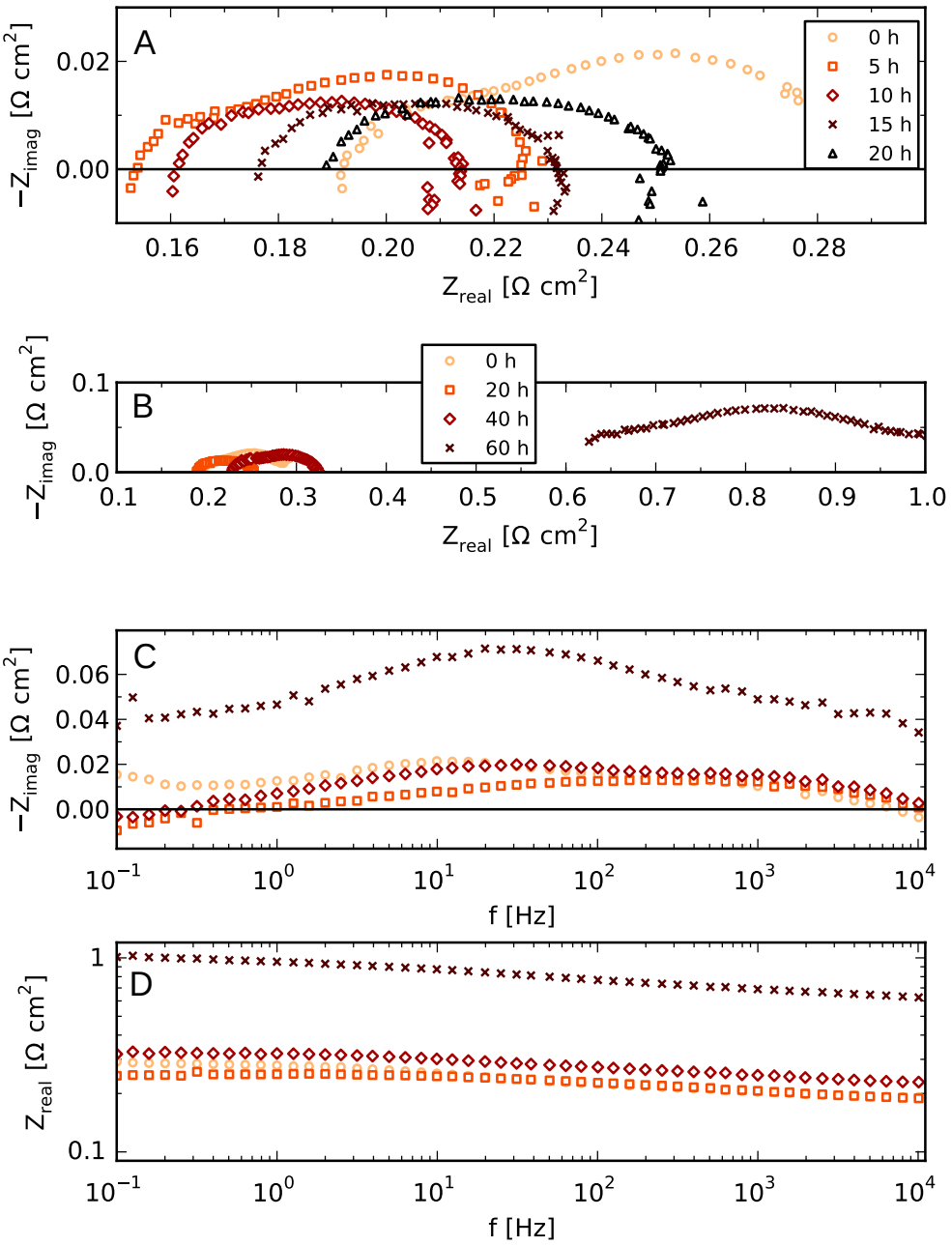

Figure 7.3: Development of the impedance spectra taken before the chronoamperometric measurements as displayed in figure 7.2. The polarization voltage for EIS was 1.5 V, at 250 °C and a pressure of 40 bar. The signs of the curves in C and D are the same as in B. Z_{real} in D is displayed in logarithmic scale.

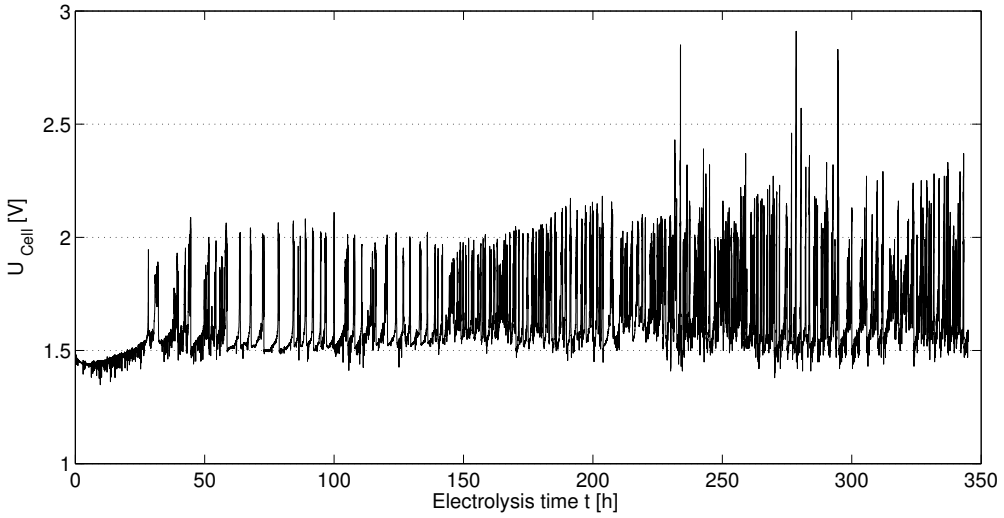

Figure 7.4: Development of the applied cell voltage over the entire measurement period of 345 hours with a constant current density of 640 $mA\ cm^{-2}$, at 250 °C and 40 bar.

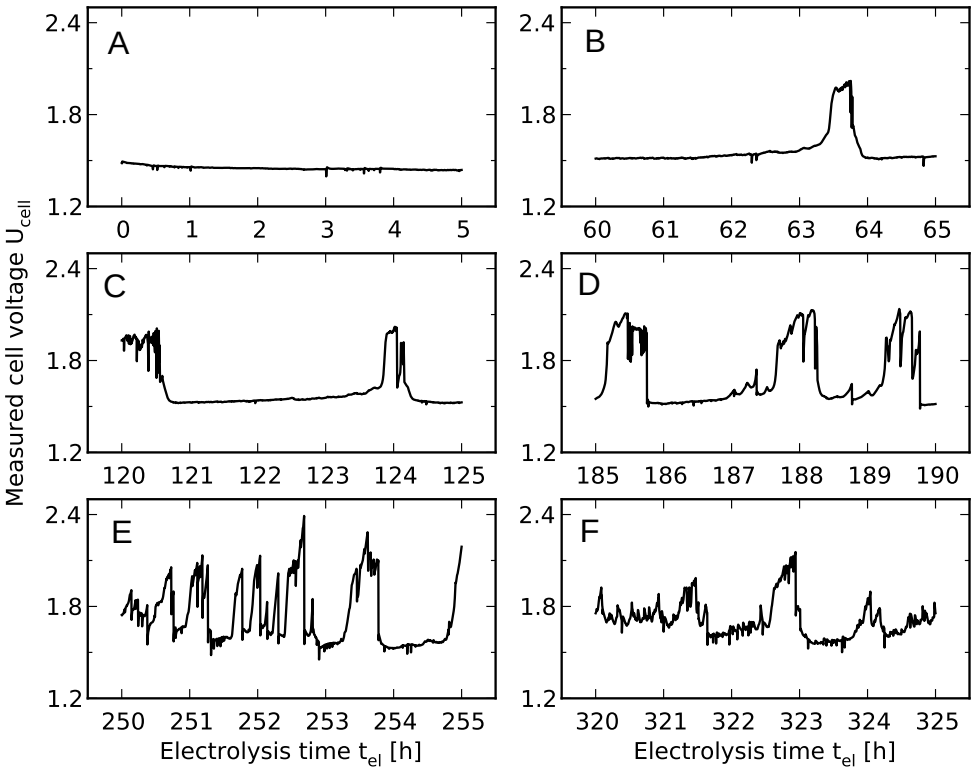

Figure 7.5: Development of the applied cell voltage over 5 h lasting periods at different time points of the entire measurement period at 250 °C and 40 bar. The current density was 640 $mA\ cm^{-2}$.

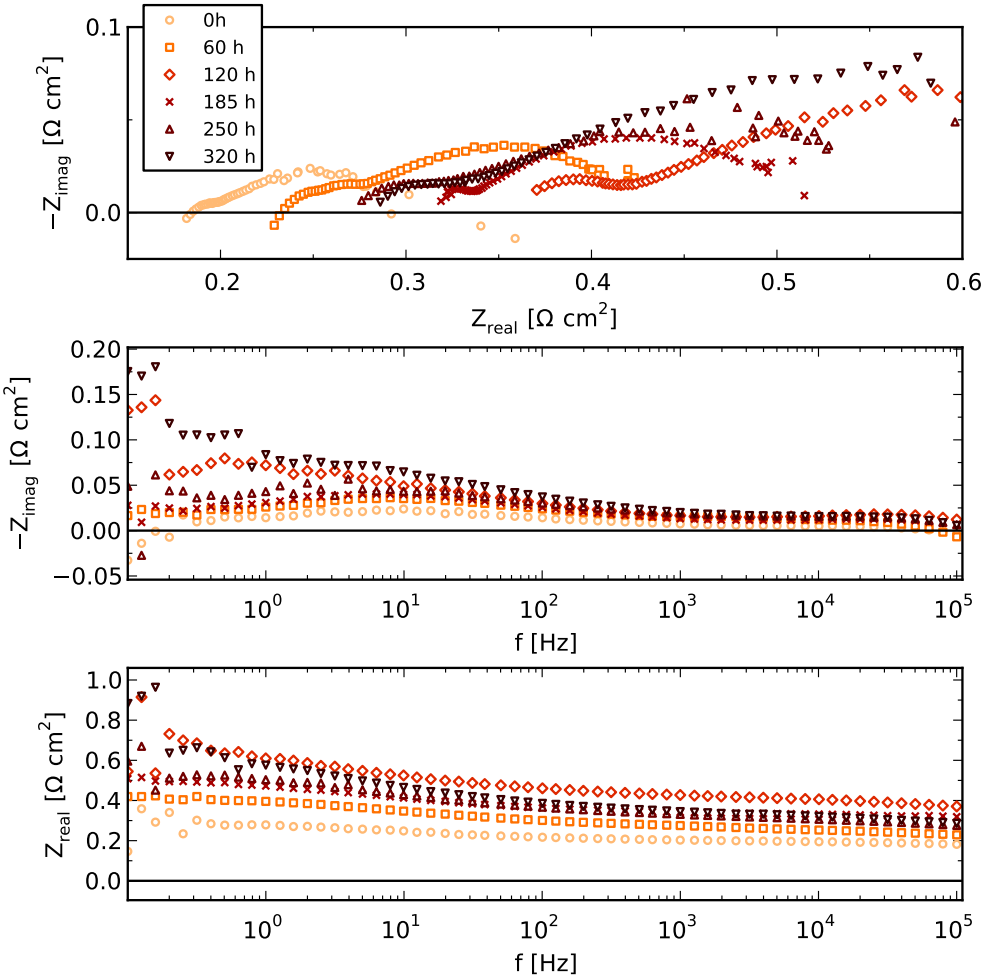

Figure 7.6: Development of the impedance spectra taken during the CPS measurement displayed in figure 7.5. The constant current density for EIS was 640 mA cm^{-2}, at 250 °C and 40 bar.

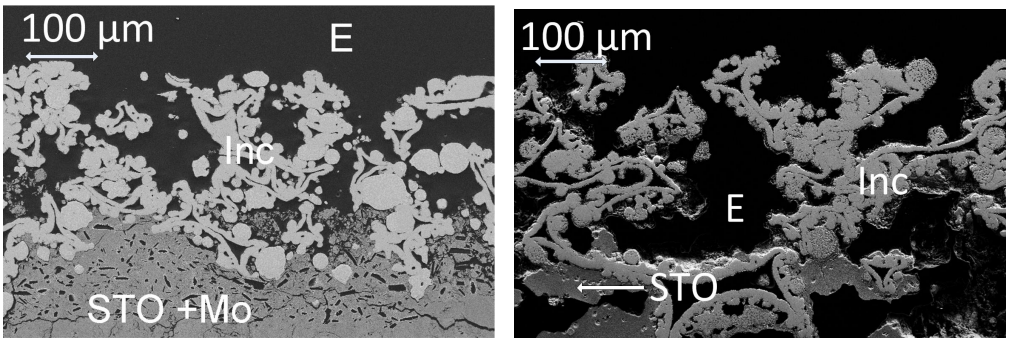

Figure 7.7: Polished cross sections of a virgin Inconel cathode of a FobAEC after the sintering process (left) and the Inconel cathode of cell 71 after the potentiostatic test at 1.5 V for 80 h (right, turned 180° for microscopy reasons). STO + Mo indicates the porous $SrTiO_3$ mixed with molybdenum, Inc indicates the Inconel foam and E indicates the epoxy used for embedding the sample.

7.4.3 *Postmortem SEM analysis of cell 71*

7.4.3.1 *Cathode*

The cell and the current collector, which were used for potentiostatic measurements, were put in epoxy and polished to obtain cross section images of the cell by scanning electron microscopy (SEM) after the test. In figure 7.7 the cathode of a similar, unused, cell is compared to the cathode of the here tested cell after the measurements. The pores of the Inconel foam cathode were still open and allowed proper gas diffusion. The edges of the Inconel foam seem to have slight tracks of corrosion since they appear smoother with reduced specific surface area. Anyway, the cathode was in fairly good condition and it is believed that the Inconel foam cathode is stable enough under the harsh conditions. The contribution to the overall degradation is believed to be small, if any.

7.4.3.2 *Anode*

In figure 7.8 the anode of a similar cell is compared to the anode of the here tested cell. The virgin anode on the left image has a fairly good porosity and open pores to allow for gas diffusion. The electrolyte structure (STO) adheres to the foam well over the entire foam surface, thereby forming a long three phase boundary (TPB). The right image shows the nickel anode after the potentiostatic test. The nickel foam is denser than in the virgin cell. Also less STO is in contact with the Ni foam. It is possible that the nickel foam oxidizes and blocks some open pores which should work as gas diffusion paths. Another possibility for the less porous structure of the used cell may result from the production procedure, i.e. if the cell was pressed with a too high force due to uncertainties in the press.

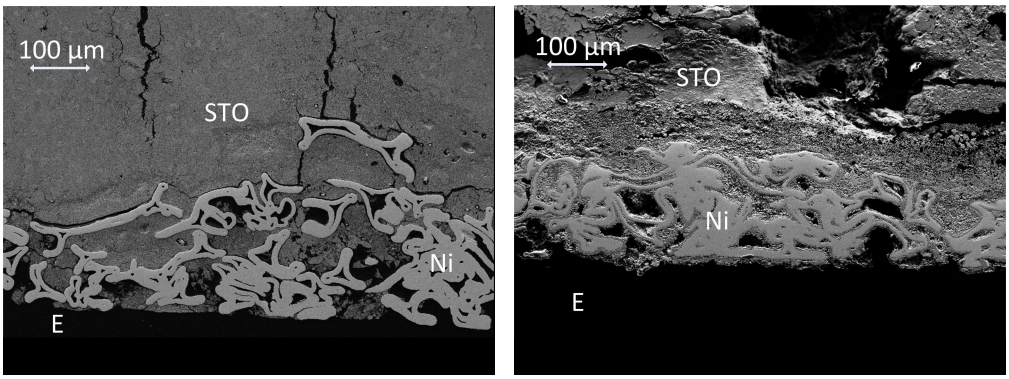

Figure 7.8: Virgin nickel anode of a FobAEC after the sintering process (left) and nickel anode of cell 71 after the potentiostatic test at 1.5 V for 80 h. STO indicates the porous $SrTiO_3$, Ni indicates the nickel foam and E indicates the epoxy used for embedding the sample.

7.4.3.3 *Current collector*

A picture of the cross section of the nickel foam current collector which was used at the anode for the potentiostatic measurements of cell 71 is shown in figure 7.9. The Nickel foam seems to suffer from corrosion , i.e. the foam had a rather smooth surface in the unused condition (not shown here), but the surface is very rough and porous after the measurements, with a high specific surface area. Also parts of the foam broke apart from the foam. This behavior can, at least partly, explain the activation and passivation process as shown in figure 7.2, assuming that a comparable process takes place at the nickel foam anode: At the beginning of the electrolysis, at $t_{el} = 0\,h$, the nickel foam of the anode is rather smooth, while it begins to corrode after the measurement started, thereby increasing the specific surface area and with that increasing the TPB length. Hence, the current density increases. After an electrolysis time of ca. 10 h to much nickel or nickel oxide particles are spalled off from the foam, thereby blocking the gas diffusion pores partially. Furthermore it is possible that the surface of the nickel foam was blocked and thereby the electrical connection of the current collector to the electrode worsened and the current density was reduced by increasing R_s.

7.4.4 *Postmortem SEM analysis of cell 70*

A post mortem analysis of the cell used for the galvanostatic experiments was performed. Figure 7.10 shows a comparison between a similar produced cell (cell 67, unused, with thicker electrolyte structure) and the used cell. The inconel foam cathode looks only gently attacked, while the nickel foam looks more attacked. Both cells have cross-plane (vertical) cracks in the electrolyte structure, but the cross-plane cracks in cell 70 are thicker. The in-plane (horizontal) cracks close to the electrodes of cell 67 are also much thinner than those of cell 70, where a complete delamination occurred. It cannot be stated clearly

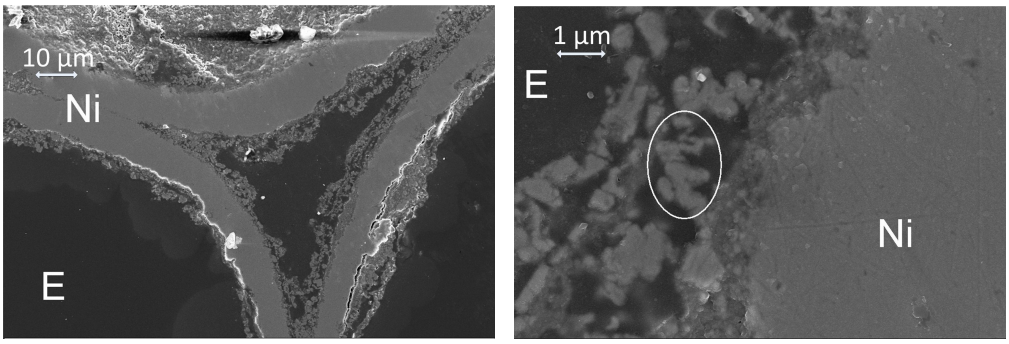

Figure 7.9: Cross section of the nickel foam current collector which was used in the measurement setup (compare figure 6.4) for the anode of cell 71. Ni indicates the nickel foam and E indicates the epoxy. The framed structure is part of the nickel foam which dissolved partly from the nickel foam current collector.

if the growth of the cracks was a result of corrosion of the electrolyte structure, mechanical stress while handling the cell before and after the tests or from sample preparation for microscopy; a combination of these is most likely the reason.

7.4.4.1 *Cathode*

The pores of the used cathode were still open, so proper gas diffusion was ensured during the measurement as can be seen in the left image of figure 7.11. Although the electrode was delaminated from the electrolyte structure (compare figure 7.10), at some places there was still good connection between the metal foam and the electrolyte structure, as seen in the right image of figure 7.11. The TPB seems to be well intact at those places. The edges of the inconel foam seem to have slight traces of surface corrosion. After all it seems that the Inconel cathode is stable enough under the harsh conditions and the contribution from the cathode to the overall degradation is believed to be small.

7.4.4.2 *Anode*

The anode of cell 70 after the 350 h test is shown in figure 7.12. It can be seen that parts of the foam have agglomerated. At the surface of the nickel foam, strong oxidation is observed; the nickel foam oxidized and blocked the gas diffusion pores at least partly. The right image of figure 7.12 shows the cutout of the white rectangle from the left image. It can clearly be seen how the Ni-oxide has grown inside the pores.

Another example of the oxide growth is shown in figure 7.13 with increasing magnification from the upper, to the lower left and to the lower right image. The white rectangle shows the magnified excerpt. It can be seen that particles of the nickel foam have been spalled off from the foam, thereby blocking some

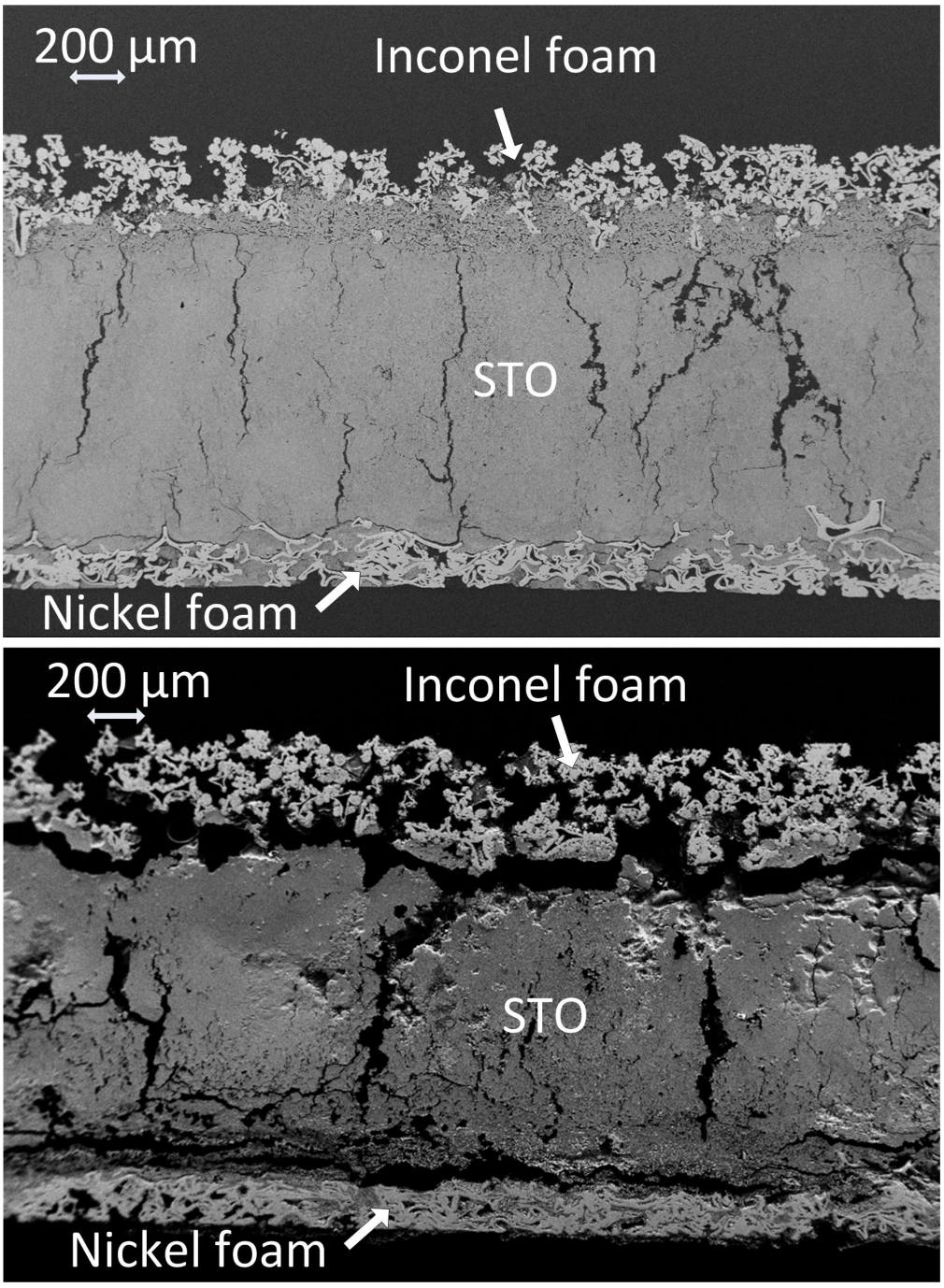

Figure 7.10: SEM image of the cross section of cell 70 (lower image) after the 350 h lasting test and an unused, similar produced cell (upper image). The image shows that the inconel foam cathode and the nickel foam anode of cell 70 are delaminated from the electrolyte structure (STO). The STO layer has cross-plane and in-plane cracks. The unused cell has cross-plane and in-plane cracks as well, but less pronounced.

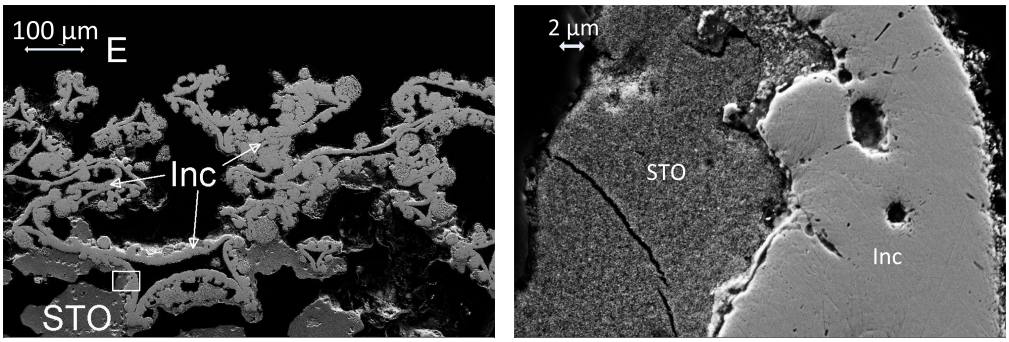

Figure 7.11: Left image: Inconel foam cathode of cell 70 with some fracture of the electrolyte structure (STO) after the 350 h lasting test under galvanostatic conditions. Right image: Magnified view of the interface of the Inconel foam (INC) and the electrolyte structure (cutout from white rectangle of the left image). E is epoxy.

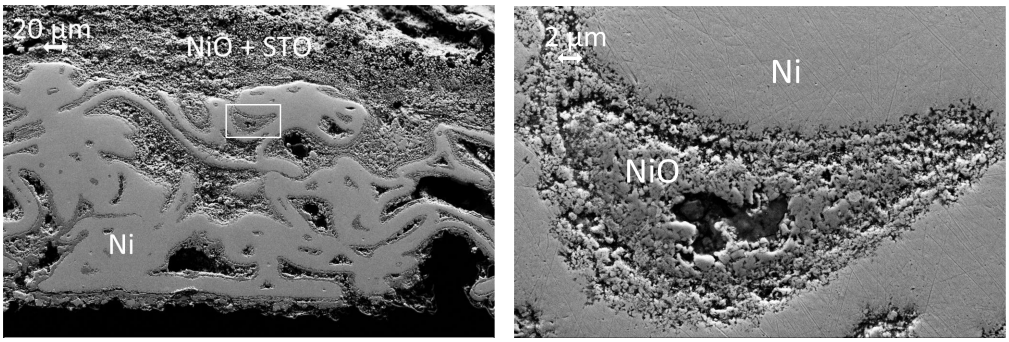

Figure 7.12: SEM image of the nickel foam anode after the 350 h lasting galvanostatic test. The nickel foam (Ni) is oxidized at the edges, thereby blocking the gas diffusion pores partly.

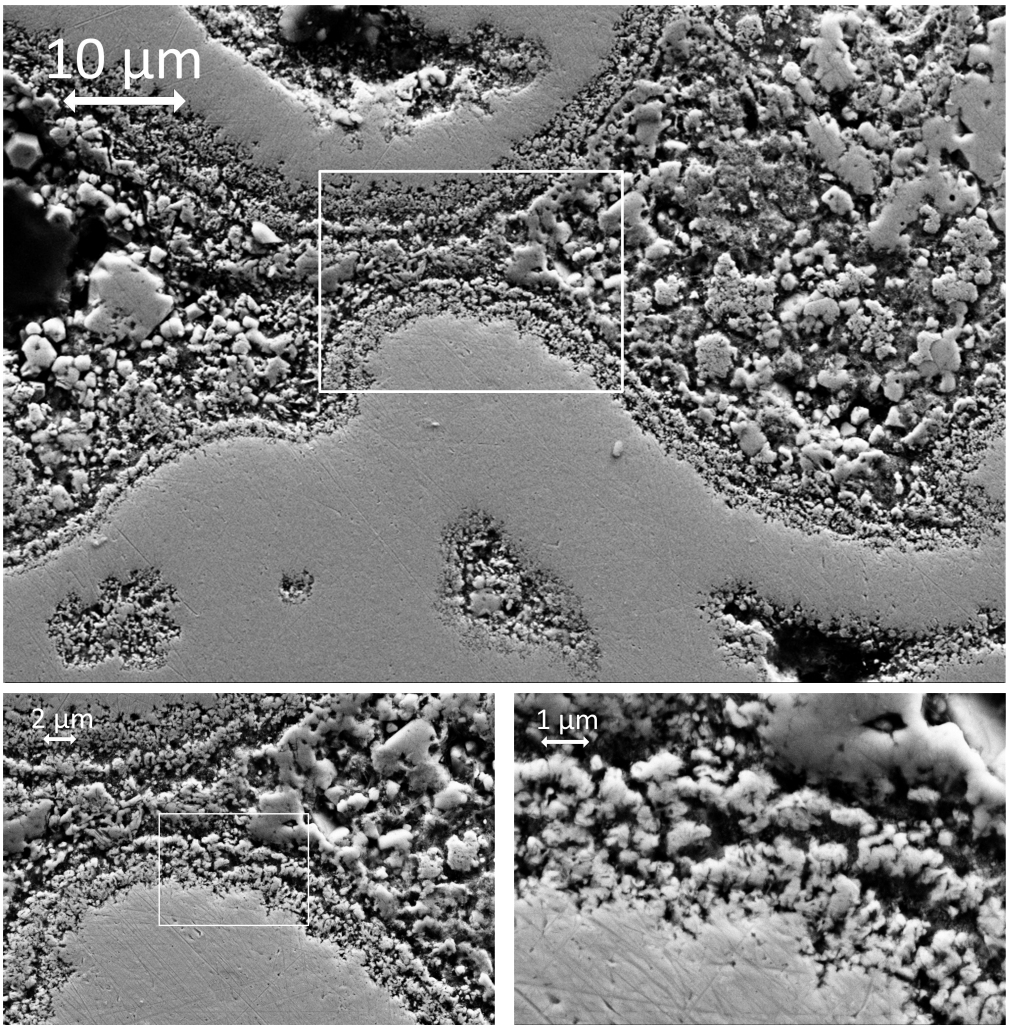

Figure 7.13: Example of the oxide growth on the nickel foam anode with increasing magnification from the upper, to the lower left and to the lower right image. The white rectangle shows the magnified excerpt.

open pores of the GDE, but also increasing the specific surface area of the electrode.

7.4.4.3 *Current collector*

A picture of the cross section of the nickel foam current collector which was used at the anode for the potentiostatic measurements of cell 70 is shown in figure 7.14. The foam was completely covered by a dense Ni-Oxide layer; some pores which were open before the measurements were completely blocked by the oxide.

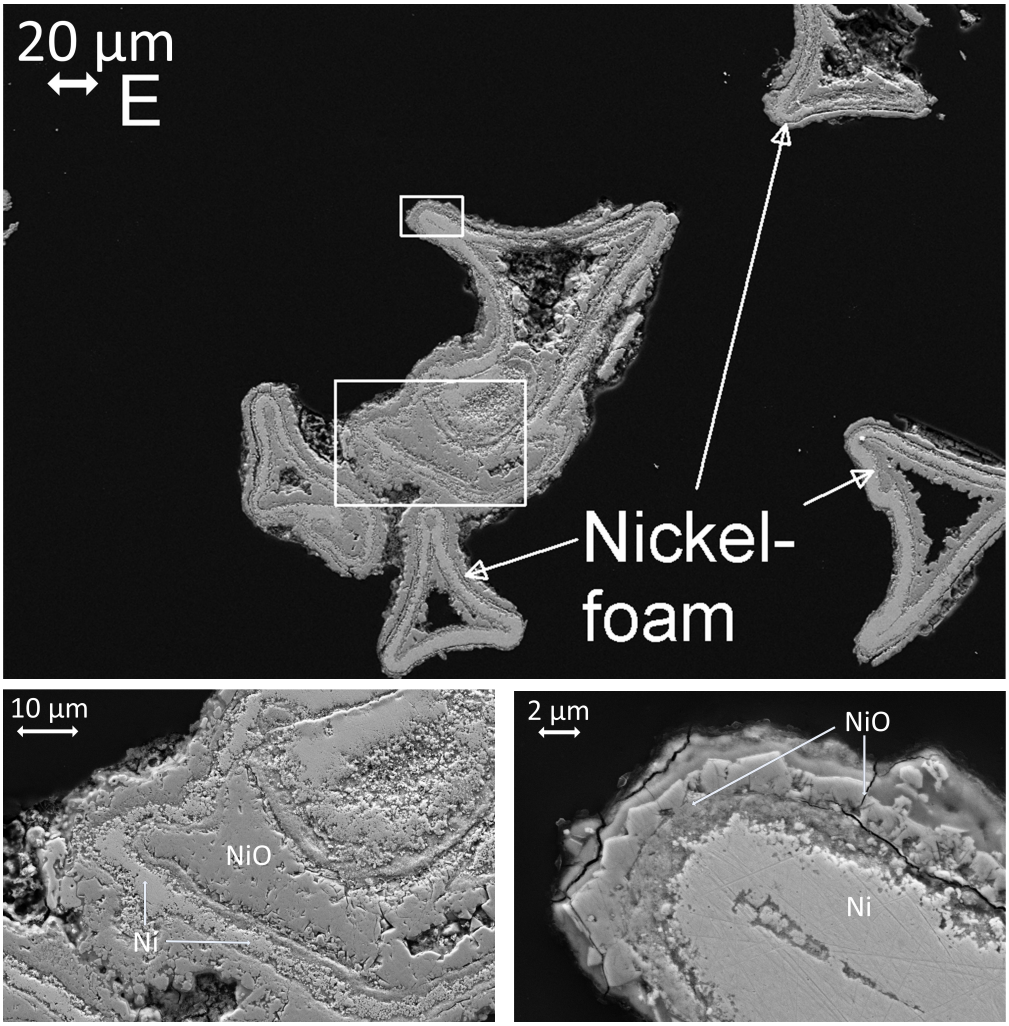

Figure 7.14: Cross section of the nickel foam current collector which was used in the measurement setup (compare figure (setup chapter 6)) for the anode of cell 70. Ni indicates the nickel foam and E indicates the epoxy used for imaging in the microscope. Parts of the upper figure are shown magnified in the lower left (lower rectangle) and lower right (upper rectangle). Ni-oxide was found at the surface of the foam as well as in the pores.

7.5 DISCUSSION

7.5.1 *Potentiostatic measurements*

The performance of cell 71 at $t_{el} = 0\,h$ was relatively weak (671 $mA\,cm^{-2}$ at $U_{cell} = 1.5\,V$ (compare figure 7.2)) if compared to the results obtained under similar conditions with identical cells in chapter 6 , where current densities around $1.0\,A\,cm^{-2}$ were measured even after discontinuous operation for 120 h. Nevertheless, an activation period followed with a peak performance of $1.48\,A\,cm^{-2}$ at $t_{el} = 7.4\,h$. This is equal to an activation rate of $109\,mA\,cm^{-2}\,h^{-1}$. Since the measured cells were soaked in KOH (aq) before they were placed in the sample holder, it is possible that some of the gas diffusion pores were filled with electrolyte, hindering the evolved gases to escape and minimizing the active area as well as the three phase boundary length TPB. The same effect could have occurred if condensed water would have dropped on top of the cell during the heating period. Furthermore it is imaginable that an oxide layer on the cathode minimized the initial performance, before it was removed due to reduction in the electrolysis process. Possible impurities may have oxidized at the anode.

The degradation of the cell could, to some extend, be explained by drying processes of the electrolyte. If more steam is consumed than provided, part of the electrolyte solution would be electrolyzed, thereby becoming more concentrated. Furthermore this could cause a decrease of the designated three phase boundary as large parts of the electrode may not be in contact with the electrolyte any more. In that case the electrolysis takes place in a limited volume of the electrode near the electrolyte layer, were bubble formation and gas diffusion limitations could result in weaker performance.

The post mortem SEM analysis of cell 71 showed also that the electrodes suffer from corrosion. Especially the nickel foam on the anodic side of the electrolysis cell showed strong degradation. The SEM analysis of the current collector used for the measurements also showed that part of the current collector spalled off. The specific surface area and with that the TPB length increased in that case. This could also explain the activation of the cell in the first hours of the experiment.

With ongoing electrolysis time it is possible that the contact between the current collector and the anode worsened due to less or non conductive oxide layers in between. The increasing R_s over time consolidates this assumption.

7.5.2 *Galvanostatic measurements*

The galvanostatic measurement on cell 70 showed an activation period at the beginning of the measurement as well, but not as pronounced as the potentiostatic measurements on cell 71. U_{cell} at $t_{el} = 0\,h$ was 1.49 V, decreasing to 1.44 V at $t_{el} = 5\,h$, resulting in a activation rate of $10\,mV\,h^{-1}$ for the first

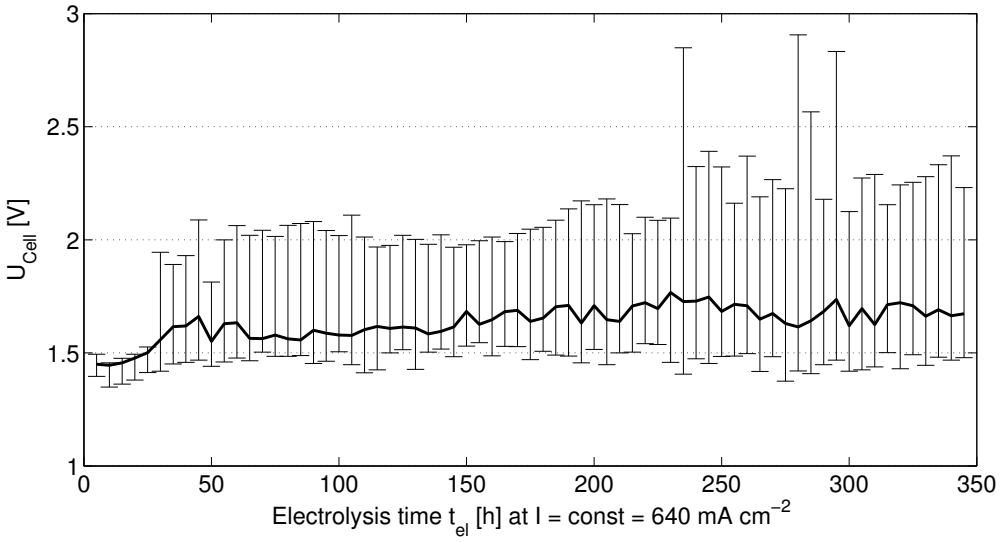

Figure 7.15: Development of the 5 h average of the applied cell voltage along the min and max values over the entire measurement period of 345 hours with a constant current density of 640 $mA\,cm^2$, at 250 °C and 40 bar.

5 h. With ongoing electrolysis time, cell voltage peaks occurred as shown in figure 7.4. The minimum and the maximum value of these peaks is shown in figure 7.15 along with the average cell voltage $U_{cell,mean}$ for each 5 h lasting measurement period. It can be seen that a relatively strong degradation takes place from $t_{el} = 5\,h$ until $t_{el} = 45\,h$, with $U_{cell,mean}$ starting from 1.45 V and ending at 1.66 V. The resulting degradation rate in this period is 5.25 $mV\,h^{-1}$. From $t_{el} = 45\,h$ until $t_{el} = 230\,h$ the degradation rate decreased to 0.6 $mV\,h^{-1}$, ending at $U_{cell,mean} = 1.77\,V$. Further on, the cell activated again to $U_{cell,mean} = 1.67\,V$ at $t_{el} = 345\,h$ with an activation rate of 0.9 $mV\,h^{-1}$.

Such an initial activation followed by a degradation process was also observed by Divisek et al. for an electrolysis cell under galvanostatic conditions (400 $mA\,cm^{-2}$, 100 °C, 10 M KOH) [19]; corrosion problems were indicated as the reason for degradation in their measurements.

Although viewed in terms of $U_{cell,mean}$ cell 70 seems to have activated during that last period, the observed cell voltage peak maximum and repeating rate increased during this time. The galvanostatic impedance measurements which were performed at the end of each 5 h interval led to too high cell voltages for the potentiostat and the measurement was stopped after 350 h.

A fast Fourier transformation FFT of the data shown in figure 7.4 was performed in order to analyze if the peaks had one or more specific repetition frequencies or if their periodicity varied randomly. The result is shown in figure 7.16 A with a period time of up to 50 h and more detailed with a period time up to 5 h in figure 7.16 B. It can be seen that no certain repetition frequency or periodic time was found, although a peak around 24 h indicates that a daily repeating process, for example a temperature dependance, may have occurred.

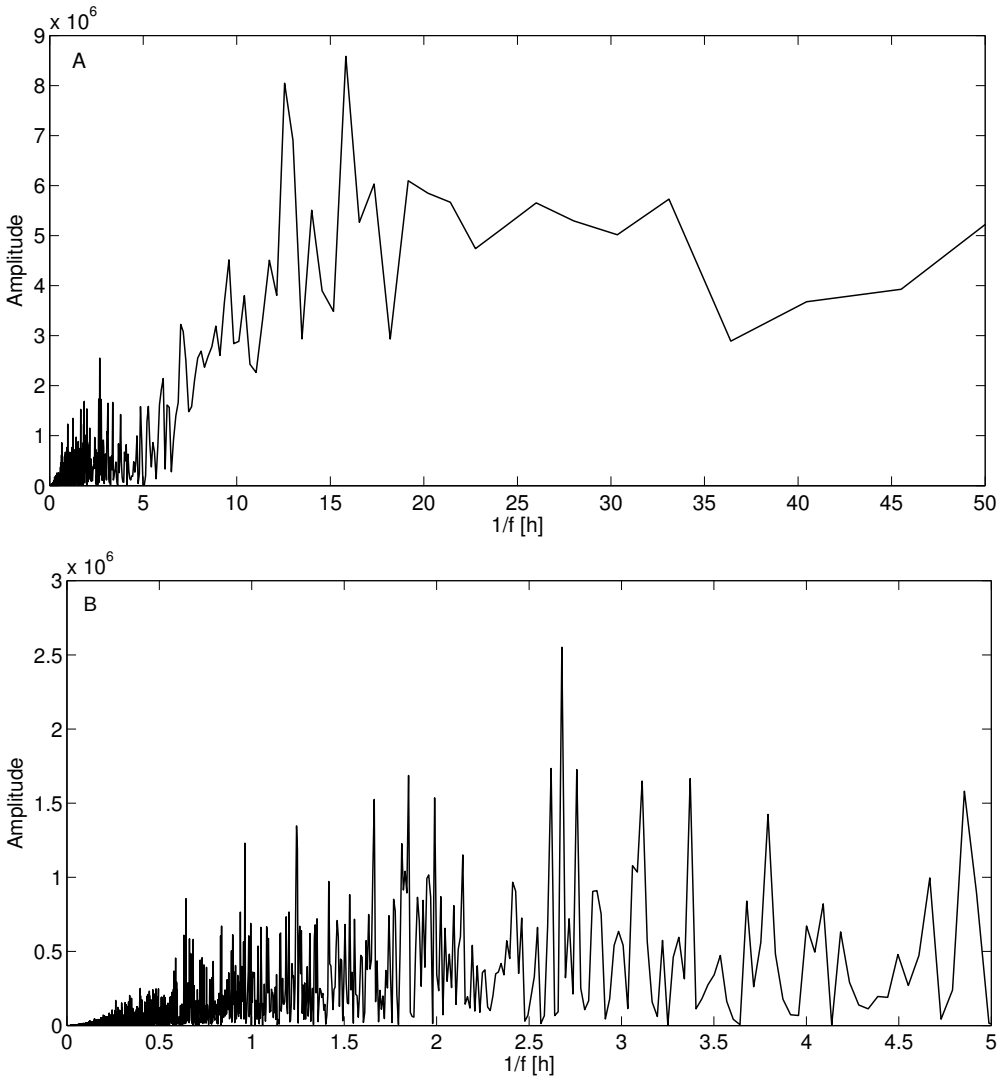

Figure 7.16: FFT of the galvanostatic measurements of cell 70 over the entire measurement period showing period durations up to 50 h (5.56 µHz) (A) and up to 5 h (55.6 µHz) (B).

The SEM analysis of cell 70 showed that the Inconel cathode was rather stable and only minor sights of corrosion were observed. It can be expected that the Inconel foam would be stable enough in an extended test as well. On the contrary, the nickel foam anode was heavily oxidized after the 350 h test. The pores were partly blocked by grown oxide layers, worsening the ability of the electrode to work as a gas diffusion electrode. The nickel foam which was used as current collector showed strong corrosion as well with closed pores and relatively thick oxide layers which most likely worsened the contact in between the electrode and the current collector; the continuously growing R_s of the cell (compare figure 7.6) substantiates this assumption.

Beside the corrosion of the anode, it was seen that the entire cell suffered from delamination of the electrodes and cross-plane cracks through the electrolyte structure. Cells that were produced in a similar similar manner showed comparable cracks in the unused condition, but less pronounced, indicating that the cell structure was weakened during the electrolysis process to some extent. On the other hand it was seen that the electrolyte structure bonded well to the Inconel foam. This could mean that the electrolyte structure is stable under the harsh conditions of the test, but delaminated stronger from the metal foams on the anodic side due to oxide formation at the TPB. It should be stated at this point that the cross-plane and in-plane cracks are of minor importance during the electrolysis process as long as they are filled by the aqueous electrolyte, thereby ensuring good conductivity and gas tightness between the cathode and the anode.

7.6 CONCLUSION

Two similar metal foam based electrolysis cells with cobalt activated anodes and molybdenum activated cathodes were produced. Aqueous KOH was immobilized in a porous $SrTiO_3$ structure. One of the cells was tested under potentiostatic conditions with a polarization of 1.5 V for 80 h and the other was tested under galvanostatic conditions with a current density of 640 $mA\,cm^{-2}$ for 350 h. Both cells showed an initial activation period during the first 5 - 10 h; a current density of almost 1.5 $A\,cm^{-2}$ was measured at the cell polarized with 1.5 V while the lowest cell voltage measured for the cell under galvanostatic conditions was as low as 1.44 V. Strong degradation of the cell under 1.5 V led to abortion of the measurement after 80 h since the current density was too low.

The measurements of the cell under galvanostatic conditions were performed for 350 h; degradation occurred (after the initial activation period) for ca. 50 h, before the 5 h averaged cell voltage stabilized. Large voltage peaks of up to 2.9 V lasting for up to one hour were observed during the measurement.

The microstructure of both cells was analyzed using scanning electron microscopy. Vertical and horizontal cracks were observed throughout the electrolyte structure. These cracks are most probably filled with aqueous elec-

trolyte during operation not influencing significantly the cell performance. It was shown that the Inconel foam cathode was relatively stable under the harsh operating conditions and it is believed to be able to withstand also more extended measurement periods. The nickel foam was oxidized heavily, especially on the cell used for the galvanostatic measurement; the pores were partly blocked. For future investigations it is therefore necessary to identify more corrosion resistant materials for the anode.

8

OVERALL DISCUSSION, CONCLUSION AND OUTLOOK

This chapter provides an overall discussion on the findings of the exploratory work that was performed in this study. A summary of the experimental results is presented. Furthermore, an outlook of future research that should be performed in order to further improve the electrolysis cell characteristics is discussed.

8.1 OVERALL DISCUSSION

8.1.1 *High temperature and pressure test setups*

The foam based electrolysis cells that were invented during this study were tested in two different testing setups, both allowing tests at a temperature of up to 250 °C and a pressure of 95 bar. Electrolysis cells without added electrocatalyst as well as with electro-deposited Ag catalyst on the anode were tested in the "Single atmosphere high temperature and pressure setup" described in chapter 3.2. The results are presented in chapter 5. Electrolysis cells which were activated by cobalt and molybdenum were tested in the "Automatized high temperature and pressure setup" described in chapter 3.5 and the results are presented in chapter 6 and 7. The main differences in between the two setups were:
a) The cells "Single atmosphere high temperature and pressure setup" where supplied with steam by partly evaporation of an aqueous solution in the bottom of the autoclave, while the cells tested in the "Automatized high temperature and pressure setup" where supplied with steam generated in a catalytic burner with the possibility to produce reducing or oxidizing atmospheres.
b) The anode and cathode of the cells were tested in the same atmosphere in the "Single atmosphere high temperature and pressure setup" until they were polarized to such a degree that hydrogen and oxygen were formed at the cathode and the anode, respectively. The "Automatized high temperature and pressure setup" allowed for cell testing at reducing or oxidizing atmospheres also without cell polarization.
c) Measurements in the "Single atmosphere high temperature and pressure setup" where time limited due to safety precautions while the "Automatized high temperature and pressure setup" allowed for continuous testing.

Electrochemical tests were performed with a Gamry potentiostat. All type of cells were analyzed using cyclic voltammetry and electrochemical impedance spectroscopy. Although the measurements have not been performed in the

Table 8.1: Obtained current densities, R_s and R_p for three different types of cells at high temperatures and pressures for three different types of cells. Cell type 1: Inconel foam cathode, nickel foam anode, cell type 2: Inconel foam cathode, nickel foam anode with Ag deposition, cell type 3: Molybdenum activated Inconel foam cathode with cobalt oxide nickel foam anode.

Cell type	Temp. [°C] / Press. [bar]	$E_{rev(t,p,m)}$	Current density [A cm^{-2}] at		R_s [mΩ cm^2]	R_p [mΩ cm^2]
			1.5 V	1.75 V		
1 (Ni | Inc)	240 / 39.0	1.184	0.68	1.57	112	328
2 (Ni+Ag | In)	247 / 42.0	1.181	0.9	2.0	124	126
3 (Ni+Co | Inc+Mo)	250 / 40.0	1.176	1.11	2.23	151	77

same setup, it is possible to compare the obtained results. The reproducibility of the obtained results was checked at least one time for each type of cell. Table 8.1 compares three different types of cells (Cell type 1: Inconel foam cathode, nickel foam anode; cell type 2: Inconel foam cathode, nickel foam anode with Ag deposition; cell type 3: Molybdenum activated Inconel foam cathode, cobalt oxide activated nickel foam anode). Cell type 1 and 2 was analyzed in chapter 5, Cell type 3 was analyzed in chapters 6 and 7. The serial resistance R_s varied from 112 mΩ cm^2, 124 mΩ cm^2 to 151 mΩ cm^2 for cell 1, 2 and 3, respectively. Differences may occur from different thicknesses of the electrolyte structure, differences in the quality of the connections or concentration changes in cell 3 due to longer measurement time. The polarization resistance R_p varied from 328 mΩ cm^2, 126 mΩ cm^2 to 77 mΩ cm^2 for cell 1, 2 and 3, respectively. It is obvious that the activation with Co and Mo significantly improved the cell performance.

Table 8.2 shows the IR- compensated cell voltage of cell 1, 2 and 3 at a current density of 0.5 A cm^{-2}, 1.0 A cm^{-2} and 2.0 A cm^{-2}. The IR compensated polarization losses U_{pol} were obtained by equation 8.1, where $U_{cell,IR}$ is the IR compensated cell voltage calculated by equation 8.2 and $E_{rev(t,p,m)}$ is the reversible cell voltage as a function of the concentration of the electrolyte, temperature and pressure (compare equation 2.9). I is the current density. U_{pol} varied from 296 mV, 219 mV to 144 mV at a current density of 1.0 A cm^{-2} for cell 1, cell 2 and cell 3, respectively. The significant differences verify the importance of proper catalyst selection. The differences in between the cells are even bigger if the difference in R_s is taken into consideration: R_s should be equal for all cells if they are produced and tested under 100 % similar conditions.

Table 8.2: IR_s compensated cell voltages ($U_{cell,IR}$) and polarization losses (U_{pol}) for three different types of cells at high temperatures and pressures. Cell type 1: Inconel foam cathode, nickel foam anode, cell type 2: Inconel foam cathode, nickel foam anode with Ag deposition, cell type 3: Molybdenum activated Inconel foam cathode with cobalt oxide nickel foam anode.

Cell type	Temp. [°C] / Press. [bar]	$U_{cell,IR}$ [V] (IR_s - comp.) at			U_{pol} [mV] at		
		0.5 A cm^{-2}	1.0 A cm^{-2}	2.0 A cm^{-2}	0.5 A cm^{-2}	1.0 A cm^{-2}	2.0 A cm^{-2}
1 (Ni | Inc)	240 / 39.0	1.39	1.48	-	206	296	-
2 (Ni+Ag | Inc)	247 / 42.0	1.34	1.4	1.5	159	219	319
3 (Ni+Co | Inc+Mo)	250 / 40.0	1.27	1.32	1.39	94	144	214

$$U_{pol} = U_{Cell,IR} - E_{rev(t,p,m)} \tag{8.1}$$

$$U_{cell,IR} = U_{cell} - I\,R_s \tag{8.2}$$

Comparing the results from the high temperature and pressure measurements in table 8.1 to the results from the measurements in the low temperature measurement setup, as displayed in figure 3.5, gives an impression on how significantly the current density of an alkaline electrolysis cell can be increased by increasing the temperature. The analyzed Raney-nickel electrode obtained a current density of 40 mA cm^{-2} at an applied cell voltage of 1.75 V and a temperature of 100 °C. Cell 1, 2 and 3 from table 8.1 reached current densities of 1.57 A cm^{-2}, 2.0 A cm^{-2} and 2.23 A cm^{-2} at temperatures and pressures around 250 °C and 40 bar. The Raney-nickel electrode reached a current density of 200 mA cm^{-2} at a relatively high cell voltage of 2.24 V at 100 °C. It should be stressed out that neither the Raney-nickel electrode nor the low temperature measurement system were optimized at the time the measurements were taken. Nevertheless, a significant improvement of the obtained current densities is obtained in case the high temperature measurements are compared to literature data. Divisek et al. reached a current density 400 mA cm^{-2} at a cell voltage of 1.55 V and a temperature of 100 °C on a Raney-nickel cell [19]. A current density 1 A cm^{-2} was reported at 2.12 V on a cell with a $NiFe(OH)_2$ anode and a Pt coated steel cathode [93] at 58 °C.

8.2 CONCLUSION

Since electricity generation from renewable and sustainable sources like wind and sun is strongly growing and in periods of high wind speeds and solar radiation more energy is produced than used, it is necessary to store the excess of produced energy. Water electrolysis was identified as one promising

technology to store the excess energy chemically in the form of hydrogen (and oxygen). Alkaline electrolysis is well proven and large hydrogen production facilities up to 160 MW have been built.

It was demonstrated that increasing the operation temperature of an alkaline electrolysis cell can reduce the losses significantly, thereby increasing the electrical efficiency and decreasing the hydrogen production costs. Operation at elevated pressures can furthermore reduce the investment costs. Measurement systems were designed and constructed to conduct electrochemical measurements at temperatures up to 250 °C and a pressure of 100 bar. The obtained results are as follows:

- The electrical conductivity of aqueous solutions of potassium hydroxide with a concentration of 35 wt%, 45 wt% and 55 wt% KOH was measured over a wide temperature range by the van der Pauw method. The 45 wt% solution showed the highest conductivity at high temperatures (3.0 S cm^{-1} at 209 °C). The conductivity of aqueous potassium hydroxide immobilized in a nano-porous structure, was measured for the same concentrations. The conductivity of the 45 wt% immobilized solution at ca. 200 °C was 0.84 S cm^{-1}, higher than those of 35 wt% and 55 wt% with 0.67 S cm^{-1} and 0.73 S cm^{-1}, respectively. A cubic regression was found adequate to describe the temperature dependence of the conductivity in the temperature range 25 °C - 200 °C.

- A new type of alkaline electrochemical cell has been developed and tested. Aqueous potassium hydroxide immobilized in a nano-porous $SrTiO_3$ structure and metal foam based electrodes were used as key-components. Current densities of almost 1.0 A cm^{-2} at 240 °C and 37 bar have been reached at 1.5 V, thereby achieving an electrical efficiency of almost 100.0 % at this current density. Ag was used as catalyst for the oxygen evolution reaction in the mentioned cell. At the industrial more relevant cell voltage of 1.75 V (industrial electrolysis systems are usually operated at or above this voltage, compare table 5 from [15]), corresponding to an electrical efficiency of 84.5 %, the current density reached 2.0 A cm^{-2} and is thereby better than the targets of the US Department of Energy DOE for 2017. Due to the fact that no scarce materials are used and metal foams are widely used in industrial processes, it is possible to produce the metal foam based electrolysis cells at raw material prices under 1000 € m^{-2}, equal to 67 € kW_{el}^{-1} if operated at 1.0 A cm^{-2}.

- Two similar electrolysis cells with foam based electrodes activated with cobalt and molybdenum, and the aqueous KOH electrolyte immobilized in a porous matrix of $SrTiO_3$, were measured at 150 °C, 200 °C and 250 °C and a pressure of 40 bar. The performance of the cells increased with increasing temperature. At an applied cell voltage of 1.5 V current densities of 0.23 A cm^{-2}, 0.36 A cm^{-2} and 1.11 A cm^{-2} were obtained at 150 °C, 200 °C and 250 °C, respectively. The current densities obtained at an

applied cell voltage of 1.75 V were as high as 0.69 A cm^{-2}, 0.9 A cm^{-2} and 2.3 A cm^{-2} at 150 °C, 200 °C and 250 °C, respectively. The conductivity of the immobilized electrolyte (45 wt% KOH) at 150 °C, 200 °C and 250 °C was 0.75 S cm^{-1}, 0.93 S cm^{-1} and 1.27 S cm^{-1}, respectively. Activation and passivation processes were observed at 250 °C; i.e. one cell degraded strongly during a 100 h lasting test, while the other recovered its initial performance during this time, thereby indicating that at least one of the indicated passivation processes is reversible. Possible degradation mechanisms include oxidation and corrosion processes at the anodic current collector or the anode itself, concentration changes in the electrolyte or electrode flooding or drying. Furthermore, it is possible that bubbles formed at the electrode-electrolyte interface were trapped and partially blocked it.

- Two similar metal foam based electrolysis cells with cobalt activated anodes and molybdenum activated cathodes were produced. Aqueous KOH was immobilized in a porous $SrTiO_3$ structure (The cells were produced in the same way as those described above). One of the cells was tested under potentiostatic conditions with a polarization of 1.5 V for 80 h and the other cell was tested under galvanostatic conditions with a current density of 640 mA cm^{-2} for 350 h; the tests were performed at 250 °C and 40 bar. Both cells showed an initial activation period during the first 5-10 h; a current density of almost 1.5 A cm^{-2} was measured for the cell polarized with 1.5 V while the lowest cell voltage measured for the cell under galvanostatic polarization was as low as 1.44 V. Strong degradation of the cell under potentiostatic conditions led to abortion of the measurement after 80 h. The cell under galvanostatic polarization showed degradation for ca. 50 h (after an initial activation period), before the 5 h averaged cell voltage stabilized at ca. 1.7 V. Large voltage peaks of up to 2.9 V lasting for up to one hour were observed during the measurement. The microstructure of both cells was analyzed using scanning electron microscopy. Vertical and horizontal cracks were observed throughout the electrolyte structure. These cracks could have been filled with aqueous electrolyte during operation, thereby not influencing the cell performance. On the other hand it is possible that they were filled with gas bubbles, which might be trapped and influenced the cell performance significantly. It was shown that the Inconel foam cathode was relatively stable under the harsh operating conditions and it is believed to be able to withstand also more extended measurement periods. The nickel foam was oxidized heavily, especially on the cell used for the galvanostatic measurement; the pores were partly blocked. For future investigations it is therefore necessary to identify more corrosion resistant structural materials for the anode, i.e. a backbone which can support NiO, or other promising electro-catalysts like Co_3O_4 which seems to be excellent electro-catalyst for the OER.

Overall it can be concluded that a new type of alkaline electrolysis cell was developed within this research work; a patent application was submitted [87]. The obtained efficiency at the high current densities is among the best known from literature. Cobalt and molybdenum activated cells performed better than cells with silver activated anodes, which were better than the cells without further activation. The electrolysis cells have been shown to operate for 350 h. Main problems remain to be solved are the too fast oxidation of the anode and the mechanical stability of the cell structure.

8.3 OUTLOOK

8.3.1 *Optimization of electro-catalysts*

Electro-catalysts for the oxygen evolution reaction, OER, and the hydrogen evolution reaction, HER, have been identified in various studies. Nickel is resistant against corrosion at temperatures up to 100 °C in caustic alkaline environment and furthermore electro-catalytically active for both the HER [36, 79] and OER [44, 46] (in the form of its oxide). Since the too fast oxidation of the nickel anode was identified as one of the possible reasons for cell degradation, it is necessary to identify and analyze more resistant nickel alloys. This could for example be Inconel loaded with an appropriate catalyst.

It has also been shown that the surface structure of the electrode is important, i.e. high specific surface area as well as connectivity of porosity and of the electron conducting phase. The cathode (Inconel foam) of the cell proposed here has already a relatively high specific surface area, but both the anodes and the cathodes surface area could for example be further optimized by the use of Raney metal coatings on the foam. Raney nickel is one of the best performing electrode materials for the HER [106]; it is produced from Ni-Al or Ni-Zn alloys from which the Al or Zn is chemically etched out in concentrated KOH, resulting in a highly nano-porous structure. Ni-Mo composites have shown to enhance the HER [107], i.e. the results presented above were obtained with Mo added to the surface layer of the solid structure used to immobilize the electrolyte, thereby creating an activated surface at the interface with the electrode. Raney type Ni-Mo alloys hold great promise for further performance enhancement. Optimization of the catalyst composition and loading has to be carried out. Methods to deposit the catalyst close to the three phase boundary could be electrodeposition, impregnation or dip-coating for both the HER and the OER electrodes. The use of Raney metals for the OER may be limited due to the fact that the obtained nano structure will be filled with oxides and thereby loose the increased specific surface area. Co_3O_4 and Co- based spinel oxides are known to be very good electro-catalysts for the OER [82] and should be tested in combination with the metal foams after an appropriate deposition method has been selected. In situ activation with cobalt oxides [96] could be a promising method, i.e. of Inconel foams.

An important step towards up-scaling cell production could be achieved if the proposed electro-catalysts were already introduced in the delivered metal foams. The Inconel foam cathodes investigated in this work were produced by coating a Nickel foam with an Inconel layer [86]. Due to its high nickel and molybdenum content it is very active for the HER as delivered. The producer of those foams also offers Ni-Al coatings, which could be tested for as Raney-type Ni electro-catalysts for the HER. Customized coatings of a Ni-Al-Mo alloy may also be delivered and considered as very promising. The same holds true for the anodes; customized coatings optimized for corrosion resistance and a good electro-catalytic activity for the OER could be applied directly at the producers facilities.

8.3.2 *Structure optimization*

The structure of the cell has been improved during the project towards higher current density and mechanical stability. Further structural optimization should be performed by identifying the optimal electrode (metal foam) thickness and pore-size. During sintering of the cells, horizontal and vertical cracks in the electrolyte structure occurred in some cases. The cracks will most likely be filled with the aqueous electrolyte during operation and not disturb the electrochemical performance, but the cracks are weakening the mechanical strength of the cells and provide a potential channel for gas diffusion. Gas bubbles might be trapped in this cracks as well. The cracks are probably originating from the production process step in which a pellet is pressed in an uni-axial press. Other fabrication methods such as tape-casting have to be implemented in order to scale up, thereby also solving the cracking problem. Possibilities to implement a water barrier to prevent blocked pores in the gas diffusion electrodes should be analyzed. This water barrier could for example be a hydrophobic PTFE layer.

8.3.3 *Long term stability*

The cells have shown to work for 350 h in an initial “long term” test. Aside from the too fast oxidation of the nickel foam some degradation occurred most likely originating from the measurement setup (too high current densities for the utilized connection wires), and lacking precise control of the operating conditions (electrolyte dilution or drying). Other cell degradation mechanisms, i.e. corrosion or deactivation of the catalysts, and bubble formation and trapping, may play a role as well. While the connection wires diameter can easily be increased to allow for the unexpectedly high current densities, precision in controlling the operating parameters is a greater challenge. Implementing a possibility to the test setup to keep the electrolyte concentration in the cell constant, for example by materials with suitable fine pores connected to a reservoir of KOH (aq), will allow for operation at a certain electrolyte concentration.

Extended long term tests of the cell performance over a period of at least 1000 h should be initiated. The cathode and anode overpotentials should be individually determined in these studies, using a suitable reference electrode. Although it can be expected from literature and own experiments that the overpotential from the OER will be dominating, it is important to precisely determine both performance and durability characteristics of each electrode. Even longer tests should be initiated if the identified problems (too fast oxidation, structural problems, electrolyte concentration, steam supply) are solved.

8.3.4 *Fuel cell performance*

A great advantage of the here shown electrolysis cells is their high efficiency and high current density along with a rather simple, scalable production method and low raw material costs. In order to re-transform the chemical energy into electrical energy, a fuel cell would be feasible. In principle it is possible to use the cell described here also as a fuel cell. This remains to be established experimentally.

BIBLIOGRAPHY

[1] Mogens Bjerg Mogensen, Frank Allebrod, Jacob R. Bowen, Christodoulos Chatzichristodoulou, Ming Chen, Sune Dalgaard Ebbesen, Christopher R. Graves, Jonathan Hallinder, Anne Hauch, Peter Vang Hendriksen, Peter Holtappels, Jens Valdemar Thorvald Høgh, S.H. Jensen, Alberto Lapina, Pia Lolk Mollerup, and Xiufu Sun. Electrolysis for integration of renewable electricity and routes towards sustainable fuels. *10th International Workshop on Large-Scale Integration of Wind Power into Power Systems as well as on Transmission Networks for OffshoreWind Farms*, 2011. isbn: 978-3-9813870-3-2.

[2] Federal ministry for the Environment nature Conservation and nuclear Safety (BmU). Renewable energy sources in figures, July 2011. http://www.erneuerbare-energien.de/files/english/pdf/application/pdf/broschuere_ee_zahlen_en_bf.pdf.

[3] The Danish Energy Agency. Danish energy outlook, May 2011. http://www.ens.dk/en-US/Info/FactsAndFigures/scenarios/scenarios/Documents/Danish%20Energy%20Outlook%202011.pdf.

[4] Ø. Ulleberg, T. Nakken, and A. Eté. The wind/hydrogen demonstration system at Utsira in Norway: Evaluation of system performance using operational data and updated hydrogen energy system modeling tools. *International Journal of Hydrogen Energy*, 35(5):1841–1852, 2010.

[5] Christopher Graves, Sune D. Ebbesen, Mogens Mogensen, and Klaus S. Lackner. Sustainable hydrocarbon fuels by recycling co2 and h2o with renewable or nuclear energy. *Renewable and Sustainable Energy Reviews*, 15(1):1 – 23, 2011.

[6] T. Smolinka, M. Günther, and J. Garche. NOW-Studie: Stand und Entwicklungspotenzial der Wasserelektrolyse zur Herstellung von Wasserstoff aus regenerativen Energien. Technical report, NOW, 2011. http://www.now-gmbh.de/fileadmin/user_upload/RE-Mediathek/RE_Publikationen_NOW/NOW-Studie-Wasserelektrolyse-2011.pdf.

[7] D. Raine, R. Williams, H. Strøm, G. Maisonnier, S. Vinot, J. Linnemann, and S. Truemper. Analysis of the current hydrogen cost structure. Technical Report R2H2019PU.1, 2009. http://www.roads2hy.com/r2h_downloads/Roads2HyComR2H2019PU-CurrentH2Costs.pdf.

[8] P. Millet, R. Ngameni, S.A. Grigoriev, N. Mbemba, F. Brisset, A. Ranjbari, and C. Etiévant. PEM water electrolyzers: From electrocatalysis to stack

development. *International Journal of Hydrogen Energy*, 35(10):5043 – 5052, 2010.

[9] Juergen Fischer, Hans Hofmann, Gerhard Luft, and Hartmnt Wendt. Fundamental investigations and electrochemical engineering aspects concerning an advanced concept for alkaline water electrolysis. *AIChE Journal*, 26(5):794–802, 1980.

[10] H. Wendt and H. Hofmann. Cermet diaphragms and integrated electrode-diaphragm units for advanced alkaline water electrolysis. *International Journal of Hydrogen Energy*, 10(6):375–381, 1985.

[11] Ø. Ulleberg. Modeling of advanced alkaline electrolyzers: A system simulation approach. *International Journal of Hydrogen Energy*, 28(1):21–33, 2003.

[12] K. Onda, T. Kyakuno, K. Hattori, and K. Ito. Prediction of production power for high-pressure hydrogen by high-pressure water electrolysis. *Journal of Power Sources*, 132(1-2):64–70, 2004.

[13] Derek Pletcher and Xiaohong Li. Prospects for alkaline zero gap water electrolysers for hydrogen production. *International Journal of Hydrogen Energy*, 36(23):15089–15104, 11 2011.

[14] Frank Allebrod, Christodoulos Chatzichristodoulou, Pia Lolk Mollerup, and Mogens B. Mogensen. Electrical conductivity measurements of aqueous and immobilized potassium hydroxide. *International Journal of Hydrogen Energy*, 37(21):16505 – 16514, 2012.

[15] Kai Zeng and Dongke Zhang. Recent progress in alkaline water electrolysis for hydrogen production and applications. *Progress in Energy and Combustion Science*, 36(3):307–326, 6 2010.

[16] H. Wendt and G. Imarisio. Nine years of research and development on advanced water electrolysis. a review of the research programme of the commission of the european communities. *Journal of Applied Electrochemistry*, 18(1):1–14, 1988. cited By (since 1996) 34.

[17] P. Ragunathan, S. K. Mitra, and M. G. Nayar. Porous nickel electrodes in water electrolysis 1. electrode preparation and polarization studies in strong alkali. *International Journal of Hydrogen Energy*, 6(5):487 – 496, 1981.

[18] W. Hug, J. Divisek, J. Mergel, W. Seeger, and H. Steeb. Highly efficient advanced alkaline electrolyzer for solar operation. *International Journal of Hydrogen Energy*, 17(9):699–705, 1992.

[19] J. Divisek, P. Malinowski, J. Mergel, and H. Schmitz. Improved components for advanced alkaline water electrolysis. *International Journal of Hydrogen Energy*, 13(3):141–150, 1988.

[20] C. W. Bale, P. Chartrand, S. A. Degterov, G. Eriksson, K. Hack, R. Ben Mahfoud, J. Melançon, A. D. Pelton, and S. Petersen. Factsage thermochemical software and databases. *Calphad*, 26(2):189–228, 6 2002.

[21] Rodney L. LeRoy, Christopher T. Bowen, and Donald J. LeRoy. Thermodynamics of aqueous water electrolysis. *Journal of the Electrochemical Society*, 127(9):1954–1962, 1980.

[22] J. Balej. Water vapour partial pressures and water activities in potassium and sodium hydroxide solutions over wide concentration and temperature ranges. *International Journal of Hydrogen Energy*, 10(4):233–243, 1985.

[23] J. Balej. Determination of the oxygen and hydrogen overvoltage in concentrated alkali hydroxide solutions. *International Journal of Hydrogen Energy*, 10(6):365–374, 1985.

[24] D. M. See and R. E. White. Temperature and concentration dependence of the specific conductivity of concentrated solutions of potassium hydroxide. *Journal of Chemical and Engineering Data*, 42(6):1266–1268, 1997.

[25] R. J. Gilliam, J. W. Graydon, D. W. Kirk, and S. J. Thorpe. A review of specific conductivities of potassium hydroxide solutions for various concentrations and temperatures. *International Journal of Hydrogen Energy*, 32(3):359–364, 2007.

[26] D. A. Lown and H. R. Thirsk. Proton transfer conductance in aqueous solution. part 1. - conductance of concentrated aqueous alkali metal hydroxide solutions at elevated temperatures and pressures. *Transactions of the Faraday Society*, 67:132–148, 1971.

[27] V. Yu Yushkevich, I. N. Maksimova, and V. G. Bullan. Electrical conductivity of potassium hydroxide solutions at high temperatures. *Elektrokhimiya*, 3(12):1491–3, 1967.

[28] L. J. Van Der Pauw. A method of measuring specific resistivity and hall effect of discs of arbitrary shape. *Philips Res. Rep.*, 13:1–9, 1958.

[29] Frank Allebrod, Christodoulos Chatzichristodoulou, Pia Lolk Mollerup, and Mogens B. Mogensen. Electrical conductivity measurements of aqueous and immobilized potassium hydroxide. *International Journal of Hydrogen Energy*, 37(21):16505 – 16514, 2012.

[30] Ph Vermeiren, J. P. Moreels, A. Claes, and H. Beckers. Electrode diaphragm electrode assembly for alkaline water electrolysers. *International Journal of Hydrogen Energy*, 34(23):9305–9315, 2009.

[31] S. Srinivasan. *Fuel cells : from fundamentals to applications*. Springer, New York, N.Y., 2006.

[32] Hartmut Wendt. *Electrochemical engineering : science and technology in chemical and other industries*, pages 27–28. Springer-Verlag, New York, 1999.

[33] H. Wendt and V. Plzak. Electrocatalytic and thermal activation of anodic oxygen- and cathodic hydrogen-evolution in alkaline water electrolysis. *Electrochimica Acta*, 28(1):27–34, 1983.

[34] M.R.G. de Chialvo and A.C. Chialvo. Hydrogen evolution reaction: Analysis of the volmer-heyrovsky-tafel mechanism with a generalized adsorption model. *Journal of Electroanalytical Chemistry*, 372(1-2):209–223, 1994.

[35] M. H. Miles, S. Srinivasan, and Y. H. Huang. Oxygen electrode reaction in alkaline solutions on oxide electrodes prepared by the thermal decomposition method. *J Electrochem Soc*, 125(12):1931–1934, 1978.

[36] J. K. Nørskov, T. Bligaard, A. Logadottir, J. R. Kitchin, J. G. Chen, S. Pandelov, and U. Stimming. Trends in the exchange current for hydrogen evolution. *Journal of the Electrochemical Society*, 152(3):J23–J26, 2005.

[37] J. Ferez, E.R. Gonzalez, and H.M. Villuiias. Hydrogen evolution reaction on gold single-crystal electrodes in acid solutions. *Journal of Physical Chemistry B*, 102(52):10931–10935, 1998. cited By (since 1996) 26.

[38] S. Pandelov, A. K. Pal, J. Meier, and U. Stimming. Unpublished results.

[39] John O'M. Bockris and Amulya K. N. Reddy. *Modern Electrochemistry*. Plenum Press, 1970.

[40] D. Eberhardt, E. Santos, and W. Schmickler. Hydrogen evolution on silver single crystal electrodes - first results. *Journal of Electroanalytical Chemistry*, 461(1-2):76–79, 1999.

[41] S. Trasatti. Work function, electronegativity, and electrochemical behaviour of metals. iii. electrolytic hydrogen evolution in acid solutions. *Journal of Electroanalytical Chemistry*, 39(1):163–184, 1972.

[42] O. Savadogo and D.L. Piron. New hydrogen cathodes in acid medium: Case of nickel electrodeposited with heteropolyacids (hpas). *International Journal of Hydrogen Energy*, 15(10):715–721, 1990.

[43] Andrzej Wieckowski, editor. *Interfacial electrochemistry theory, experiment, and applications*. Marcel Dekker, New York, 1999.

[44] J. Balej. Electrocatalysts for oxygen evolution in advanced water electrolysis. *International Journal of Hydrogen Energy*, 10(2):89–99, 1985.

[45] H. J. Miao and D. L. Piron. Electrodeposition of Ni-transition alloys for the oxygen evolution reaction. *Journal of Applied Electrochemistry*, 21(1):55–59, 1991.

[46] S. Trasatti. Electrocatalysis in the anodic evolution of oxygen and chlorine. *Electrochimica Acta*, 29(11):1503–1512, 11 1984.

[47] S. Trasatti. Electrocatalysis by oxides - attempt at a unifying approach. *Journal of Electroanalytical Chemistry*, 111(1):125–131, 1980.

[48] John O'M Bockris and Takaaki Otagawa. The electrocatalysis of oxygen evolution on perovskites. *Journal of the Electrochemical Society*, 131(2):290–302, 1984.

[49] Houcheng Zhang, Guoxing Lin, and Jincan Chen. Evaluation and calculation on the efficiency of a water electrolysis system for hydrogen production. *International Journal of Hydrogen Energy*, 35(20):10851–10858, 10 2010.

[50] D. Tromans. Oxygen solubility modeling in inorganic solutions: Concentration, temperature and pressure effects. *Hydrometallurgy*, 50(3):279–296, 1998.

[51] P. Ruetschi and R. F. Amlie. Solubility of hydrogen in potassium hydroxide and sulfuric acid. salting-out and hydration. *Journal of Physical Chemistry*, 70(3):718–723, 1966.

[52] M. B. Knaster and L. A. Apel'baum. Solubility of hydrogen and oxygen in concentrated potassium hydroxide solution. *Russian Journal of Physical Chemistry*, 38:120, 1964.

[53] H. A. Pray, C. E. Schweickert, and B. H. Minnich. Solubility of hydrogen, oxygen, nitrogen, and helium in water at elevated temperatures. *Industrial & Engineering Chemistry*, 44(5):1146–1151, 1952.

[54] Betty Y. S. Lin, Donald W. Kirk, and Steven J. Thorpe. Performance of alkaline fuel cells: A possible future energy system? *Journal of Power Sources*, 161(1):474–483, 10/20 2006.

[55] E. Gülzow. Alkaline fuel cells: A critical view. *Journal of Power Sources*, 61(1-2):99–104, 1996.

[56] G. Kreysa and M. Schütze. *DECHEMA Corrosion Handbook - Revised and Extended 2nd Edition*, volume 9. Wiley VCH, 2007.

[57] Bank IC. Electrode - easy - exchange fixture diskfix, 2009. http://www.bank-ic.de/encms/downloads/diskfix-e.pdf.

[58] Gaskatel. Hydrogen reference electrode, 2012. http://gaskatel.org/eng/produkte/hydroflex/eng_hydroflex_index.html.

[59] E.E. Oguzie, G.N. Onuoha, and A.I. Onuchukwu. The inhibition of aluminium corrosion in potassium hydroxide by "congo red" dye, and synergistic action with halide ions. *Anti-Corrosion Methods and Materials*, 52(5):293–298, 2005. cited By (since 1996) 9.

[60] Karl A. Schwetz and Juergen Hassler. Stability of high-performance ceramics against liquid corrosion. part 1. experimental. *CFI, Ceramic Forum International*, 79(10):D15–D18, 2002.

[61] J. M. Gras and P. Spiteri. Corrosion of stainless steels and nickel-based alloys for alkaline water electrolysis. *International Journal of Hydrogen Energy*, 18(7):561–566, 1993.

[62] A. Garat and J. Gras. Corrosion study of nickel for alkaline water electrolysis. *International Journal of Hydrogen Energy*, 8(9):681–688, 1983.

[63] Special Metals Corporation. High-performance alloys for resistance to aqueous corrosion, 2000. http://www.specialmetals.com/documents/SM

[64] F. W. Pement, I. L. W. Wilson, and R. G. Aspden. Stress corrosion cracking studies of high nickel austenitic alloys in several high temperature aqueous solutions. *Materials Performance*, 19(4):43–49, 1980.

[65] Ane Sælland Christiansen. Immobilized K_2CO_3 electrolyte for low-temperature CO_2 electrolysis, 2010.

[66] Heaney Michael. *Electrical Conductivity and Resistivity*, volume null of *The Measurement, Instrumentation and Sensors Handbook on CD-ROM*. CRC Press, 02/26; 2010/08 1999.

[67] R. J. Guanti and P. J. Moran. Measurement of electrolytic conductivity in highly conducting solutions. *Journal of Applied Electrochemistry*, 16(5):678–682, 1986.

[68] Yu N. Shebeko, S. G. Tsarichenko, A. V. Trunev, A. Ya Korol'chenko, and A. Yu Kaplin. The influence of inert retardants on the combustion of hydrogen-oxygen mixtures under elevated temperatures and pressures. *Combustion, Explosion, and Shock Waves*, 30(2):183–188, 1994.

[69] V. Schroeder and K. Holtappels. Explosion characteristics of hydrogen-air and hydrogen-oxygen mixtures at elevated pressures. *International Conference on Hydrogen Safety*, 2005.

[70] M. H. Miles, G. Kissel, P. W. T. Lu, and S. Srinivasan. Effect of temperature on electrode kinetic parameters for hydrogen and oxygen evolution reactions on nickel electrodes in alkaline solutions. *Journal of the Electrochemical Society*, 123(3):332–336, 1976.

[71] O. Führer, S. Rieke, C. Schmitz, B. Willer, and M. Wollny. Alkaline eloflux fuel cells and electrolysis cells using a new kind of gas diffusion electrodes. *International Journal of Hydrogen Energy*, 19(4):343–348, 1994.

[72] Z. Moroń. Investigations of van der Pauw method applied for measuring electrical conductivity of electrolyte solutions: Measurement of electrolytic conductivity. *Measurement: Journal of the International Measurement Confederation*, 33(3):281–290, 2003.

[73] W. M. Vogel, K. J. Routsis, V. J. Kehrer, D. A. Landsman, and J. G. Tschinkel. Some physicochemical properties of the koh-h2o system range: 55 to 85 weight *Journal of Chemical and Engineering*, 12(4):465–472, 1967.

[74] Ph Vermeiren, R. Leysen, H. Beckers, J. P. Moreels, and A. Claes. The influence of manufacturing parameters on the properties of macroporous Zirfon ® separators. *Journal of Porous Materials*, 15(3):259–264, 2008.

[75] H. Wendt, H. Hofmann, and V. Plzak. Materials research and development of electrocatalysts for alkaline water electrolysis. *Materials Chemistry and Physics*, 22(1-2):27–49, 1989.

[76] Ruth Knibbe, Anne Hauch, Johan Hjelm, Sune D. Ebbesen, and Mogens Mogensen. Durability of solid oxide cells. *Green*, 16:141–169, 2011.

[77] G. Kreysa and H. J. Kuelps. Experimental study of the gas bubble effects on the ir drop at inclined electrodes. *Journal of the Electrochemical Society*, 128(5):979–984, 1981.

[78] P. S. Jørgensen, K. V. Hansen, R. Larsen, and J. R. Bowen. High accuracy interface characterization of three phase material systems in three dimensions. *Journal of Power Sources*, 195(24):8168–8176, 12/15 2010.

[79] L. A. Kibler. Hydrogen electrocatalysis. *ChemPhysChem*, 7(5):985–991, 2006.

[80] E. Gülzow, N. Wagner, and M. Schulze. Preparation of gas diffusion electrodes with silver catalysts for alkaline fuel cells. *Fuel Cells*, 3(1-2):67–72, 2003.

[81] M. A. Kostowskyj, R. J. Gilliam, D. W. Kirk, and S. J. Thorpe. Silver nanowire catalysts for alkaline fuel cells. *International Journal of Hydrogen Energy*, 33(20):5773–5778, 10 2008.

[82] M. Hamdani, R. N. Singh, and P. Chartier. Co_3O_4 and Co-based spinel oxides bifunctional oxygen electrodes. *International Journal of Electrochemical Science*, 5(4):556–577, 2010.

[83] J. Divisek, H. Schmitz, and J. Balej. Ni and mo coatings as hydrogen cathodes. *Journal of Applied Electrochemistry*, 19(4):519–530, 1989.

[84] John Banhart. Manufacture, characterisation and application of cellular metals and metal foams. *Progress in Materials Science*, 46(6):559–632, 2001.

[85] F. Bidault, D. J. L. Brett, P. H. Middleton, N. Abson, and N. P. Brandon. A new application for nickel foam in alkaline fuel cells. *International Journal of Hydrogen Energy*, 34(16):6799–6808, 2009.

[86] M. Gerber, R. Poss, A. Tillmann, G. Walther, B. Kieback, K. Wolf, and F. Hanel. Fabrication and properties of stainless steel foams for sandwich panels. *Journal of Sandwich Structures and Materials*, 14(2):181– 196, 2012.

[87] F. Allebrod, C. Chatzichristodoulou, P. L. Mollerup, and M. B. Mogensen. High performance reversible electrochemical cell for H_2O electrolysis or conversion of CO_2 and H_2O to fuel, 2012. Patent Pending No. 12164019.7-2119.

[88] S. Guo, D. Li, Q. Guo, Z. Wu, H. Peng, and J. Hu. Investigation on hot workability characteristics of inconel 625 superalloy using processing maps. *Journal of Materials Science*, 47(15):5867–5878, 2012. cited By (since 1996) 1.

[89] C. Graves. RAVDAV data analysis software, version 0.9.7, 2012.

[90] F. W. Pement, I. L. W. Wilson, and R. G. Aspden. Stress corrosion cracking studies of high nickel austenitic alloys in several high temperature aqueous solutions. *Materials Performance*, 19(4):43–49, 1980.

[91] W. M. Haynes, editor. *CRC Handbook of Chemistry and physics : A ready-reference book of chemical and physical data*. CRC Press, Boca Raton, FL, 2011.

[92] Sune Dalgaard Ebbesen, Søren Højgaard Jensen, Anne Hauch, and Mogens Mogensen. *High temperature electrolysis*. Electrolysis. 2012.

[93] X. Li, F. C. Walsh, and D. Pletcher. Nickel based electrocatalysts for oxygen evolution in high current density, alkaline water electrolysers. *Physical Chemistry Chemical Physics*, 13(3):1162–1167, 2011.

[94] Detlef Stolten. *Alkaline Electrolysis - Introduction and Overview*, page 245. Hydrogen and Fuel Cells: Fundamentals, Technologies and Applications. Wiley-VCH, 2010.

[95] A. Ursúa, L. M. Gandís, and P. Sanchis. Hydrogen production from water electrolysis: Current status and future trends. *Proceedings of the IEEE*, 100(2):410–426, 2012.

[96] T. Schmidt and H. Wendt. Electrocatalysis of cathodic hydrogen and anodic oxygen evolution in alkaline water electrolysis by in situ activation procedures. *Electrochimica Acta*, 39(11-12):1763–1767, 1994.

[97] G. Schiller, R. Henne, and V. Borck. Vacuum plasma spraying of high-performance electrodes for alkaline water electrolysis. *Journal of Thermal Spray Technology*, 4(2):185–194, 1995.

[98] K. Bouzek, J. Hnát, M. Paidar, J. Schauer, and J. Žitka. Novel polymer electrolyte and catalytic layer binder for process of the alkaline water electrolysis. World Hydrogen Energy Congress 2012, Toronto, 2012.

[99] G.S. Tasic, S.P. Maslovara, D.L. Zugic, A.D. Maksic, and M.P. Marceta Kaninski. Characterization of the Ni-Mo catalyst formed in situ during hydrogen generation from alkaline water electrolysis. *International Journal of Hydrogen Energy*, 36(18):11588–11595, 2011.

[100] J. Bao and D.D. Macdonald. Kinetics of the hydrogen electrode reaction on platinum in alkaline solutions at elevated temperatures. volume 11, pages 1–11, Washington, DC, 2008.

[101] C. Davidson, G. Kissel, and S. Srinivasan. Electrode kinetics of the oxygen evolution reaction at $NiCo_2O_4$ from 30% KOH. Dependence on temperature. *Journal of Electroanalytical Chemistry*, 132(C):129–135, 1982.

[102] E Cussler. *Diffusion : mass transfer in fluid systems*. Cambridge University Press, New York, 1997.

[103] Joseph Hirschfelder. *Molecular theory of gases and liquids*. Wiley, London, 1964.

[104] M. H. Miles. Effect of temperature on electrode kinetic parameters for hydrogen and oxygen evolution reactions on nickel electrodes in alkaline solutions. *Journal of the Electrochemical Society*, 123(3):332, 1976.

[105] Raymond Schmid. Electrolysis for grid balancing - where are we?, 2012. "http://www.hydrogennet.dk/fileadmin/user_upload/PDF-filer/Aktiviteter/Kommende_aktiviteter/Elektrolysesymposium/Raymond_Schmid_Hygrogenics_120510_Copenhagen_Symposium_Final.pdf".

[106] P. W. Brennecke and H. H. Ewe. Hydrogen evolution of highly porous raney nickel cathodes in alkaline electrolyte. *Energy Conversion and Management*, 31(6):585–594, 1991.

[107] L. Birry and A. Lasia. Studies of the hydrogen evolution reaction on raney nickel-molybdenum electrodes. *Journal of Applied Electrochemistry*, 34(7):735–749, 2004.

DECLARATION

I hereby declare that this thesis is my own work and effort. Furthermore, I certify that the material has not been submitted, either in whole or in part, for a degree at this or any other university.

Roskilde, November 2013

Frank Allebrod